Physik-Department E11
Lehrstuhl für
Laser- und Röntgenphysik

Attosecond Metrology – Characterization of X-ray Free-electron Laser Pulses via Angular Streaking and Application of Attosecond Spectroscopy on Liquid H_2O

Rupert P. Heider, M. Sc.

Vollständiger Abdruck der von der
Fakultät für Physik der Technischen Universität München
zur Erlangung des akademischen Grades eines

Doktors der Naturwissenschaften

genehmigten Dissertation.

Vorsitzender:
Prof. Dr. Andreas Weiler

Prüfer der Dissertation:
1. Prof. Dr. Reinhard Kienberger
2. Prof. Dr. Christian Back

Die Dissertation wurde am 16.05.2018 bei der
Technischen Universität München eingereicht und durch die
Fakultät für Physik am 11.09.2018 angenommen.

Zusammenfassung

Freie-Elektronen-Laser (FELs) sind fest etablierte, konkurrenzlose Quellen von extrem kohärenten, ultrahellen Röntgenpulsen im Femtosekundenbereich und ermöglichen somit hochaufgelöste, ultraschnelle Experimente mit Röntgenstrahlung. Dies macht sie zu einem leistungsfähigen Werkzeug für etliche Felder der Naturwissenschaften. Röntgen-FELs basieren vorwiegend auf dem Prinzip der selbstverstärkten spontanen Emission (SASE) und erzeugen Pulse mit zufälliger, noch ungeklärter zeitlicher Substruktur, welche sich erheblich von Schuss zu Schuss unterscheidet. Darüber hinaus zeigen Röntgenpulse aus einem FEL eine beträchtliche Schwankung der relativen Ankunftszeit zu einer extern synchronisierten, aber unabhängigen Laserquelle. Dies stellt ein erhebliches Problem für ultraschnelle, zeitaufgelöste Anrege/Abfrage-Experimente mit Röntgenpulsen und optischen Laserpulsen dar, da die zeitliche Auflösung auf das Niveau dieser Schwankung begrenzt ist. Bis heute ist keine direkte Messmethode verfügbar, um die Pulsdauer bzw. das zeitliche Intensitätsprofil von einzelnen SASE FEL-Pulsen mit nur wenigen Femtosekunden Dauer exakt zu bestimmen. Eine genaue Pulscharakterisierung wird daher dringend benötigt und stellt eine Grundvoraussetzung für jede Art von ultraschnellen, spitzenintensitätsabhängigen Untersuchungen oder zeitaufgelösten Anrege/Abfrage-Experimenten dar. Darüber hinaus ist auch eine simultane, präzise Bestimmung der relativen Ankunftszeit zwischen Röntgenpuls und optischem Puls für Einzelschüsse schwer erreichbar.

Die Durchführung von winkelaufgelösten Streaking-Messungen an der Linac Coherent Light Source (LCLS) stellen das zentrale Thema dieser Arbeit dar. Für diese Messungen wird ein spezielles, winkelaufgelöstes Spektrometer-Array von 16 konzentrisch angeordneten, einzelnen Flugzeit-Detektoren eingesetzt. Ein neuartiger, selbstentwickelter Rekonstruktionsalgorithmus wird dann für eine direkte, zeitliche Charakterisierung von Röntgen-FEL-Pulsen verwendet. Die zentrale Idee hinter diesem Algorithmus ist eine Integration über das Intensitätssignal von winkelaufgelöst gestreakten Photoelektronen über einer Schwellenenergie. Das Ergebnis stellt die Rekonstruktion des zeitlichen Intensitätsprofils von Röntgenpulsen mittels des Prinzips der *Attoclock* dar. Dadurch wird die erste direkte und eindeutige, nichtinvasive Messung der zeitlichen Substruktur und der Pulsdauer von einzelnen Röntgenpulsen aus einem FEL mit einer Auflösung von wenigen Femtosekunden erreicht. Außerdem wird mit derselben Messung eine simultane, präzise Bestimmung der relativen Ankunftszeit demonstriert. Die charakteristische zeitliche Substruktur von einzelnen Röntgen-FEL-Pulsen wird durch das Retrival aufgelöst. Die erwartete Abfolge von zufälligen Pulsformen, bedingt durch den SASE-Prozess, wird bestätigt und die Pulsdauer zuverlässig bestimmt. Außerdem werden Doppelpulse an einem Röntgen-FEL erfolgreich charakterisiert, indem die Substruktur der einzelnen Pulse, sowie deren Verzögerung eindeutig gezeigt werden. Dieser Ansatz eignet sich somit für eine zuverlässige Pulscharakterisierung in Form eines intelligenten und schnellen Online-Tools. Dies wird dringend benötigt für die Realisierung einer Echtzeit-Pulserkennung an den XFEL-Einrichtungen der nächsten Generation.

In dieser Arbeit wird auch kurz ein weiteres Projekt beschrieben: Eine neuartige und vielseitige, hochmoderne Beamline für Attosekunden-Metrologie, die neue Perspektiven für die nächste Generation von Experimenten in der Attosekunden-Physik eröffnen soll, wird konzipiert und in Betrieb genommen. Die Möglichkeiten dieser neu entwickelten Beamline werden anhand der ersten Untersuchung von Wasser (H_2O) in der flüssigen Phase durch Streaking-Spektroskopie mit Attosekunden-Auflösung demonstriert. Diese Messungen werden im Rahmen einer Kollaboration mit der ETH Zürich durchgeführt. Die Elektronendynamik, sowie die strukturellen Eigenschaften von Wasser auf der molekularen Ebene, insbesondere Wasserstoffbrückenbindungen, sind immer noch unzureichend verstanden. Solvatation in Wasser beeinflusst die elektronische Struktur und die Photoionizations-Dynamik der gelösten Moleküle in hohem Maße. Dementsprechend ermöglicht die Ausweitung der Attosekunden-Spektroskopie auf die flüssige Phase neue Einblicke in die Solvatationsdynamik und ultraschnelle Prozesse in chemischen Systemen in ihrer natürlichen Umgebung. Über die erstmalige Bestimmung einer Verzögerung der Photoemission zwischen den Elektronen der inneren und der äußeren Valenzschalen des H_2O-Moleküls im Attosekunden-Bereich wird kurz berichtet. Die theoretische Interpretation durch dreidimensionale Monte-Carlo-Simulationen der Elektronen-Propagation wird Einblicke in die Mechanismen von Elektronen-Wechselwirkung geben und verlässliche Werte für die mittleren, freien Weglängen von Elektronen in Wasser liefern.

Abstract

Free-electron lasers (FELs) are well-established, unrivalled sources of extremely coherent, ultra-bright X-ray pulses in the femtosecond regime and hence enable high-resolution, ultrafast X-ray experiments, making them a powerful tool for several fields in natural sciences. X-ray FELs are primarily based on the self-amplified spontaneous emission (SASE) process and generate pulses with a still unresolved, stochastic temporal substructure. They considerably differ from shot to shot. Furthermore, X-ray FEL pulses exhibit a substantial, inherent arrival time jitter relative to any externally synchronized yet independent laser source. This presents a considerable issue for ultrafast, time-resolved X-ray pump/optical probe experiments, as it limits the temporal resolution down to the level of that jitter. Up to today, no direct measurement method has become available to accurately determine the pulse duration or rather the substructure of the temporal intensity profile of few-femtosecond SASE FEL pulses on a shot-by-shot basis. An accurate pulse characterization is therefore desperately needed and a fundamental prerequisite for any time-resolved, peak intensity-dependent or ultrafast pump/probe studies. Moreover, a simultaneous, precise determination of the relative optical/X-ray arrival time on a single-shot basis remains elusive as well.

Two-color angular streaking measurements are conducted at the Linac Coherent Light Source (LCLS) and feature the key task of this thesis. These are accomplished by use of a special, angle-resolved spectrometer array of 16 concentrically arranged, individual time-of-flight detectors. A novel, self-developed reconstruction algorithm is applied for a direct X-ray FEL pulse characterization in the time domain. The central idea of the algorithm is a thresholded integration of the angularly streaked photoelectron intensity. The outcomes constitute the reconstruction of the temporal intensity profile of the X-ray pulse via the *attoclock principle*. As a result, the first direct and unambiguous, non-invasive single-shot determination of the temporal substructure and the pulse duration of X-ray pulses emitted by a free-electron laser with few-femtosecond resolution is achieved. A simultaneous, precise determination of the relative arrival time within the same measurement is also successfully demonstrated. The distinctive temporal substructure of single X-ray FEL pulses is clearly resolved by the retrieval. The anticipated series of SASE-induced, random pulse shapes is confirmed and the pulse duration is reliably ascertained. In addition, a single-shot characterization of X-ray FEL double-pulse trains, distinctly revealing the substructure of the two individual pulses as well as their delay, is reported. Thus, this approach is qualified for a smart and fast online tool for reliable pulse characterization, urgently required for the implementation of real-time pulse tagging at the next-generation XFEL facilities.

This thesis also shortly describes a next project: a novel and versatile, state-of-the-art attosecond metrology beamline, designed and commissioned to open new perspectives for next-generation experiments in attosecond physics.

Capabilities of the newly designed beamline are demonstrated by the first-time attosecond streaking spectroscopy measurements on liquid-phase water (H_2O) that are performed within a collaboration with the ETH Zurich. The electron dynamics and structural characteristics of water on the molecular level, particularly of the hydrogen bond, are still understood poorly. Solvation in water highly effects the electronic structure and photoionization dynamics of the solute molecule. Thus, the extension of attosecond spectroscopy to the liquid phase paves the way to new insights into solvation dynamics and ultrafast processes within chemical systems in their natural environment. The first determination of an attosecond photoemission delay between inner- and outer-valence shell electrons of the H_2O molecule is briefly reported. Theoretical interpretation via 3D Monte-Carlo simulations of electron propagation will reveal insights into electron correlation mechanisms and deliver reliable values on mean free paths of electrons in liquid water.

List of Publications

In order of relevance to this work:

Heider, R., Wagner, M. S., Hartmann, N., Ilchen, M., Buck, J., Hartmann, G., Shirvanyan, V., Lindahl, A. O., Grünert, J., Krzywinski, J., Liu, J., Ossiander, M., Lutman, A. A., Maxwell, T., Miahnahri, A. A., Moeller, S. P., Planas, M., Robinson, J., Viefhaus, J., Feurer, T., Kienberger, R., Coffee, R. N., & Helml, W. Online, single-shot characterization of few-femtosecond X-ray temporal pulse substructures at free-electron lasers via angular streaking. submitted to *Nature Communications* (2018).

Hartmann, N., Hartmann, G., **Heider, R.**, Wagner, M. S., Ilchen, M., Buck, J., Lindahl, A. O., Benko, C., Grünert, J., Krzywinski, J., Liu, J., Lutman, A. A., Marinelli, A., Maxwell, T., Miahnahri, A. A., Moeller, S. P., Planas, M., Robinson, J., Kazansky, A. K., Kabachnik, N.M., Viefhaus, J., Feurer, T., Kienberger, R., Coffee, R. N., & Helml, W. Attosecond time–energy structure of X-ray free-electron laser pulses. *Nature Photonics* **12**, 215–220 (2018).

Ossiander, M., Riemensberger, J., Neppl, S., Mittermair, M., Schäffer, M., Duensing, A., Wagner, M. S., **Heider, R.**, Wurzer, M., Gerl, M., Schnitzenbaumer, M., Barth, J. V., Libisch, F., Lemell, C., Burgdörfer, J., Feulner, P. & Kienberger, R. Absolute Timing of the Photoelectric Effect. *Nature* **561**, 374–377 (2018).

Hütten, K., Mittermair, M., Stock, S. O., Beerwerth, R., Shirvanyan, V., Riemensberger, J., Duensing, A., **Heider, R.**, Wagner, M. S., Guggenmos, A., Fritzsche, S., Kabachnik, N. M., Kienberger, R. & Bernhardt, B. Ultrafast quantum control of ionization dynamics in krypton. *Nature Communications* **9**, 719 (2018).

Hutzler, D., Werhahn, J. C., **Heider, R.**, Bradler, M., Kienberger, R., Riedle, E. & Iglev, H. Highly Selective Relaxation of the OH Stretching Overtones in Isolated HDO Molecules Observed by Infrared Pump–Repump–Probe Spectroscopy. *The Journal of Physical Chemistry A* **119**, 6831–6836 (2015).

Bradler, M., Werhahn, J. C., Hutzler, D., Fuhrmann, S., **Heider, R.**, Riedle, E., Iglev, H. & Kienberger R. A novel setup for femtosecond pump-repump-probe IR spectroscopy with few cycle CEP stable pulses. *Optics Express* **21**, 20145–20158 (2013).

Contents

List of Figures

Chapter 1

Introduction

If attosecond techniques do become reality, the immeasurable will have to redefined once again [1].

With this joking sentence, the recipient of the 1999 Nobel prize in chemistry [2] and founder of the femtochemistry – the study of chemical reactions across femtoseconds – Ahmed Zewail [3, 4], has been cited in August 2001. Only a few weeks later, at 11 September 2001, the very first observation of isolated attosecond XUV pulses has been reached by Michael Hentschel and Reinhard Kienberger [5]. Attosecond science (1 as = 10^{-18} s) suddenly increased the temporal resolution of time-resolved spectroscopy by two orders of magnitude [6–10] and thus advanced this field of research from the molecular to the electronic timescale.

One attosecond is a billionth of a billionth of a second: is is the time, light needs to travel the length of two hydrogen atoms. The ratio of one attosecond to one second corresponds to approximately the ratio of one second to the age of the universe. According to the Bohr model of the hydrogen atom, an electron necessitates about 150 attoseconds for one complete orbit of the proton, defining the characteristic timescale for electron dynamics in the electronic shell of atoms and thus constituting the fundamental motivation for attosecond science [11]. Hence, reaching the attosecond timescale has been an important step for ultrafast spectroscopy, as this is the natural timescale for dynamics of many electronic processes, such as the formation or breaking of chemical bonds and electron transfer processes. Many major questions of our century in physics and chemistry cannot be resolved without direct control and observation of electron motion. Ultrafast electron dynamics in atoms and molecules are of broad scientific interest for many modern technologies like optoelectronics, information processing, molecular electronics, photovoltaics and semiconductor electronics. Observing and controlling of electron dynamics in atomic and molecular systems in real time has been a long-time desire [12] and will enable the exploration of the ultimate limits of the aforementioned technologies and the identification of novel ways to approach these limits.

Over the past one and a half decades, attosecond science has become a fast-growing research field and has already revealed plenty new insights into fundamental processes in physics [13, 14]. Attosecond spectroscopy enables an unprecedented look at a wide range

of essential photophysical, photochemical and electrochemical processes: Key achievements comprise exemplary the invention [5, 11, 15, 16] and versatile application [17–19] of the attosecond streak camera, the time-resolved study of Auger decay [20], electron tunneling in atoms [21], attosecond photoionization delays in the gas-phase [18, 22] and from solid-state samples [17, 23, 24], as well as electron localization in molecules [25]. Attosecond techniques have also revealed very promising insight into band-gap dynamics in bulk silicon excited by attosecond pulses [26], electron dynamics in atoms [27] and atomic as well as molecular ions [28, 29], strong-field induced dynamics in dielectrics [30] and finally the determination of the absolute timing of the photoelectric effect [31].

Even in view of these numerous publications so far, the field of attosecond metrology has not even exploited its full potential. The rapid development and the early, striking successes of this still young and exciting research field have been strongly promoted by progressive improvements and extensions of the experimental techniques: from developments concerning lasers and pulse compression via improvement of generation techniques of isolated attosecond pulses through to the design of sophisticated, steadily advanced attosecond beamlines for attosecond streaking measurements. As another step in the experimental and conceptual development and to further advance this research field, a novel and versatile, state-of-the-art attosecond metrology beamline should be developed and commissioned at the *Technical University of Munich (TUM)* within the frame of this thesis. Building on the experimental, hands-on experiences gained from high-end attosecond beamlines operated at the *Max-Planck-Institute of Quantum Optics* [32] within the last decade and incorporating recent experimental developments, this sophisticated and thoroughly designed, new-generation beamline shall open up new experimental perspectives in attosecond metrology.

In contrast to solid and gas phases, attosecond streaking spectroscopy has not been accomplished in the liquid phase yet. Nevertheless, an application of the techniques of attosecond spectroscopy to e.g. the disciplines of chemistry and biology naturally demands an extension to the liquid phase. Hence, this paves the way to new insights into the influence of a surrounding solvent on the electron dynamics in molecules and ultrafast processes in chemical systems, such as solvation dynamics, solvent reorganization and electron transfer [33]. Naturally, liquid water (H_2O), being doubtlessly most important substance on earth [34], is the first candidate for time-resolved attosecond streaking spectroscopy in the liquid phase.

Acting as a solvent in many biological and chemical reactions water plays an essential role for almost all life processes on earth. The origin of many of its extraordinary physical and chemical properties is the famous intermolecular network of hydrogen bonding (H-bonding), as it highly influences chemical processes and governs solvation of ionic and neutral species. Especially solvation in water is known to substantially modify the molecule's electronic structure and photoionization dynamics through electrostatic

interactions and hydrogen bonding. The measurement of photoemission delays between inner- and outer-valence shell electrons of an H_2O molecule, having not reported yet, is expected to reveal insight into electron-correlation mechanisms, which are imprinted into these delays. Thus, photoemission studies have a great potential of identifying and quantifying the role of electron-molecule scattering in the condensed phase [35]. Within the frame of this thesis, the first-time performance of attosecond streaking spectroscopy on a liquid-phase H_2O sample should be conducted at the newly designed and commissioned attosecond beamline at TUM within a collaboration with the group of Prof. Hans Jakob Wörner from ETH Zurich.

At present time, attosecond science also experiences an extension concerning the wavelength of the applied laser pulses and thus the experimentally accessible energy range by the arising availability of sub-femtosecond X-ray pulses at free-electron laser (FEL) facilities. Free-electron lasers have been invented by John Madey [36] and demonstrated experimentally in the 1970s [37]. A highly relativistic electron beam propagates freely through a structure of periodically altering magnets, whereas emitting, interacting with and amplifying electromagnetic radiation. FELs can be operated from the extreme ultraviolet (XUV) to the hard X-ray regime and deliver broadly tunable, extremely coherent, high-power femtosecond pulses [38–40], that are almost ten orders of magnitude brighter than femtosecond pulses emitted by any other synchrotron radiation source [41–45]. Therefore, FELs are well-established as unrivalled sources of coherent, ultra-bright X-ray pulses that allow high-resolution, ultrafast X-ray pump/probe experiments as a powerful tool for several fields in natural science [46, 47], such as atomic and molecular physics [48–52], structural biology [53–57], femtochemistry [4, 58–60], solid-state physics [61–64], materials science [65] and high energy density science [66, 67].

Currently, X-ray FELs are primarily based on the self-amplified spontaneous emission (SASE) process [68] and generate pulses with a stochastic temporal substructure, where any single X-ray pulse is inherently differing from the previous one [69–71]. Most intensity-dependent experiments at X-ray FEL facilities, especially time-resolved X-ray spectroscopy, molecular imaging studies or nonlinear X-ray sciences, are strongly influenced by the effective pulse duration or peak power, and therefore by the SASE-caused temporal substructure of the FEL pulses. As the time resolution of FEL studies is already reaching the few-femtosecond and even attosecond regime [55, 72, 73], a reliable and non-invasive technique for directly and precisely measuring the temporal structure of these ultrashort FEL pulses on a shot-by-shot basis is crucial [74]. Nevertheless, up to today no direct, single-shot measurement method is available to determine not merely the pulse duration, but rather the temporal intensity profile of SASE FEL pulses [75, 76] in the few-femtosecond range.

Another formidable challenge for ultrafast, time-resolved two-color experiments, is a precise determination of the relative arrival time between the two lasers, which is a prerequisite for any X-ray pump/optical probe experiment [77] on the few-femtosecond time scale. Unfortunately, without an accurate knowledge of this relative delay, X-ray pulses at FEL facilities exhibit a considerable inherent arrival time jitter relative to any externally synchronized yet independent laser source [78, 79]. That fact limits the temporal resolution of X-ray pump/optical probe experiments to the level of that timing jitter. Despite steady progress regarding both challenges [38, 70, 71, 80–86], a direct and simultaneous determination of both the exact temporal substructure and the arrival time on a single-shot basis still remains elusive. By applying a two-color angular streaking approach and developing a novel, suitable analysis algorithm, a direct and non-invasive, single-shot measurement of the X-ray pulse duration and its temporal substructure with few-femtosecond resolution, as well as a precise determination of the relative arrival time, shall be performed at the Linac Coherent Light Source (LCLS) at the SLAC National Accelerator Laboratory in California, USA [41] as the main task of this thesis. Furthermore, the characterization of X-ray FEL double pulses with a delay of just a few femtoseconds shall be achieved.

Albeit all three sub-projects presented in this thesis have been realized in close and distinguished teamwork with my colleague Martin Wagner [87], I have been the scientist in charge for the pulse characterization of X-ray FEL pulses via angular streaking and through a self-developed reconstruction algorithm, whereas Martin Wagner has been responsible for the attosecond streaking measurements in the liquid and gaseous phase of water. This is reflected in the emphasis of the two respective theses. Regarding the design and commissioning of the AS101 beamline within the first years of our work, no leading position has been defined. According to the explained responsibilities, this thesis is organized as follows: Chapter 2 presents the concepts of X-ray free-electron physics, focusing on the operating principle of a high-gain FEL based on the SASE process. This is followed by an overview of the principles of ultrashort laser pulses and the field of attosecond metrology. The chapter ends with an introduction to the angular streaking technique. Chapter 3 presents the Linac Coherent Light Source (LCLS) and the entire instrumentation employed for the two-color angular streaking experiment. In Chapter 4, the novel pulse retrieval algorithm and its application on the measured two-color angular streaking data for direct X-ray FEL pulse characterization in the time domain are comprehensively elaborated as the centerpiece of the present thesis. Eventually, the findings are comparatively evaluated. In chapter 5, the novel, state-of-the-art attosecond metrology beamline at TUM is introduced illuminating the most prominent parts of the setup. Chapter 6 concisely summarizes the first attosecond streaking spectroscopy measurements on liquid-phase H_2O and the primary results. The thesis finishes with a conclusion of the main results and an outlook.

Chapter 2

Theoretical Principles

This chapter is intended to introduce the theoretical concepts that provide a basic understanding and traceability of both types of experiments presented in this work. Firstly, the principle of a high-gain free-electron laser (FEL) based on the self-amplified spontaneous emission (SASE) process is elaborated. Secondly, an overview of the fundamental concepts of attosecond metrology is given. Starting with the mathematical description and the physical phenomena of ultrashort light pulses and their interaction with matter, the attention is then directed to the photoelectron streaking method and its application as a tool for time-resolved attosecond spectroscopy. Finally, based on the previous elaborations, the two-color angular streaking method as the main experimental approach within this thesis is presented.

2.1 X-ray Free-electron Laser Physics

For a basic understanding of the functional principle of a free-electron laser and as a foundation for the angular streaking experiments conducted at an FEL facility, one should consider the theoretical framework of X-ray FEL theory in the 1-dimensional limit. The generation of undulator radiation, the general characteristics of the self-amplified spontaneous emission process and of high-gain FELs are concisely presented in the following. An extensive, in-depth description of the fundamental principles explained here, as well as the derivations of the subsequently introduced equations can be found in [40, 88, 89].

2.1.1 Undulator Radiation

The driving mechanism of a free-electron laser is the creation of 'bremsstrahlung' in a periodic magnetic dipole arrangement (undulator) by high-energy electrons, that have been accelerated in a linear accelerator before. The X-ray beam inherits most of its properties from the electron bunch. For successfully operating a state-of-the-art X-ray FEL, a linear accelerator (linac) at high energies with a high-performance radiofrequency photocathode electron gun as an injector, transport optics including longitudinal bunch compression for guiding electron beams of tremendous brightness (photon flux per frequency bandwidth per unit phase space volume) and eventually a high-quality undulator are required.

In a planar undulator — a succession of magnetic north and south poles — the magnetic field is oriented in the vertical y-direction and alters periodically along the z-direction:

$$B_y = B_0 \sin(k_u z) \; . \tag{2.1}$$

B_0 is the peak magnetic field strength on the electron propagation axis and $k_u = 2\pi/\lambda_u$ is the undulator wave number with the undulator period λ_u. Therefore, in the radiation process, an electron bunch with relativistic velocity ($v \simeq c, \gamma \simeq 10^2 - 10^5$) that entered the undulator with a kinetic energy $E_{kin} = \gamma mc^2$ starts to wiggle on an almost sinusoidal pathway in the horizontal x-direction due to the Lorentz force, as shown in figure 2.1. The expression $\gamma = W_e/mc^2$ denotes the kinetic energy of the electron in units of the rest energy. Hereby, the electrons spontaneously emit fundamental undulator radiation ('bremsstrahlung' or synchrotron radiation) in a small cone with an opening angle proportional to γ in forward direction at the resonance wavelength [89]

$$\lambda_r = \frac{\lambda_u}{2\gamma^2}\left(1 + \frac{K^2}{2}\right) \; . \tag{2.2}$$

Here [40],

$$K = \frac{eB_0}{mck_u} = 0.934 \cdot B_0[\mathrm{T}] \cdot \lambda_u[\mathrm{cm}] \tag{2.3}$$

defines the dimensionless undulator strength parameter, which for FELs usually amounts to 1–3. Here, e is the electron charge, c is the speed of light and m is the mass of the electron and ω_r is the fundamental undulator frequency. As electrons in a free-electron laser are not bound to atoms and consequently not restricted to any specific transitions, the wavelength of FEL radiation is adjustable over a wide range by modifying either the peak magnetic field of the undulator or the kinetic energy of the electrons [90].

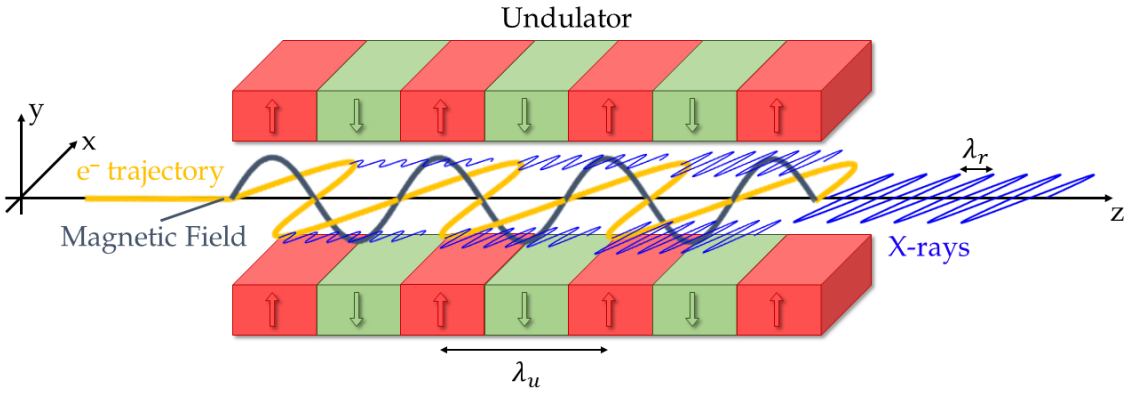

Figure 2.1: Undulator radiation. The succession of north and south magnetic poles in a planar undulator with the undulator period λ_u, the resulting magnetic field and the sinusoidal path of the wiggling electron bunch are displayed. The emitted undulator radiation at the resonance wavelength λ_r is continuously amplified along the undulator.

2.1.2 Fundamentals of High-gain SASE Free-electron Lasers

At the beginning, the motion of the single electrons is uncorrelated, resulting in an incoherent radiation. Hence, the power of the created X-rays is directly proportional to the number of electrons: $P_{\mathrm{X-ray}} \propto N_e$. The emitted electromagnetic wave is co-propagating with the electron bunch and is exchanging a small fraction of kinetic energy with the relativistic electron beam in the undulator. The electric field of the radiation can be written as $E_x(z,t) = E_0 \cos(k_r z - \omega_r t + \phi_0)$, where ϕ_0 is a phase offset. The radiation is linearly polarized in horizontal direction, perpendicularly orientated to the magnetic field and the beam path of the electrons [46]. Basically, the transfer of energy between radiation and electrons can be determined to

$$\frac{dW_e}{dt} = \vec{v} \cdot \vec{F} = -e v_x(t) E_x(t) \; . \tag{2.4}$$

This resonant beam–radiation interaction cannot be preserved in free space due to the electrons moving slower than the radiation. However, in an undulator this dephasing can be avoided and a net energy transfer from the electron bunch to the X-ray beam occurs: While co-propagating in the undulator at the speed of light, the intense electromagnetic wave overtakes the electrons by exactly one optical wavelength λ_r once per undulator period (*slippage length*), so the alignment between the electric field of the radiation and the transverse component of the electron velocity is iterated periodically. Consequently, the interaction and the exchange of energy between the electron bunch and the electric field of the co-propagating radiation can be sustained over a longer distance, if the X-ray wavelength λ_r is set equal to the advance per undulator period of the X-ray beam relative to the electron bunch, see figure 2.2.

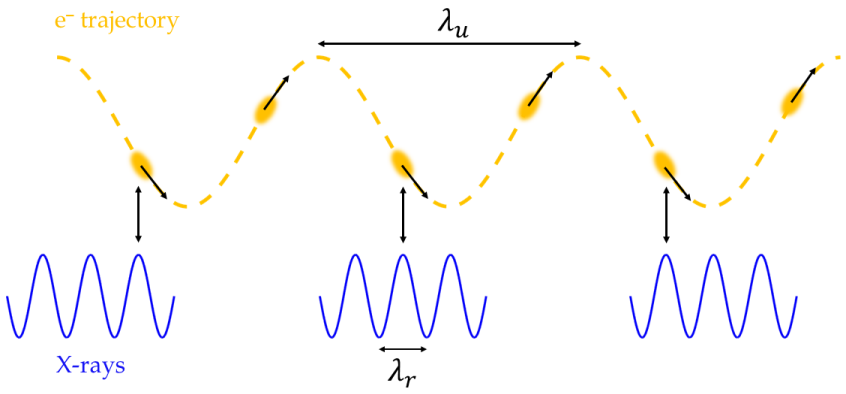

Figure 2.2: Electron–radiation interaction in an undulator. The self-interaction and the exchange of energy between the electron bunch (yellow) and the electric field of the co-propagating radiation (blue) is sustained over a longer distance, if the X-ray wavelength λ_r is equal to the so-called *slippage length*. The electromagnetic wave overtakes the electrons by exactly one resonance wavelength λ_r while the electron bunch is traveling on its sinusoidal trajectory one undulator period λ_u due to the periodicity of the undulator system.

According to the phase of the electrons with respect to the electromagnetic wave, certain electrons in the bunch give off energy to the co-propagating radiation $\left(\frac{dW_e}{dt} < 0\right)$,

whereas other electrons gain energy from the radiation. This results in a modulation of the energy distribution within the electron bunch developing from an initially monoenergetic electron beam. This energy modulation in turn evolves into a longitudinal, periodic density modulation of the electron bunch with the periodicity λ_r, the so-called *microbunching*: Electrons ceding energy to the electromagnetic wave travel on a sinusoidal trajectory of greater amplitude than electrons receiving energy from the electromagnetic field. Hence, electrons with higher energies move faster and catch up to the slower-moving electrons with lower energies from the same 'phase bucket', resulting in the formation of clumps of electrons (microbunches). These microbunches are evident as longitudinally distributed, thin slices of high electron concentration within a longer electron bunch, with a regular spacing equal to the radiation wavelength [40, 90]. These slices are close to that positions within the bunch, where the maximum energy transfer to the radiation can occur.

If the electron beam is sufficiently bright and traveling in an undulator of sufficient length, the resonant interaction between electron beam and undulator radiation gives rise to a coherent exponential growth of the radiation intensity along the undulator distance. The radiation experiences a net energy gain and an arising FEL amplification at the cost of kinetic energy of the electrons [40]. Within a microbunch, all electrons radiate more and more in phase just like a single high-charge particle, reinforcing an increasingly coherent superposition and thus a growth of the radiation intensity. The increasing electromagnetic field, in turn, further reinforces the microbunching and causes the exponential rise of the X-ray power. Since all the electrons within a microbunch emit in phase, the amplitude of the X-ray electric field is directly proportional to the number of electrons within a microbunch, which causes a quadratic dependence of the radiation power on the number of electrons $P_{\mathrm{X-ray}} \propto N_e^2$ [89]. Eventually, the exponential gain halts, since the energy loss of the electron beam disrupts the resonance condition. Consequently, X-ray power and microbunching reach a maximum saturation level, as displayed in figure 2.3.

Such a high-gain free-electron laser has no need of an optical cavity and can amplify within a single pass either spontaneous undulator radiation generated by electron shot noise or an external seed signal. However, in the X-ray wavelength range (particularly for $\lambda < 100$ nm) suitable sources providing a coherent input signal and especially optical elements like mirrors are hardly available. The reflectivity of metals or different mirror coatings decreases dramatically to zero at normal incidence in this wavelength range. Therefore, the self-amplified spontaneous emission (SASE) process [68, 91] is commonly applied to produce intense and quasi-coherent X-rays. Hereby, the initial random field of spontaneous radiation emerging from spatially and temporarily uncorrelated fluctuations in the electron beam current is amplified until a single mode is dominating [68, 92, 93]. Since the 'seed signal' originates from the favorable electron shot noise, the amplification is initiated independently and simultaneously at different spots within the electron bunch without enforcement of overall coherence [90]. For the SASE operation mode, a high-gain

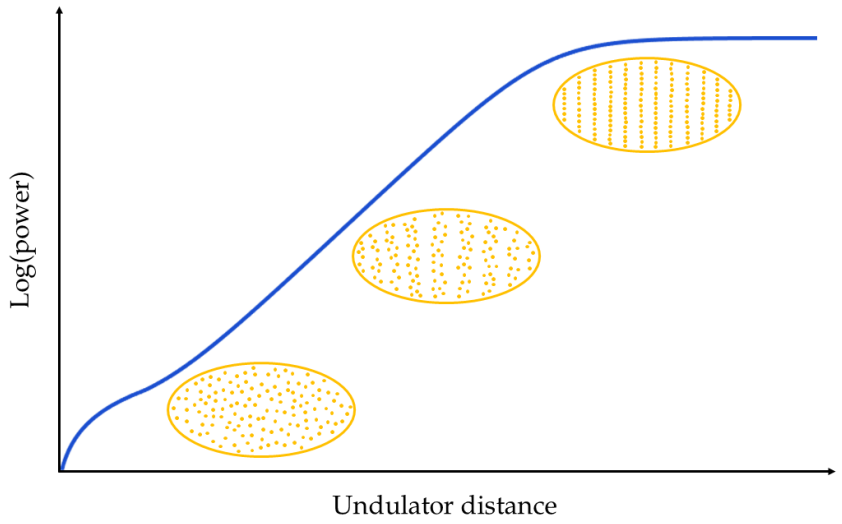

Figure 2.3: Schematic of a high-gain SASE free-electron laser. Microbunching of the electron beam along the undulator and according exponential rise of FEL radiation power as a function of the undulator distance up to saturation.

FEL requires a precise matching between the phase space of the X-ray mode being amplified and the phase space occupied by the electron bunch. In the X-ray wavelength range, a short-pulse, high-energy, high-charge, low-energy-spread and low-emittance electron beam of extremely high brightness is necessary for a close match of these phase space volumes [46]. The emittance is a measure for the position–momentum phase space area occupied by the electrons. It bears mentioning, that the SASE process can happen at any wavelength and is continuously adjustable in wavelength as the process scales with the energy of the electron bunch. The saturation level can thus be achieved by applying an undulator of sufficient quality and length and an electron beam of adequate quality and energy [94].

2.1.3 Characteristics of SASE FEL X-ray Pulses

A key scaling parameter and figure of merit for high-gain FELs is the dimensionless so-called FEL Pierce parameter ρ that is defined as [46, 68]

$$\rho = \left[\frac{1}{64\pi^2}\frac{I_p}{I_\mathrm{A}}\frac{K^2[JJ]^2\lambda_u^2}{\gamma^3\sigma_x^2}\right]^{1/3} . \tag{2.5}$$

Here, the Bessel function factor $[JJ]$ equals the $[J_0(\xi) - J_1(\xi)]$ with $\xi = K^2/(4+2K^2)$ for a planar undulator trajectory. I_p is the electron peak current, $I_\mathrm{A} = 4\pi\epsilon_0 mc^3/e = 17.5$ kA is the Alfvén current [89] and σ_x is the root mean square (rms) transverse size of the electron beam. For typical short-wavelength FELs and high-energy electron bunches, ρ is typically on the order of 10^{-3} [40].

Due to the progressing microbunching, the FEL power exponentially rises with the undulator distance z following the relation

$$P(z) \propto e^{\left(\frac{z}{L_G}\right)} . \tag{2.6}$$

The so-called power gain length (1D) L_G of a monoenergetic beam given by [40]

$$L_G = \frac{\lambda_u}{4\pi\sqrt{3}\rho} , \tag{2.7}$$

which is consequently of the order of 100 undulator periods [94]. The phase relation between the electron density modulation and the electric field of the radiation in the exponential gain regime mainly cause the electrons to lose energy. Even so, due to this energy loss this phase relation is shifted continuously and in the end the conditions are reversed and the electrons start to regain energy from the radiation [94]. At that moment, the gain of the X-ray power terminates, so a saturation stage is entered at an undulator length of approximately $L_{\mathrm{sat}} \approx 10 - 20\ L_G$ [89, 95]. At saturation, the relative bandwidth of the FEL is close to ρ and the FEL power is given by [46]

$$P_{\mathrm{sat}} \approx \frac{\rho\gamma mc^2 I_p}{e} , \tag{2.8}$$

with ρ determining the efficiency of the FEL with respect to the power of the electron beam.

Due to its shot noise start up and the finite bandwidth of SASE, the temporal characteristic of SASE FEL radiation is like that of chaotic light, showing shot-to-shot intensity fluctuations and a limited temporal coherence [75, 76, 96]. From the first-order time correlation function, one gets the coherence time, a measure for the pulse duration of the radiation set free by a single microbunch, as [76, 96]

$$t_c = \frac{\sqrt{\pi}}{\sigma_\omega} . \tag{2.9}$$

The coherence time is inversely proportional to the rms spectral bandwidth σ_ω of the SASE pulses, which basically decreases to about $\sigma_\omega \sim \rho\omega_{\mathrm{X-ray}}$ at saturation level [93, 97].
The energy of a single SASE pulse W with a flattop pulse duration T fluctuates under the terms of the Gamma probability distribution [40, 76]:

$$p(W) = \frac{M^M}{\Gamma(M)} \frac{W^{M-1}}{\langle W\rangle^M} e^{\left(-M\frac{W}{\langle W\rangle}\right)} . \tag{2.10}$$

Here, $\Gamma(M)$ is the Gamma function and $\langle W\rangle$ is the average energy of the radiation.
The relative rms energy fluctuation σ_W is determined by [76, 96]

$$M = \frac{1}{\sigma_W^2} = \frac{\langle W\rangle^2}{\langle W^2\rangle - \langle W\rangle^2} = \begin{cases} T/t_c & \text{when } T \gg t_c \\ 1 & \text{when } T \leq t_c \end{cases} . \tag{2.11}$$

Accordingly, the parameter M determines the number of 'temporal modes' of the SASE pulse. For the hard X-ray range, the coherence time t_c amounts to just a few hundred attoseconds. The pulse duration T of SASE FEL pulses is normally on the same order as a characteristic electron bunch of tens to several hundred femtoseconds (fs), leading to $T \gg t_c$ or $M \gg 1$, respectively. Additionally, the Gamma distribution of single-shot pulse energies approaches a Gaussian distribution that has a small relative rms energy fluctuation $\sigma_W \sim 1/\sqrt{M}$ [40]. Consequently, a statistical evaluation reveals that the mean number of intensity spikes in the time regime amounts to roughly $0.7M$ [69]. The longitudinally coherent and ultrashort intensity spikes from the microbunching of a single SASE pulse are separated by approximately t_c and can be considered as independent sources of radiation [46]. The frequency width of a single spike is determined to [89]

$$\Delta\omega_{\text{spike}} = \frac{2\sqrt{2\ln 2}}{T_{\text{bunch}}} \tag{2.12}$$

In a standard mode of operation, a 'flattop' electron bunch at LCLS issues approximately 1000 microbunches with coherent SASE spike durations of 0.3 fs to 2 fs [46]. Thus, a characteristic FEL pulse, consisting of 10^{12} to 10^{13} photons, is built of a series of several tens to hundreds of coherent SASE spikes that have no fixed phase relation to each other.

2.2 Attosecond Metrology

In the following section, the principles of ultrashort high-energy laser pulses and the classical treatment of their interaction with matter, as well as the fundamental phenomena in nonlinear optics are just briefly presented. This section is in part based on the respective sections in the master thesis of Markus Wurzer [98], a former master student under my supervision. A more detailed description can be found in standard textbooks [99–101]. Afterwards, the application of such laser pulses and these nonlinear effects for the generation of isolated attosecond pulses in the XUV regime via high harmonic generation and the methodology of attosecond streaking spectroscopy are depicted. The streaking method is introduced classically and furthermore, the complex quantum-mechanical concept is explained. This enables the retrieval of the waveforms of the applied laser pulses and essential insights into ultrafast electron dynamics studied by a streaking experiment.

2.2.1 Fundamentals of Ultrashort Laser Pulses

The propagation of light, considered as an electromagnetic wave, in isotropic and homogeneous dielectric, non-magnetic media and in absence of free electric currents can be derived in a classical way starting from the Maxwell equations and is described by the wave equation [101]

$$-\nabla^2\vec{E} + \mu_0\frac{\partial^2\vec{D}}{\partial t^2} = 0\,, \tag{2.13}$$

with $\vec{E}$ being the electric field and μ_0 being the permeability of free space. The dielectric displacement $\vec{D}$ is defined by

$$\vec{D} = \epsilon_0 \vec{E} + \vec{P} \,, \tag{2.14}$$

with the dielectric vacuum permittivity ϵ_0 and $\vec{P}$ the macroscopic polarization, which is the medium's response to the intrusion of an electric field $\vec{E}$. The dimensionless, scalar quantity χ, the linear electric susceptibility, represents the dielectric properties of the medium [99]. In isotropic media and on the assumption of a linear response of the medium, χ and the polarization $\vec{P}$ are related by

$$\vec{P} = \epsilon_0 \chi \vec{E} \,. \tag{2.15}$$

A possible, general solution of the wave equation 2.13 are plane waves

$$\vec{E}\,(\vec{r}, t) = \frac{1}{2}\left[\vec{A} e^{-i\left(\vec{k}\cdot\vec{r} - \omega t + \phi\right)} + c.c.\right] \,, \tag{2.16}$$

with the complex amplitude $\vec{A}$, the wave vector $\vec{k}$, the angular frequency ω and the starting phase ϕ. Here, $c.c.$ stands for the complex conjugate. Regarding ultrashort laser pulses, primarily temporal and spectral characteristics at a specific position $\vec{r}$ are of special interest, so one can make some simplifications regarding this solution, leading to a simplified version of the wave function

$$E(t) = \sqrt{I}(t) e^{i(\omega_0 t + \phi(t))}. \tag{2.17}$$

Here, ω_0 is the central angular frequency and $\sqrt{I}(t)$ is the time-dependent amplitude envelope and $\phi(t)$ the temporal phase. The optical intensity is defined by $I(t) = |E(t)|^2$. By a Fourier transformation of equation 2.17 in the time domain, one can derive a description of the electric field in the frequency domain

$$E(\omega) = \sqrt{S(\omega)} e^{i\varphi(\omega)} \tag{2.18}$$

with the spectral phase $\varphi(\omega)$ and the spectral intensity $S(\omega)$.
The temporal and spectral widths Δt and $\Delta\omega$ of a pulse are defined by the full-width at half-maximum (FWHM) of $I(t)$ and $S(\omega)$, respectively. Due to the Fourier transform relation between 2.17 and 2.18 the temporal width and the spectral width are inversely proportional to each other. The proportionality coefficient is dependent on the definition of the width and on the shape of the light pulse. The so-called *time-bandwidth product* (TBP) being derived from the uncertainty principle has a minimum value for a specific pulse shape and is given by

$$\Delta t \cdot \Delta\omega = 0.44, \tag{2.19}$$

being valid for pulses with a Gaussian shape and a constant phase [99]. A transform-limited pulse is hence the shortest pulse achievable for a given spectrum. Therefore, a larger spectral bandwidth of the pulse enables shorter pules durations. Furthermore, the minimum pulse duration is limited by the central frequency of the pulse, as at least one

full oscillation of the central carrier wave is necessary for the propagation of a light pulse. Thus, a higher frequency (shorter wavelength) allows an even shorter transform-limited pulse duration.

Chromatic Dispersion

Nevertheless, due to the dispersion relation, the frequency-dependence of the refractive index of a medium, several effects during generation and propagation of ultrashort pulses can induce non-constant phases $\phi(t)$ or $\varphi(\omega)$. This causes a prolongation or even a distortion of transform-limited pulses. The frequency domain can be utilized for an explanation of the consequences of the so-called *chromatic dispersion* raised by the propagation of a light pulse in a dispersive medium. For this purpose, the spectral phase $\varphi(\omega)$ can be expressed in a Taylor expansion in angular frequency ω_0

$$\varphi(\omega) = \varphi_0 + \varphi_1 \cdot (\omega - \omega_0) + \frac{1}{2}\varphi_2 \cdot (\omega - \omega_0)^2 + ... + \frac{1}{n!}\varphi_n \cdot (\omega - \omega_0)^n, \tag{2.20}$$

where φ_n is the n-th order derivative of the spectral phase

$$\varphi_n = \left(\frac{\mathrm{d}^n \varphi}{\mathrm{d}\omega^n}\right)\Bigg|_{\omega=\omega_0}. \tag{2.21}$$

The zeroth order of the expansion φ_0 (independent of ω) is the so-called *carrier-envelope offset phase* (*CE-phase* or *CEP*) φ_{CE}, which is the phase shift between the carrier wave and the peak of the pulse envelope in the time regime [101, 102]. The effect of $\varphi_{\mathrm{CE}} \neq 0$ on the waveform and the duration of a pulse is normally negligible for longer pulses with multiple cycles under the envelope. However, for few-cycle pulses, where the electric field passes only a few periods, a varying CE-phase causes dramatical changes of the waveform of the electric field, see figure 2.4 a). Thus, a precise control of the CEP is crucial for the generation of isolated attosecond pulses via the highly nonlinear process of high harmonic generation in the strong-field regime, where the interaction time of light and matter is in the range of a oscillation period of the electric field [103]. The first order spectral phase φ_1 is called *group delay* and induces a shift in the time domain, whereas neither the shape of the envelope nor the pulse duration are affected.
Nevertheless, higher orders of the spectral phase indeed affect pulse duration and shape. The second order φ_2, usually referred to as *group delay dispersion* (GDD), induces a linearly altering frequency modulation throughout the pulse, a so-called *chirp*. A positive GDD, for instance, causes lower frequencies to arrive earlier than higher ones, see figure 2.4 b).

However, due to dispersion the propagation through dispersive media unavoidably changes the temporal profile of a few-cycle light pulse, but the envelope of linearly chirped pulses stays unaltered. Besides that, dispersion causes different phase and group velocities of the wave inducing a steadily varying CE-phase. On the contrary, higher-order terms of the spectral phase (n$\geq$ 3) raise a distortion of the envelope.

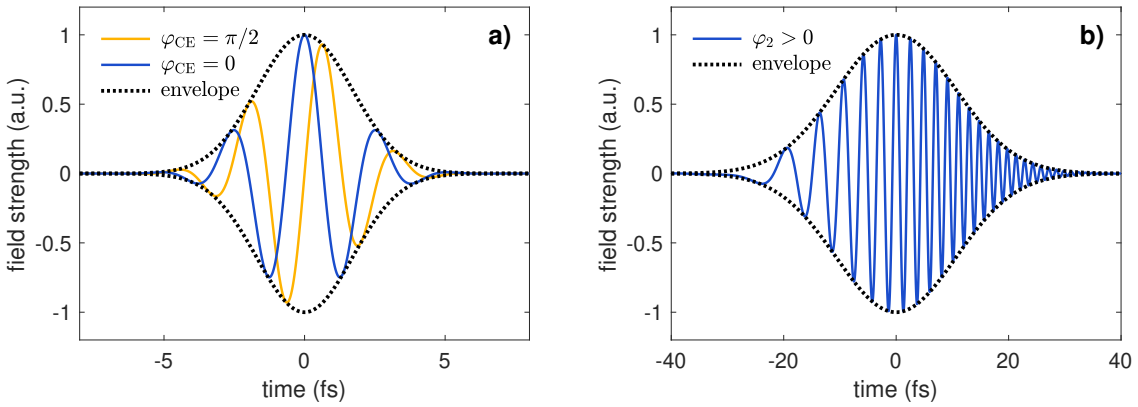

Figure 2.4: Chromatic dispersion – Illustration of CE-phase and linear chirp. (a) Depiction of a few-cycle light pulse with a pulse duration of 4 fs (FWHM) and a Gaussian envelope (black) at a central wavelength of λ = 800 nm for two different waveforms: The electric field of the light pulse is sketched for a cosine waveform (φ = 0, blue) where the maximum of the electric field coincides with the maximum of the envelope and also for a sine waveform ($\varphi = \pi/2$, green) where the maximum is shifted below the envelope and hence smaller. (b) The positive group delay dispersion (GDD, $\varphi_2 > 0$), a so-called linear chirp, of a light pulse with a pulse duration of 25 fs (FWHM) is depicted. It is clearly visible that higher frequency components are succeeding the lower ones. Adapted from [87].

For the generation of isolated attosecond pulses by CEP-stable, few-cylce laser pulses and for time-resolved photoelectron spectroscopy, bandwidth-limited pulses of a few femtosecond pulse duration are a main prerequisite. Thus, a beam path in vacuum with its non-dispersive character and a compensation for inevitable dispersive effects are required urgently to preserve the pulse characteristics as effectively as possible. Dispersion control up to the fourth order can be achieved with gratings [104], dispersive mirrors (so-called *chirped mirrors*) [105, 106] and acousto-optical modulation [107, 108]. More detailed information on this can be found in the stated references and in [87, 109].

2.2.2 Nonlinear Optics

In the case of ultrashort laser pulses with high intensities and strong fields, nonlinear optical phenomena appear and higher orders of the macroscopic polarization $\vec{P}$ have to be taken into account. The response of the material to the electric field, which is much weaker than the interatomic binding fields, affects the propagation of the laser pulse. Therefore, in the *perturbative regime* a series expansion of the macroscopic polarization $\vec{P}$ (defined in 2.15) is introduced [100]

$$\vec{P}(t) = \sum_n \vec{P}^{(n)}(t) = \vec{P}^{(1)}(t) + \vec{P}^{(\mathrm{NL})}(t) = \tag{2.22}$$

$$= \epsilon_0 \left[\boldsymbol{\chi}^{(1)} \vec{E}(t) + \boldsymbol{\chi}^{(2)} \vec{E}(t)^2 + \boldsymbol{\chi}^{(3)} \vec{E}(t)^3 + \ldots \right] , \tag{2.23}$$

where $\vec{P}^{(1)}$ is the linear part and $\vec{P}^{(\mathrm{NL})}$ is the nonlinear part of the polarization, respectively. Here, $\boldsymbol{\chi}^{(n)}$ represents the n^{th} order electric susceptibility tensor (for n $>$ 1), that can be reduced to a scalar for an isotropic medium and corresponds to the susceptibility χ in

linear optics. Most of the nonlinear optical effects can be ascribed to a field- or intensity-dependence of the susceptibility χ, which is the fundamental connection between the electric field and the polarization. However, this nonlinearity is quite small, so the macroscopic polarization $\vec{P}$ shows only a tiny deviation from the linearity with an increasing $\vec{E}$.

Merging the wave equation 2.13 and the series expansion of the polarization 2.22, one can describe the propagation of light in a nonlinear medium by the nonlinear wave equation [110]

$$\nabla^2\vec{E} - \frac{n^2}{c^2}\frac{\partial^2\vec{E}}{\partial t^2} = \frac{1}{\epsilon_0 c^2}\frac{\partial^2\vec{P}^{(\mathrm{NL})}}{\partial t^2} \,, \tag{2.24}$$

where n is the refractive index and c is the speed of light in vacuum. The additional term on the right side acts as a source of driven radiation in the medium. This source depends on the electric field of the original driving field, but has different, new frequency components and is weak compared to the linear susceptibility ($\chi^{(2)}/\chi^{(1)} \approx 10^{-12}$, $\chi^{(3)}/\chi^{(1)} \approx 10^{-24}$) [101]. Nonlinear polarization induces several optical phenomena, such as difference-frequency, sum-frequency and second harmonic generation, optical parametric amplification, the optical Kerr effect and all other kinds of self-modulation. Only the most relevant ones for this thesis will be mentioned subsequently, a more detailed discussion about nonlinear optics can be found in [100] or in any other textbook about nonlinear optics.

Optical Kerr Effect

The *optical Kerr effect*, one of the principal phenomena in nonlinear optics, is the impact of an external electric field applied on an optical, anisotropic medium. It constitutes an intensity dependence of the refractive index, which is commonly described by the relation

$$n(I) = n + n_2 I \,, \tag{2.25}$$

with n being the ordinary, linear refractive index, the optical intensity I and the second-order nonlinear refractive index (or optical Kerr coefficient) n_2. The latter is linearly correlated with the third-order electric susceptibility $\chi^{(3)}$. As the spatial as well as the temporal intensity distribution alters, a spatially and temporally changing refractive index is induced by the optical Kerr effect, causing phenomena such as self-focusing and self-phase modulation.

Self-focusing

The physical effect of lenses (and also gratings or prisms) is the phase shift that is induced by the lens to the wavefront of an incoming optical wave: the optical path length $l = n \cdot d$ in a common, convex lens is continually changed along the radial axis, depending on the amount of material d in the pathway of the beam. This causes a nonuniform phase shift and an altered beam divergence dependent on the radial distance to the center of the lens. However, a similar phase shift is induced by the Kerr effect in a planar optic (d = const.), where a difference in l is achieved by the variation of the refractive index n due to the

presence of a high-intense laser pulse with a spatial intensity distribution, see 2.25. As this effect is caused by the laser pulse itself, it is called *self-focusing* or *Kerr lens*.

Self-phase Modulation and Self-steepening

A further nonlinear optical effect correlated with the intensity-dependent refractive index is the so-called *self-phase modulation* (SPM). A high-intensity, ultrashort laser pulse propagating in a medium induces a time-varying refractive index due to the optical Kerr effect (see equation 2.25). This in turn introduces a nonlinear phase modulation in the pulse, thus a change of the frequency spectrum. A laser pulse with a Gaussian temporal profile, propagating in a nonlinear medium, leads to a shift of the temporal phase according to

$$\phi_{\mathrm{SPM}}(t) = -n_2 I(t)\omega_0 \frac{L}{c} \,. \tag{2.26}$$

with L being the propagated distance inside the medium and the central carrier frequency ω_0 [100]. This temporal phase shift leads to a corresponding frequency shift (via the Fourier theorem), which in turn is described by the *instantaneous frequency*

$$\omega_{\mathrm{inst}}(t) = \omega_0 + \Delta\omega(t) = \omega_0 + \frac{d\phi_{SPM}(t)}{dt} \,. \tag{2.27}$$

Provided that the pulse duration is long compared to one optical oscillation $2\pi/\omega_0$, the electric field can be referred to a certain frequency for every specific time frame of the pulse, defined as the instantaneous frequency. Merging equations 2.26 and 2.27 one gets

$$\omega_{\mathrm{inst}}(t) = \omega_0 + \frac{d}{dt}\phi_{\mathrm{SPM}}(t) = \omega_0 - n_2\omega_0 \frac{L}{c}\frac{dI}{dt} \,, \tag{2.28}$$

where the second term describes the frequency shift. One can clearly see that this shift is proportional to the derivative of the pulse intensity. The preceding part of the pulse is shifted to lower frequencies and the trailing part is shifted to higher frequencies, leading to an additional, positive second-order chirp. According to the time-bandwidth product (eq. 2.19), an increasing bandwidth allows a shorter pulse duration. The maximum frequency shift induced by SPM is approximately determined by

$$\Delta\omega_{\mathrm{max}} \simeq \frac{n_2\omega_0 I_0 L}{c\tau} \tag{2.29}$$

for a pulse duration τ and an amplitude I_0. SPM results in a symmetric spectral broadening of the pulse around ω_0, if the maximum frequency shift is exceeding the bandwidth of the incoming pulse [100]. The shorter the incoming pulse and the longer the interaction length, the higher the efficiency of the process.

In parallel to SPM, the *self-steepening* effect of the pulse occurs, while propagating in a Kerr medium. In contrast to self-focusing, where a transverse alteration of the refractive index and thus of the optical path length occurs, a longitudinal alteration due to the time-dependent intensity distribution of the pulse takes place in the case of self-steepening.

Hence, different group velocities are introduced for the peak and the edges of the pulse. The central, high-intensity peak of the pulse undergoes a maximum deceleration due to the self-induced refractive index, whereas the lower-intensity parts of the pulse, the preceeding and trailing edges, are exceeding the group velocity of the peak. Eventually, for $n_2 > 0$ this leads to a pulse shape distortion with a flattened preceding edge and a steepened trailing edge, where the peak of the pulse got shifted to the end of the pulse. Combined with the SPM effect, which increases with the derivative of the intensity, both processes result in a asymmetrically broadened and inhomogeneously blue-shifted spectrum with an increased ω_0 [111].

2.2.3 Generation of Isolated Attosecond Pulses

Regarding the shortest possible pulse duration of a propagating electromagnetic wave, the irrefutable condition holds that the electric field of the pulse must accomplish at least one entire oscillation period. Therefore, for a given central wavelength λ_c the pulse duration τ is limited by

$$\tau \geq \frac{\lambda_c}{c} \,. \tag{2.30}$$

Thus, for a wavelength of λ_c = 790 nm, such a full cycle takes 2.6 fs. The Gaussian-shaped output pulses of commercial, state-of-the-art laser systems in the near-infrared (NIR) wavelength range ($\lambda_c \approx 800nm$) have a pulse duration of roughly 20 fs due to their small spectral bandwidth. This is caused by gain-narrowing during the amplification processes [112]. Utilizing a hollow-core fiber compressor, pulses can be distinctly broadened via SPM and afterwards compressed in time using so-called *chirped mirrors* [106], that compensate for the introduced dispersion. That way, according to equation 2.30, for these pulses with a central wavelength of approximately $\lambda_c = 650nm$, the shortest pulse duration achievable is $\tau = 2.2$ fs. Accordingly, for the generation of attosecond pulses, radiation with a distinctly shorter wavelength is required. Proceeding from bandwidth-limited NIR pulses, as provided by a hollow-core fiber compressor, attosecond pulses in the extreme ultraviolet (XUV) spectral regime can be produced via the process of high harmonic generation (HHG). In the following, the theoretical basics underlying a hollow-core fiber compressor and the generation of isolated attosecond pulses via high harmonic generation, are elaborated.

Hollow-core Fiber Compressor

Temporal pulse compression is achieved by two subsequent steps within a hollow-core fiber compressor: In a first step, new frequencies are generated within the pulse via self-phase modulation (spectral self-broadening) in a hollow-core fiber (HCF), so that the theoretical shortest pulse duration is reduced. In a second step, dispersion compensation as well as compression in time of the spectrally broadened pulse are accomplished utilizing chirped mirrors, which induce negative GDD [105, 113]. Following the elaboration in [98], we concentrate on the process within the HCF in this section.

As can be seen from equation 2.29, the self-broadening depends on intensity I_0, interaction length L and the nonlinear refractive index n_2. The latter is a material constant and can be optimized by the selection of a medium with high third-order electric susceptibility. High intensities are simply achievable by strong focusing to a tiny spot size, but unfortunately, this leads to a shorter Rayleigh length and thus to a shorter interaction length within a common environment. For energies in the nanojoule range, that issue can be overcome utilizing small-diameter optical single-mode fibers [114–116]. Nevertheless, due to material damage and high-order nonlinearities these waveguides are not applicable to higher pulse energies [117]. Instead, noble gas-filled, cylindrical hollow-core fibers, enabling single mode transmission at large mode diameters, have been introduced by Nisoli et al. [117] and are the means of choice for very high pulse intensities. Utilizing a noble gas as nonlinear medium comes along with numerous advantages: Spatially uniform, spectral broadening takes place, resulting in a better beam profile after the fiber. Noble gases are comparatively robust in the face of large intensities, because of their high threshold for multiphoton ionization (e.g. for helium [118]: $I_{\mathrm{th}} \approx 6 \cdot 10^{13} \frac{\mathrm{W}}{\mathrm{cm}^2}$), especially regarding femtosecond pulses. Moreover, noble gases with their high third-order electric susceptibility induce a large, nonlinear refractive index n_2 [119]. Finally, the extent of the nonlinearity can be further controlled by the gas pressure or even an exchange of the gas type [117]. However, the gas pressure has to stay below a specific level to prevent self-focusing within the gas.

Besides the enhancement of the nonlinear refractive index n_2 by the choice of gas type and gas pressure, the degree of self-broadening can be further optimized in respect of intensity and interaction length within certain limits. The latter is limited for practical reasons like available space in the laboratory, or the production, mounting and alignment of the fiber itself, which become more difficult with rising fiber length. Regarding the intensity, there is a trade off between the change of the refractive index induced by the Kerr effect and by gas ionization (plasma effects), where the latter needs to be negligible small. The following relation for the minimum inner fiber radius of the HCF and thus the highest, reasonable intensity has been determined numerically to [120]

$$a_{\mathrm{min}} = A \cdot {\tau_0}^{-0.45} \cdot {E_0}^{0.51} \,, \tag{2.31}$$

with A being a gas-dependent constant ($A_{\mathrm{He}} \simeq 2.62 \cdot 10^{-9} \mathrm{ms}^{0.45} \mathrm{J}^{-0.51}$ and $A_{\mathrm{Ne}} \simeq 2.99 \cdot 10^{-9} \mathrm{ms}^{0.45} \mathrm{J}^{-0.51}$), τ_0 being the pulse duration and the pulse energy E_0. Contrary to conventional, optical fibers, where the confinement of the light pulse is based on total internal reflection at the interface between core and cladding, the propagation of the light pulse results from grazing incident reflections at the inner surface of the capillary. Basically, inside hollow-core fibers there are different possible modes [121, 122].

However, for fused-silica HCFs the highest transmission occurs in the so-called hybrid EH_{11} mode (lowest loss mode) with an intensity profile given by [123]

$$I(r) = I_0 J_0^2 \left(\frac{2.405 \cdot r}{a} \right) , \tag{2.32}$$

with the peak intensity I_0, the zero-order Bessel function J_0 and the inner capillary radius a. For an incoming Gaussian-shaped pulse with a beam diameter of $2w$ ($1/e^2$), a maximum efficient coupling is reached, if the inner radius of the capillary a fulfills the relation [124]

$$2w = 0.65 \cdot 2a . \tag{2.33}$$

The usage of a hollow-core fiber together with a subsequent chirped mirror array is therefore a suitable instrument for the transformation of laser pulses from standard laser systems into few-cycle NIR pulses with pulse durations less than 5 fs [113, 125]. Thus, these pulses are ideally suited for the creation of attosecond pulses via high harmonic generation.

High Harmonic Generation

Proceeding from few-cycle NIR pulses, the extreme ultraviolet (XUV) regime and thus laser pulses with durations on the attosecond timescale (see eq. 2.30) can be reached via high harmonic generation (HHG). For this purpose, high-intensity, linearly polarized, few-cycle NIR pulses are strongly focused onto noble gas atoms [126, 127]. For the consideration of the HHG process, the perturbative approach loses its validity due to the extreme peak intensities ($I > 10^{13}\mathrm{W/cm^2}$): For such intensities and beyond, in the *strong-field regime*, the electric field strength of the laser pulse reaches the same magnitude as the atomic binding potential for the outer valence electrons and can therefore not be treated as a minor perturbation any more [103]. HHG is in principle a sum-frequency (SFG) process, where several photons of a specific frequency are converted to one photon of higher frequency. For the generation of the n-th harmonic, such an up-conversion process requires at least n photons being coincidentally located at the same spot within the gas target. The typical HHG spectrum is a line series of discrete, odd harmonics that are separated by twice the central frequency of the NIR driving pulse. Since neon, mostly used for HHG, is an inversion symmetric, nonlinear medium, even terms have to be cancelled and only odd harmonics are produced.The inherent structure of an HHG spectrum is displayed in figure 2.5 a). For low-order harmonics the intensity is decreasing exponentially, but subsequent higher-order harmonics occur with a nearly constant efficiency inducing a plateau, which reaches to the so-called *cut-off region*, where the intensity abruptly decays [128].

Commonly, the mechanism of HHG is described semi-classically by the intuitive three-step model proposed by Corkum [129], that is presented subsequently and introduced in figure 2.5 b). A complete quantum mechanical description of the HHG process, which is not discussed in this thesis, has been developed by Lewenstein et al. [130] and delivers outcomes that are very similar to the semi-classical ones.

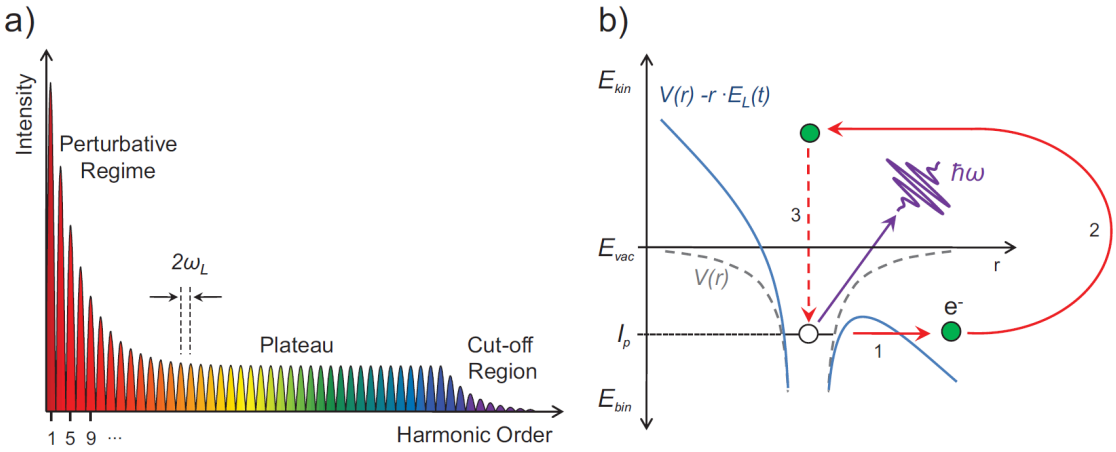

Figure 2.5: Spectrum and mechanism of higher harmonic generation with high-intensity, few-cycle laser pulses. (a) Schematic of a typical photon energy spectrum created by HHG in noble gases with its three distinctive regions. (b) Sketch of the semi-classical model for the HHG process. Distortion of the coulomb binding potential and tunnel ionization (step 1). Acceleration of the free electron in the electric field of the laser (step 2). Recombination of the electron with its parent ion and emission of an XUV photon (step 3). Adapted from: [128]

In presence of the NIR pulse, due to its enormous electric field strength, the Coulomb potential of the noble gas atoms is substantially, asymmetrically and oscillatingly distorted. Close to the largest oscillation peaks of the electric field of the pulse the atomic binding potential is extremely suppressed. Thus, it enables strong-field tunnel-ionization of a weakly bound valence electron. Subsequently, the electron is torn away from its nucleus and accelerated by the electric field of the laser pulse like a classical particle until the field oscillation approaches its amplitude of opposite sign. The free electron is firstly decelerated and then stopped, several nanometers away from its parent ion. Eventually, after a quarter of the oscillation period, the electron is accelerated back towards the ion gaining energy by the now reversed NIR field [131]. Thereby, an energy transfer from the laser field to the electron occurs, which is strongly dependent on the instant of ionization relative to the actual phase of the laser field. The energy gain reaches its highest value of $3.17 \cdot U_p$ when the ionization happens shortly after ($\omega_L t = 17°$) a maximum of the field oscillation [129]. ω_L is the angular frequency of the field and U_p is referred to as *ponderomotive potential*, which can be described as an cycle-averaged interaction energy originating from a charged particle exposed to an intense light field [132]:

$$U_p = \frac{e^2 {E_0}^2}{4 m_e {\omega_L}^2} \,. \tag{2.34}$$

Here, E_0 is the amplitude of the electric field of the NIR driving laser. Three quarters of a period of the electric field after the moment of ionization, the ionized and then thrown back electron has a small probability (conversion efficiency $\approx 10^{-6}$ [133]) for a radiative recombination with its abandoned parent ion. Hereby, the electron releases its entire, gathered energy within a radiation burst. This burst can have a considerably shorter pulse

duration than the driving NIR pulse, at a high harmonic frequency of the initial NIR pulse. The energy of the emitted XUV photon is given by

$$E_{XUV} = I_p + E_{\text{kin}} \ , \tag{2.35}$$

with the ionization potential I_p of the noble gas and the energy E_{kin} gained from the laser field. This procedure happens every half-cycle of the NIR field, so twice per complete cycle T. It is producing an XUV pulse train, that is separated by gaps of $T/2$ in the time domain, corresponding to a spacing of $2\omega_L$ in the frequency domain [134–136]. Many-cycle driving pulses produce XUV pulses of similar frequency with a slight time offset to each other. This results in an interference of the radiation produced in adjacent half-cycles, which builds the distinctive plateau in the high harmonic spectrum. The periodicity of the process causes the discrete peaks in the spectrum, see figure 2.5 a). However, the shortest XUV pulses released by this process build a high-energy cut-off in the resulting HHG spectrum. The so-called *cutoff energy* is given by

$$E_{\text{cut}-\text{off}} = 1.3 \cdot I_p + 3.17 \cdot U_p \ . \tag{2.36}$$

The prefactor of the ionization potential of roughly 1.3 results from quantum-mechanical calculations [130]. The efficiency of the HHG mechanism declines exponentially with photon energy above $E_{\text{cut}-\text{off}}$. In general, higher cut-off energies are achieved by tuning a lower central angular frequency ω_L or providing higher intensities. Unfortunately, there is a dilemma as the HHG efficiency otherwise rises with a higher ω_L due to an increasing ionization rate [129, 130]. Input NIR pulses with a central wavelength of approximately λ_c = 650 nm and peak intensities of about $1.5 \cdot 10^{15} \frac{\text{W}}{\text{cm}^2}$ results in a ponderomotive potential of $U_p \approx$ 50 eV. Utilizing a neon gas target with I_p = 21.6 eV, this yields a HHG cut-off energy of about 180 eV being far in the XUV range.

Selection of Isolated Attosecond Pulses

The cut-off domain of the high harmonics is greatly influenced by the CE-phase of the few-cycle NIR driving pulse, as it has a strong impact on the evolution of the few-cycle electric field. Therefore, the CE-phase is of utmost interest for eventually receiving isolated attosecond pulses [137, 138]. This fact can be elucidated considering the two extreme cases of a sine and a cosine-waveform of the electric field of the pulse, corresponding to a CE-phase of $\Delta\varphi = 0$ and $\Delta\varphi = \pi/2$, displayed in figure 2.6 a) and b).

For a sine-waveform, the highest-energy electron trajectories are induced by two field extrema of even strength. This results in the yield of two temporally separated, equally intense XUV bursts and an interference-induced modulation in the cut-off region, see figure 2.6 a) and d). On the contrary, for a cosine waveform there is only a single field maximum driving a single electron trajectory and thus generating a single XUV burst in the cut-off energy regime. Consequently, this temporally confined radiation implies the formation of a spectral continuum in the cut-off regime [137, 139], see figure 2.6 b) and d). The 2ω modulation known from the plateau in the spectrum vanishes and the spectrum

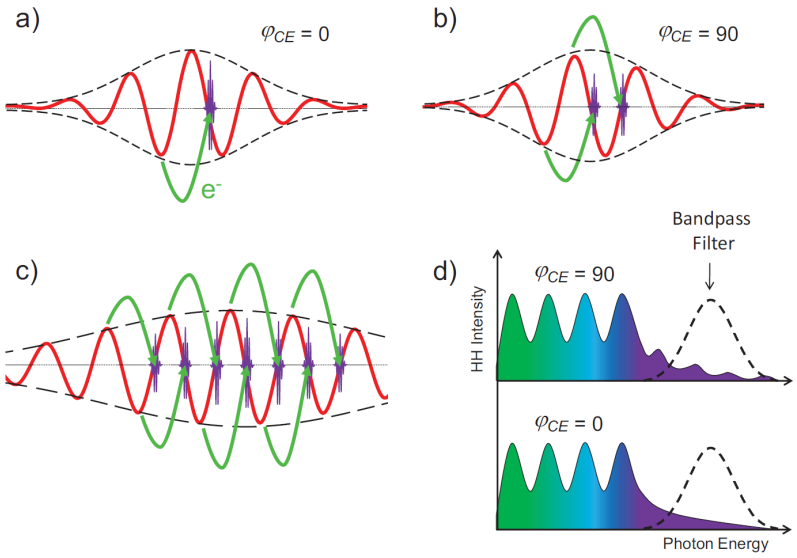

Figure 2.6: Consequences of waveform (CE-phase) and duration of the driving NIR pulse on the cut-off domain of the high harmonics spectrum. A few-cycle driving pulse with a cosine-waveform ($\varphi_{CE} = 0°$) generating a single XUV burst (a), one with a sine-waveform ($\varphi_{CE} = 90° = \pi/2$) creating two bursts (b) and a multi-cycle pulse producing an interfering pulse train (c) are illustrated. The cutoff region of the HHG spectrum is displayed for the two extreme cases of the CE-phase of few-cycle pulses. In the case of $\varphi_{CE} = 90° = \pi/2$, the cut-off region has a clearly visible modulation, whereas in the $\varphi_{CE} = 0°$ case, the cut-off shows a flat continuum (d). The dashed line depicts the transmission curve of an adequate bandpass filter, which can isolate a single attosecond pulse out of the cut-of region for a cosine-waveform. Adapted from [128].

remains unmodulated in the cut-off regime for cosine-waveforms, as the periodicity of the process is suppressed by the emission of a single highest-energy burst. However, this does not apply for sine-waveforms. Hence, for attosecond streaking experiments, the cosine-waveform case is clearly preferred. A pulse train of temporally isolated attosecond pulses can be eventually obtained [5, 133, 140–142] by a subsequent filtering of certain HHG spectra utilizing specially designed dielectric, multilayer mirrors [143–146]. These mirrors reflect only a specific, narrow range of the XUV spectrum in the cut-off region due to periodic and aperiodic stack of multiple, alternating layers from various materials.

Another issue of high harmonic generation, especially and most distinct for few-cycle driving pulses [126], is the fact of varying amplitudes for successive field extrema for both mentioned waveforms. So multi-cycle pulses generally give rise to several electron trajectories that contribute to the cut-off regime, (see figure 2.6 c) and thus prevent the isolation of single attosecond pulses. Therefore, an effective yield of isolated attosecond pulses via HHG, which is a prerequisite for attosecond streaking experiments [14], depends on both, a CE-phase of $\Delta\varphi = 0$ and a preferably single-cycle driving pulse [125]. Commonly, standard laser systems do not deliver pulses with a constant waveform, as the CE-Phase changes on a single-shot basis. Therefore, control and active stabilization of the CE-phase is of ultimate importance [128].

One characteristic of the high harmonic spectra produced via the HHG mechanism are their small divergence angles θ_n, which are scaling with the divergence angle of the driving NIR laser beam and for the n-th harmonic given by [147, 148]

$$\theta_n \approx \frac{\theta_L}{\sqrt{n}} \,. \tag{2.37}$$

A consequence of this slight divergence is the possibility for a separation of the higher harmonics and the co-propagating NIR driving laser by spatial filtering. Because of the nature of the HHG mechanism, both beams are intrinsically synchronized in time. In practice, not a single atom, but a macroscopic ensemble of atoms confined in a gas jet generates the high harmonics. A crucial condition for the efficiency of the HHG process is, that the driving pulse and the released harmonics propagate coherently with the same phase velocity. Otherwise, the produced single harmonics from various atoms in the vicinity would not add up constructively [149]. The so-called *phase matching* condition is accomplished by a congruent interplay of gas density, interaction length and laser beam focusing [128]. An upper limit for the conversion efficiency is set by re-absorption of XUV photons by atoms of the local gas jet environment [103, 150].

2.2.4 Attosecond Streaking Spectroscopy

To temporally resolve a motion or a process by measuring a specific quantity with a certain temporal resolution, one must utilize a measurement toll on at least the same order of precision. Concerning the profiling of ultrashort laser pulses this prerequisite becomes more and more challenging with decreasing pulse duration and accordingly increasing time-resolution. Down to the femtosecond regime quite sophisticated techniques such as autocorrelation [99] or frequency-resolved optical gating [151], using a replica of the pulse itself, have been established and are state-of-the-art approaches for the characterization of ultrashort laser pulses. For lack of nonlinear media and optical elements, such as beamsplitters for the XUV spectral range, these methods are not easily extendable to measurements on sub-fs laser pulses [26]. However, these problems are solved by the streaking method.

The *attosecond streaking* technique (*attosecond streak camera*) [5, 11, 15] is routinely implemented with isolated, sub-femtosecond extreme ultraviolet (XUV) pulses, synchronized to a few-cycle, phase-controlled near-infrared (NIR) light pulse [137]. With its unprecedented time resolution, it permits studying ultrafast electron dynamics, emerging on the sub-fs timescale, and monitoring of these processes directly in the time domain with sub-femtosecond resolution. Hence, it enables direct access to electron motion on the atomic scale [16, 18, 140, 142, 152]. Attosecond streaking spectroscopy is one of the most impressive techniques within attosecond science [10, 12, 14], it has evolved into a mighty tool to reach a sub-100 attosecond time resolution [17, 18, 20, 153, 154]. It got its name from the conventional *streak camera*, wherewith the characteristics of ultrashort light pulses on the order of picoseconds and a few hundred femtoseconds can be studied [155, 156].

A light pulse ionizes a target medium and generates photoelectrons in a photocathode. They are then accelerated into the direction of a detection screen, while being exposed to a fast-changing electric field perpendicular to their movement direction during the whole route. Thus, the electron trajectory is strongly influenced by this *streaking field* and the electrons are transversally deflected. Consequently, with knowledge of the applied electric field, the instant of ionization and the pulse shape of the original, ionizing light pulse can be derived from the spatial pattern on the screen caused by the electrons. Unfortunately, due to the limited speed of the electronics inducing the deflecting electric field, this technique cannot be used to resolve dynamics in the sub-fs range.

Attosecond streaking works quite similar: An XUV pulse of a few hundred attoseconds of pulse duration creates electrons by ionization of a target material within a very narrow time window defined by the temporal XUV pulse profile. Thereupon the ejected electrons are exposed to and manipulated by the strong electric field of a waveform-controlled, few-cycle NIR laser pulse, the *streaking laser pulse*. Hereby, the temporal development of photoelectron emission is mapped to modulations in the kinetic energy of the released photoelectrons as a function of the relative delay between the exciting XUV pulse and the linearly polarized, modulating NIR streaking pulse with a defined electric field E_L [11, 15]. As a prerequisite for an attosecond streaking experiment the optical period, T_{NIR}, of the NIR pulse must be much longer than the pulse duration of the XUV pulse, τ_{XUV} ($T_{\mathrm{NIR}} \gg \tau_{\mathrm{XUV}}$). Comparably to the HHG process, the moment of ionization strongly decides which phase of the electric field of the streaking laser effects the modulation of the electron's kinetic energy, measured by time-of-flight spectrometers. In streaking experiments, the time of flight of the emitted electrons from the sample to the spectrometer is detected and then translated into kinetic energy or momentum. By continuously changing the delay between both laser pulses one obtains a set of photoelectron spectra with periodically shifted and distorted photo lines. In this way, the temporal evolution of the vector field of the deployed streaking laser (see figure 2.7), a so-called *streaking trace* [153], is reproduced.

The kinetic energy of photoelectrons at the instant of ionization is basically solely depending on the binding energy of the electron and the frequency of the exciting photon. So photoelectrons, stemming from various bound states of the sample, create streaking traces classifiable and discriminable by their energy in a recorded spectrogram. The relative time delay of photoemission from distinct electronic states can be extracted by the determination of the offset along the delay axis between the respective streaking traces. For any specific relative delay, an electron emitted $\Delta\tau$ later will be exposed to a slightly different phase of the NIR streaking field than electrons emitted earlier, albeit the release of all electrons is caused by the same attosecond pulse. Therefore, via attosecond streaking one can access electron dynamics occurring on a time scale much shorter than the pulse duration of the ionizing XUV pulse [128]. Nowadays, these delays can be determined with temporal resolution of down to the sub-attosecond level (10^{-19} s) [19].

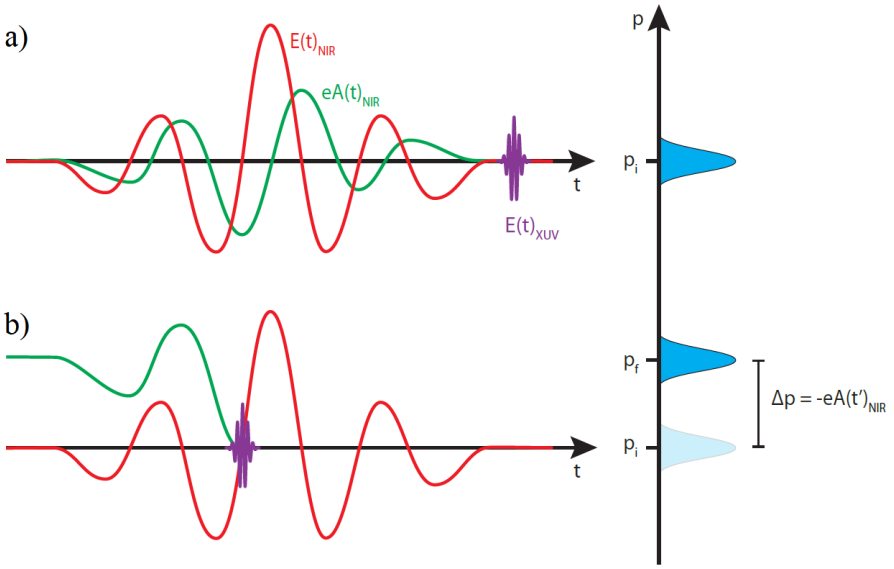

Figure 2.7: Principle of the attosecond streaking process with a linearly polarized laser pulse. The relations between the streaking field $E_L(t)$, the vector potential $A_L(t)$ and the momentum shift Δp are displayed. Photoelectrons obtain a momentum shift, depending on the actual vector potential of the electric field at the instant of ionization. (a) A photoelectron is generated by XUV photoionization prior to the presence of the NIR streaking field. Thus, an integration of the momentum change over the entire pulse duration amounts to zero, due to the oscillating nature of the streaking field. (b) An electron is emitted in presence of the streaking field. The integration of the momentum change from the moment of ionization is non-zero and results in a shift of the momentum distribution. Source: [157].

A semiclassical, intuitive description of the attosecond streaking mechanism, following the elaboration in [15], and a more complex but coherent, quantum mechanical description are shortly introduced in the following. More detailed elaborations on this can be found in [15] and [16], respectively.

Classical Picture

In the classical picture, the electron emitted via ionization by a high-energy XUV photon is treated as a charged particle instead of a wave packet. A relation between the final kinetic energy distribution of the released photoelectrons and the relative delay between the applied XUV and NIR laser pulses shall be derived subsequently. We make simplifying assumptions and neglect the effect of the electric field of the NIR streaking laser (*streaking field*) on the initial electronic state as well as any influence of the atomic binding potential of the parent ion on the emitted electron after ionization (strong-field approximation, SFA) [158, 159]. Thus, the kinetic energy of the photoelectron can be split up into two separated contributions attributable to the emission of an electron via ionization by an XUV photon and the acceleration in the NIR streaking field. Over the course of the ionization process an XUV photon with an energy $\hbar\omega_{\mathrm{XUV}}$ is absorbed by an atom emitting an electron

with an initial momentum of

$$p_i = \sqrt{2m_e E_{\mathrm{kin,i}}} = \sqrt{2m_e(\hbar\omega_{\mathrm{XUV}} - E_{\mathrm{bind}})}\,, \tag{2.38}$$

where E_{bind} is the binding energy of the electron and $E_{\mathrm{kin,i}} = \frac{1}{2}m_e v_i^2$ is its initial kinetic energy just after the ionization.

In a second step, the freed electron is accelerated in the presence of the electric field $E_L(t)$ of the streaking pulse and thus receives a net momentum transfer depending on the actual oscillation phase of the field at the time of birth of the electron. Given that the NIR streaking field is linearly polarized (z-axis) and considering the electron as a classical particle, the z-component of the motion equation of the electron can be described by

$$m_e\ddot{z} = -eE_L(t) = -eE_0(t)\cos(\omega_L t + \varphi_{CE})\,, \tag{2.39}$$

with $\Delta\varphi_{CE}$ being the CE-phase of the NIR pulse. Consequently, the integration of this classical approach starting from the instant of ionization over the rest of the NIR pulse delivers the resulting momentum shift Δp_z of the electron as a function of the vector potential $A_L(\tau)$ at the moment of XUV emission τ:

$$\Delta p_z(\tau) = -e\int_{\tau}^{\infty} E_0(t)\cos(\omega_L t + \varphi_{CE})dt = -eA_L(\tau)\,. \tag{2.40}$$

Here, we use the Coulomb gauge of the vector potential $A_L(t) = \int_t^{\infty} E_L(t')\,dt'$. This streaking-induced shift of the electron momentum distribution follows the vector potential $A_L(t)$. Due to the finite duration of the envelope $E_0(t)$ electrons will obtain a net momentum change, if and only if they are set free during the presence of the laser pulse.

One now uses the *adiabatic approximation*, that implies only a slight temporal deviation of the envelope of the NIR pulse compared with the frequency of its carrier wave: $\frac{dE_0(t)}{dt} \ll E_0\omega_L$ [140]. Thereby, one can integrate equation 2.40 and obtains an analytical expression for the momentum change of the streaked electron:

$$\Delta p_z(\tau) \approx \frac{eE_0(\tau)}{\omega_L}\sin(\omega_L\tau + \varphi_{CE}) = \sqrt{4U_p(\tau)m_e}\sin(\omega_L\tau + \varphi_{CE}) \tag{2.41}$$

For a general case, utilizing the law of cosines, the final momentum p_f of the electron is defined by

$$p_f^2 = p_i^2 + 2\Delta p_z p_i\cos\theta + \Delta p_z^2\,, \tag{2.42}$$

where θ is an arbitrary angle between the axis of the linear polarization of the streaking laser and the final momentum p_f (compare also figure 2.8). Thus, the detection angle θ is decisive for the final momentum of the electron. The final kinetic energy of the electron can be derived by inserting equation 2.41 into equation 2.42 and by applying the legitimate

assumption, that the ponderomotive potential U_p at the moment of photoionization is small compared to the initial kinetic energy $E_{\mathrm{kin,i}}$ of the electron [15]

$$E_{\mathrm{kin,f}}(\tau) = \frac{{p_i}^2}{2m_e} = E_{\mathrm{kin,i}} + 2\,U_p(\tau)\cos(2\theta)\sin^2(\omega_L\tau + \varphi_{\mathrm{CE}}) + \sqrt{8E_{\mathrm{kin,i}}\,U_p(\tau)}\cos(\theta)\sin(\omega_L\tau + \varphi_{\mathrm{CE}})\,. \tag{2.43}$$

Eventually, neglecting a constant CE-phase, the final kinetic energy $E_{\mathrm{kin,f}}$ of the electron solely depends on the time-dependent part of the phase of the NIR streaking laser pulse at the instant of ionization τ or on the relative delay between the two laser pulses. Furthermore, the experimental geometry highly influences the modulation strength through the detection angle θ. In this description, the distribution of the momenta of the electrons at the instant of ionization τ is supposed to be isotropic.

In principle, there are two detection schemes, as can be seen in figure 2.8: First, a perpendicular orientation with an detection angle of $\theta = 90°$ between detector axis and polarization axis of the NIR laser field. In this configuration, one detects only an asymmetrical broadening in energy and a periodic shift by twice the laser frequency ($2\omega_L$) to lower energies in the photoelectron spectra [5, 140]. Hereby, the third term on the right side of equation 2.43 is cancelled. In the parallel configuration with an angle of $\theta = 0°$ between NIR polarization and detector axis, a periodic up- and down-shift in energy of the photoelectron lines is detected in the spectra, following the vector potential of the NIR pulse without any considerable broadening [153]. In this case, the induced change of the final kinetic energy of the photoelectrons as a function of τ is reduced to

$$\Delta E_{\mathrm{kin}}(\tau) = E_{\mathrm{kin,f}} - E_{\mathrm{kin,i}} \approx \sqrt{8U_P(\tau)E_{\mathrm{kin,i}}}\sin(\omega_L\tau + \varphi_{CE})\,, \tag{2.44}$$

with the premise that $E_{\mathrm{kin,i}} \gg U_p$. This is satisfied in the streaking experiments presented in this thesis, since U_p is on the order of a few tens of meV, being negligible compared to the detected electron energies. In practice indeed, one finds always a mixture of both extreme cases due to the restricted acceptance angle of the detector.

The momentum (eq. 2.41) as well as the energy shift (eq. 2.44) are CEP-sensitive, so with an actively stabilized CE-phase there only remains a dependency on τ, which is the instant when the electron reaches the laser-dressed continuum. Hence, scanning the time τ of ionization by varying the delay between both laser pulses, the vector potential $A_L(t)$, which contains complete information about the electric field of the NIR laser pulse, can be directly retrieved [11, 153, 161] from the recorded series of streaked electron spectra (*spectrogram*). From this, the relative arrival times of electrons originating from different electronic states can be determined.

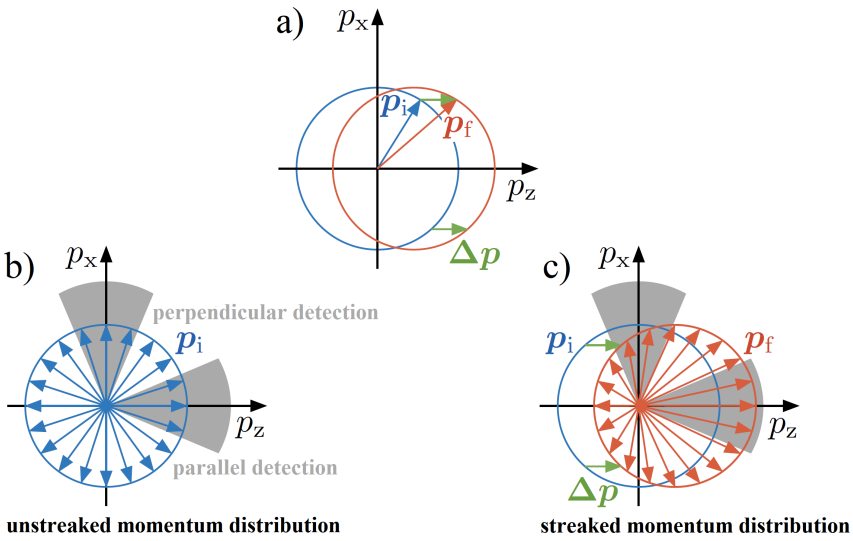

Figure 2.8: Depiction of the angle-dependent streaking effect on the initial, isotropic electron momentum distribution. (a) The initial electron momentum distribution is shifted by Δp_z (green) along the z-direction due to the electric field of the streaking laser. The final momentum p_f is given by $p_f = p_i + \Delta p_z$ (red circle). (b) Unstreaked momentum distribution (blue circle). For both extreme detection angles the same isotropic momentum distributions are measured in absence of the streaking field. (c) Illustration of the effect of the detector axis in the streaking case, where a momentum shift Δp_z is induced. For a detection orientation parallel to the z-axis ($\theta = 0°$), an alternating shift dependent on the phase of the streaking field is observed. In the case of a detection angle perpendicular to the laser polarization ($\theta = 90°$), one can record an asymmetric, periodic broadening accompanied by a down-shift in momentum [5]. Adapted from [160].

Quantum Mechanical Picture

The classical approach presented above allows an intuitive and basic understanding of the streaking method, but it fails by involving more realistic features of the ionizing XUV pulse without using the concept of the electron wave packet: The limited pulse duration or a potential chirp, for example. In the quantum mechanical approach, the electron as a classical particle is exchanged for a wave packet and atomic units are used. The following, short elaboration is adapted from [16], where this topic has been presented in very great detail and comprehensively. An in-depth derivation is elaborated in [162].

We start with the ionization process initiated by the XUV electric field, generating an electron wave packet in the continuum. This process can be quantum mechanically considered as a transition from an initial bound state to a final continuum state. As per first-order perturbation theory, for times after disappearance of the attosecond pulse, the transition amplitude $a_{\vec{p_f}}$ from an initial ground state i to a final continuum state f of an electron with momentum p is depicted by

$$a_{\vec{p_f}} = -i \int_{-\infty}^{\infty} dt \; d_{\vec{p_f}} \vec{E}_{\mathrm{XUV}}(t) \; e^{i(\vec{p_f}^{\,2}/2 + I_p)} \; . \tag{2.45}$$

Here, I_p is the ionization potential, $E_{\mathrm{XUV}}(t)$ is the electric field of the attosecond XUV pulse, $W = p_f^2/2$ is the energy of the final continuum state and $d_{\vec{p_f}}$ is the dipole transition matrix element. The latter is commonly well known and can be assumed as constant

over the energy bandwidth of the ionizing XUV field in this context. Hereby, the *single active electron approximation* has been utilized, which says that only a single electron is considered and possible interactions with other electrons are neglected. One can see, that the attosecond field and the generated photoelectron spectrum are directly connected in phase and amplitude.

Having connected the XUV attosecond pulse and the emitted electron wave packet, we now concentrate on the effect induced by the NIR streaking field. In case of photoionization in the presence of the streaking laser field, once again the strong field approximation is applied. So after ionization, one neglects any effect of the potential of the parent ion on the free electron propagation [130]. As discussed in [16], the approximation also holds for moderate laser intensities. Consequently, the transition amplitude for a specific delay between XUV and NIR field is given by [163]

$$a_{\vec{p_f}}(\tau) = -i \int_{-\infty}^{\infty} dt\, d_{\vec{p_f}+\vec{A_L}(t)} \vec{E}_{\mathrm{XUV}}(t-\tau)\, e^{iI_p t - i\int_t^{\infty} dt' \left(\vec{p_f}+\vec{A_L}(t')\right)^2/2}\,, \tag{2.46}$$

with the vector potential $\vec{A_L}(t)$ of the NIR field in the Coulomb gauge. Here, the field-dependent dipole matrix element $d_{\vec{p_f}+\vec{A_L}(t)}$ together with a further phase term describes the effect of the NIR streaking field on the electron wave packet. This equation can be derived from the time-dependent Schrödinger equation [163] and can also be conceived quite intuitively: $a_{\vec{p_f}}(\tau)$ can be understood as the sum of probability amplitudes of all electron trajectories, which result in the same final momentum $\vec{p_f}(\tau)$. The photoelectron spectrum is then given by $S = \left|a_{\vec{p_f}}\right|^2$. The fact that the electron can be released at any time t is taken into consideration with the integration over t . The probability for this is calculated by the instantaneous amplitude of the XUV field multiplied with the dipole transition matrix element at the instant right after ionization. The exponential in the integral allows for the phase of this process. This phase is composed of the phase $I_p t$, which is accumulated in the ground state up to the time t, and the phase, which is subsequently accumulated in the continuum state [16]. Equation 2.46 can be reformulated providing a useful version for the understanding of attosecond streaking:

$$a_{\vec{p_f}}(\tau) = -i \int_{-\infty}^{\infty} dt\, d_{\vec{p_f}+\vec{A_L}(t)}\, \vec{E}_{\mathrm{XUV}}(t-\tau)\, e^{i\left(\vec{p_f}^{\,2}/2 + I_p\right)t}\, e^{i\phi_V(t)}\,. \tag{2.47}$$

Here, ϕ_V is the so-called *Volkov phase* [164]

$$\phi_V(\vec{p_f}, t) = -\int_t^{\infty} dt' \left(\vec{p_f}\cdot\vec{A_L}(t') + \frac{1}{2}\vec{A_L}^{\,2}(t')\right)\,. \tag{2.48}$$

A comparison of equations 2.45, 2.47 and 2.48 shows that the principal consequence of the streaking field is a phase modulation in time $\Phi(t)$ on the electron wave packet. The angle-dependence of the final momentum as we know it from equation 2.43 in the classical picture is here expressed by the vector product $\vec{p_f}\cdot\vec{A_L}(t')$ in the Volkov phase.

2.2.5 Pulse Retrieval and Extraction of Attosecond Delays

As already mentioned in section 2.2.4, one can retrieve the pulse characteristics of both, the XUV and the IR laser pulse from a recorded streaking spectrogram, a series of photoelectron spectra as a function of the delay time between XUV and IR pulse. Moreover, within the analysis of a spectrogram with more than one streaked photoline (*streaking trace*) at various energies, there is a chance of discovering a generic phase shift between individual streaking traces, as if the wave packets were created with a certain time offset. Such phase shifts are ascribed to delays $\Delta\tau$ in photoemission and are naturally in the range of attoseconds (in the sub-femtosecond range). The existence of a delay in photoemission of electrons, escaping the atomic binding potential from different atomic orbitals, was first theoretically proposed by Wigner [165] in 1955 within the context of nuclear scattering theory. Experimentally, it has been discovered for the first time by Schultze et al. in 2010 [18] by the use of attosecond streaking spectroscopy. Thus, attosecond streaking spectroscopy and an associated theoretical research open new perspectives and profound understanding of electron dynamics and their underlying mechanisms on the attosecond timescale.

In the course of this thesis, attosecond streaking experiments on liquid water have been conducted and the new, scientific insights thereof are presented in chapter 6. By now, a few different data analysis algorithms for the retrieval of pulse characteristics and photoemission delays out of streaking spectrograms have been developed. Proceeding from the analysis method presented in [18], the algorithm, which has been applied on the recorded streaking data for pulse retrieval and a determination of the attosecond delays, as well as the appropriate software have been further developed and presented in detail by Marcus Ossiander [160]. The algorithm is referred to as restricted time-dependent Schroedinger-equation (TDSE) fit in the following. Simply put, it solves the TDSE in the strong-field approximation yielding Volkov states to retrieve the spectrogram by use of parameterized IR and XUV pulses. Utilizing a nonlinear optimization method, a Levenberg-Marquardt algorithm [18], it conducts a least-squares fit of reasonably predefined electron wave packets to a 'differentiated' streaking spectrogram, using a reduced number of fit parameters.

Within the frame of the algorithm, a standard energy calibration and an adequate background subtraction have to be conducted. Instead of the common, well-established [23] splitted-Shirley background subtraction method [166], which corrects for the inelastic electron scattering background, a more sophisticated technique for the background subtraction is performed for streaking spectrograms presented in this thesis: Each spectrogram is differentiated along its delay axis and all temporally constant contributions are thereby identified and removed from the spectrogram [18]. Hereby, one assumes that inelastically scattered electrons are not streaked (energy-shifted) in an accurately defined way due to the statistical nature of electron scattering. Thus, the background of inelastically scattered electrons is justifiably supposed to be constant over all XUV/NIR delays and is consequently subtracted from the spectra [160]. In a nutshell, by the differentiation of

both, the measured and the reconstructed spectrograms, prior to their comparison, any time-independent components of the recorded spectra can be eliminated. Instead of the measured and reconstructed spectrograms, their derivatives are compared. This approach provides reasonable and valid results that are more reliable and objective compared to the splitted-Shirley approach [18], as can be seen in figure 6.5.

2.3 Angular Streaking Approach

One of the oldest methods of time measurement developed by mankind is the observation of a rotating hand, as it is implemented on the face of an analogue watch. Applying this primordial principle, attosecond angular streaking (*attoclock*) [167–170], an auspicious alteration of attosecond streaking, is a different method to determine pulse durations and measure electron dynamics with a temporal resolution in the range of attoseconds. When it was first proposed, angular streaking was intended to measure the CE-phase of ultrashort pulses on a single-shot basis [171]. In conventional *energy streaking* or *linear streaking*, presented in section 2.2.4, a linearly polarized NIR electric field is utilized to translate time into energy [129, 141], whereas in angular streaking a circularly polarized NIR pulse is applied to map time onto angle [15, 131, 167].

Contrary to angular streaking experiments, using the very same NIR laser pulse for ionization and streaking of photoelectrons [167–169], a two-color approach with an ionizing, linearly polarized, femtosecond X-ray pulse and a synchronized, rotating infrared streaking field shall be considered here. Applying two-color angular streaking, experiments for the measurement of pulse duration and temporal substructure of SASE FEL pulses (see chapter 2.1) have been successfully conducted within the scope of this work. The experimental outcomes and the subsequent data analysis are presented in chapter 4 as the main results in this thesis.

In a nutshell, the angular streaking approach utilizes the continuously revolving vector potential of a circularly polarized, infrared laser pulse for deflecting photoelectrons after ionization in the angular spatial direction. In the presence of the streaking field, the initial angular distribution of the released photoelectrons gets redistributed, depending on the actual angular orientation of the streaking vector potential at the instant of their ionization. Electrons that are ejected from different phases within the X-ray pulse envelope are streaked at different angles, varying from shot to shot. Thus, the moment of ionization is here imprinted onto the electron energy distribution with respect to the detection angle in the polarization plane, which is comparable with the hand of a clock whose face is determined by the oscillation period of the streaking field [131, 167]. The temporal structure of the photoionizing, ultrashort pulse is in this way mapped to the angle-resolved photoelectron energy distribution. Out of this, amplitude and phase of the streaking field as well as intensity structure, pulse duration and chirp of the ultrashort X-ray pulse can be retrieved.

The main principle of our angular streaking experiments [172] is illustrated in figure 2.9. Exemplary streaking spectra as a function of the electron emission angle generated by a simulation of two-color angular streaking are shown in figure 2.10.

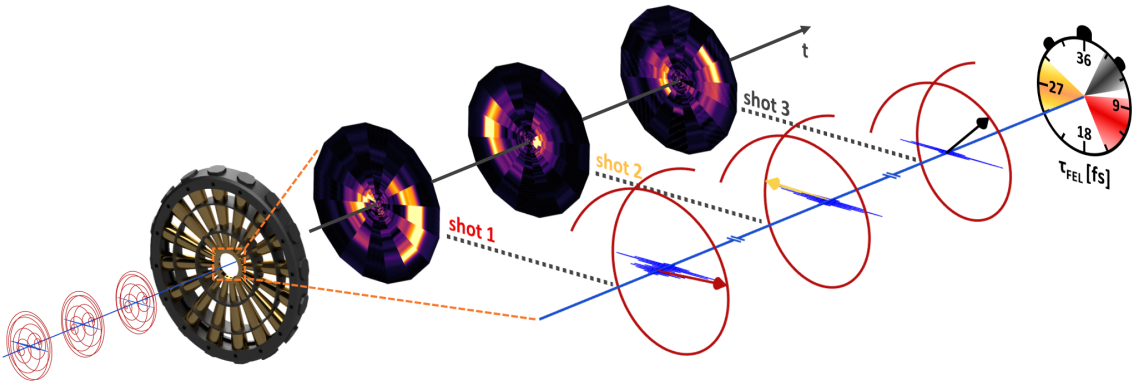

Figure 2.9: Angular streaking resolves the X-ray pulse structure via angle-dependent change of the kinetic energy of photoelectrons. X-ray pulses ionize the target gas in the center of the detector array. The rotating IR laser field streaks photoelectrons in different angular directions dependent on their ionization time. Three individual X-ray pulses, denominated as shots 1, 2 and 3, overlap in the interaction region (dashed orange rectangle, enlarged depiction on the right) with three IR pulses at different phases of their circular field and generate clearly distinguishable photoelectron time–energy distributions, shown as false color polar plots of experimental data. In these plots, the intensity is proportional to the number of photoelectrons, the distance from the center represents the photoelectrons' kinetic energy and the angle along the circle corresponds to the IR phases during photoionization by the X-ray pulse.

Just as a watch hand, the streaking vector potential revolves one complete turn within one polarization period. Thus, a measurement of the electron emission angle allows timing at a precision well below one optical period. The resolution of angular streaking can be simply adjusted by the chosen streaking wavelength, as the time for one circumvolution is determined by the carrier period of the infrared laser:

$$t = \frac{\varphi}{2\pi} \cdot \frac{\lambda}{c_0} \,. \tag{2.49}$$

The rotation period of the streaking laser must be longer than the expected pulse durations of the FEL pulses to avoid ambiguities from multiple revolutions of the *clock* within one FEL pulse. However, multiple cycles of the streaking vector potential during the presence of the X-ray pulse must be prevented to avoid ambiguities in the data. A photoelectron emitted at time t_0 is deflected into a direction $\theta(t_0)$ in the polarization plane and perpendicular to the orientation of the electric field vector at t_0. An electron that is emitted with a time offset of δt with respect to the first one propagates into the direction $\theta(t_0+\delta t) = \theta(t_0)+2\pi\ \delta t/T_0$. Here, T_0 is the period of the streaking field [131].

Both, energy and angular streaking have assets and drawbacks: Conventional energy streaking is limited to approximately a quarter of a cycle when the streaking field alters nearly linearly with the time [15], whereas angular streaking can be performed over a whole cycle. Within a 360°-rotation of the field its amplitude is nearly constant due to the

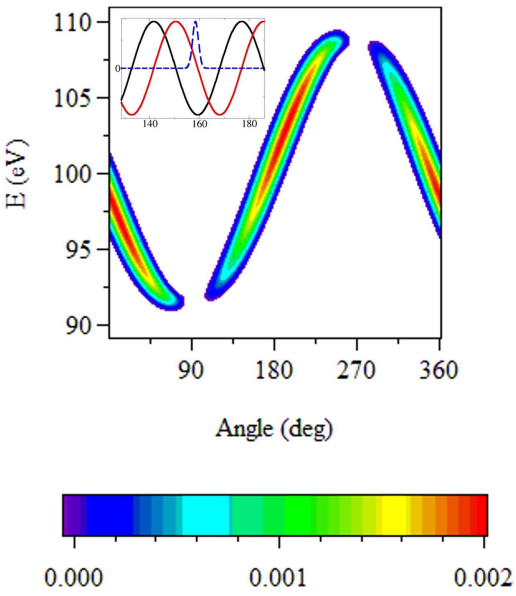

Figure 2.10: Simulation of two-color angular streaking. Color-scaled photoelectron streaking spectra are plotted as a function of the electron emission angle. The photoelectrons are generated by an X-ray pulse of 2.8 fs (FWHM) and angularly streaked by a circularly polarized THz field with a pulse duration of 300 fs and at a frequency of 28.2 THz. The unstreaked, kinetic energy of the photoelectrons is 100 eV. In the inset, the X-ray and THz pulse are shown, the red and black lines depict the x- and y-component of the streaking field, respectively. Adapted from [173].

flat slope of the field envelope for the long IR streaking pulse. Moreover, angular streaking is defined only by the frequency of the streaking field and is mainly independent from its intensity. However, angular streaking requires an elaborate detector (see section 3.2.3).

The electric field of a circularly polarized streaking pulse can be expressed by the sum of two orthogonal components

$$E_x(t) = E_{0,x}(t)\cos(\omega_L t + \varphi_{\mathrm{CE,x}}) \tag{2.50}$$

$$E_y(t) = E_{0,y}(t)\cos(\omega_L t + \varphi_{\mathrm{CE,y}})\ , \tag{2.51}$$

where the pulse envelopes in time are the same $E_{0,x}(t) = E_{0,y}(t)$ and the CE-phases are shifted to each other by $\pi/2$. In the more general case of an elliptically polarized streaking field ($E_{0,x}(t) \neq E_{0,y}(t)$), the resulting magnitude of the field $E(t) = \sqrt{E_x^2(t) + E_y^2(t)}$ is time-dependent. Under the assumption $E_{0,x}(t) < E_{0,y}(t)$, the ellipticity is determined by the ratio $E_{0,x}(t)/E_{0,y}(t)$.

The vector potential of the streaking field revolves along the polarization ellipse and passes hereby the minor and the major semi axes of the polarization ellipse. This results in a minimum and a maximum magnitude of the vector potential within the pulse envelope, naturally separated by an angle of $\pi/2$. Hence, in the case of a temporally unchirped streaking pulse, the vector potential at a certain spatial point along the propagation axis revolves at the optical central frequency with a rising and dropping amplitude.

Analytic Description

Accompanying the experiments presented in this thesis, the angular streaking method, as an application to determine pulse durations of femtosecond pulses and the time evolution of atomic processes, has been studied theoretically by Kazansky *et al.* [173, 174]. A detailed semiclassical description combined with numerical calculations, starting from a quantum-mechanical approach, is given there. In the following, an intuitive, classical description of the two-color angular streaking method, with the focus on the derivation of the angle- and time-dependent final kinetic energy of an angularly streaked electron and the derivation of an expression for the resulting experimental photoelectron intensity distribution, are presented. A description of the X-ray pulse retrieval from angular streaking data is presented in chapter 4. The subsequent section is based on [15] and mainly adapted from the supplementary information of [172].

In general, the electric field of an elliptically polarized laser field can be written as

$$\vec{E}(t) = \frac{E_0(t)}{\sqrt{1+\epsilon^2}} \cdot \{\cos(\omega_L t + \varphi_{\mathrm{CE}})\ \vec{e_x} + \epsilon(t)\ \sin(\omega_L t + \varphi_{\mathrm{CE}})\ \vec{e_y}\}\ , \tag{2.52}$$

with $E_0(t)$ being the time-dependent field envelope and ϵ being the ellipticity parameter. ϵ = 0 for linearly polarized and $\epsilon = \pm 1$ for circularly polarized light, respectively. Similarly to the classical derivation for the linear/energy streaking case in section 2.2.4, for angular streaking employing a circularly polarized streaking field, the final kinetic energy $E_f(\theta)$ of the angularly streaked photoelectrons at an observation angle θ is eventually given by [15]

$$E_f(\theta) = E_i - U_p\ \cos 2(\varphi_L - \theta) + \alpha_c\ \sqrt{4E_i U_p}\ \cos(\theta - \varphi_L)\ , \tag{2.53}$$

with the optical phase $\varphi_L = \omega_L t + \varphi_{\mathrm{CE}}$ of the streaking field and the ponderomotive potential U_p. On the assumption $E_i \gg U_p$, which we already applied in section 2.2.4 for energy streaking, the second term on the right in equation 2.53 can be neglected and the correction term α_C reduces to α_C = 1. Thus, equation 2.53 can be simplified to

$$E_f(\theta) \approx E_i + \sigma \cdot \cos(\theta - \varphi_L)\ , \tag{2.54}$$

which is modulated with φ_L. Here, $\sigma = \sqrt{4E_i U_p}$ is referred to as *streaking kick amplitude*. Since the optical laser pulses at angular streaking experiments for the characterization of ultrashort pulses are not forced to be in the few-cycle regime, the CE-phase of the laser field can be neglected. Therefore, the angle-dependent, final kinetic energy of the photoionized electrons $E_f(E_i, \theta, t_i)$ as a function of the observation angle θ and the initial electron energy E_i, which is offset by the streaking kick σ in the direction of the vector potential at the instant of ionization t_i, can be expressed by

$$E_f(E_i, \theta, t_i) \propto E_i + \sigma \cdot \cos(\theta - 2\pi \frac{ct_i}{\lambda_L})\ , \tag{2.55}$$

with the wavelength λ_L of the optical streaking laser pulse.
The distribution of the photoelectron kinetic energy E_i in the absence of a streaking field can now be defined as

$$I(E_f) \propto e^{-\frac{(E_f-E_i)^2}{2\beta^2}} , \tag{2.56}$$

with β being the limited energy resolution of the detecting spectrometer. In general, the energy-related photoelectron intensity distribution $I(E_f, \theta)$ can also depend on the detection angle θ perpendicular to the propagation axis of the X-ray pulse. As an anticipation to chapter 4 we assume here that the photoelectrons originate from the neon 1s orbital. Due to the spherical symmetry of this orbital [35], combined with the ionization by a linearly polarized X-ray pulses, one must consider the resulting angle dependence, which leads to

$$I(E_f, \theta) \propto (1 - \cos(2(\theta - \theta_x))\ e^{-\frac{(E_f-E_i)^2}{2\beta^2}} , \tag{2.57}$$

where θ_x determines the angle of the X-ray polarization from the perspective of the detector array and is set to $\pi/2$ within the scope of this thesis.

In a next step, the effect of a time-dependent, precisely circularly polarized streaking field is taken into consideration. The angle- and energy-dependent electron intensity distribution can approximately be expressed as follows:

$$I(E_f, \theta, t) \propto [1 - \cos(2(\theta - \theta_x))]\ e^{-\frac{\left(E_f-E_i-\sigma\cos(\theta-\omega_L t)\right)^2}{2\beta^2}} . \tag{2.58}$$

Considering the more general case of an elliptically polarized streaking field, the effect induced by this ellipticity ($\epsilon < 1$) can be incorporated by implementing an angle-dependent streaking kick

$$\sigma(\theta) = \bar{\sigma}(t) \cdot \left[\sin(\theta - \theta_0)^2 + \epsilon^2 \cos(\theta - \theta_0)^2\right]^{1/2} , \tag{2.59}$$

where θ_0 determines the tilt of the polarization ellipse with respect to the 0° axis of the detector array. The amplitude of the streaking kick $\bar{\sigma}(t)$ is time-dependent and proportional to the intensity envelope of the streaking pulse $I_L(t)$. Nevertheless, on a single-shot basis the streaking kick $\bar{\sigma}(t)$ can be regarded as constant, if a single period of the streaking field is set to be much longer than the anticipated, mean X-ray pulse duration. In this way, the change of $I_L(t)$ within the presence of the X-ray pulse can be neglected. Furthermore, the photoelectron distribution $I(E, \theta, t)$ increases directly proportional with the actual intensity of the X-ray pulse $I_{\mathrm{X-ray}}(t)$. In the general case of a chirped X-ray pulse with a specific bandwidth, the primary electron kinetic energy E_i may be considered as a function of time. Implementing all three ideas, equation 2.58 has to be adapted leading to

$$I(E, \theta, t) \propto I_{\mathrm{X-ray}}(t)\ [1 - \cos(2(\theta - \theta_x))]\ e^{-\frac{\left(E-E_i(t)-\sigma(\theta)\cos(\theta-\omega_L t)\right)^2}{2\beta^2}} . \tag{2.60}$$

Eventually, an integration of the photoelectron intensity distribution over time provides an expression for the experimentally measured angular streaking spectrogram:

$$I_{\mathrm{total}}(E,\theta) = \int dt\; I(E,\theta,t)\;. \tag{2.61}$$

Chapter 3

Two-colour Angular Streaking at the Linac Coherent Light Source

As already mentioned at the beginning, time-resolved pump/probe experiments, especially at the arising high-repetition rate X-ray FELs, enable the study of atomic and molecular structural motion and the direct observation of electronic configuration changes originating from inner-shell electron transitions. Consequently, an X-ray pulse characterization is a fundamental prerequisite for pump/probe experiments, since the temporal resolution is highly affected by the pulse durations of the pump and the probe pulse. This holds true not only for the pulse duration itself, but also for the complete temporal coherence features including the sub-spikes of the SASE X-ray pulses. Furthermore, the inherent jitter of the relative optical/X-ray arrival time at the experiment, emerging from the single-shot jitter of the electron energy in the accelerator and the corresponding fluctuations in the flight times towards the undulator, adversely influences any time-resolved measurements and pulse characterizations at a SASE FEL. Therefore, a pulse characterization including a precise arrival time measurement is crucial for any intensity-dependent experiments and especially for time-resolved pump/probe experiments.

Some indirect measurement methods have been applied to retrieve SASE X-ray FEL pulse durations from the electron bunch length prior to the undulator [38] or from the coherence properties of the FEL pulses in the spectral domain [175]. Nevertheless, these methods are not capable of retrieving the full time structure of the FEL pulses and considerable deviations of these results from the actual pulse durations have been demonstrated [81]. The introduction of the X-band radiofrequency transverse deflector (XTCAV) at LCLS, which studies the electron bunch after passing the undulator, constituted a considerable increase in reliability and resolution regarding the X-ray pulse characterization [84]. However, all these indirect techniques do not fully provide the desired results and are still dependent on an accurate calibration using direct measurements in the time domain [47].

Common state-of-the-art techniques for directly measuring optical pulse durations, just as autocorrelation or FROG among others, cannot be utilized for X-ray pulses owing to the lack of suitable optics and the vanishingly low nonlinear interaction cross sections in the X-ray regime. Several techniques based on solid-state targets for the characterization of X-ray pulses are utilizing the transient change of the target's refractive index caused by the

FEL pulse or measuring the cross-correlation between X-ray and mid-infrared pulses [85, 176]. Unfortunately, these techniques are invasive concerning the X-ray beam and their temporal resolution is restricted owing to the inherent electron relaxation dynamics in condensed mater. Hence, they are not applicable for few-femtosecond pulse durations [47].

Therefore, the streaking spectroscopy method commonly used for the characterization of XUV attosecond pulses from HHG sources is the means of choice: Time-resolved photoelectron energy streaking measurements (see 2.2.4) of X-ray FEL pulses, utilizing a linearly polarized streaking field and mapping the temporal structure to the photoelectron energy, have been previously applied to X-ray FEL pulses [70, 71, 80, 81]. For conventional energy streaking, the X-ray pulse should be overlapped with the maximum slope of the mid-infrared (MIR) streaking field to achieve an optimal temporal resolution. However, an accurate time overlap with this streaking ramp or any certain phase of the streaking field is not guaranteed on a single-shot basis at SASE FELs, owing to the inherent arrival time jitter between optical and X-ray pulses [86, 177, 178], which causes ambiguities in the data analysis.

Nevertheless, due to the stochastic nature of SASE FEL pulses a direct, single-shot pulse characterization is required. Up to now energy streaking measurements cannot provide reliable information about the unresolved spike structure and the pulse duration of few-femtosecond SASE X-ray pulses [70, 71]. Hence, a direct, precise single-shot determination of the temporal X-ray pulse substructure and the relative optical/X-ray arrival time coincidentally usable for a wide range of X-ray pulse settings, is still highly desired and not yet available. Two-color angular streaking (see 2.3) copes with all these issues using a circularly polarized streaking laser and an angle-dependent detection method for the photoelectrons. Recently, this method has been theoretically studied for a THz streaking field applied at realistic X-ray FEL parameters by means of quasiclassical considerations as well as numerical calculations in a quantum mechanical approach [173, 174].

In the following chapter, a two-color angular streaking experiment for the single-shot determination of the X-ray pulse substructure and the arrival time conducted at the Linac Coherent Light Source at SLAC National Accelerator Laboratory in Menlo Park, CA, USA in 2015 shall be presented in detail. The corresponding data analysis and the experimental results will be presented in the subsequent chapter.

3.1 Linac Coherent Light Source at SLAC National Accelerator Laboratory

The Linac Coherent Light Source is the free-electron laser facility situated at SLAC National Accelerator Laboratory in Menlo Park, California, USA. (see figure 3.1). Besides LCLS, the most important current FEL facilities are FERMI in Trieste, Italy [45], SACLA at SPring-8 in Japan [44], the SwissFEL at the Paul-Scherer Institute in Switzerland [179], the

new European XFEL in Germany [180] and the PAL-XFEL facility in South Korea [181]. At LCLS, hard and soft coherent X-ray pulses are generated with a peak brightness of approximately a billion times ($\sim$ ten orders of magnitude) brighter than previously provided at conventional synchrotrons [46]. LCLS achieved first lasing in April 2009. A summary of typical X-ray beam parameters at LCLS is presented in table 3.1.

Figure 3.1: Aerial view of LCLS. The major components of LCLS are highlighted and labeled. Source: [182].

Photon Beam parameters	Hard X-rays	Soft X-rays	Unit
Photon energy	2000 – 12800	280 – 2000	eV
X-ray pulse energy	up to 5	up to 4	mJ
Peak Brightness	0.08 – 1.4	0.003 – 0.14	10^{33} §
SASE bandwidth (FWHM)	0.1 – 0.4	0.1 – 0.8	%
Pulse duration (FWHM)	50 – 250	70 – 400	fs
Pulse energy stability	<10	<10	%
Repetition rate	120	120	Hz
§Brightness units are photons/sec/mm^2/mrad^2/0.1%-BW			

Table 3.1: Typical measured LCLS parameters for hard and soft X-rays. The values of the LCLS parameters are just general guidelines and vary for particular operation modes with respect to the actual energy, bandwidth and pulse length. Source: [183, 184].

For the electron acceleration at LCLS, the last kilometer of the old, 3-km long SLAC linac [185] has been partially reconstructed for driving the FEL. The layout of LCLS is displayed in figure 3.2. The electron injector at LCLS [186] is a radio-frequency photocathode gun [187], comprising a copper cathode that is striked by UV pulses from frequency-tripled, amplified Ti:sapphire laser light. The RF gun produces a nominal electron bunch charge of 150 pC to 250 pC with a pulse length in the range of a few picoseconds at a peak current of 35 A. It rapidly accelerates the electrons from the cathode in order to suppress space charge effects on the achievable photon beam brightness [41]. The so-called *laser heater* in the injector induces a small amount of uncorrelated energy spread in the electron

beam using a co-propagating MIR laser. Thus, microbunching instabilities are suppressed (Landau damping) avoiding a potential breakup of the electron beam [188, 189].

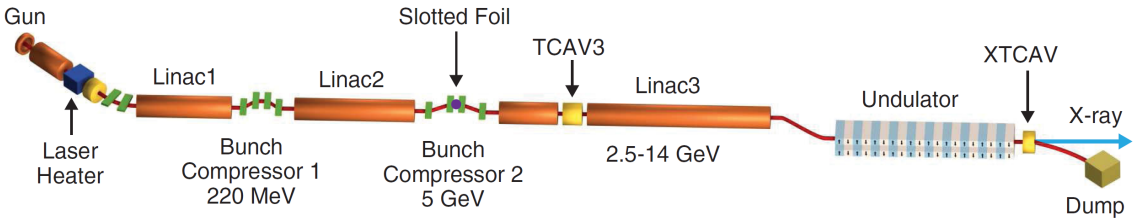

Figure 3.2: LCLS machine layout. Layout from the electron gun (injector) to the beam dump with the laser heater, the two bunch compressor chicanes (BC1 and BC2) subdividing the linac into three sections and the 132-m long undulator. Taken from [46].

The electron beam is focused by a solenoid magnet into the next acceleration stage to counteract the space charge induced growth of emittance. The electron bunch is accelerated in the linac and its relative angular and energy spread are reduced. A temporal overlap of the electron bunch with the ramp of the accelerating RF field induces a linear chirp in energy during acceleration. In a pair of subsequent bunch compressors in between the linac sections, the chirped electron bunch is compressed, shortening the length of the bunch and increasing the peak current in the bunch up to 3.5 kA at a maximum electron energy of 17 GeV at the end of the accelerator [41]. A bunch compressor consists of a dispersive delay line built by a sequence of dipole magnets, normally a plain chicane of four dipoles, that induces an energy-dependent travel distance eventually compressing the chirped bunch in length [46]. The LCLS undulator has a length of 132 m with quadrupole magnets situated in between the undulator sections in order to keep the beam focused and small. Thus, the active undulator is 112 m long and is built of 33 planar, 3.4-m long, permanent-magnet (neodymium iron boron) undulator segments with a period of 3 cm, generating X-rays with horizontal polarization. At the full gap height, which is fixed to 6.8 mm, the undulator magnetic deflection parameter is determined to $K = 3.5$, corresponding to a peak magnetic field of 1.25 T [41, 190].

Special LCLS Modes for the Generation of Ultrashort Pulses and X-ray Double Pulses

At LCLS, two methods are available to shorten the duration of the X-ray pulses to just a few femtoseconds, both being delivered in routine operation. In the *low-charge mode* the electron bunch charge is reduced to 20 pC, improving transverse emittance as well as mitigating collective effects in the accelerator. This allows extreme bunch compression (bunch length of ~ 1 µm) and consequently the production of ultrashort, intense X-ray pulses of less than 5 fs, albeit with an X-ray power significantly dropped to 0.1 mJ – 0.2 mJ [38].

As a second option for the reduction of the pulse duration, an emittance spoiling foil can be inserted into the electron beam path in the middle of the magnetic bunch compressor chicane BC2 (see figure 3.2), where the time–energy correlated electron bunch is tilted

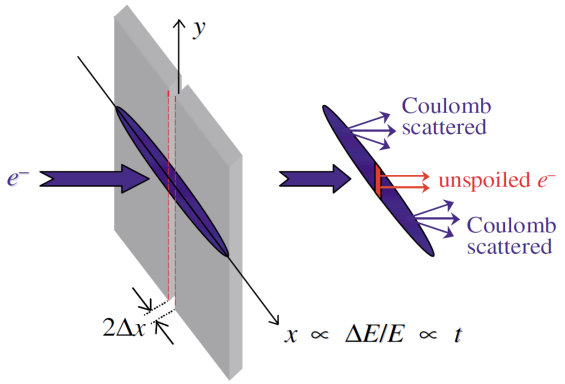

Figure 3.3: The functionality of the emittance spoiling foil at LCLS. A narrow, unspoiled part in the center of the electron bunch is left after the passage through the variable-width slot of the foil in the middle of bunch compressor BC2. Adapted from [39].

at a large angle in relation to the propagation axis of the beam [39]. Figure 3.3 displays the functionality of the emittance spoiling foil (slotted foil) at LCLS. This aluminum foil with various slot arrays has a thickness of 3 µm and increases the emittance of most of the chirped and dispersed electron bunch (*spoiling*) via Coulomb scattering, therefore suppressing lasing and FEL amplification in the undulator [191]. Only a small fraction of the bunch passes through the slot, preserves its emittance and consequently contributes to lasing. A photography of the slotted foil is shown in figure 3.4 a. The duration of the central, unspoiled time slice of the bunch is governed by the insertion depth of the narrow, vertically V-shaped slot in the foil (see figure 3.4 b). With a variable width of 220 µm –1580 µm, the X-ray pulse duration can thus be adjusted from about 50 fs – 6 fs for soft X-rays and even down to 0.3 fs for hard X-rays [192]. This technique takes advantage of the fact that the SASE process is extremely sensitive to the transverse emittance of the electron bunch.

Applying a double-slot geometry with an adjustable slot separation on the emittance spoiler (double-slotted foil), two unspoiled slices of the electron bunch and eventually temporarily closely spaced FEL X-ray double pulses with variable pulse duration and separation for X-ray pump/X-ray probe experiments can be generated at LCLS. The two V-shaped double slots have a variable centroid slot separation of 0.6 mm – 1.4 mm at a fixed width of 300 µm and 430 µm, respectively [191, 192], as displayed in figure 3.4 c. Thus, temporal separations ranging from about 10 fs to 80 fs can be provided [194].

3.2 Instrumentation for Angle-Resolved Time-of-flight Detection

For the successful performance of a two-color angular streaking experiment at LCLS, considerable yet reasonable effort of experimental hardware must be expended. Most of the needed vacuum setup is available at the AMO beamline at LCLS, where X-ray pulses from the FEL as well as an optical laser beam with widely adjustable beam parameters are guided into the instrument hutch. The most important component of the setup is a

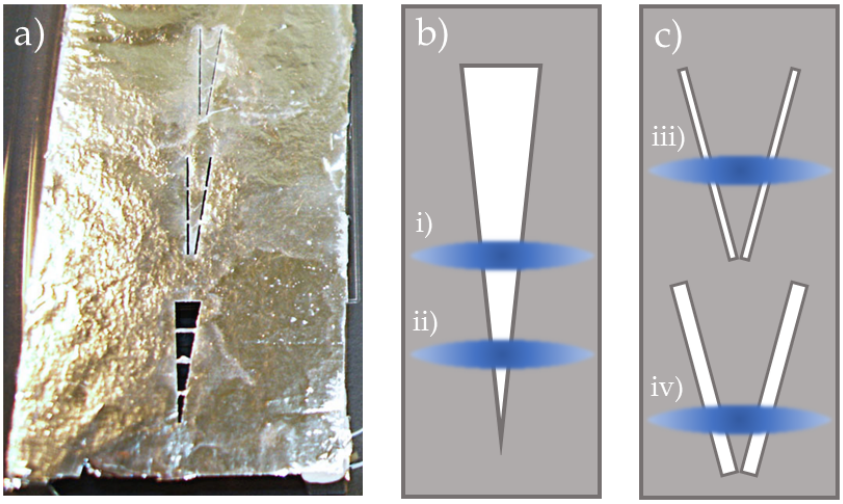

Figure 3.4: Photography (a) and sketch (b, c) of the emittance spoiling foil. The various slot and double-slot geometries on the aluminum foil are clearly visible. Firstly, by purely adjusting the insertion depth of the foil, the single (b) or double-pulse mode (c) can be selected. There are two double-slot patterns (c) with different slot widths (iii, iv) available on the foil, determining the pulse duration of the double pulses (iii, iv). Secondly, the vertical position of the foil determines the pulse duration of the single X-ray pulses (i, ii) via the slot width as well as the separation between the double pulses via the distance between the two slots. Photography (a) taken from [193].

custom-built, angle-resolved time-of-flight spectrometer array consisting of 16 concentrically arranged, independent detectors brought along to LCSL by our collaborators from Deutsches Elektronen-Synchrotron (DESY) and European XFEL. The relevant parts of the entire instrumentation involved in the experiment are introduced in the successive sections.

3.2.1 Atomic, Molecular and Optical Science Instrument

We conducted the experiment at the Atomic, Molecular and Optical Science (AMO) instrument at the LCLS [195, 196]. The AMO hutch in the Near Experimental Hall (NEH) is located about 140 m downstream of the undulator array, see figure 3.5. The beamline has been designed to achieve a small focus for maximal soft X-ray (SXR) power densities.

To maintain the high peak brightness of the X-ray beam, a minimal set of optics is applied for the delivery of the beam to the experimental targets. Deflected from the axis of the electron beam by three SXR offset mirrors (SOMs) the X-ray beam enters the hutch through an aperture slit. The beam is subsequently focused by two planar-elliptically bendable Kirkpatrick-Baez mirrors, two 400-mm long silicon substrates with a B_4C coating and an effective clear aperture of at least 2.77 mm. The two mirrors have a focal length of 1100 mm (horizontal mirror) and 1600 mm (vertical mirror), respectively and can be dynamically bent to various radii, so the focus can be moved along the instrument or the size of the beam in the interaction region can be adjusted as necessary for the specific experiment. The angle of incident for both mirrors is 13.85 mrad. The incoming beam (unfocused ≥ 1 mm^2) can be focused down to approximately 1.5 μm^2 in the interaction region, achieving peak intensities of about 10^{18} W/cm^2 and more [196, 198].

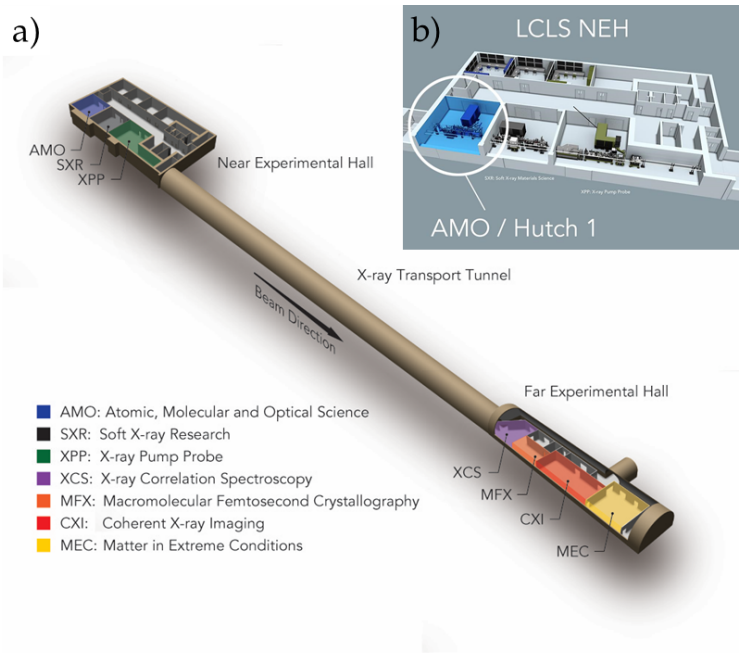

Figure 3.5: Location of the AMO instrument. The illustration shows the location of the AMO instrument in the LCLS layout (a) and in the LCLS Near Experimental Hall (b). Adapted from [197].

The position of the X-rays and the optical laser (available at the AMO hutch, see 3.2.2) in the experimental chamber can be ascertained from fluorescence caused by the X-rays hitting a scintillator, e.g. a cerium-doped yttrium aluminum garnet (Ce:YAG) screen that is moved to the same plane as the sample in the experiment. Unfortunately, when using MIR laser radiation that is not directly visible, it is not possible to use such a screen for finding the spatial overlap. In this case, one applies a pinhole that is adjusted to the X-ray beam by optimizing the X-ray transmission. After that, the MIR laser is displaced in order to maximize MIR transmission. Measuring the transmitted fraction of the laser beam enables a rough assessment of the focus size. Alternatively, position and size of the two foci can be ascertained by knife-edge measurements [199].

At LCLS, a high-throughput data acquisition (DAQ) as well as high-capacity data storage systems are installed. Data are recorded on a single-shot basis from each detector at the repetition rate of 120 Hz. For this experiment, the main DAQ system, composed of two Agilent Acqiris DC282, 8 GHz bandwidth 10-bit digitizers. Single-shot data from the detectors are bundled in data structures together with accelerator parameters and front-end detector data and stored with data rates up to 5 MB per shot. Data can be accessed in real time in the control room during ongoing experiments. Complete shot-to-shot data storage requires huge amounts of disk space, but allows providing raw data for post-beamtime data analysis [198].

3.2.2 Optical Laser Setup at LCLS

In the Near Experimental Hall, the optical lasers are situated in a separate laser hall, one floor above the experiments at the X-ray beamlines. Three almost identical, high power lasers providing a variety of wavelengths and pulse lengths are available for X-ray/optical pump/probe experiments among others, one system for each beamline. The core of each laser system is a Ti:sapphire oscillator (CoherentTM Vitara) that is synchronized to the master clock of the FEL and runs with a repetition rate of 68 MHz. Thus, it matches the seventh subharmonic of the 476 MHz frequency, that is applied for generation and acceleration of the electron beam. The oscillator provides pulses with a central wavelength of approximately 800 nm with a bandwidth between 30 nm and 125 nm (FWHM) and seeds the first amplifier stage. The pulses are stretched in a dispersive grating stretcher before entering the amplifier. A commercial Ti:sapphire, chirped-pulse amplification regenerative amplifier system (Coherent Legend Elite USP) provides $\sim$ 3 mJ, 35 nm (FWHM) laser pulses with a pulse duration of 40 fs. The second stage of amplification is a home-built, diode-pumped multi-pass amplifier (four-pass) boosting the pulses up to 30 mJ pulse energy with 100 fs pulse duration (FWHM) and an energy stability of 0.2% (rms) at a repetition rate of 120 Hz. Furthermore, an Optical Parametric Amplifier (OPA) with a wavelength range from 4 to 20 µm is available for the generation of narrowband MIR pulses via Difference Frequency Generation (DFG) [196, 199]. LCLS runs at a repetition rate of 120 Hz and exhibits a pulse-to-pulse timing jitter of at least better than 100 fs between the X-ray pulses and the optical lasers [199].

3.2.3 Experimental Setup at the AMO Instrument

The experimental setup at the AMO instrument for the angular streaking beamtime is introduced in the following. First, the utilized experimental vacuum setup and then the settings of the optical laser system in use are briefly described.

Experimental Vacuum Setup

We conducted our measurements at the AMO end station at LCLS. In addition to the UHV setup provided at the beamline, we employed a custom-built electron time-of-flight (e-TOF) spectrometer array integrated into an experimental vacuum chamber. The 16 detectors of this e-TOF spectrometer array are incorporated into the experimental chamber and concentrically arranged around the interaction region in the center of the chamber. A more detailed description of the array (*cookiebox*) is presented below. The subsequent paragraphs are partly based on the Methods parts of [172].

The whole apparatus is positioned in the path of the X-ray beam, downstream of the focusing optics at the very end of the AMO beamline, see figure 3.6. Inside the vacuum chamber, both laser beams, the X-rays from the FEL and the MIR streaking laser, are focused into a neon gas jet emitted by a stainless-steel gas nozzle with an inner diameter of $\sim$ 70 µm. The MIR beam is guided from the laser system via broadband optics and

is coupled into the FEL vacuum beamline through a window (KBr) and via a reflection off an in-coupling mirror that is mounted at an angle of 45 degrees with reference to the X-ray beam path. The mirror has a hole in its center, where the X-rays can pass straight through. The IR beam is focused to a spot size ($1/e^2$ diameter) of 500 µm in the interaction region, using a 2-inch ZnSe lens (focal length of 150 mm) with a 2-mm central aperture. The lens is positioned just outside of the in-coupling window of the experimental chamber. The X-rays are focused to a spot size with approximately 50 µm diameter ($1/e^2$) into a dilute neon gas target centered in the common acceptance volume of the spectrometer array [172]. The IR focus is spatially overlapped with the X-ray focus, since the cross section of the gas jet and the X-ray beam defines the interaction region [172].

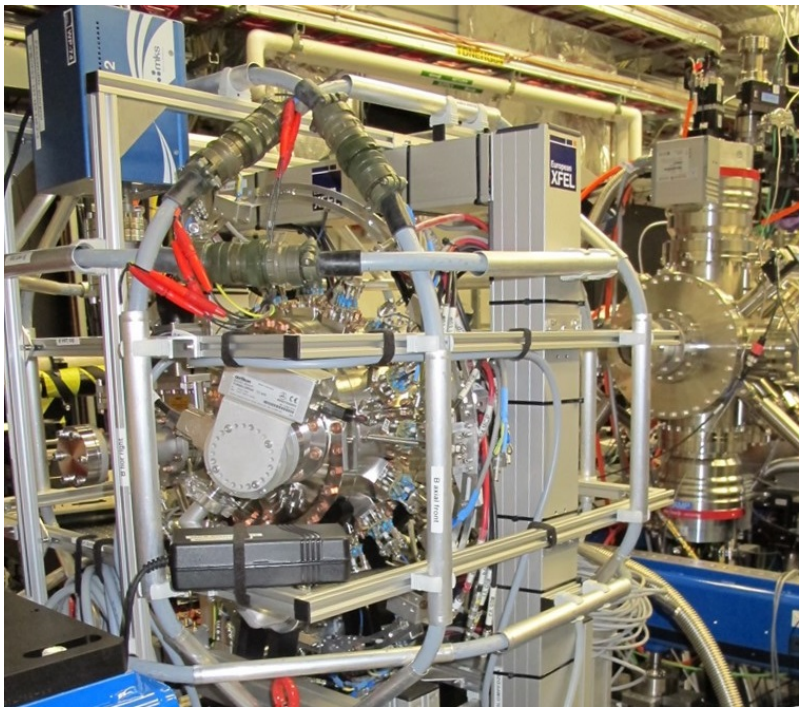

Figure 3.6: Overview photograph of the experimental apparatus. The e-TOF spectrometer array with the incorporated experimental vacuum chamber setup at the AMO end station.

Inside the experimental vacuum chamber, the X-ray pulses with a photon energy of 1180 eV non-resonantly ionize a dilute neon gas target centered in the common acceptance volume of the spectrometer array [172]. The gas target induces an ambient pressure of 4.4 $\times 10^{-6}$ mbar. The electrons are set free from neon atoms and released with a kinetic energy matching the photon energy of the X-rays less the distinctive electron binding energy of the specific electron shell the electron is excited from. For this experiment, either direct photoelectrons or indirect Auger electrons[1] [200–203] can be used. After the ionization, the electrons are deflected by the rotating electric field of the concomitant close-to-circularly polarized mid-infrared laser in different radial directions, depending on the orientation of

[1]Within the *Auger decay*, an inner-shell vacancy of an atom, for example caused by a previous photoionization, is filled by an electron from a higher-energy shell. The resulting excess energy is transferred to another electron that is then emitted from the atom. This secondary electron is called *Auger electron*. The kinetic energy of an Auger electron is fixed by the involved shells and hence, is unique to a specific element.

the streaking vector at the time of ionization. Consequently, the temporal substructure of the ionizing X-ray pulse is imprinted on the angle-dependent, characteristically modulated photoelectron yield and can be retrieved from the recorded spectra, see 2.3. We deliberately used a streaking laser wavelength of λ = 10.6 µm, corresponding to a 35-fs period of rotation of the polarization vector of the streaking field. This period was chosen so that the time for one revolution of this 'attoclock' is longer than the expected X-ray pulse duration to avoid any ambiguities from several revolutions of the clock within one XFEL pulse [131, 172].

Time-of-flight Electron Spectrometer Assembly – The *Cookiebox*

In this section, a more detailed description of the e-TOF spectrometer, the applied data acquisition and the experimental energy resolution of the single detectors is presented. The section is an adapted version of the methods parts of [172].

The e-TOF spectrometer array is a proprietary development of our collaborators from Deutsches Elektronen-Synchrotron (DESY) and European XFEL and has been brought along to LCLS for this experiment [172, 204]. It is assembled from 16 independently working time-of-flight detectors that are aligned and evenly distributed in steps of 22.5° in the plane perpendicular to the beam propagation axis, see figure 3.7 [204]. The interaction region of the experiment is centered in the common acceptance volume of the spectrometer array [172]. Due to the compact design of the assembly, the travel range for the electrons is quite short and only amounts to about 22 cm. To cover the whole 2π angular detection region by simultaneously observing photoemission spectra at 16 equally spaced angles over a full circle, the acceptance volumes of the single flight tubes are overlapping with each other and the X-ray/IR beam.

Resulting from the distance of the detector entrance from the interaction center and the size of the circular entrance aperture, and depending on the adjustable deceleration voltage (ranging from 270 V to 770 V in the present experiment) the angular acceptance of each time-of-flight detector has an upper limit of $3.8 \cdot 10^{-2}$ sr, in accordance with a full aperture angle of 12.6°. Consequently, the detected signal corresponds to an integral over that aperture. The single detectors combine high detection efficiency over a broad range of photoelectron energies with good spectral resolution. This is necessary due to the distinct streaking effect that spreads the spectrum of the photoelectrons over more than 50 eV [172]. In the detectors, a stack of three multi-channel plate (MCP) amplifiers with a capacitive outcoupling of the area-integrated signal is assembled. The detected signal is processed via Acqiris DC282 digitizers (available at AMO hutch), run either in an interleaved mode at 4 GS/s or at 2 GS/s in a non-interleaved mode. A single electron impinging on the MCP amplifiers engenders a measurable narrow voltage spike with a FWHM duration shorter than 1 ns. The duration of the single-electron response of the MCP amplifier amounts to $\sim$ 1 ns (FWHM) and is not substantially broadened by the following signal processing.

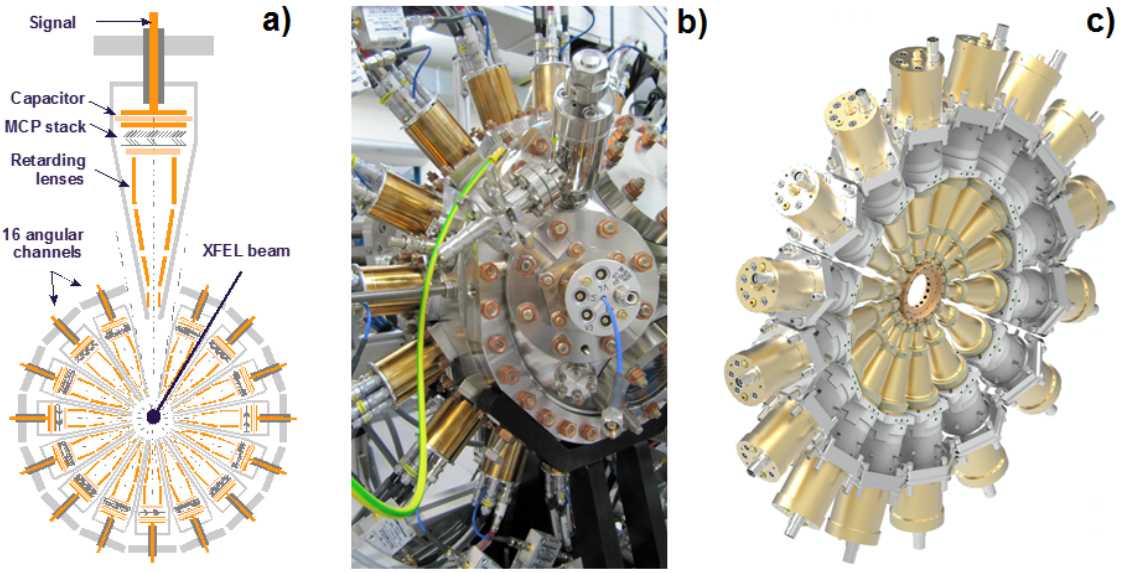

Figure 3.7: Overview of the *Cookiebox* spectrometer array. A sketch (a), a photograph (b) and a 3D computer drawing (c) of the time-of-flight spectrometer array with its 16 evenly distributed, stand-alone detectors, integrated into the experimental vacuum chamber (b). Source: Private communications with Jens Buck, DESY.

The individual detector's energy resolution depends on the resolvable signal pulse width over the obtained energy window, because the time of flight of every arriving photoelectron is inherently correlated to its kinetic energy. The detected streaking signal is mostly spread over roughly 50 ns. Within this time interval a few hundred of events in the relevant energy range can be recorded without leaving the linear amplification regime, ensuring single-shot spectroscopy. Hence, the number of detected electrons per unit of time – namely 0.25 ns in the bridged Acqiris mode – acquired in each channel is translated to the recorded voltage through the MCPs. Thus, the energy resolution of the stand-alone time-of-flight detectors is directly depending on the actual time of flight of the detected electrons and is declining for shorter flight times and hence for high-energy electrons. Under these terms, the resolution of a single flight tube is experimentally determined to 0.75 eV to 1 eV for the highest-energy electrons under the experimental conditions [172].

Optical Laser Settings

For our experiment, the OPA system, situated downstream of the Ti:sapphire amplifier system, was adjusted to generate 10.6 µm output pulses out of the 800-nm wavelength input via DFG of signal and idler. The output pulses have a pulse duration of 340 fs (FWHM) and an average pulse energy of 38 µJ on target, measured on a single-shot basis. The linear polarization of that output pulses is converted to a close-to-circular polarization with an ellipticity of 0.73 ± 0.03 by means of a reflective phase retarder, known from CO_2 lasers. The ellipticity is measured as the ratio of the two half axes of the polarization ellipse. The stability of the ellipticity is related to the inherently stable, linear polarization of the OPA output. Further, only one fixed reflective optic was used in the setup for conversion from linear to close-to-circular polarization. Therefore, the ellipticity

of the polarization can be considered as stable within the measurement error during the experiment. The major axis of the ellipse is tilted by $22.5° \pm 5°$ with respect to the vertical detector orientation in our setup [172].

3.3 FEL settings and Experimental Schedule

For our angular streaking experiments, a beamtime of five 12-hours-shifts (with always a 12-hours-break in between) at AMO hutch has been at our disposal in March 2015. The first two shifts have been used for alignment work of the FEL beam path and the FEL timing, for a few test runs of diverse components and for finding the temporal and spatial overlap between the MIR focus and the X-ray focus. For this a pinhole, a so-called 'knife edge' as well as an oscilloscope with a large bandwidth have been utilized. Furthermore, for the energy calibration of the time-of-flight detectors and for finding an appropriate ambient gas pressure in the chamber to get an acceptable signal strength, various calibration runs at different FEL pulse energies had to be conducted. Simultaneously, the adjustment of the favored streaking wavelength had to be accomplished. The three remaining shifts have been spent for angular streaking measurements with diverse settings of the FEL, with different streaking wavelengths and with electrons stemming from two different generation processes as a measurement probe, as explained in the following. The subsequent section concerning the FEL machine settings has been adapted from [172].

The FEL has been operated at 120 Hz with an average electron beam energy of 5087 MeV, a mean bunch charge of approximately 150 pC and a peak current (measured at bunch compressor BC2) of 1500 A. The generated X-ray pulses have an average pulse energy of 60 µJ at a mean photon energy of $\sim$ 1180 eV. The length of an electron bunch is 85 fs, but due to the position of the emittance spoiler (*slotted foil*) the effective lasing part of the bunch is distinctly shorter, dependent on the position of the slotted foil [191, 192]. We conducted different measurements employing X-ray pulses with estimated, average pulse durations being set to 3.5 fs, 6.5 fs and 10.5 fs (rms) — or 8 fs, 15 fs and 25 fs (FWHM) — by tuning the slotted foil position to -6000 mm, -4500 mm and -3300 mm, respectively, for the ionization of the neon gas target [39]. Those specifications on the mean pulse durations have been provided by LCLS and are indirectly determined using a transverse deflection cavity (XTCAV) [84]. During the calibration runs for the energy calibration of the photoelectron data, the FEL is operated with a low bunch charge of 130 pC, a peak current of 1460 A (measured at bunch compressor BC2) and an average electron beam energy of 5087 MeV. The emittance spoiler is positioned to -8900 mm and the photon energy is tuned to four calibration points by a Vernier scan to 1166 eV, 1180 eV, 1193 eV and 1214 eV. It should be mentioned here, that indeed the absolute photon energy values may be inaccurate, whereas the relative changes of the photon energy — which are relevant for the calibration — are very accurate during the Vernier scan.

In order to achieve the X-ray FEL double-pulse operation mode with an rms pulse duration of roughly 3.5 fs (8 fs fwhm) and an average, estimated pulse separation of 20 fs, the position of the double-slotted emittance spoiler [191, 192] is set to -13000 mm.

For the pulse characterization experiment via angular streaking measurements with single X-ray pulses, we worked with electrons stemming from two different generation processes as measuring probes: neon 1s core shell electrons and neon K-LL Auger electrons. The basic idea here is the proof, that this method is not only suitable for ordinary photoelectrons, but also for Auger electrons despite the time delay due to their release process. For the angular streaking measurements of Ne 1s photoelectrons (E_{bind} = 870 eV [205]), emitted with a mean kinetic energy of E_{kin} = (1180 - 870) eV = 310 eV, the maximum retardation voltage of the time-of-flight detectors is set to 270 V (see 3.2.3), eventually resulting in a recorded unstreaked photoelectron energy of 40 eV. The released photoelectrons show a dipolar emission pattern along the horizontal, linear X-ray polarization due to the spherically symmetric Ne 1s orbital and its interaction with the linear polarized ionizing X-rays. In equal measure, the energy calibration runs for the Ne 1s photoelectron data sets have been conducted with the same retardation voltage of 270 V.
Additional to the neon core level electrons, also neon Auger electrons have been used for the angular streaking measurements. With an inherent time delay after the ionization of the neon atoms, the K–LL Auger electrons are emitted with a fixed kinetic energy of $\bar{E}_{\mathrm{kin}}^{\mathrm{Aug}} \approx$ 803.5 eV [206]. For resolving the energy of the Auger electrons the maximum retardation voltage of the detectors is set to 770 V.

In addition to the measurements with a single ionizing X-ray pulse, we also performed streaking measurements with instead an X-ray double-pulse train for the ionization of the target. The two pulses, generated by the insertion of the double-slotted foil [192] into the electron bunch, have an identical photon energy of $\sim$ 1180 eV and the same average pulse duration of 3.5 fs (rms) with a time delay of about 20 fs between.

On average, for each of the distinct measurement types listed above, a run of $\sim$50000 FEL shots ($\sim$7 min measurement at 120 Hz) has been recorded, adding up to more than $\sim$20 runs.

Chapter 4

Characterization of Few-femtosecond X-ray FEL Pulse Structures

The performed experiments, described in the last chapter, have been the very first two-color angular streaking experiments. Thus, up to now no concrete concept for the data analysis and pulse retrieval from two-color angular angular streaking data had been developed yet. Expectations on the analysis method have been: determination of the pulse duration with the best achievable temporal resolution (ideally in the sub-fs range) and uncovering the temporal intensity spike substructure of the SASE FEL, which is completely random due to the stochastic generation process of SASE FEL pulses (see section 2.1.3). Furthermore, a very fast running routine with a speed comparable to the repetition rate of the FEL as well as a pulse characterization in the spectral regime have been optionally desired.

In the aftermath of the beamtime at LCLS, two completely different analysis and retrieval approaches have been pursued within our collaboration:
The integration pulse characterization approach is simple, straightforward and intuitive with respect to the classical concept of angular streaking. Thus, it is a fast and robust method to determine substructure and pulse duration, but it provides no spectral information about the X-ray pulse. The algorithm has been developed together with Martin Wagner and with support by Dr. Wolfram Helml and is described very detailed in this chapter as the main achievement within this thesis. The resulting outcomes on the time structure of X-ray FEL pulses are presented and subsequently its capabilities as a smart online tool for X-ray pulse characterization at FELs are evaluated.
Additionally, a complex, iterative projection algorithm, which decomposes the recorded streaking traces into a time–energy representation of an ultrashort X-ray pulse has been developed by Nick Hartmann and improved by Gregor Hartmann [172]. Hence, it retrieves nearly the full attosecond time–energy information of the pulse. Nevertheless, this full reconstruction is only suitable for pulse-sorting after the experiment due to its high requirements on computation time. This so-called *Pacman algorithm* is introduced in section 4.3.1. Furthermore, its successful application on simulated angular streaking data as well as a comparison with a state-of-the-art yet rough X-ray pulse duration estimation method (XTCAV), which currently is in use at LCSL, is shown. Eventually the good agreement with the integration pulse characterization algorithm is presented.

4.1 Integration Pulse Characterization Alghorithm

The pulse characterization algorithm pursues a quite simple idea: For each shot the spectra of all single 16 time-of-flight (TOF) detectors are evaluated regarding the streaking-induced energy shift in the electron energy distribution (photolines). In each spectrum the photoelectron signal intensity is integrated over a narrow energy window just below the most up-shifted electron energy, which is corresponding to the maximum streaking amplitude of the respective shot. The number of detectors that detect such a shift and the integrated intensity of the shifted streaking traces in combination with the optical cycle period of the streaking laser deliver pulse duration and substructure of the photoionizing, ultrashort X-ray pulse. The procedure of the method is presented in detail subsequently. Starting from the data preprocessing and filtering, the energy calibration and normalization of all detectors, a correction considering the elliptical polarization and eventually, the central retrieval algorithm itself are thoroughly explained.

4.1.1 Data Treatment and Preprocessing

At LCLS, any kind of data measured in the experiment and all machine parameters measured along are completely stored to disk in data bundles ordered by run number. For the post-experiment data analysis, all these data are converted into large-sized hdf5-files, each containing all relevant data for a single run, and can be downloaded from the SLAC drive. At the beginning of the data analysis, some effort should be expended for the preprocessing of the raw data.

Raw Data Inspection and Evaluation

As a very first step of the data preprocessing, the raw time-of-flight data recorded from the 16 individual time-of-flight detectors are coarsely inspected. They are evaluated with respect to their usability, concentrating on signal strength, resolution and noise level. Hereby, issues regarding the overall data quality of three of the single detectors have emerged.

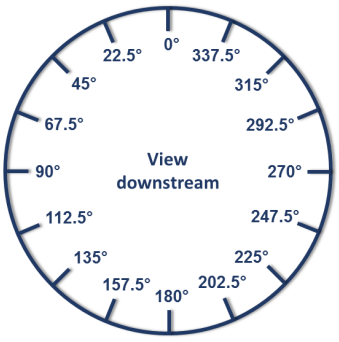

Figure 4.1: Detector numbering sketch. The angle specification of the 16 TOF detectors of the *Cookiebox* e-TOF spectrometer array is depicted in downstream view.

Due to an electrical short in the wiring of two flight tubes (located at the 22.5° and the 45° position, see figure 4.1) their signal strength is dramatically low compared to the signals of the remaining detectors that worked properly (clearly visible in figure 4.2). The two shortcuts have been perceived during a hardware test shortly before the first shift of the beamtime and could not be repaired anymore for time reasons. Unfortunately, within subsequent steps in the integration algorithm it turned out that the data from these two detectors must be discarded for the analysis of data sets regarding the streaking of neon Auger electron data sets. However, for the Ne1s data sets the two detectors can be employed due to the different retardation voltage settings ($V_{\mathrm{ret,Ne1s}} = 270$ V, $V_{\mathrm{ret,Auger}} = 770$ V). In the case of the high retardation voltage applied for the Auger data, the shortcut distinctly and adversely affects the measurement of the decelerated electrons, causing hardly exploitable signal heights in the traces. The distinctly lower retardation voltage applied for the Ne1s data delivers usable signal strength and thus allows an exploitation of the spectra despite the shortcut.

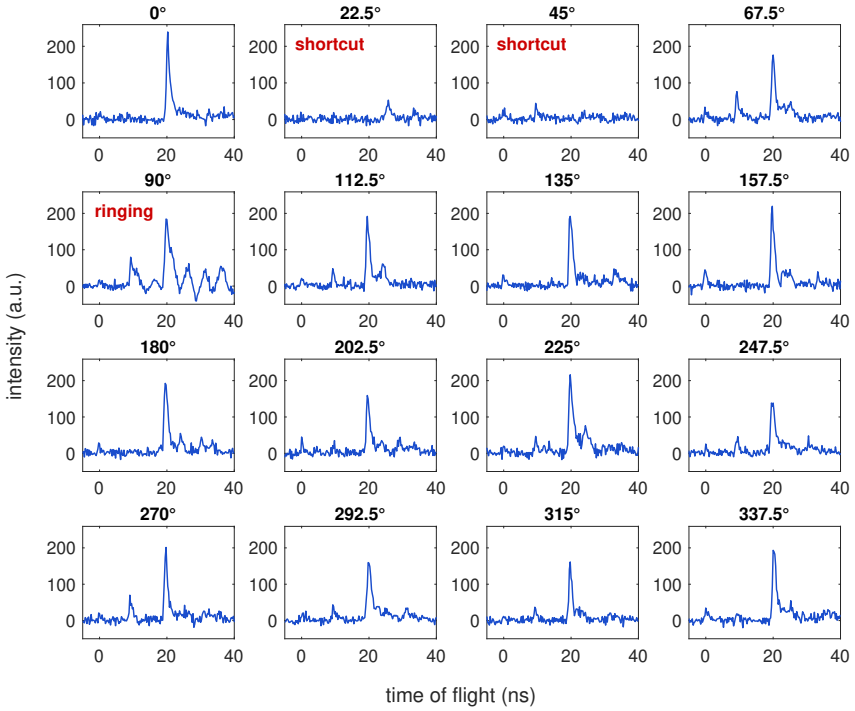

Figure 4.2: Overview of the data quality of the 16 single TOF detectors. Single-shot time-of-flight traces of all 16 detectors for the excitation of neon at an FEL photon energy of 1080 eV are shown. The two shortcut TOFs at the 22.5° and 45° position, as well as the ringing TOF at the 90° position are clearly discernible by their traces.

Additionally, the detector mounted at the 90° position shows a strong electronic ringing effect (see figure 4.2), but its signal fortunately appeared to be viable enough for our analysis method concerning both, photoelectrons and Auger electrons. A further inspection of the Ne1s data sets revealed that the two detectors located at the 0° and the 180° position show nearly no signal. This is because of the dumbbell-shaped emission characteristic of the neon 1s core electrons ionized by the linearly polarized XUV pulse. Therefore, for

the analysis of the Ne1s data sets these two detectors had to be excluded. Summarized, for the data sets of both electron types only 14 out of 16 detectors are involved to the following data analysis to avoid misleading retrieval results caused by weak or skewed signals. Unfortunately, for the integration algorithm this results in a 'blind spot' extending over an angle of 45° in the angular streaking measurements, which one should bear in mind. However, for the determination of the polarization ellipse in section 4.1.3 also these detectors, which are discarded for the single-shot pulse structure characterization, are involved.

Shot Filtering on FEL Machine Parameters

The actual data preprocessing after the raw data inspection starts with a shot sorting by means of filtering on selected FEL machine parameters (see figure 4.3), provided by the DAQ system at LCLS on a single-shot basis. The objective is to reduce the data sets to shots that are suitable for scientific evaluation and thus to eventually obtain reliable results. Firstly, shots are discarded by a filter routine, if the electron bunch charge shows a deviation of more than 25 % from its median. The latter is ascertained by statistical evaluation of several thousand shots within the treated run. These deviations are mainly caused by dropouts of the electron accelerator. The threshold value for this filter, just as the ones for the following filters, are determined empirically based on the distributions of the respective machine parameters, aiming at cleanest possible data sets by simultaneously discarding as few shots as possible.

Secondly, shots are discarded by a subsequent routine, if the electron beam energy deviates by more than 5 MeV from its likewise statistically determined mean of 5087 MeV. Such deviations are raised by instabilities of the electron accelerator (see figure 4.3 a)). The next filter eliminates all shots, where the monitored photon energy shows a deviation of more than 2 eV from its mean value in the respective run due to FEL fluctuations, see figure 4.3 b). Subsequently, a filter on the linear correlation between electron beam energy and monitored photon energy is applied, as can be seen in figure 4.3 c). For this purpose, a linear fit is executed and all shots with a deviation of more than 2 sigma from the fit curve are removed from the data set. The deviations of the discarded shots can be explained by readjustments of the undulator during the respective run. Finally, a filter is deployed on the distribution of the X-ray pulse energy. Hereby, shots are discarded, if the X-ray pulse energy shows a deviation of more than 1 sigma from its mean value, which is again determined by statistical evaluation of all shots within the treated run. Hence, only shots with an X-ray pulse energy close to the set value are further considered, as displayed in figure 4.3 d).

The filter routines are applied consecutively, so the actual data set is reduced and thus cleaned from step to step. Using a bottom-up method, the sequence of the filters is selected in such a way, that one identifies failed shots by checking the different parameters starting from general accelerator parameters towards FEL beam parameters.

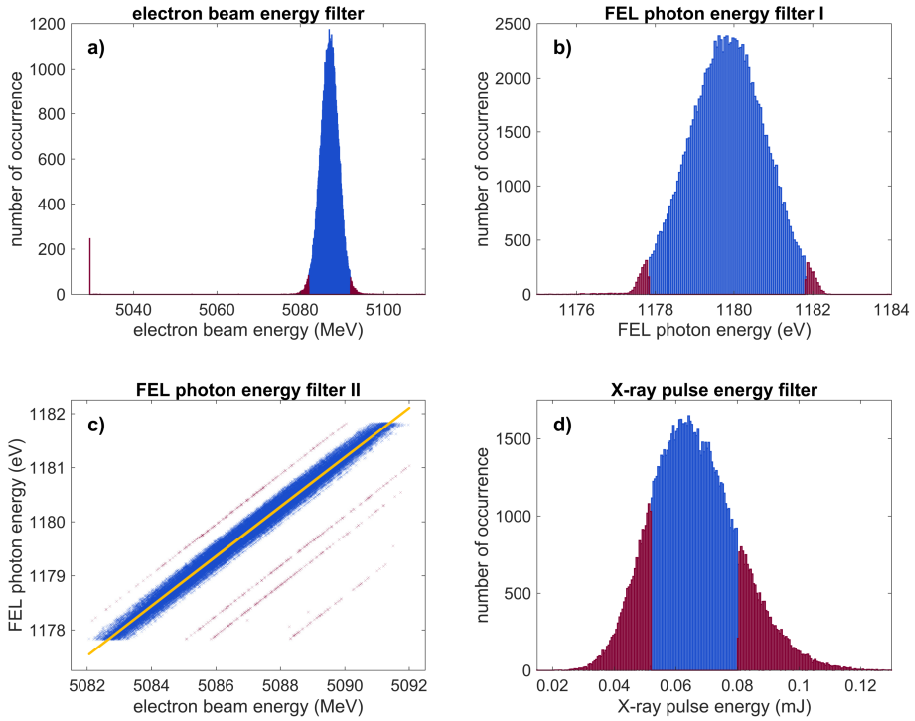

Figure 4.3: Pulse sorting by means of filtering on selected FEL machine parameters. The consequences of the consecutively applied filters on FEL machine parameters are displayed. FEL shots that are sorted out by the respective filter routine (red) and those that remain in the data set (blue) are displayed for (a) the electron beam energy filter, (b) the pure FEL photon energy filter, (c) the consecutive FEL photon energy filter considering the relation to the electron beam energy and (d) the X-ray pulse energy filter. The linear fit applied to the data points during the second filter on the FEL photon energy in panel (c) is depicted in yellow.

Noise reduction and Background Subtraction

The filtered, raw data sets are treated successively by two methods to reduce the noise background: First, a standard Wiener filter routine for noise reduction is applied. The Wiener deconvolution (via fast Fourier transform, FFT) is performed in the frequency domain and reduces the impact of noise at high frequencies that have a poor signal-to-noise ratio. After the noise filter routine, the energy calibration of the spectra is conducted as explained below in section 4.1.2. For a further improvement of the signal-to-noise ratio or more specifically, to eliminate preferably any remaining background from the signal, a background signal is subtracted in the energy domain. For this, we first define an average background level for each single detector and shot and subtract this value from the respective, entire spectrum. This average background is determined by calculating the mean of the ten highest values in a predefined high-energy part of the single spectra, where certainly no electron-induced signal is expected. All negative, thus unphysical values occurring after that subtraction are set to zero. This generous background estimation is chosen to ensure a noise-free and artifacts-free signal to the greatest extent as the reliability of the further analysis is strongly dependent on that.

Normalization and Transmission Correction

Since we compare spectra measured by 14 independent detectors for each shot, one should carefully adjust the relative signal strengths. The normalization is performed differently for Auger and photoelectron data sets, as one has to consider an additional, angle-dependent transmission correction of the Ne1s spectra due to the non-isotropic emission of the Ne1s electrons after ionization by the linearly polarized X-ray pulse.

In case of the normalization of the 14 single Auger traces per shot with respect to each other, an isotropic emission characteristic of the Auger electrons is assumed. The most prominent K-LL Auger peak in unstreaked time-of-flight traces is utilized as a measure for the normalization level. For each detector, the traces of 2.000 shots from a calibration run in absence of the MIR laser are averaged and integrated over a 6 ns-broad time interval around the maximum of the Auger peak. After the energy calibration, all spectra of the single TOF detectors are then normalized to each other by dividing the spectra by the respective integral values as weighting factors. These once determined normalization factors are equally applied to all Auger data sets. By the performance of the normalization in the energy domain any potential distorting effects on the spectra within the energy calibration due to a normalization conducted already in the time domain shall be prevented. A potential energy dependence of the transmission has been checked, it shows to be flat within the range of our detector noise level. Thus, the usage of one single factor for the whole spectrum for each detector is justified.

For the normalization of the neon 1s data sets, the same procedure as for the Auger data is performed. Here, the Ne 1s photopeak is used for the integration of the signal to perceive the normalization weighting factors. The integration window around the photopeak has a width of 4 ns. Furthermore, a correction of the anisotropic emission characteristic must be performed for the Ne1s data. Generally, the angular distribution of photoelectrons originating from neutral and randomly oriented atoms in the gas phase is well-studied. The probability of observing a photoelectron at a specific angle mainly depends on the polarization of the incident laser pulse and the atomic shell the electron is ionized from. It is described by the differential ionization cross section [207–210]

$$\frac{d\sigma(h\nu)}{d\Omega}(\theta) = \frac{\sigma(h\nu)}{4\pi}\ \left[1 + \beta(h\nu)\ P_2\left(\cos\theta\right)\right]\ , \tag{4.1}$$

which explains the angular emission distribution by means of the electron emission angle θ with respect to the polarization vector of the ionizing, linearly polarized X-ray laser pulse. Here, P_2 is the second order Legendre Polynomial and the energy-dependent anisotropy (asymmetry) parameter β basically reflects the orbital symmetry of the atomic shell from where the photoelectron is emitted [35, 211].

This dumbbell-shaped angular emission characteristic of the Ne1s photoelectrons is reflected by the scaling factors calculated via averaged integration over the main photopeak

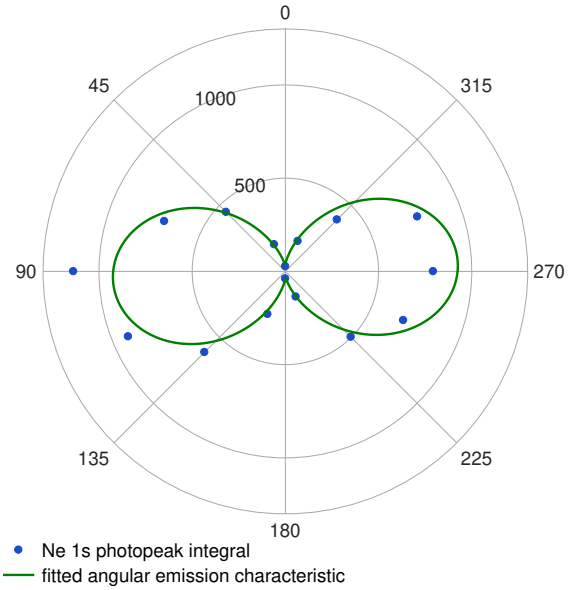

Figure 4.4: Correction for the angular emission distribution of Ne 1s photoelectrons. Ne1s photopeak integral values (blue circles) for the individual e-TOF detectors are fitted (green) with the expected dumbbell-shaped angular emission characteristic for ionization with horizontally polarized X-ray pulses from the Ne 1s shell. The individual scaling factors for each detector are shown in table A.1.

for each individual e-TOF detector, as can be seen in figure 4.4. This is verified by fitting these normalization factors with the differential cross section of the angular emission characteristic [172].

$$\sigma_{\mathrm{fit}}(\theta) = \frac{A}{2} \cdot (1 - \cos(2 \cdot (\theta - B))) + C \,, \tag{4.2}$$

where θ is the detection angle and A = 883.7, B = 3.2° and C = 41.9 are the fitted parameters for amplitude, an angle offset and a directional emission shift.
Due to the good agreement of the fit to the data, the single detectors are normalized to each other by division of the single-shot spectra by the experimentally determined normalization factors in the energy domain. In the same way as for the Auger data, the determined normalization factors are equally applied to all Ne1s data sets. The individual scaling parameters are summarized in table A.1 in the appendix.

4.1.2 Energy Calibration

The energy calibration of the time-of-flight data must be conducted differently for the photoelectron and the Auger electron data sets and is therefore presented individually for both data set types.

Energy Calibration of Neon 1s Photoelectron Data Sets

The recorded X-ray photon energy can be derived from the final kinetic energy of the photoelectrons, the electron binding energy and the retardation voltage settings applied to the detectors. Neon 1s core electrons have a binding energy of $E_{\mathrm{Ne1s,bind}}$ = 870.2 eV [207, 208]. Every individual detector is partitioned into four sections along the length of the

flight tubes, where the retardation is incrementally altered from 0 V, via 180 V and 243 V to 270 V in the end [172]. For the energy calibration, the retardation is locally approximated by a single effective retardation voltage U_{ret}. Since the energy range examined in the experiments is comparatively narrow, this approximation is valid for our analysis. Eventually, the X-ray photon energy is given by

$$E_{\mathrm{X-ray}}(t) = \frac{m_e}{2}\left(\frac{s}{t-t_i}\right)^2 + E_{\mathrm{Ne1s,bind}} + eU_{\mathrm{ret}} \ , \tag{4.3}$$

where, m_e is the electron mass, s is the field-free drift length, t the drift time, t_i is the instant of ionization and U_{ret} is the effective retardation voltage.

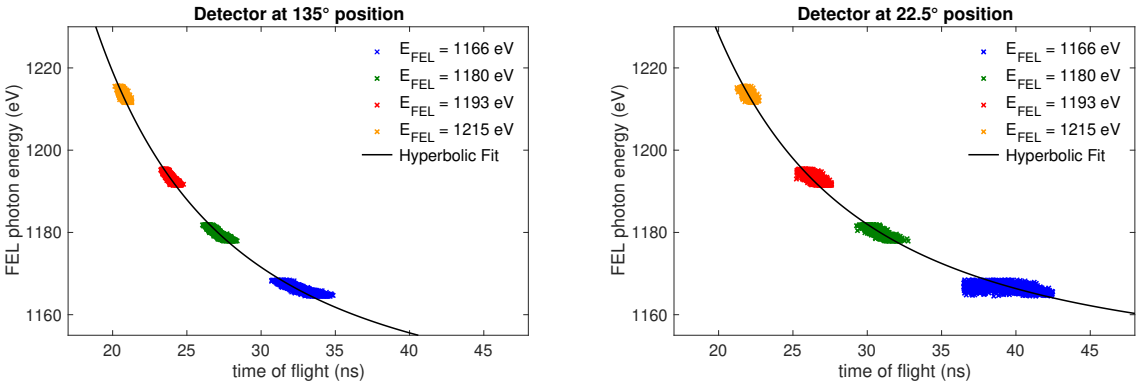

Figure 4.5: Energy calibration of the Neon 1s photoelectron spectra. A hyperbolic time-to-energy transformation function fitted to single-shot, raw time-of-flight traces for four different X-ray photon energies is depicted for a properly working detector at the 135° position (left) and for a detector with an electrical shortcut at the 22.5° position (right).

For the energy calibration of the neon 1s data sets we utilize the positions of the Ne1s photopeak in the time-of-flight traces recorded at four different FEL excitation energies with well-defined energy separation, namely with 1166 eV, 1180 eV, 1193 eV and 1215 eV. Hence, unstreaked time-of-flight traces are used to properly identify positions of the photopeak on a single-shot basis for every X-ray photon energy setting. As depicted in figure 4.5, these photopeak positions are assigned to the measured X-ray photon energies $E_{\mathrm{X-ray}}(t)$. Thus, these are utilized for the time–energy transformation by fitting them with the appropriate energy calibration function

$$E(t) = A \cdot (t - t_0)^{-2} + E_0 \ , \tag{4.4}$$

with $A = m_e/2 \cdot s^2$, $t_0 = t_i + t_{\mathrm{off}}$ and $E_0 = E_B + eU_{\mathrm{ret}} + E_{\mathrm{off}}$ being the summarizing fitting parameters for curvature, time offset and energy offset. The fit optimizes the free parameters s, t_0 and E_0. For preserving the actual signal integrals, also the Jacobian must be considered for an accurate energy calibration. This procedure is conducted individually for every single detector by applying the calibration function with its respective fit coefficients (see table A.2 in the appendix) to the signal in the time regime.

Energy Calibration of Neon Auger Electron Data Sets

For the energy calibration of the neon Auger data sets, a different method must be applied, as the Auger electron energy does not depend on the ionizing X-ray photon energy. Hence, neon Auger electron emission energies from synchrotron measurements, presented in figure A.1 in the appendix, are compared to an averaged signal of 2.000 unstreaked time-of-flight traces out of a calibration run without the MIR streaking laser. Due to the isotropic emission characteristic of the Auger electrons, the energy calibration is performed for only one detector and transferred to the other, identically constructed detectors. The detector at the 112.5° position, providing very good data quality, has been used for this purpose. In that averaged trace, the photon prompt, the Ne 2s/2p line and three additional Auger electron-induced peaks can be identified in accordance to the synchrotron data (see figure 4.6)) as follows:

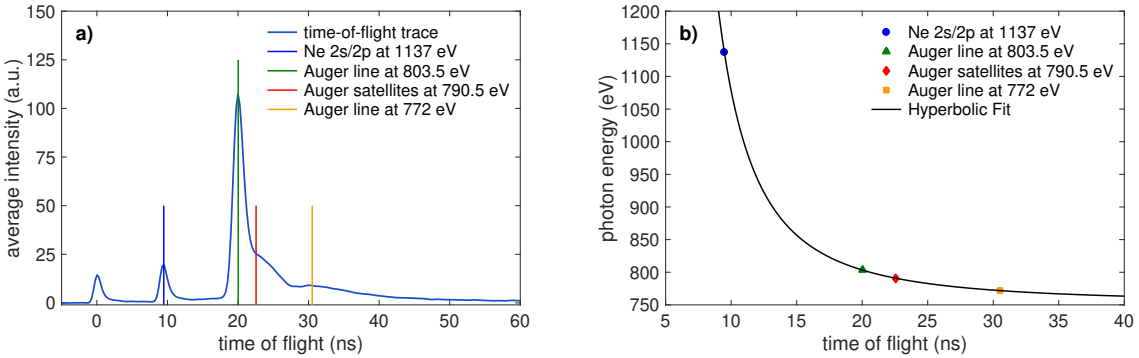

Figure 4.6: Energy calibration of the Auger electron spectra. (a) Averaged time-of-flight trace recorded with a retardation voltage of 770 V. The four different peaks utilized for the calibration are marked. (b) The hyperbolic fit to the time–energy data points for the Auger electron energy calibration is displayed.

Since the energy resolution of the single detectors cannot separate all Auger lines appearing in the synchrotron spectrum, some of the Auger peaks in our spectra must be considered as a convolution of the respective Auger lines with the available energy resolution. The Auger line K–$L_1L_{2,3}$ ($^1P_1$) at 772 eV corresponds to the peak recorded at 30.5 ns in the time-of-flight trace. The peak measured at 22.6 ns can be assigned to a weighted convolution of the K–$L_1L_{2,3}$ ($^3P_{012}$) line and the $KL_{2,3}$–$L_{2,3}$ $L_{2,3}$ $L_{2,3}$ satellites determined to 790.5 eV. A weighted convolution of the two Auger lines K–$L_{2,3}$ $L_{2,3}$ ($^1S_0$) and K–$L_{2,3}$ $L_{2,3}$ ($^1D_2$) determined to 803.5 eV corresponds to the peak observed at 20.0 ns. Additionally, the fourth peak, recorded at 9.5 ns, can be assigned to a convolution of the Ne 2s and 2p photolines [206]. These four data points (time–energy pairs) are used for the time–energy transformation by fitting them with the same calibration function used for the neon 1s data sets (see eq. 4.4), as displayed in figure 4.6). The fit delivers the parameters A = 13700 ns^{-2}, t_0 = 3.51 ns and E_0 = 753.10 eV, which are applied for the energy calibration of all 14 working TOF detectors used in the further analysis of the various Auger data sets.

4.1.3 Determination and Correction for the Elliptical Polarization

Due to the elliptical, hence non-circular polarization of the infrared streaking field its amplitude shows a sinusoidal characteristic depending on the direction of the streaking field vector potential in the polarization plane. Consequently, certain TOF detectors intrinsically measure a weaker or stronger streaking effect than other ones, since the magnitude of the vector potential varies within one circumvolution. The extent of the shift of the electron energy distribution to lower or higher energies induced by the streaking field is inherently dependent on the angle position of the respective detector with respect to the orientation of the polarization ellipse.

Therefore, it is indispensable to consider these differences in the maximum possible streaking shift for every detector and to correct this deviation from a perfectly circularly polarized streaking field. For this purpose, the polarization ellipse is determined: For each TOF detector and each FEL shot, the maximum measured streaking shift to higher energies is identified by the energy value in the spectrum, where the signal intensity drops below 10% of its maximum value. This single-shot *cutoff energy* $E_{\mathrm{cut}}(\varphi)$ is plotted for each detector in a histogram over all shots of the respective data set. Figure 4.7 depicts these cutoff histograms exemplary for two detectors perpendicular to each other and for data sets of both electron species.

The *overall streaking limit* $E_{\mathrm{ell}}(\varphi)$ of the detector is set to the energy value where the distribution of these cutoff energies over all shots has dropped below 2% of its maximum on the high-energy side of the distribution. This procedure ensures that the actual maximum streaking shift is independently determined for each detector and individually for each data set and mostly eliminates the influence of shot noise. Eventually, orientation, shape and size of the polarization ellipse of the MIR streaking field are reflected by the resulting, detector-related energy values for the overall streaking limit, as shown in figure 4.8 a) for the three studied Auger electron data sets.
The determination of the ellipse is analogously conducted for the neon 1s electron and the Auger electron data sets. However, the method must be slightly adapted in case of the neon 1s data sets, owing to the anisotropic emission characteristic and consequently a higher noise level in the spectra of certain detectors. Thus, the determination of the polarization ellipse is split up into three steps. First, for the determination of the magnitude of the ellipse only those TOF detectors with a sufficiently high signal-to-noise ratio are considered. For this step, only seven out of 14 detectors are selected based on their angular position with respect to the dumbbell-shaped Ne 1s emission characteristic, thus the average signal strength in their spectra. Secondly, the shape of the polarization ellipse is determined involving all detectors. Owed to the higher noise level in the spectra, a more robust determination compared to the procedure applied to the Auger electron data sets is deployed. In this case, the energy value of the maximum of the distribution of the cutoff energy $E_{\mathrm{cut}}(\varphi)$ over all shots is used as a measure for the angular dependence of the streaking shift. Finally, the overall streaking limit and thus the polarization ellipse are

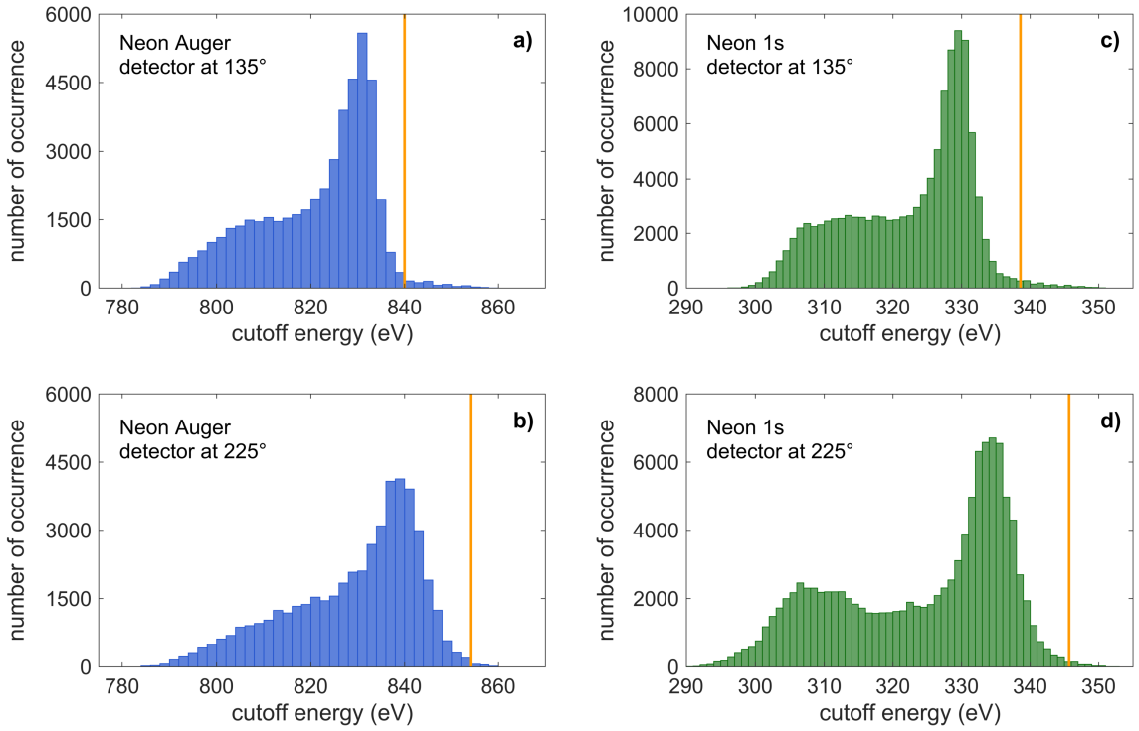

Figure 4.7: Distribution of the single-shot cutoff energy $E_{\mathrm{cut}}(\varphi)$ for the determination of the polarization ellipse. The histograms of the single-shot cutoff energy $E_{\mathrm{cut}}(\varphi)$ for two detectors positioned perpendicularly to each other are displayed for both, an Auger electron data set (a, b) and a photoelectron data set (c, d). The orange line marks the determined overall streaking limit $E_{\mathrm{ell}}(\varphi)$ in the respective detectors. The selected detectors represent the orientation of the minor (a, c) and major semi-axes (b, d) of the polarization ellipse. The energy shift between the two respective histograms is clearly visible.

obtained by scaling this elliptical shape up to the magnitude of the ellipse, which has been previously calculated in the first step. The final ellipses calculated for the three studied photoelectron data sets are depicted in figure 4.8 b). The respective polarization ellipses for the X-ray double-pulse data sets (see sections 4.1.5 and 4.2.3) are depicted in figure A.2 in the appendix.

Subsequently, the cutoff energy $E_{\mathrm{cut}}(\varphi)$ measured by each detector for every FEL shot can now be corrected for the elliptical polarization of the MIR laser. To begin with, all shots where the cutoff energy is detected to be apparently higher than this overall streaking limit $E_{\mathrm{ell}}(\varphi)$ for at least one detector are discarded. For the further analysis, a normalized polarization ellipse $Ellipse_{\mathrm{norm}}(\varphi)$ is determined by dividing the angle-dependent, overall streaking limits by their maximum value:

$$Ellipse_{\mathrm{norm}}(\varphi) = \frac{E_{\mathrm{ell}}(\varphi)}{max\left(E_{\mathrm{ell}}(\varphi)\right)} \,. \tag{4.5}$$

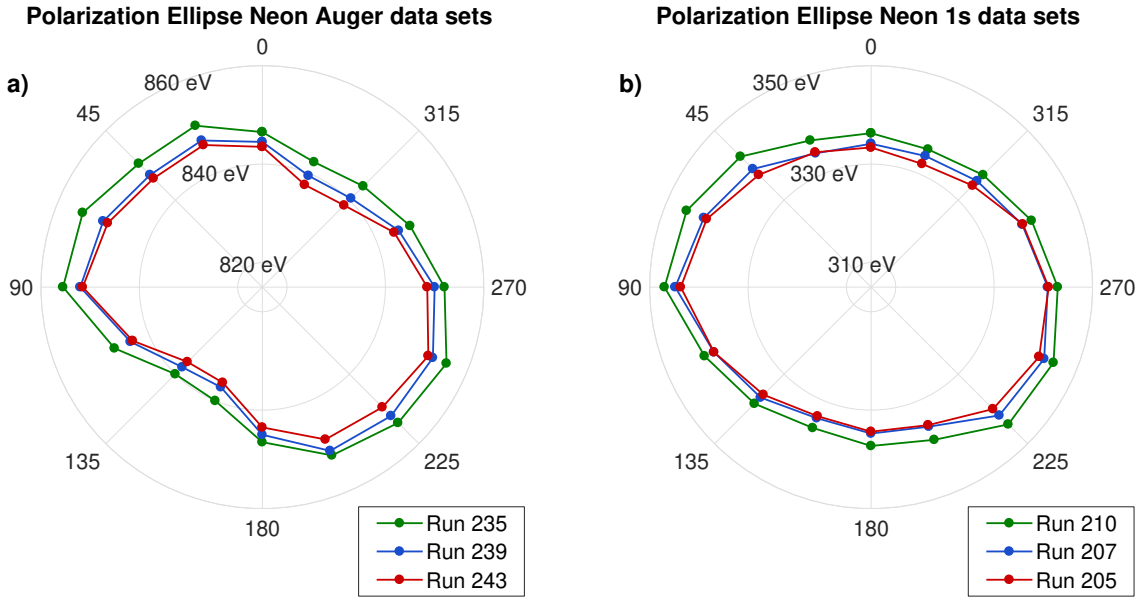

Figure 4.8: Illustration of the ascertained polarization ellipse. The polarization ellipse illustrated by the angle-dependent overall streaking limit $E_{\mathrm{Ell}}(\varphi)$ is depicted in a polar plot for (a) the three Auger electron and (b) the three photoelectron data sets, respectively.

The succeeding steps are conducted on a single-shot basis. First, the angle-dependent, maximum energy shift to higher energies caused by the streaking field in every single TOF detector is determined:

$$E_{\mathrm{shift}}(\varphi) = \frac{E_{\mathrm{cut}}(\varphi) - E_0}{Ellipse_{\mathrm{norm}}(\varphi)} \,, \tag{4.6}$$

where $E_{\mathrm{cut}}(\varphi)$ is the single-shot cutoff energy, $Ellipse_{\mathrm{norm}}$ is the normalized polarization ellipse and E_0 is the unstreaked energy of the Ne 1s photoline or the main Auger line, respectively. Then, the ellipse-corrected, maximum energy shift of all flight tubes a_{ell} for the respective shot is ascertained:

$$a_{\mathrm{ell}} = max\left(E_{\mathrm{shift}}(\varphi)\right) \,. \tag{4.7}$$

This scaling factor a_{ell}, the so-called *streaking kick*, varies from shot to shot, since the amplitude of the streaking field envelope depends on the relative X-ray/optical arrival time (see section 4.2.2). Eventually, by multiplying the current streaking kick as a scaling factor with the normalized ellipse and adding the unstreaked energy E_0 again one obtains an ellipse-corrected, single-shot upper energy limit for the shifted electron signal in each detector:

$$E_{\mathrm{up}}(\varphi) = a_{\mathrm{ell}} \cdot Ellipse_{\mathrm{norm}}(\varphi) + E_0 \,. \tag{4.8}$$

The values of E_{up} for each detector shape a single-shot, *streaking kick ellipse* that indicates the maximal possible electron energy that could be detected by the respective detector with respect to the current magnitude of the streaking kick, if the streaking vector potential pointed in the direction of this detector at the instant of ionization.

4.1.4 Retrieval of the Temporal Pulse Structure

The main idea of the two-color angular streaking experiment and the analysis procedure so far can be recalled in figure 4.9 a) and b). The angle-dependent shift in energy of the photoelectrons due to the orientation of the streaking vector at the instant of ionization is clearly visible by the comparison of the angle-dependent spectrogram-like polar images $S(E, \varphi)$ for an unstreaked and a streaked FEL shot. For a specific detector, the independently detected spectrum experiences a shift to higher energies only if the vector potential of the MIR streaking field passes the angular range of the detector in the polarization plane during the presence of the X-ray pulse. As a single-shot measure for the relative temporal overlap of the X-ray and the MIR pulses, the maximum up-shifted part of the spectrum or rather the highest photoelectron energy recorded in each detector, which we already know as the cutoff energy $E_{\mathrm{cut}}(\varphi)$ from the determination of the polarization ellipse, is utilized (see figure 4.9 c) and d)).

The X-ray intensity at a given time is directly proportional to the number of electrons generated [205]. However, the transmission and the different emission characteristics of the Ne 1s and Auger electrons should be considered. Thus, for eventually obtaining a meaningful measure of the X-ray pulse structure, one needs to integrate the spectral intensity signal over a specified, sufficiently broad energy range below the cutoff energy for each individual detector. This is done in due consideration of the correction of the spectra for the ellipticity of the polarization of the streaking field. On the downside, one should bear in mind that even barely below its cutoff energy every detector additionally records to some degree energy-shifted electrons resulting from projections of the streaking vector potential pointing at angles close to the direction of the detector under consideration during the presence of the ionizing X-ray pulse. Thus, for achieving a good resolution regarding the retrieval of the temporal intensity structure of the X-ray pulses, one must set the integration window as narrow as possible, depending on the actual amplitude of the streaking field for each shot.

By our definitions (see section 4.1.3), the single-shot values of $E_{\mathrm{up}}(\varphi)$ given by the streaking kick ellipse constitute an upper limit of the streaking shift for each detector (see figure 4.9 c) and d)). For the determination of the lower bound for the integral

$$E_{\mathrm{low}}(\varphi) = E_{\mathrm{up}}(\varphi) - w_{\mathrm{int}} \tag{4.9}$$

an integration window

$$w_{\mathrm{int}} = \left(1 - \cos\left(\frac{\pi}{5}\right)\right) \cdot a_{\mathrm{ell}} \tag{4.10}$$

must be defined, which also adjusts from shot to shot depending on the streaking kick a_{ell}. The cosine-prefactor in equation 4.10 sets a finite integration width and thus the lower bound of integration E_{low} (see figure 4.9 c) and d)), corresponding to a projection angle coverage of $\pm\frac{\pi}{5}$ rad or $\pm$ 36° in the polarization plane. This can be interpreted as an angular resolution of roughly one and a half times the angular separation between

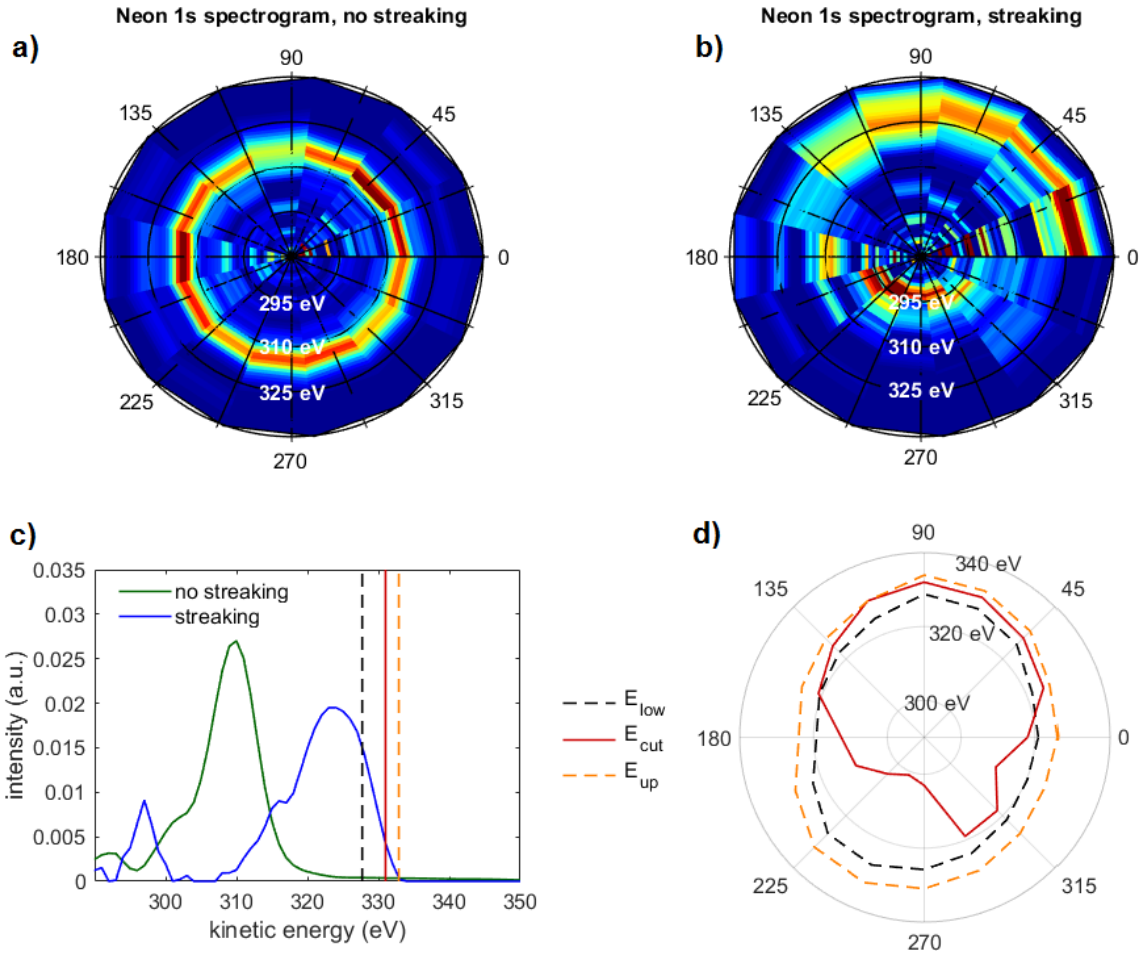

Figure 4.9: Visualization of the effect of two-color angular steaking based on experimental data in the spectral domain. Single-shot, normalized and energy-calibrated Ne 1s photoelectron spectrogram-like polar images $S(E, \varphi)$ recorded by the e-TOF spectrometer array in the plane perpendicular to the FEL beam propagation direction, in absence (a) and in presence (b) of the MIR streaking laser field. In the non-streaking situation (a), the kinetic energy of the photoelectrons excited by an FEL photon energy of 1180 eV is constant over all angles, whereas the close-to-circularly polarized streaking field (b) modulates the spectra depending on the X-ray pulse substructure and the detection angle, according to the principle of angular streaking. In panel (c), the streaked spectrum recorded by the detector at the angular position of 67.5° (blue) is displayed in comparison to an unstreaked spectrum (green). Additionally, the energy values E_{low} (black dashed line), E_{cut} (red line) and E_{up} (yellow dashed line) relevant for the integration pulse characterization algorithm are marked for this specific shot and detector. In panel (d), these angle-dependent energy values are shown in a polar plot, where the maximum energy shift is recorded at 112.5°.

neighboring detectors in each direction. This integration width represents a compromise between a sufficiently broad, thus well-defined integral and a best possible temporal resolution resulting from a narrow integration window.

Hence, according to the rules of our previously presented logic, the actual upper bound of integration is set to the individual cutoff energy E_{cut} of each detector on a single-shot basis. Eventually, the detector signal is integrated over the range determined by the lower

integration bound E_{low} and the cutoff energy E_{cut} as the upper bound. In case that the cutoff energy is situated below the lower bound of integration, the integral is set to zero:

$$I_{\mathrm{X-ray}}(\varphi) \sim \int_{E_{\mathrm{low}}(\varphi)}^{E_{\mathrm{cut}}(\varphi)} S(E,\varphi)\, dE \;\;,\; E_{\mathrm{cut}}(\varphi) > E_{\mathrm{low}}(\varphi) \tag{4.11}$$

$$I_{\mathrm{X-ray}}(\varphi) = 0 \;\;,\; E_{\mathrm{cut}}(\varphi) \leq E_{\mathrm{low}}(\varphi) \tag{4.12}$$

Conclusively, as an upper integration limit naturally the cutoff energy $E_{\mathrm{cut}}(\varphi)$ is utilized, which constitutes the most up-shifted electron energy detected in the respective detector for the current FEL shot. The lower integration bound is calculated via the integration window w_{int}, starting from the maximally allowed up-shifted electron energy $E_{\mathrm{up}}(\varphi)$ for each detector dependent on the current streaking kick a_{ell}. The integration window also scales with the streaking kick of the current shot in order to adjust the width to the actual streaking amplitude. By doing this, one ensures that always the same, relative number of photoelectrons is integrated for each FEL shot, independent of the streaking kick. For a constant integration width, a small streaking kick would imply that much more electron signal is situated within the integration window with respect to a larger streaking kick, which spreads the electron distribution over a broader energy range. Within the clearly defined integration window any signal is only integrated, if the cutoff energy is higher than the lower bound of the integration window, $E_{\mathrm{cut}} > E_{\mathrm{low}}$. For a specific detector, the integration result is therefore nonzero only if any electrons are energetically up-shifted into the integration window due to the streaking field. Otherwise the result of the integration is set to zero. The basic principle of a similar method for pulse retrieval, including the determination of an integration window in the vicinity of the cutoff energy E_{cut}, has recently been theoretically studied and published by Kazansky et al [173].

At this point the idea of the 'attoclock' (see section 2.3) is employed. The integration result, the angle-dependent electron intensity $I_{\mathrm{X-ray}}(\varphi)$, is referred to the angular position of the respective detector. This angular relation can be converted into a time dependence of the FEL pulse intensity by plotting the integration results of all detectors versus the appropriate time axis (see section 2.3). Thus, one obtains a replica of the X-ray pulse shape in the time regime or, more precisely, a reconstruction of the temporal intensity profile of the X-ray pulse. The pulse duration is determined by calculating the root-mean-squared (rms) widths of the reconstructed intensity profiles instead of a full width at half maximum, since for SASE pulses a Gaussian pulse shape is not fulfilled. According to the detector spacing of 22.5° and the 35.3 fs rotation period of the electric field vector, the best possible resolution in the time domain is determined to 2.2 fs. However, owing to a potential smearing of the signal resulting from the occurring projections mentioned above, the temporal resolution might be lower for a majority of the shots, amounting to an upper limit of 3.5 fs in the worst case. Thus, one can assume an average temporal resolution of about 2.8 fs.

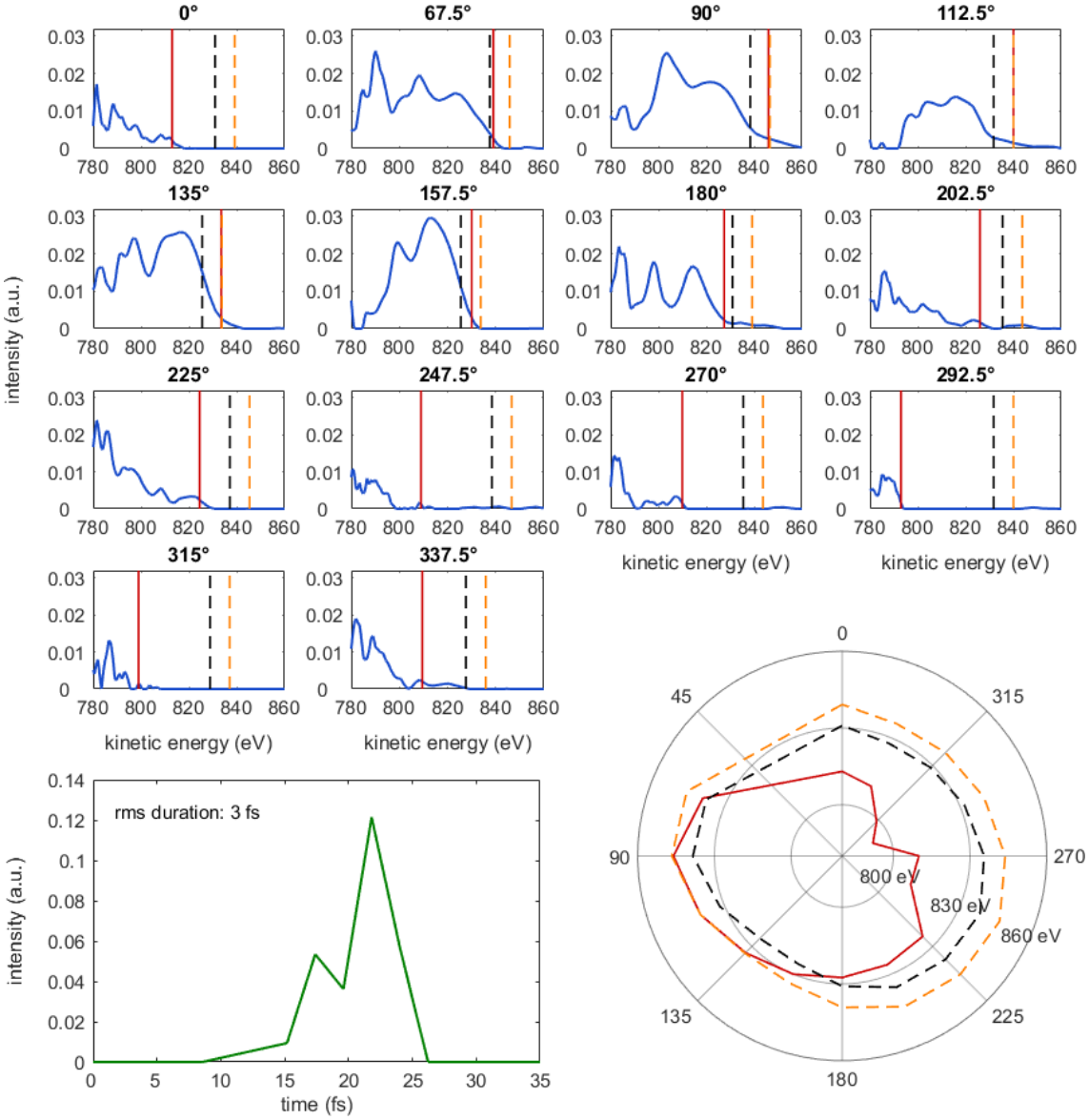

Figure 4.10: Compact overview of the integration X-ray pulse retrieval algorithm. Single-shot, angle-related spectra recorded by the individual detectors with calculated cutoff energy E_{cut} (red), streaking kick ellipse value E_{up} (yellow) and lower integration bound E_{low} (black) are displayed. The two bottom panels show a polar depiction of these energy values on the right and the final reconstructed temporal intensity profile of the pulse (green) on the left. The latter is generated by integrating any spectral intensity $S(E, \varphi)$ between E_{cut} and E_{low} for each detector, as long as E_{cut} is a higher energy value than E_{low}. Otherwise, the intensity signal is set to zero. Converting the angular axis to a time axis by using the rotation period of the MIR polarization vector of 35.3 fs, the corresponding intensity profiles of the X-ray pulses are derived and shown in the lower left panel.

As a summary, the entire retrieval procedure presented so far is illustrated in figure 4.10 for a single shot from an Auger electron data set. The single spectra of the 14 independent e-TOF detectors are presented, where the respective cutoff energy E_{cut} as well as the value of the streaking kick ellipse E_{up} and the lower integration bound E_{low} are distinctly marked. Moreover, a combined depiction of the three characteristic energy values for all 14 detectors in a polar view and the final reconstructed temporal intensity structure of the X-ray pulse are displayed. After the retrieval, we sort out less reliable reconstructions by

discarding those where the summed-up intensity of the entire temporal pulse profile is lower than an empirically defined threshold of 50% of its maximum value of all shots of that run. The summarized results of the analysis of the single pulse data sets are presented in section 4.2.1.

4.1.5 Algorithm Extension for FEL Double-pulse Trains

As already introduced (see section 3.3), angular streaking experiments not only using single X-ray FEL pulses, but also utilizing X-ray FEL double-pulse trains for the ionization have been conducted. X-ray double-pulse trains are generated by the insertion of a double-slotted foil into the electron bunch, as presented earlier in section 3.1. For our measurements, the average pulse duration was set to 3.5 fs (rms) for both pulses with a time delay of about 20 fs between the individual pulses. It is the aim to achieve a pulse retrieval like the single pulse retrieval, but additionally to the pulse duration and shape, the separation between the two individual pulses shall be determined. Therefore, the same integration pulse characterization algorithm as before is applied, but the procedure is extended by an additional part for the analysis of the double-pulse trains.

For the double-pulse data sets, the analysis procedure must be adapted concerning the calculation of the root-mean-squared width as a measure for the pulse duration of the individual pulses and the determination of the separation between the two pulses. The following procedure is equally applied to both, the Ne 1s and the neon Auger data sets. As a first step, a standard peak finding routine using first and second derivatives of the intensity signal is applied. For a clear division into two prominent pulses, it is assumed that the signal between two intensity peaks must drop to at least 5% of its maximum for at least 2 femtoseconds, corresponding to the time covered by the angular range of one detector. All FEL shots where more or less than two prominent intensity peaks are found by the routine, are discarded to select only those shots that would be most suitable for typical pump/probe experiments. Nevertheless, the routine indeed allows shots where one or both pulses consist of more than a single intensity spike, as long as they are clearly separated. The edges of both individual pulses must be determined to reasonably calculate the pulse durations within these bounds for each pulse. We define the outer edges (the rising edge of the first pulse and the falling edge of the second pulse) of the double pulses by the value where the peak intensity of the respective pulse has dropped to less than 5% on each side of the pulse. Instead of the inner edges of the pulses the separation position is set to the center of the range between the two pulses, where the intensity stays below 5% of its maximum for at least 2 femtoseconds.

The separation between both individual pulses is defined as the temporal distance of the centers of mass of both pulses, which is calculated within the defined bounds of the pulses. Since our time axis is circular, this reveals of course two separations between the pulses. For the decision, which of the pulses is the temporally first and which one is the second, a calibration run must be taken, since the angular streaking method does by definition

not reveal this information. For this purpose, a further FEL run with different separation settings is additionally required. In our case, an FEL run with 20 fs and one with 30 fs nominal separation of the two pulses are available. The idea is the following: The one distance along the circular time axis that is extended while comparing the dataset with the shorter separation setting to the one with the longer nominal separation setting can be identified as the real temporal separation between the pulse earlier and the pulse later in time. The summarized results of the analysis of the double-pulse data sets are presented in section 4.2.3.

4.2 Time Structure of X-ray FEL Pulses

The integration pulse characterization algorithm presented above has been applied to various data sets with different FEL pulse settings. Single pulse data with three different pulse durations as well as double-pulse data with different pulse separation have been analyzed by the algorithm for both types of electron signals: photoelectron and Auger electron streaking traces. The outcomes concerning the time structure of the X-ray FEL pulses and their interpretation as well as the determination of the relative arrival time between X-ray and optical pulses are introduced in this section.

4.2.1 Time Structure of X-ray FEL Pulses

In the following section, the condensed outcomes of our data concerning the characterization of the time structure of single, few-femtosecond X-ray FEL pulses generated by the SASE process are presented. The integration pulse characterization algorithm has been applied on neon 1s photoelectron as well as neon Auger electron data sets, where X-ray pulses of three different pulse duration settings had been utilized for the ionization.

Polar depictions for three FEL shots of different pulse durations, showing the radially shifted cutoff energy values $E_{\mathrm{cut}}(\varphi)$, the calculated integration window for all detectors and the corresponding temporal intensity profiles of the X-ray pulses revealing the pulse substructure are displayed in figure 4.11, together with the determined pulse durations. With the application of the presented retrieval procedure on angular streaking measurements, the distinctive SASE pulse substructure can be clearly resolved and the pulse duration can reliably be ascertained. As a demonstration of the huge variety of the pulse shape and the substructure of SASE FEL pulses revealed within the data analysis, a selection of distinct shots with different pulse durations is presented in figure 4.12. As one can see from the irregular pulse shape structures, the specification of an rms pulse duration makes much more sense than a full width at half maximum definition, usually applied to ultra-short Gaussian-like pulses.

A few ten thousand shots for each of three independent FEL settings providing estimated, averaged pulse durations of 3.5 fs, 6.5 fs and 10.5 fs have been evaluated, utilizing not only Ne 1s core electrons but also Neon Auger electrons as measuring probes.

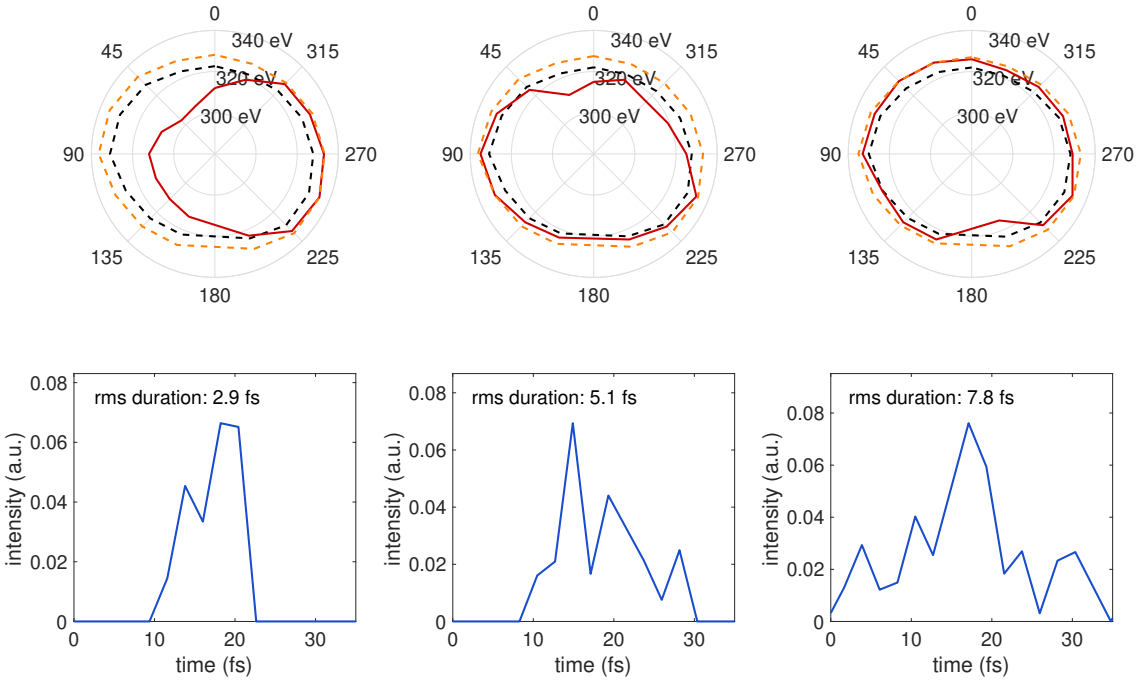

Figure 4.11: Retrieval of the pulse substructure and duration for three different pulse duration settings. In the upper panels, the cutoff energy $E_{\mathrm{cut}}(\varphi)$ (red line), as well as the maximal integration window delimited by the lower integration limit $E_{\mathrm{low}}(\varphi)$ (black dashed line) and the maximal upper border $E_{\mathrm{up}}(\varphi)$ (yellow dashed line), which are deduced from the close-to-circular polarization and the strength of the IR streaking field are shown in a polar plot for three distinct pulse duration settings of the FEL. The spectral intensity $S(E, \varphi)$ between $E_{\mathrm{low}}(\varphi)$ and $E_{\mathrm{cut}}(\varphi)$ is integrated, as it is proportional to the X-ray pulse profile. The corresponding intensity profiles of the X-ray pulses are derived by converting the angular axis to a time axis, and shown in the lower panels.

The resulting histograms of the pulse duration and their mean values derived by the pulse retrieval algorithm for the different FEL settings are displayed in figure 4.13. The Gaussian-like distributions of the pulse durations for each setting match very well with the expectations. Both electron detection settings produce remarkably consistent results and prove the robustness and versatility of the algorithm.

The measured temporal substructure of X-ray FEL pulses clearly shows the expected series of random pulse shapes and one can observe that the number of SASE spikes within the pulse changes considerably from shot to shot. This delivers fundamental and urgently required information not only for time-resolved experiments on the femtosecond time scale, but also for any study of nonlinear processes relying on the precise knowledge of X-ray peak intensities [172]. Either Auger electrons or photoelectrons from a dilute gas target can be used — without substantial X-ray beam intensity losses and independent from simultaneously ongoing experiments — to measure the profile of single X-ray SASE FEL pulses with a resolution of about 2.2 fs.

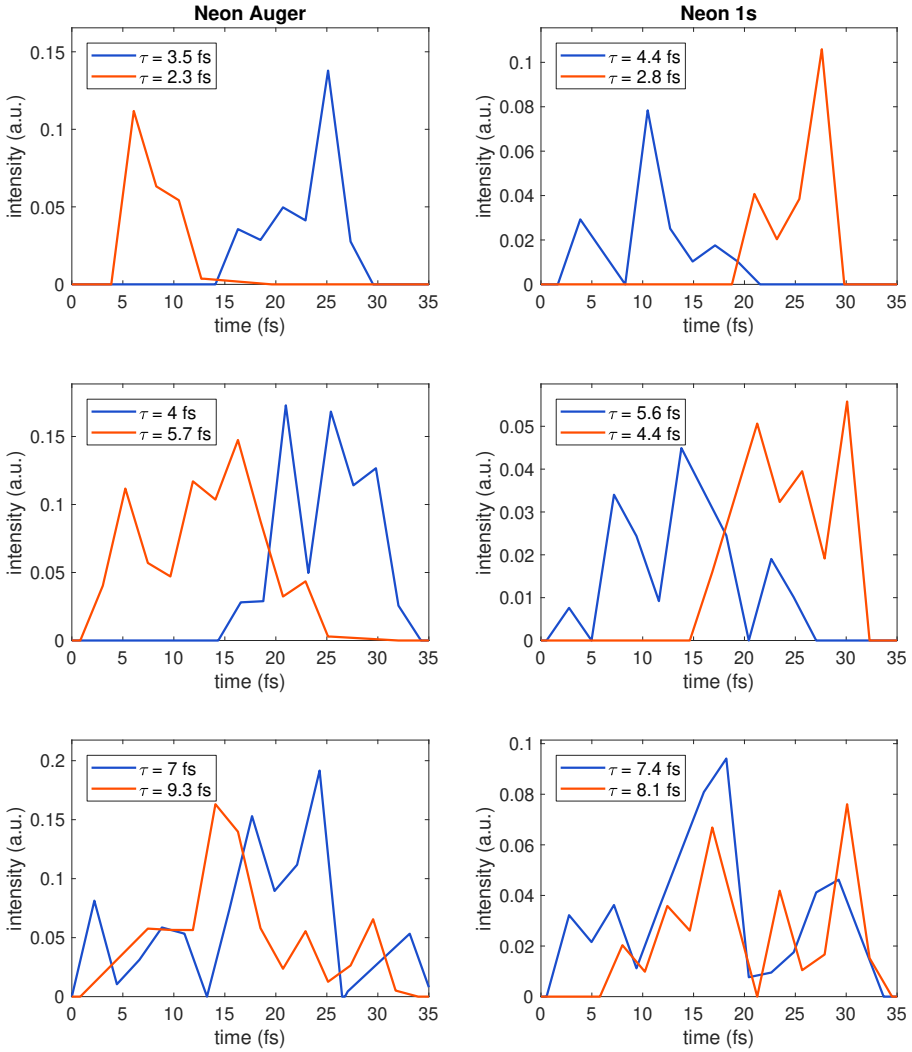

Figure 4.12: Variety of the pulse shape and substructure of SASE FEL pulses due to their stochastic nature. A selection of different reconstructed temporal pulse profiles and respective rms pulse durations from neon Auger data sets (left row) and neon 1s data sets (right row) is shown. The nominal rms pulse duration settings provided by LCLS for the data set presented in three rows are from top to bottom: 3.5 fs, 6.5 fs and 10.5 fs. For each setting, two different shots are plotted together in one panel.

4.2.2 Determination of the Relative X-ray/Optical Arrival Time

X-ray pump/optical probe experiments at FEL facilities suffer from the inherent arrival time jitter of the two synchronized yet independent light sources, which adversely affects the temporal resolution. At LCLS, this jitter is in the order of 50 fs or larger. Besides the characterization of individual X-ray SASE FEL pulses, angular streaking can simultaneously measure the relative X-ray arrival time with few-femtosecond resolution. State-of-the-art arrival time monitors are based on X-ray/optical cross correlation in solid samples and are generally used at FEL facilities [85, 86, 177]. Within the frame of the two-color angular streaking experiments, the X-ray pulses are overlapped with the trailing ramp of the streaking pulse envelope [172]. Therefore, in addition to the pulse structure retrieval, the presented algorithm is also capable of measuring the single-shot arrival time jitter of the X-ray pulses.

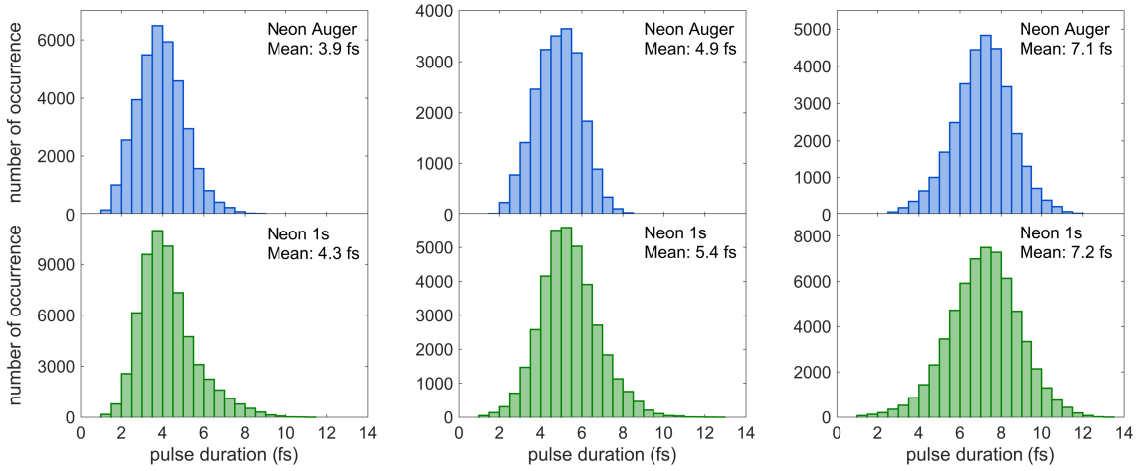

Figure 4.13: Distribution of the determined pulse durations within FEL runs with fixed nominal pulse duration settings. Histograms of the pulse duration and the related mean values derived by the pulse retrieval algorithm for different FEL and detection settings. The upper panels show the results from neon Auger data sets with LCLS pulse duration estimates (rms) of 3.5 fs (left), 6.5 fs (middle) and 10.5 fs (right). The lower panels show the corresponding histograms for neon 1s data sets with the same FEL settings as above.

Provided that the envelope of the MIR streaking pulse is initially characterized, this is done by converting the observed streaking kick a_{ell} into arrival time information for each single shot, as displayed in figure 4.14.

As mentioned earlier, the streaking kick a_{ell} is a shot-dependent variable owing to the inherent arrival time jitter of the X-ray pulses with respect to the MIR field envelope. The latter is Gaussian-shaped and has a FWHM duration of τ_{IR} = 480 fs. Thus, the amplitude of the streaking field can be mapped to a Gaussian distribution of the streaking shift, which is described by

$$a_{\mathrm{ell}} = E_{\mathrm{max}} \cdot \exp\left(-\frac{t_{\mathrm{arrival}}^2}{2\left(\frac{\tau_{\mathrm{MIR}}}{2.35}\right)^2}\right) , \tag{4.13}$$

where E_{max} is the maximum possible streaking shift corresponding to the maximum of the MIR amplitude. For even more accuracy, a_{ell} and E_{max} are corrected for the power fluctuations of the MIR streaking laser, which have been logged for each shot during all experiments. E_{max} is determined by evaluating an overlap scan, where the temporal delay of the X-ray and MIR pulses has been varied. For the optimum time overlap, the maximum streaking shift is reached at E_{max} = 58 eV. Since the integration retrieval algorithm determines the streaking kick on a single-shot basis, the arrival time can thus be calculated by

$$t_{\mathrm{arrival}} = \sqrt{-2 \cdot \ln\left(\frac{a_{\mathrm{ell}}}{E_{\mathrm{max}}}\right) \cdot \left(\frac{\tau_{\mathrm{MIR}}}{2.35}\right)^2} . \tag{4.14}$$

Prerequisite for this is that the calibration with an MIR/X-ray overlap scan as mentioned above is performed. The average jitter is then determined by the FWHM of the distribution of t_{arrival} looking at many thousand shots. For all Auger runs evaluated, one obtains an average arrival time jitter of 56 fs FWHM over the course of a 15-min experimental run

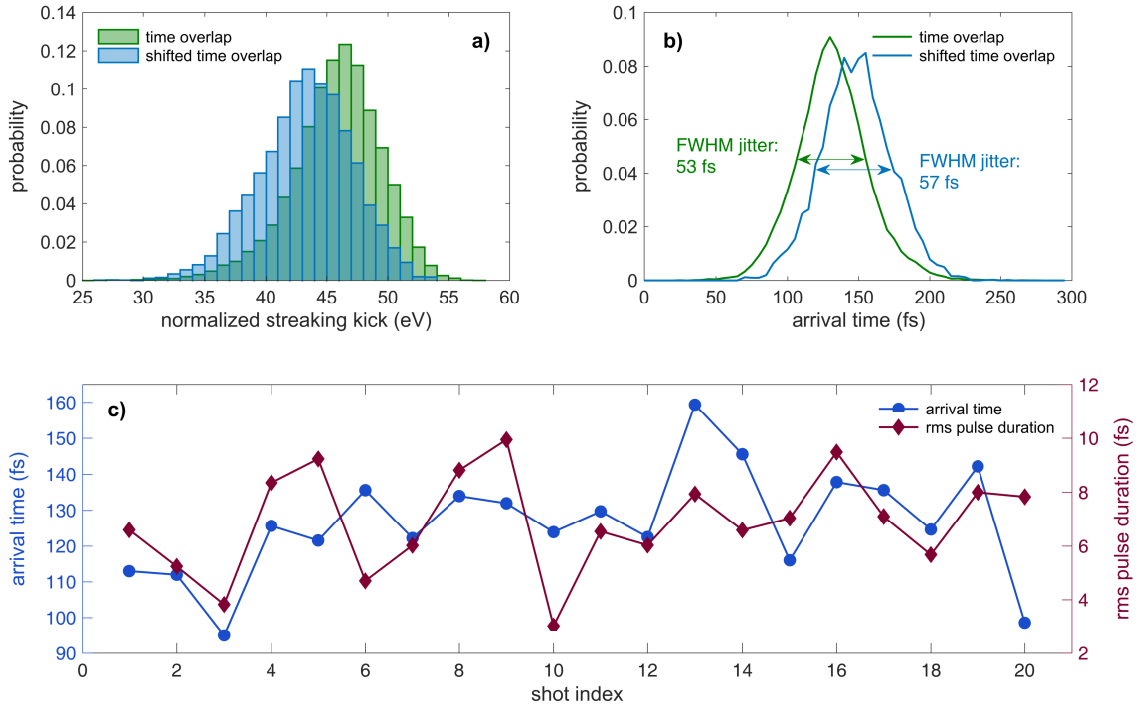

Figure 4.14: Determination of the relative X-ray/optical arrival time and the arrival time jitter. In panel (a), the distribution of the retrieved streaking kick a_{ell}, which is additionally corrected for the MIR power fluctuations, is depicted for many thousand shots at two different time overlap positions. The shift to lower energies can be clearly observed while moving out of the optimum temporal overlap. The streaking kick can be converted to the arrival time (b) of the X-ray pulses after a calibration with an MIR/X-ray overlap scan, from which the maximum streaking amplitude and the pulse duration of the MIR laser can be extracted. Here, the relative arrival time is given with respect to the maximum of the IR envelope. The width of these distributions (b) is a measure for the arrival time jitter. In panel (c), the single-shots results for the pulse duration and the arrival time are illustrated for a series of consecutive shots.

with an estimated arrival time resolution of 2.2 fs. The determined value is in very good agreement with the result delivered by the complex *Pacman* algorithm [172].

4.2.3 Characterization of X-ray FEL Double-pulse Trains

In the following section, the condensed outcomes of our data concerning the characterization of X-ray FEL double-pulse trains are presented. The pulse characterization algorithm has been applied on neon 1s photoelectron as well as neon Auger electron data sets with an average pulse duration set to 3.5 fs (rms) for both individual pulses and with a time delay of about 20 fs between both pulses.

Time Structure of X-ray FEL Double Pulses

The insertion of a double-slotted foil into the electron bunch leads to X-ray double-pulse trains, which have already been characterized using terahertz streaking, with a resolution limit for the pulse delay of 38 fs [71, 212]. The results of the extended retrieval algorithm for double-pulse trains applied on many thousand shots are collectively presented in figure 4.15, showing an even shorter mean pulse separation than ever measured before.

The substructure of the two individual pulses and their separation are clearly resolved on a single-shot basis (figure 4.15 a) and d)). The retrieved double-pulse delay fits very well to the estimated average value provided by LCLS, revealing a mean pulse separation of 23 fs (figure 4.15 b) and e)). The single-peak pulse duration statistics (figure 4.15 c) and f)) yield a mean rms duration of 2 fs, also fitting very well to the nominal duration predicted. As may be imagined, the presented technique is capable of resolving even smaller double-pulse delays through a variation of the streaking laser rotation period.

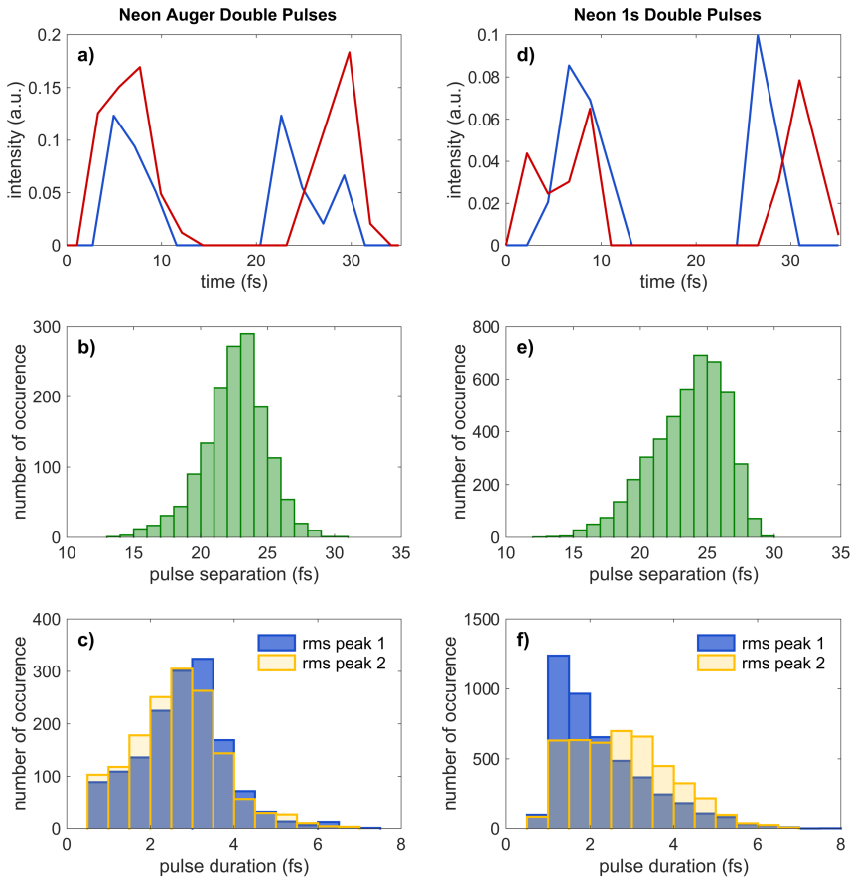

Figure 4.15: Temporal characterization of X-ray FEL double-pulse trains. Results of the pulse retrieval algorithm for Neon Auger (a – c) and Neon 1s (d – f) double-pulse data sets with an LCLS-estimated pulse separation of 20 fs. In panels (a) and (d), the retrieved signals for two exemplary, well-separated double pulses are given in blue and orange. Panels (b) and (e) show the distributions of the separation between the two individual peaks of the double pulse for a few thousand shots, respectively. In panels (c) and (f), the corresponding rms pulse durations for each of the two peaks constituting the double pulse are shown in histograms, which are overlapping to a large extent.

For studies of correlation dynamics on the femtosecond time scale, the development of an X-ray pump/probe setup with an adjustable delay and enough pulse intensity has been a long-desired goal. Utilizing the now accessible unique properties of SASE FEL pulses, the demonstrated measurements proof that this research avenue is already within reach of today's FEL facilities [172].

Sequence of the Double Pulses

For the determination of the temporal order of the double pulses, an FEL run with 20 fs and one with 30 fs nominal separation of the two pulses are analyzed, as explained in section 4.1.5. Unfortunately, the results do not prove the sequence beyond doubt, as visualized in figure 4.16. The results only provide a tendency, but do not reconstruct the nominal separation well for the data sets with a longer separation. This observation can be explained by a nascent merging of the two pulses in our integrated signal intensities: Since the longer double-pulse delay of 30 fs is close to the rotation period of the close-to-circularly polarized MIR streaking vector of 35.3 fs, the integrated intensity signals of both individual pulses might already be overlapping, which can lead to ambiguities in the analysis. Under these circumstances, the detected shift in pulse separation can be seen at least as an indication for the directionality of the shift.

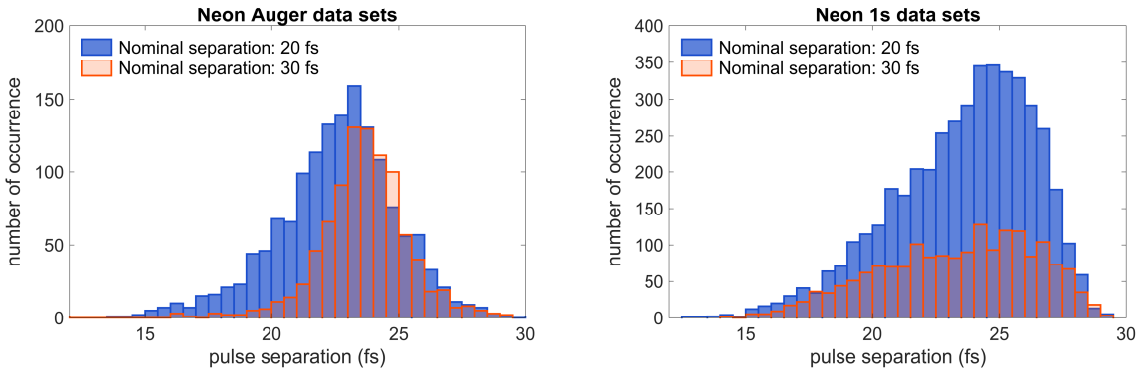

Figure 4.16: Derived sequence of the double-pulse trains. Determined pulse separations of the data sets with nominal settings of 20 fs and 30 fs separation for both, the Neon Auger (left) and the Ne 1s data sets (right). It is clearly visible that the results only provide a tendency, but do not map the nominal separation well for the data sets with a longer separation, owing to the adverse relation between separation and the rotation period of the close-to-circularly polarized MIR streaking field.

4.3 Evaluation of the Capabilities of the Algorithm

Recently, the Pacman algorithm mentioned above has proofed its validity by its application on simulated angular streaking data and by comparison with the estimation on the pulse duration provided by the X-band radio-frequency deflector (XTCAV) tool installed at LCLS [172]. This proof of concept is described subsequently. Afterwards, the complex and time-consuming Pacman algorithm and the integration algorithm presented above shall be compared. For this purpose, both algorithms are applied to an identical angular streaking data set containing a random selection of recorded shots. Furthermore, the capabilities of the integration algorithm with respect to an implementation as a smart online veto at FEL facilities are evaluated. Hereby, special attention is paid to the speed for compatibility with high repetition rates and robustness of the algorithm.

4.3.1 Benchmarking with an Established Analysis Routine

In parallel to the integration pulse characterization algorithm presented above, a complex, iterative projection algorithm, the so-called *Pacman* algorithm, which retrieves the attosecond time-energy distribution of X-ray SASE FEL pulses, has been developed by Nick Hartmann and improved by Gregor Hartmann [172]. The principle of the algorithm shall be introduced in the following, a more mathematical description can be found in appendix A.1. This section is in parts an adaption of the supplementary information from [172].

The Iterative Pacman Algorithm

The algorithm decomposes the recorded angular streaking spectrogram $I(E,\theta)$ into a sum of angle projections of contributions from all infrared phase settings that overlapped with the actual X-ray pulse. The single angular projections are determined by iteratively fitting Neon 1s photoelectron streaking traces. These traces are constructed for this out of very narrow Gaussian X-ray pulses in the presence of a close-to-circularly polarized, infrared streaking field, thus imitating the experimental settings. For each single FEL shot, those fitting curves get parametrized utilizing the initial photoelectron energy E_0 at the instant of ionization, the actual streaking laser phase φ_L, and the fixed streaking shift σ, that is adjusted for various detection angles θ considering the respective magnitude of the polarization ellipse of the streaking pulse:

$$I_{\mathrm{fit}}(E,\theta) \sim e^{-(E-(E_0+\sigma\cdot\cos(\theta-\varphi_L)))^2} \tag{4.15}$$

The first fit iteration defines the streaking shift σ from the experimental data, that is set constant over the entire duration of the X-ray pulse due to the comparable long MIR pule duration, as already mentioned above. For each iteration, the best fit $I_{\mathrm{fit}}(E,\theta)$ found for the two remaining parameters E_0 and φ_L is subtracted from the input spectrogram, see figure 4.17. This sequence of fitting and subsequent subtraction is re-iterated until the remaining intensity in the spectrogram arrives at the background noise level. Eventually, the X-ray temporal structure of the X-ray pulse $P(t)$ is obtained from the histogram of the incrementally fitted phase values of the streaking laser φ_L through $t = \varphi_L\lambda/(2\pi c)$. The appropriate values determined for E_0 provide the instantaneous frequency via $\omega(t) = E_0(t) + E_{\mathrm{Ne1s}}$ [172].

The temporal resolution regarding the retrieved intensity profiles of the X-ray pulses not only depends on the angular detection of the photoelectron distribution. Solely the streaking wavelength of 10.6 µm, resulting in a 35-fs polarization period of the streaking field that has been applied in the actual experiment, in combination with the 16 evenly distributed TOF detectors would lead to a time resolution of 2.2 fs. Nevertheless, due to the streaking effect the inherent energy resolution of the single detectors of about 0.75 eV – 1 eV must also be considered. This results in a time resolution of about 0.44 fs for the Pacman algorithm applied on the data sets from the angular streaking experiments [172].

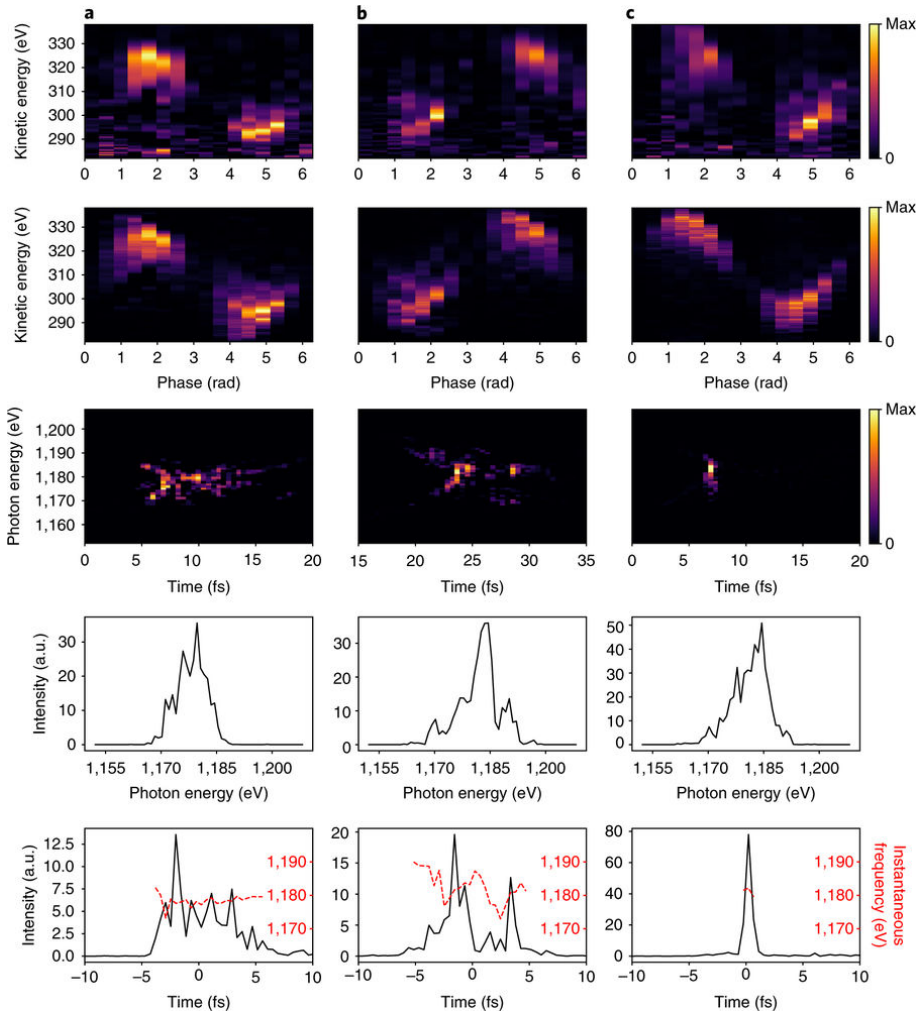

Figure 4.17: X-ray pulse time–energy reconstruction of three typical SASE XFEL shots by the Pacman algorithm. The outcomes of the reconstruction are presented for three randomly selected X-ray pulses a, b and c. One column for each XFEL shot, from top to bottom: A measured, angularly streaked photoelectron spectrum (row 1), the retrieved photoelectron spectrum (row 2), a retrieved X-ray spectrogram (time–energy distributions, row 3), the X-ray spectrum (row 4) and the reconstructed temporal intensity profile (row 5) are shown for each pulse. Taken from [172].

Subsequently, the capabilities of the Pacman algorithm are shortly proofed by applying it on simulated angular streaking data sets and by comparison with the temporal X-ray pulse profile provided by the X-band radiofrequency deflector (XTCAV) tool installed at LCLS.

Application of the Pacman Algorithm on Simulated Angular Streaking Data

For a corroboration of the validity of the Pacman algorithm, a quantum mechanical simulation of the experimental setting in the conducted angular streaking experiments like the one presented in [173] has been employed. Starting point is the photoionization of a neon 1s electron by a linearly polarized, ultrashort and soft X-ray FEL pulse as well as the subsequent modulation of the photoelectron distribution by a close-to-circularly polarized streaking field, which is synchronized to the X-ray pulse.

The streaking laser pulse parameters such as wavelength, pulse duration, spot size and the ellipticity of the polarization ($\epsilon = 0.7$) as well as the X-ray photon energy and bandwidth have been selected according to the actual circumstances. Utilizing a theoretical approach on the basis of the strong-field approximation, the double differential cross section (DDCS) for the electron energy versus yield angle in the plane perpendicular to the beam is computed. Thus, the experimental mechanism can be modelled within the first-order time-dependent perturbation theory as well as the rotating wave approximation for the interaction between electron and X-ray photon [172], similarly to the quantum-mechanical description of the conventional streaking as presented in section 2.2.4. A more detailed explanation of the approach for the simulation is given in [174, 213].

The outcoming DDCS is illustrated in figure 4.18 a). A convolution of the DDCS with detector resolution and acceptance angle is depicted in figure 4.18 b), however, divided into bins according to the experimental bins and shifted by 90° owing to a different choice of the coordinate system. Eventually, the Pacman algorithm has been applied to this simulated cross section treating it like real data. The reconstruction results perfectly agree with the original X-ray pulse, as illustrated in figure 4.18 d). Consequently, the validity of the Pacman algorithm is impressively corroborated and is therefore utilized in the following section as an approved reference for the integration pulse characterization algorithm presented within this thesis.

Comparison to XTCAV Estimations on the X-ray Pulse Structure

Two diagnostics tools are utilized at LCLS for an estimation of the X-ray pulse duration based on the electron bunch length. Similarly, to a classical streak camera, the radiofrequency field of the so-called *transverse deflecting cavity* (TCAV3) introduces a time-dependent vertical momentum to the electron bunch. Hereby, the time is converted into the transverse position determined by a downstream located beam monitoring system. The temporal resolution of this invasive method amounts to about 10 femtoseconds (rms), thus being not applicable to ultrashort, few-femtosecond or even attosecond X-ray pulses.

The second diagnostic tool, the *X-band transverse cavity* (XTCAV), which is located just after the FEL undulator [214] and is indirectly observing the temporal X-ray pulse structure by analyzing the electron bunch after its propagation through the undulator. It has an increased resolution owing to a higher voltage and frequency compared to TCAV3. Near the zero-crossing of the RF-field the tool induces a time-dependent sweep in the horizontal direction, while the magnetic bend in the electron dump after the undulator causes a vertical electron deflection inversely proportional to the electron energy. Hence, the tool records a two-dimensional time–energy distribution of the spent electron bunch. During the lasing process within the undulator the electrons lose energy, as this amount of energy is transferred to the amplified X-ray radiation. Therefore, sections within the electron bunch experience a lasing-induced energy loss being proportional to the intensity of the X-ray pulse emitted by the respective slice of the longitudinal profile of the electron bunch.

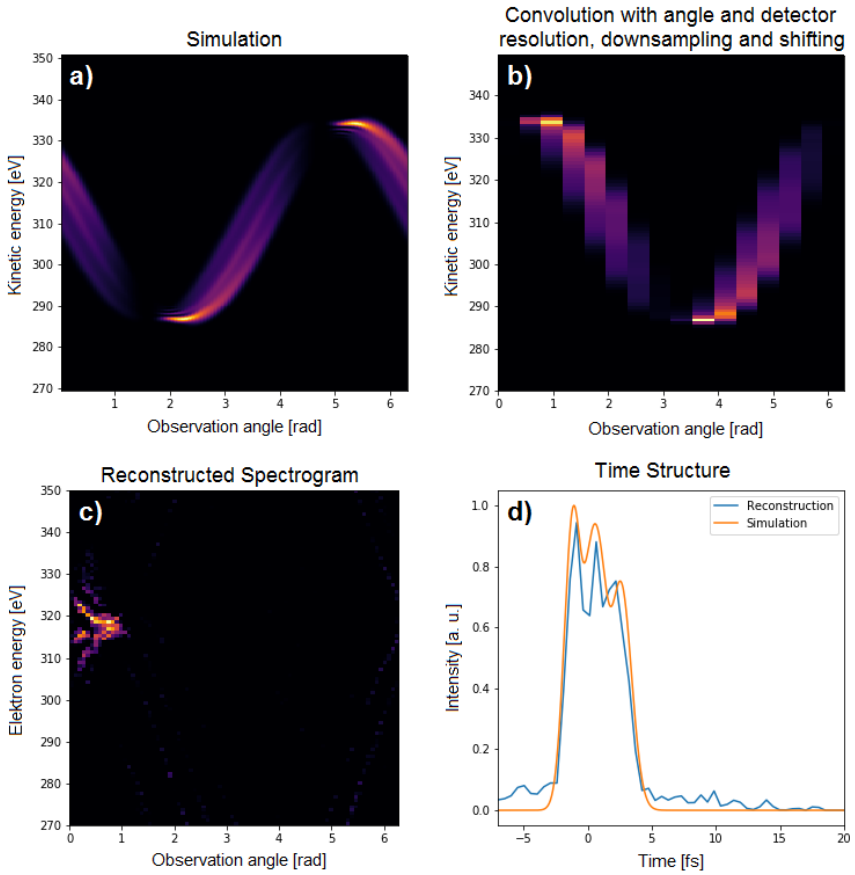

Figure 4.18: X-ray pulse reconstruction by the Pacman algorithm for a comparison with a full quantum mechanical simulation. The simulated double differential cross section (DDCS) is shown at the full resolution of the theoretical calculation (a). This DDCS is convolved with the experimental energy and angle resolution and the grid size is reduced to the experimental values and accordingly shifted by $+90°$ (b). Thus, the different coordinate system of the simulation is considered and the quality of the reconstruction is evaluated under the real conditions of the angular streaking experiment. For the X-ray pulse reconstruction, the Pacman algorithm with exactly the same set of parameters as utilized for the analysis of the experimental data has been applied. The reconstructed outcomes for the simulated X-ray pulse are presented in the bottom row: the retrieved spectrogram (c) and the comparison of the temporal pulse structure (d) between the simulation (orange) and the reconstruction one (blue). Clearly, the result of the Pacman algorithm fits nearly perfectly to the original simulation, hence proving the reliability and validity of this evaluation approach. Taken from [172].

The 'footprint' of the lasing along the bunch is determined by comparison with reference records from electron bunches of an FEL shot where lasing was suppressed and is then utilized for a retrieval of the temporal intensity profile of the X-ray pulse [172].

An advantage of the XTCAV is, that it does not affect the X-ray lasing process. The XTCAV tool reaches a time resolution of about 4 fs (rms) [84], reconstructed from the minimum, unstreaked horizontal electron bunch detectable on the XTCAV screen [172]. For a comparison of the XTCAV tool and the Pacman algorithm in combination with two-color angular streaking measurements, a random shot is exemplary depicted in figure 4.19. After considering the coarser temporal resolution of the XTCAV, a comparison of the pulse

intensity profiles of both approaches reveals a good agreement [172]. Consequently, also the application of the Pacman algorithm on real data is corroborated by the XTCAV results.

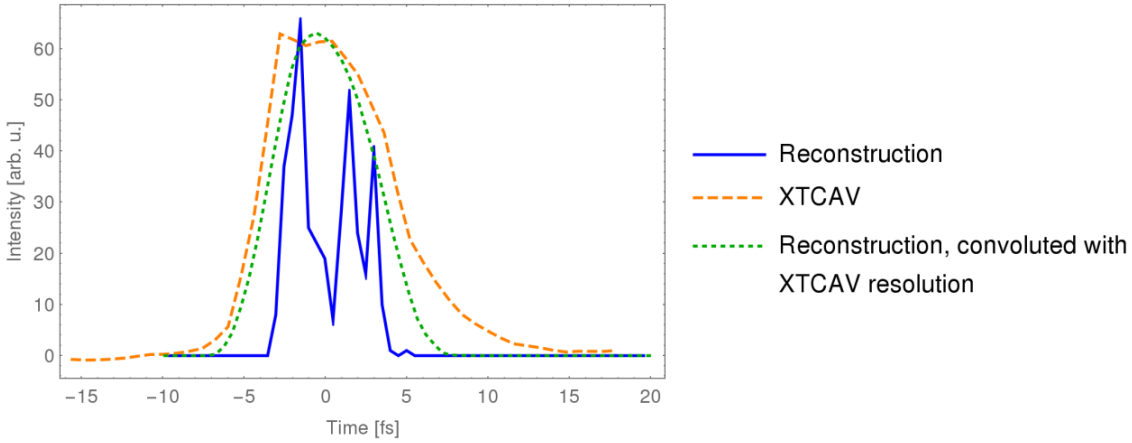

Figure 4.19: Comparison of X-ray FEL pulse intensity profiles determined by the Pacman algorithm via angular streaking and the XTCAV reconstruction approach for a randomly selected shot. The pulse structure retrieved by the Pacman algorithm via angular streaking is depicted in blue, the XTCAV reconstruction in orange. A convolution of the angular streaking outcome with a Gaussian distribution with a sigma of 3.6 fs, which accounts for the lower temporal resolution of the XTCAV (3.6 fs, rms) is illustrated in green. Regarding the overall shape of the pulse, there is a good agreement of the XTCAV outcome with the angular streaking result convoluted with the XTCAV resolution (green). Obviously, the XTCAV technique mostly blurs the temporal substructure of the X-ray pulse, emphasizing the unprecedented temporal resolution of the angular streaking method in combination with the Pacman algorithm. Taken from [172].

Nevertheless, for the upcoming sub-femtosecond FEL pulses the resolution of this method is basically insufficient, owing to a mismatch between the speed of light and the effective velocity of the electron bunch within the undulator. Additionally, the pulse shape estimation of the XTCAV tool cannot be transferred to the actual location of the experiment, This restricts its applicability regarding upcoming experiments using X-ray pulse shaping due to dispersive X-ray optics [212]. Furthermore, XTCAV measurements can only provide limited temporal resolution for ultrashort XFEL pulse settings with the slotted foil and are thus not sufficient to resolve the intensity substructure or individual pulses with sub-femtosecond duration. Therefore, it is not possible to deduce definite single-shot pulse durations or even time–energy information from these measurements. Again, this shows the urgent need for a direct X-ray pulse characterization at FEL facilities.

4.3.2 A Smart Online Tool for Pulse Characterization

In the following, the outcomes of the angular streaking data analyzed by the integration pulse characterization algorithm presented above shall be evaluated. Thus, both, the Pacman algorithm as well as the integration algorithm are applied to an identical angular streaking Ne1s data set, containing a random selection of recorded FEL shots, in order to provide the single-shot pulse duration and to reconstruct the temporal pulse substructure. The nominal, averaged pulse duration of the X-ray FEL pulses is set to about 3.5 fs (rms) for all the selected shots. The data set contains only FEL shots that overcome all filter

routines mentioned before. Both algorithms are applied independently to raw data of about 46.500 FEL shots. Then, the reconstructed pulse intensity profiles of the SASE XFEL pulses, as well as the calculated pulse durations are comparatively evaluated. Standard data analysis steps such as noise filtering and background subtraction, transmission correction and signal normalization, energy calibration and a correction for the ellipticity of the polarization ellipse are similarly considered by both routines.

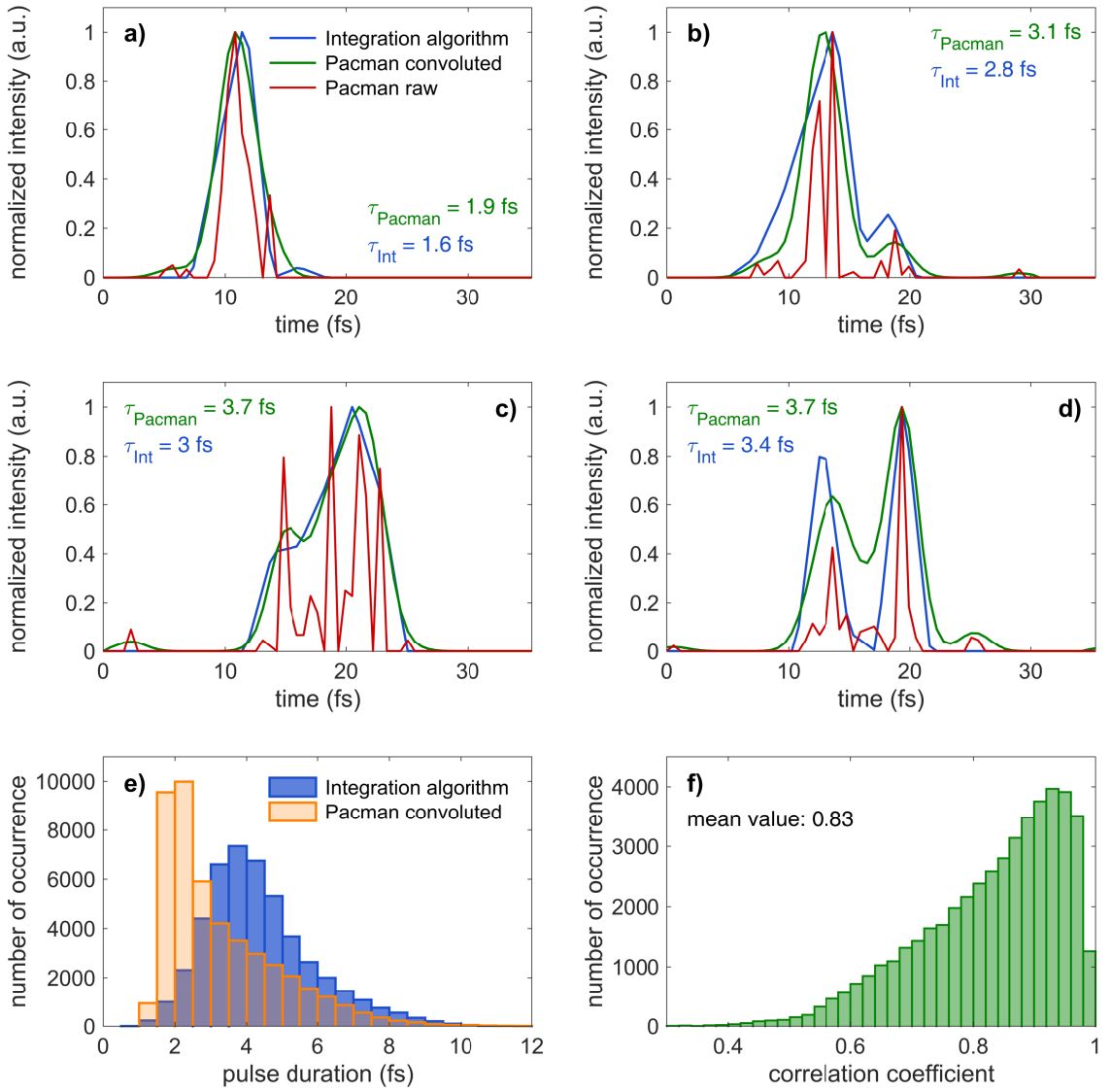

Figure 4.20: Evaluation of the integration algorithm by a benchmarking test with the Pacman algorithm. A comparison of the reconstructed temporal intensity profiles of exemplary X-ray FEL pulses is presented (a – d). The respective reconstruction of both algorithms, as well as the Pacman reconstruction convoluted with a Gaussian response function, corresponding to the average temporal resolution of the integration algorithm (2.85 fs), are displayed for four X-ray FEL pulses. The rms pulse durations determined by the integration algorithm and the convoluted Pacman reconstruction are also denoted. (e) The histograms of the distributions of the rms pulse durations determined by both algorithms are plotted. Despite a small shift due to the temporal resolution of the integration algorithm, the distributions show a good agreement. (f) The distribution of the Pearson correlation coefficient is illustrated, together with its mean value.

For four exemplary X-ray pulses, the reconstructions of the integration pulse characterization algorithm and the Pacman algorithm are comparatively shown in figure 4.20 (a – d). For an even better, more reasonable comparability, the high-resolution retrieval of the complex Pacman algorithm has been additionally convoluted with a Gaussian response function corresponding to a temporal resolution of 2.85 fs. This convolution is applied in order to reflect the average temporal resolution of the integration algorithm. Overall, these results verify our time resolution once again. Both algorithms reveal very consistent results on the reconstructed substructure of the individual X-ray pulses composed of SASE spikes of varying number and shape. Also the respectively calculated pulse durations are very similar. This very good agreement proves the validity of the described fast integration procedure. For a more detailed evaluation of the similarity of the pulse substructures retrieved by both routines for the same SASE pulse, additional statistical methods are applied. The reconstructed intensity profiles from the integration algorithm have been cross-correlated with those of the convoluted Pacman reconstruction for each shot in order to optimize the overlap of both pulse shapes on the time axis. Then the Pearson correlation coefficient for the two reconstructed intensity profiles is determined for all shots of the data set. The according distribution is displayed in figure 4.20 f). The mean of the correlation coefficient amounts to 0.83, constituting a strong correlation between the reconstructed pulse shapes. Furthermore, the distributions of the calculated rms pulse durations, delivered from both algorithms, are comparatively displayed for all shots of the data set in figure 4.20 e). Regarding the integration algorithm, the mean of the distribution amounts to 4.3 fs, while the mean value for the Pacman algorithm is calculated to 3.3 fs. Both results are close to the nominal, averaged pulse duration of 3.5 fs. Again, the good agreement of the respective distributions is clearly visible. The constraints of the temporal resolution of the integration algorithm are visualized by the shift of the two distributions to each other.

One has to bear in mind, that the distributions comprise shots, where the agreement of both reconstructions is not satisfactorily, e.g. due to an abortive retrieval for one of the algorithms. With a shot sorting by means of filtering on the Pearson correlation coefficient, one can get a better understanding of the remaining discrepancy and can evaluate the agreement of the pulse duration distributions, limited to reconstructed shots with a good correlation. The objective is to consider solely FEL shots for the comparison of the pulse duration distributions, where the correlation coefficient has a value of better than its mean value of 0.83. The comparison of the resulting, filtered distributions of the pulse durations is presented in figure 4.21. The mean of the distribution for the integration algorithm amounts to 3.8 fs, while the mean value for the Pacman algorithm is determined to 3.2 fs. The latter value is barely influenced. One can see that the agreement of the two distributions is considerably improved and the histograms match quite well.

Eventually, the fidelity and the capabilities of the fast integration pulse characterization routine presented in this thesis are very well corroborated by this comparison with

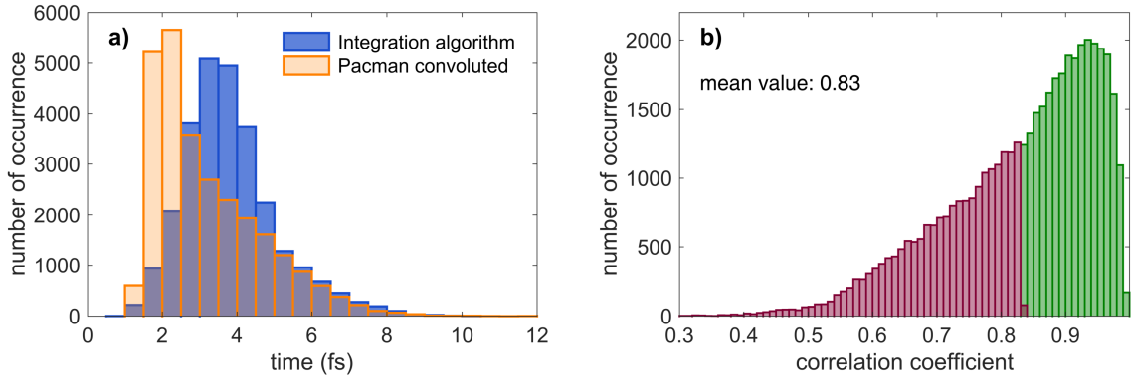

Figure 4.21: Distribution of the retrieved pulse duration for strongly correlated reconstructions. (a) The histograms of the distributions of the pulse durations (rms) determined by both algorithms are presented solely for FEL shots with a strong correlation between convoluted Pacman reconstruction and the reconstruction from the integration algorithm. (b) The same distribution of the Pearson correlation coefficient as in figure 4.20 is presented. Here, FEL shots that are sorted out by the filter are highlighted in in dark red and those that remain in the data set are depicted in green.

the powerful Pacman algorithm. The comparison further proves the relatively high confidence level at orders of magnitude lower computing time and hence its applicability as an online tool for pulse characterization. The Pacman algorithm provides an attosecond time–energy retrieval of X-ray SASE FEL pulses. Nevertheless, this detailed reconstruction is only suitable for pulse-sorting after the experiment due to its high requirements on computation time. Therefore, the fast integration pulse characterization algorithm with its here demonstrated capabilities is the only currently available possibility for the implementation of online pulse tagging, urgently required at FEL facilities in the near future.

Speed Optimization of the Pulse Characterization Routine

Initially, the source code for the algorithm was written in MATLAB without any concerns regarding the runtime per single shot, determining the speed of the routine. Nevertheless, with a repetition rate of roughly 125 Hz (runtime of 8 ms per shot) the routine has been already fast enough for an online analysis of FEL shots at LCLS. This is also faster than the complex Pacman algorithm. However, the latter provides a time–energy reconstruction, but at the price of an orders of magnitude slower performance repetition rate. Thus, this is far too slow for the planned high repetition rate of LCLS II, amounting to 1 MHz in its final expansion stage and the repetition rate of the European XFEL, which shall exceed 2.7 kHz in its planned standard mode.

Therefore, with strong support by our colleague Vahe Shirvanyan[1] the code has been optimized with respect to its runtime. In a first step, the code has been streamlined in MATLAB. Hereby, internal MATLAB functions utilized in the routine and generally programmed in a very complex manner have been simplified and reduced to the essential functions for their application in the routine or replaced by compact, simple and hence

[1]Technical University of Munich, Chair for Laser- and X-ray physics

speed-optimized versions. Moreover, several self-programmed, time-consuming parts of the code have been streamlined for a better performance. Especially, the Wiener deconvolution utilized in the routine for the noise filtering is an extremely time-consuming section in the code. This noise filter has been replaced by a standard two-point binning of the data, since a thorough comparison of both methods showed similar results within the tolerances regarding the generated, noise-filtered time-of-flight traces. Likewise, the reconstructed single-shot intensity profiles showed comparable results. Albeit the Wiener deconvolution is scientifically the more sound method, the binning routine provides acceptable results in a fraction of the time and is thus utilized for the speed-optimized version. Eventually, using the internal MATLAB stopwatch timer for chronometry, this streamlined version of the MATLAB routine exhibits a runtime of 58 µs per shot ($\widehat{=}$ 17 kHz repetition rate) on a standard quad-core (3.6 GHz) workstation.
The runtime measurement basically comprises solely the single-shot pulse retrieval part of the algorithm. The coefficients for the energy calibration and the polarization ellipse as well as the normalization factors for the detectors must be statistically determined by averaging thousands of shots in a calibration run a priori. Therefore, these parameters are considered as prerequisites for the pulse shape retrieval and their determination is not included in the runtime measurement. For obtaining a meaningful value for an online single-shot runtime, these calibration parameters together with the raw time-of-flight data are preloaded in the main memory.

In a second step, the runtime of the routine has been even further reduced by a translation of the MATLAB code into a C code. This translation has been translated automatically by the MATLAB Code Generator. After small, manual adaptions of this automatically generated C code for a simple execution of the routine by a common C compiler (with support by Marcus Ossiander [2]), the C version of the retrieval algorithm achieves a runtime of 0.47 µs per shot, corresponding to a repetition rate of roughly 2.1 MHz. As a stopwatch for the execution of the C code the CPU time has been used. Additionally, for a cross-check, the single-shot runtime has been determined by measuring the runtime for a few thousand shots through the real-time clock. Both methods delivered comparable results. Executed on a workstation with 18 cores, the runtime is reduced by a factor of 10, showing a good parallelization of the code to many cores, and can thus be further reduced by using large-scaled clusters. A professional, thorough coding of the algorithm in C would certainly decrease the runtime of the routine even further. However, already in the current state with the actual repetition rate of 2 MHz, the algorithm is capable of an application as a smart, online pulse vetoing tool. It constitutes a fast, yet robust and reliable online analysis, able to process the recorded data in real-time not only at every modern XFEL facility currently existing worldwide, but even at the next-generation XFEL facilities such as the European XFEL or LCLS-II [215–217] operating at repetition rates up to a MHz.

[2] Technical University of Munich, Chair for Laser- and X-ray physics

Capabilities of the Integration Pulse Characterization Algorithm via Angular Streaking

For single-shot measurements at the future high-repetition rate FELs in the kHz or even MHz range such as the European XFEL in Hamburg, Germany and LCLS-II in CA, USA, there is an urgent need for a smart veto logic for data reduction by a fraction of up to 10^{-3}. The angular streaking concept is readily scalable to the higher repetition rates of these new-generation XFEL facilities. Thus, only recording data when a few-femtosecond or even attosecond X-ray pulse with desired pulse shape and duration is detected, the high repetition rate compensates this shot selection, whereas the sorting simultaneously alleviates the need for full-rate detector and data systems. With exact profiling of SASE pulses available during ongoing measurements, the resolution of few-femtosecond X-ray imaging experiments can be further, substantially improved by incorporating the X-ray substructure intensity distribution into the analysis process. Single-shot knowledge of the separation and the single-peak pulse duration of X-ray double pulses also paves the way for high-repetition rate X-ray pump/ X-ray probe experiments.

Chapter 5

Design of a Novel Beamline for Attosecond Spectroscopy

The successful performance of attosecond streaking spectroscopy experiments imposes exceptional and most stringent requirements on the employed laser pulses, the experimental facilities and the laboratory environment. Especially the beam parameters of the involved laser pulses, such as beam power, wavelength, phase, bandwidth, pulse duration and pointing stability are crucial for measurements on the attosecond time-scale and must be adjusted as precisely as possible or must be carried to extremes. Within the frame of this thesis, funding, design and commissioning of a novel, fully functional and versatile attosecond metrology beamline have been achieved at the *Chair of Laser- and X-ray physics (E11)* in close and distinguished teamwork with my great colleagues Martin Wagner, Andreas Duensing, Michael Mittermair and Markus Wurzer, as the entire project is out of range of a single person. In the following, the basic conception of the laboratories and the commercial laser system, providing ultrashort laser pulses as a starting point for the beamline, are introduced. Furthermore, a custom-built hollow-core fiber (HCF) pulse compressor and the subsequent vacuum setup for high harmonic generation and characterization are explained. Eventually, the self-designed ultra-high vacuum (UHV) experimental end station including an XUV/NIR double-mirror assembly, especially developed for attosecond streaking experiments in the gaseous phase, is introduced. Finally, pulse characterization measurements, concerning ultra-short NIR and isolated attosecond XUV pulses, are presented as an evaluation and proof of operation of the beamline specifications. This chapter is similarly presented in the dissertation of Martin Wagner [87], as both of us have been working together on this project with equal contributions.

5.1 Beamline Conception

For the setup of the new, state-of-the-art attosecond beamline, three derelict and vacant, but particularly suitable laboratories, arranged in a row (~ 45 m^2 each), at the *Chair of Laser- and X-ray physics (E11)* have been provided. First, a complete renovation of the laboratories had to be conducted in cooperation with the *Staatliches Bauamt München* and several specialist firms. Besides new electrical installation and cooling water systems dimensioned for a state-of-the-art laser laboratory, particularly the wall breakthroughs for

the future laser beam transport between the laboratories, the dimensioning of a new high-precision air conditioning system and adequate cleanroom air locks had to be planned and implemented. The central room has been destined for the laser laboratory, the two outer ones as experimental laboratories, so the laser system can serve both laboratories alternately, depending on the beamline schedule.
The air conditioning system in the laser laboratory provides the essential high-precision stabilization of the room temperature to 22.0 ± 0.5 °C and a humidity of maximal 40%, which is crucial for a stable operation of the laser system. In the experimental laboratories, the temperature is stabilized to 22 ± 1 °C. Access to the central laser laboratory is only possible via the two outer experimental laboratories and cleanroom air locks installed at their entrances. This ensures maximal undisturbed laser operation under preferably dust-free and highly stable climate conditions, which is crucial for the extremely sensitive laser system.

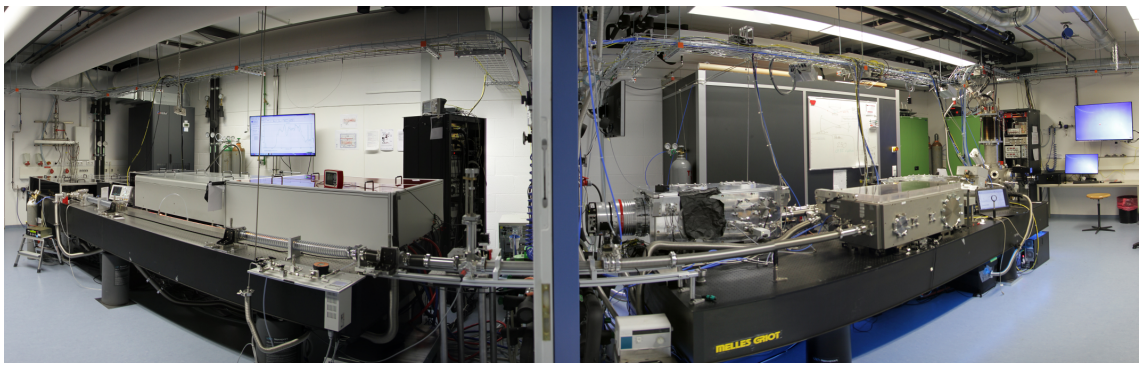

Figure 5.1: Panorama view of the entire beamline AS101. The laboratory on the left hosts the commercial front-end laser system (in the back) and the double-differentially pumped hollow-core fiber for spectral pulse broadening (in the front). The experimental laboratory on the right contains the various vacuum chambers for pulse compression, high harmonic generation and characterization as well as the experimental UHV endstation (in the back). The black air lock is also visible in the back.

In the following, the setup of the laser system and only one of the two beamlines (*AS101 beamline*) are described, as the setup of the second beamline has been another project within our working group. In the period after the renovation and prior to the laser installation, the concrete planning and construction for the future beamline, as extensive as possible without a laser system, especially concerning the HCF pulse compressor and the vacuum beamline. The front-end laser system has been installed in September 2015. After a commissioning phase of the laser system, an on-the-fly completion of the newly-designed, double-differentially pumped HCF pulse compressor and the first high harmonic generation, the very first attosecond streaking measurements on liquid water have been successfully performed even within less than a year in August 2016 [87]. A photography of the entire AS101 beamline is shown in figure 5.1.

5.2 Chirped Pulse Amplification Laser System

The front-end laser system of the newly-designed attosecond beamline is a commercial master oscillator power amplifier (MOPA) system, comprising a FEMTOSOURCE™

rainbow^{TM} oscillator and a FEMTOPOWER^{TM} HEHR CEP4 amplifier manufactured by the former Austrian *Femtolaser Produktions GmbH*. The output specifications of the entire system are given in table 5.1.

Output power	P_0	10.0 W – 12.3 W
Pulse energy	E_{pulse}	2.5 mJ – 3.1 mJ
Pulse duration	τ_0	23 fs
Central wavelength	λ_0	789 nm
Spectral width	$\Delta\lambda$	62 nm
Pulse repetition rate	f_{rep}	4 kHz
Pulse-to-pulse stability	rms	0.5%
CE-phase stability	$\Delta\varphi_{CE}$	< 200 mrad

Table 5.1: Output specifications of the MOPA front-end laser system.

The oscillator is a mirror-dispersion-controlled, Kerr-lens mode-locked Ti:Sapphire (Ti:Sa) oscillator generating sub-7 fs, bandwidth-limited pulses with outstanding stability and reproducibility at a repetition rate of 75 MHz. The basic principle of a Ti:Sa oscillator is based on the control of the broadband intra-cavity group-delay-dispersion (GDD) with negatively chirped dispersive mirrors in combination with a thin titanium-doped sapphire crystal [218, 219]. The pump source of the Ti:Sa crystal is a *Lighthouse Photonics Sprout-D*, a frequency-doubled, diode-pumped Nd:YVO_4 continuous-wave laser with an output power of 3.5 W at a wavelength of 532 nm. The output power of the oscillator and the subsequent CEP4 module amounts up to 100 mW corresponding to a pulse energy of 1.4 nJ.

Since their pulse energy is too weak for high harmonic generation by five orders of magnitude, the oscillator output pulses are seeded into an amplifier for further enhancement. The FEMTOPOWER^{TM} HEHR CEP4 is a two-level multi-pass Ti:Sa amplifier, consisting of a preamplifier and a subsequent booster stage, where a modified version of the *chirped-pulse-amplification* is applied [220–222]. Hereby, the input pulses from the oscillator are temporally stretched in a dispersive stretcher (Brewster-angled glass blocks) before entering the preamplifier by passing a suitable amount of optical glass, which results in lower peak intensities. Otherwise, the high peak intensity of the short pulses would seriously damage the amplifier crystal during the amplification process. The pulses are then amplified (up to approx. 1.2 mJ) by nine passes through the gain medium, a Ti:Sa crystal that is cooled down to 180 K and mounted in a vacuum chamber at 0.1 mbar. The crystal is pumped by a 4-kHz repetition rate, Q-switched, frequency-doubled 10 mJ Nd:YLF laser (*Photonics Industries Inc. DM-30-527*). After the first four passes, a Pockels cell combined with two crossed polarizers reduces the repetition rate from 75 MHz to 4 kHz by the selection of a single pulse with the highest amplification from the MHz-pulse train. The selected pulse will be further amplified in the subsequent five passes. After the Pockels cell, the beam passes an acousto-optical, programmable dispersive filter (*Fastlite DAZZLER*). This device facilitates the pre-compensation for second, third and fourth order dispersion of all dispersive elements in the setup until the entrance of the hollow-core fiber

(in combination with a grating compressor after the amplifier) and to shape the spectral amplitude, which reduces gain-narrowing [107, 108]. After the pre-amplifier, the pulses are further amplified to about 4 mJ by a double pass through the booster stage of the amplifier. The booster crystal is pumped by a Q-switched, frequency-doubled 16 mJ Nd:YLF laser (*Photonics Industries Inc. DM-60-527*). Owing to the high pulse energy of the laser pulses, the Ti:Sa crystal is cooled down to 110 K and is mounted in a vacuum chamber at 10^{-7} mbar. After the booster, the picosecond pulses are guided into a grating compressor, comprising two transmission gratings, for compensation of the stretcher-induced chirp and thus a re-compression to the femtosecond range [98]. An overview photography of the laser laboratory is presented in figure A.3 in the appendix.

The CE-phase of the pulses provided by the front-end laser system is stabilized to at least $\Delta\varphi_{\mathrm{CE}} < 200$ mrad after the hollow-core fiber pulse compressor. In a first step, the CE-phase of the output pulses of the oscillator is stabilized by the CEP4$^{\mathrm{TM}}$ SEED module [223]. According to a 0-to-f scheme, the *carrier envelope offset frequency* (f_{CEO}) is measured and then subtracted from every single comb line by the usage of an acousto-optical frequency shifter (AOFS) in order to balance short-time deviations [224]. Thus, the CEO-frequency is set to zero, resulting in a constant CE-phase of the output pulses [225]. Additionally, a compensation of slower but larger variations over a long time is achieved through a slow feedback loop of the CEP4 module via control of the oscillator crystal temperature in the range of a few Kelvin or via moving glass wedges inside the oscillator cavity [223].

5.3 Hollow-core Fiber Pulse Compressor

After the front-end laser system, the laser pulses (central wavelength 790 nm, 23 fs pulse duration, roughly 60 nm bandwidth) are stabilized and focused to the entrance of the hollow-core fiber (HCF). By propagating through the HCF filled with a noble gas (He or Ne), the pulses are then spectrally broadened via self-phase modulation in order to get temporally compressed to pulse durations of approximately 3 fs afterwards according to the time-bandwidth product (see eq. 2.19).

5.3.1 Conjugated Gradient Hollow-core Fiber

As already mentioned in section 2.2.3, regarding the maximization of the self-broadening effect, the most important specifications of the waveguiding HCF are its inner diameter and its length as well as the refractive index of the nonlinear medium, hence the used gas type and gas pressure. The following sections describing the in-house developed hollow-core fiber pulse compressor are adapted from the respective sections in [98].

According to formula 2.31 a minimum inner diameter of the HCF, geared to the output pulse parameters of the laser system, is determined to d_{He} = 378 µm for helium gas and d_{He} = 431 µm for neon gas. Enabling operationality for both gas types and allowing for deviations of the laser beam from a perfect TEM_{00}-mode, the core diameter of the HCF

amounts to 500 µm. The maximum length of the HCF is limited by the length of the laser table (4.8 m). Moreover, one needs a part of this distance for the beam focusing. As the spot size is rapidly decreasing between the focusing mirror and the fiber entrance, the entrance window of the vacuum pipe hosting the HCF, as well as the last folding mirror in front of the entrance window must be as far as possible away from the fiber entrance. Otherwise, both components are quickly damaged owing to the high intensities. As a compromise, the fiber has a total length of 3.0 m and is split up into two fused silica glass capillaries of 1.5 m length each, with an outer and inner diameter of 500 µm and 2 mm, respectively. The entrance window is positioned 1.35 m and the last folding mirror 1.45 m before the fiber entrance [98].

For the application in the novel beamline, a double-differentially pumped HCF design utilizing the conjugate-gradient pressure method has been selected [226–228] instead of a statically filled HCF setup [113, 117, 123]. In the static HCF case, the HCF would be mounted within a vacuum pipe, filled with noble gas up to a specific, constant pressure and closed by two windows. Unfortunately, the high-intensity laser beam undergoes nonlinear propagation effects causing deterioration of the spatial and temporal profile especially at the two fiber ends and hence, inferior coupling efficiency and beam power throughput [98]. In our case of a double-differentially pumped HCF design, the gas is inserted in the middle of the fiber with a pressure $p_{\max} \approx 2$ bar –3 bar at the connection between the two 1.5m-capillaries and is pumped down to a pressure $p_{\min}$ of a few millibar both ends of the fiber. Thus, a pressure gradient, symmetrically decreasing to the fiber ends from a maximum pressure at the gas inlet is induced [87, 98]. Therefore, despite an increased supply intensity this low pressure at the fiber ends eliminates most of the degrading effects mentioned before.

The HCF setup is a distinctly modified and improved redesign of a conjugated-gradient HCF compressor setup existing at the *Max-Planck-Institute of Quantum Optics* in Garching [229]. Besides its increased length and a variety of sophisticated, redesigned details at the setup, the major difference is, that the HCF is entirely integrated into the subsequent high-vacuum beamline and has hence no output window.

Laser Beam Focusing and Stabilization

For achieving an ideal fiber incoupling, as well as transmission and broadening of the pulse along the fiber, the focus size at the fiber entrance must be finely adjusted to an appropriate value and actively stabilized to prevent damages at the fiber entrance and to preserve an optimum throughput. Geared to the core diameter of the fiber, the focus diameter is set to $2w = 0.65 \cdot 500$ µm = 325 µm (according to equations 2.31 and 2.33) for avoiding plasma effects or a beam breakdown for both applied gas types and for ensuring an optimal incoupling of the beam into the fiber. The beam focusing is realized by reflective focusing by the use of a concave curved mirror with a radius of curvature of 5 meters. Thus, a beam focus size at the fiber entrance of $d = 335$ µm being close to the calculated

value of 325 µm is achieved. The focus position along the beam path is finely adjusted by moving the focusing mirror, mounted on a linear translation stage, in the beam axis [98].

The beam path from the stabilized incoupling into the amplifier in the front-end laser system to the fiber entrance has a length of roughly 20 meters. Consequently, thermal fluctuations or drifts, air turbulences and other disturbances induce beam fluctuations and pointing drifts that must be actively compensated to guarantee a stable and ideal incoupling at the HCF entrance. The high-precision air conditioning system and a complete enclosure of the beam path on the laser table already reduce air turbulences. Moreover, for a maximum suppression of any pointing fluctuations, an advanced beam stabilization system, comprising of two motorized mirror mounts and two position-sensitive detectors (PSD), is implemented. One detector each is positioned in the collimated beam and in the beam focus (in a secondary beam path after a beam splitter). Both mirror mounts are equipped with servo motors for large movements and piezo actuators for fast and precise compensation. The *Aligna* 4D-stabilization system produced by the *TEM Messtechnik GmbH* separately and simultaneously corrects for spatial as well as angular displacements applying a complex software-based learning algorithm [87, 109].

Hollow-core Fiber Vacuum Setup

The 0.5-mm thin fused silica, Brewster entrance window is located about 1.4 meters in front of the fiber entrance to minimize high beam intensities and thus damage in the window and to ensure a vacuum beam path until the fiber entrance avoiding self-phase modulation in air prior to the fiber. Nonetheless, within a few days of laser operation dark spots evolved on the window that caused an unacceptable performance loss of the HCF at the beginning. Since carbon atoms in the window are assumed to be the core of the problem, an oxygen plasma treatment has been successfully implemented. A tiny oxygen flow with a partial pressure of about 10^{-1} mbar is installed on the vacuum-side of the window to provide a reaction agent to the carbon atoms for a synthesis of gaseous carbon oxide which can be easily pumped down. Hence, no more damage of the entrance window has occurred after this sophisticated modification, which is explained in more detail in [98].

As already mentioned before, the two fused silica glass capillaries (1.5-m long each, 2 mm outer diameter) must not be curved at all to ensure efficient fiber operation. Thus, the capillaries rest on a V-shaped groove milled on the top of a flexural rigid support bar (3000 mm x 30 mm x 15 mm) made from high-grade stainless steel [98, 109]. This support bar with the fiber on top is mounted on just two points, close to the so-called *Bessel points*. This ensures a minimum bending according to the Euler-Bernoulli bar theory. The vacuum pipe of the Brewster window extends to a 4-way cross at the fiber entrance, where a vibration-decoupled connection to the vacuum pump, a pressure gauge and T-piece with a view port and a flexible, transparent vacuum hose, which extends the vacuum environment until the first fiber support mount, are connected [98, 109]. At the second support mount, another vacuum hose is installed. It re-establishes the vacuum environment around the

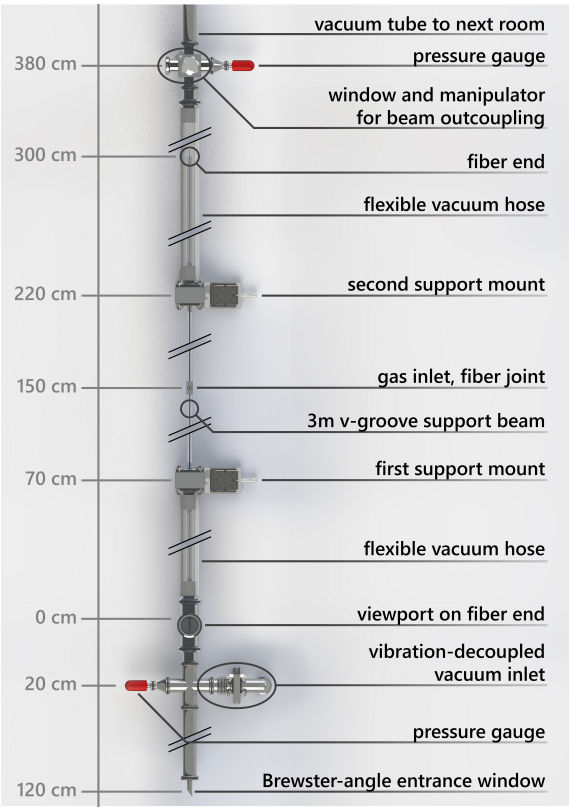

Figure 5.2: Overview sketch of the hollow-core fiber setup. The entire vacuum setup of the hollow-core fiber is illustrated in a top view. On the left side, an indication of distance is given in centimeters. Taken from [109].

HCF and is extended beyond the end of the HCF on the support bar. The sole contact point between the support mounts and the support bar is a recess in the vacuum flange, where the support bar with the fiber rests in and is glued in for a sealed vacuum connection. In between the two mounts, the HCF is freely resting on the support bar and exposed to air. Both fiber support mounts comprise two precise, linear translation stages, by which the mounts can be accurately positioned along the two axes perpendicular to the beam axis. Thus, a precise and straight alignment of the entire HCF construction, thus an optimal fiber performance, are ensured. At the junction of the two capillaries in the middle of the support bar, an especially designed, slide-like, vacuum-sealed gas inlet from stainless steel is glued onto the fiber ends and the support bar. It provides a 6 mm Swagelok$^{\mathrm{TM}}$ connection for the gas lead via a sophisticated feed line system, enabling a precisely adjustable and stable gas pressure [87, 109]. An overview of the HCF setup is depicted in figure 5.2 and a photography of the fiber during operation is shown in figure A.5 in the appendix.

In the rear of the fiber, the second connection to the vacuum is located directly in front of a self-designed skimmer, which is crucial for the reduction of the noble gas flow into the subsequent, differentially pumped high-vacuum beamline. The skimmer is a closed KF40 centering ring with a 3mm-aperture for the laser beam and is adjustable via two perpendicular translation stages. It serves as a pressure barrier and in combination with the vacuum pump. Thus, it ensures high-vacuum conditions in the rest of the beamline by

reducing the pressure in the subsequent vacuum chamber by two orders of magnitude. After the skimmer, the broadened beam can be guided out of the vacuum for a characterization and optimization of the beam parameters. More details on the HCF setup can be found in [98, 109, 230].

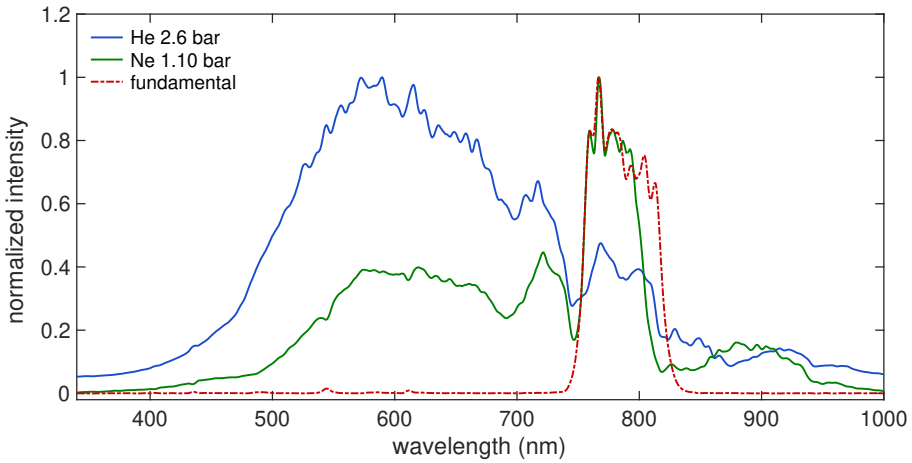

Figure 5.3: Output characterization of the HCF setup. For a comparison of the HCF output for the two input gas types helium and neon, a spectrum of the original input laser pulse (red, dashed line) and the respective output spectra for helium (blue) and neon (green) are depicted. The spectra have been recorded for the case of maximum spectral broadening. All presented spectra are smoothed with a moving-average routine for a better visualization.

The output beam of the HCF setup has been comprehensively characterized in the course of bachelor and master theses [98, 109, 230]. A fundamental spectrum of the incoming laser pulses is presented in figure 5.3, together with typical HCF output spectra at a close-to-maximum spectral broadening for helium and neon gas applied as nonlinear medium. Besides the alignment of the entire HCF via the translation stages at the two support mounts, the main optimization parameter for the magnitude of the spectral broadening is the gas pressure, affecting the refractive index. Depending on the daily performance of the laser system and the HCF alignment, the best results regarding spectral broadening and output intensity are achieved using helium gas at a pressure between 2.3 bar and 2.7 bar at the gas inlet. Neon provides comparable results at a pressure around 1.1 bar, sometimes with a more uniformly distributed broadening effect [230]. Nevertheless, despite the lower gas consumption using neon, helium is preferred due to the considerable better performance results and especially the huge price difference of more than an order of magnitude between the two gas types. The output power of the HCF is nearly constant in the useful pressure range for both gas types, but significantly higher for helium than for neon gas. Around the optimal gas pressure, the transmission amounts to 55% – 60% for helium and to 50% – 55% for neon [230]. Analyzed with an inverse Fourier transform, best performance output spectra of the HCF — supplied with helium — deliver a minimal achievable pulse duration of 2.74 fs after compression, starting from a pulse duration of 22.13 fs of the fundamental [230]. This is slightly smaller than the minimal pulse duration of 2.89 fs actually measured after compression.

5.3.2 Chirped Mirror Pulse Compressor

After the HCF vacuum setup, the broadened beam is guided in vacuum into the high-vacuum pulse compression chamber in the experimental laboratory. An important feature of this compression setup is the fact that the whole pulse compressor is evacuated. This facilitates a single vacuum system from the HCF entrance window to the UHV experimental end station without any need of further material transmission. Thus, no additional chirp is introduced to the pulse and the number of chirped mirrors can be small. The chamber is pumped down by a turbomolecular pump, so with gas load from the HCF in operation, a background pressure of 10^{-4} mbar (10^{-7} mbar without gas load) is achieved. The chamber itself is a standard design developed within our working group and is realized for the two subsequent vacuum chambers as well. The chamber comprises a massive, rectangular frame with a base plate from stainless steel, where four exchangeable side plates from aluminum are vacuum-sealed affixed. The cover plate from Plexiglas can be opened and closed via supporting pneumatic springs. The optical breadboard above the base plate is vibrationally decoupled from the chamber frame for minimizing any vibrations (especially from the turbomolecular pump). The pulse compression chamber with all the relevant components installed inside, which are explained below, and the beam path within the chamber are depicted in figure A.6 in the appendix.

The actual pulse compression is achieved by utilizing two pairs of negatively chirped mirrors in combination with a pair of thin fused silica wedges mounted in the Brewster angle. The spectrally broadened pulses are temporally compressed as good as possible, approaching their Fourier limit. For the HCF output pulses, as shown in figure 5.3 using helium gas, the minimum achievable pulse duration amounts to about 3 fs. The chirped mirrors (*Ultrafast Innovations* classification: PC306) are manufactured for our working group within the *Munich Advanced Photonics* excellence cluster [229]. After four reflections on the chirped mirrors, the beam passes the glass wedges, where one wedge is motorized in order to introduce more or less glass material into the beam. Consequently, the aggregate amount of glass, inducing a positive chirp, can be precisely adjusted, thus the temporal pulse compression can be efficiently fine-tuned. Moreover, by moving the motorized wedge, one can shift the CE-phase of the laser pulses in a controlled manner. For this purpose, one of the reflections from the first wedge is guided out of the vacuum chamber through a small-diameter window to the *Femtolasers CEPset*^{TM} device, a f-to-2f interferometer which measures and controls the CE-phase of the pulses. In the compression and the subsequent high harmonic chamber, a second *Aligna* system is installed. Two mirror mounts in the compression chamber, in combination with two detectors in the HHG chamber, stabilize the focus of the laser beam into the HHG gas target. Consequently, any drifts between the two different laser tables in the two laboratories are compensated and stable conditions for the subsequent generation of attosecond pulses is guaranteed [87].

A stable and controlled CE-phase is crucial for the subsequent HHG process, as the shape of the XUV spectrum strongly depends on it. In addition to the 0-to-f CEP stabilization of the oscillator output pulses (see 5.2), in the CEPset^{TM} module a f-to-2f scheme is applied for the required compensation for long-term drifts of the CE-phase within the amplifier system and the HCF pulse compressor. Here, the incoming beam is focused into a BBO crystal and by overlapping the frequency combs of the fundamental and the second harmonic the actual CEP is determined via a Fast Fourier Transform analysis of the interference fringes [231]. Effective control and stabilization of the CE-phase by the CEPset^{TM} module is obtained via control of the dispersive stretcher just before the preamplifier system. Within the stretcher, a prism on a piezo actuator allows a simple alignment of material and consequently the CE-phase [98]. Therefore, under the assumption that any CE-phase shifts after the wedges are constant, all considerable alteration of material and air fluctuations along the entire beamline after the oscillator causing fluctuations in the CE-phase can be compensated by the CEPset^{TM} module down to a CEP jitter of less than 200 mrad. The CE-phase can be altered to any specific value in the corresponding software, which enables a precisely adjustment of the CEP for an optimization of the HHG output pulses [87].

5.4 Experimental XUV Vacuum Beamline

After the pulse compression, the approximately Fourier-limited, few-cycle pulses have enough peak intensity for an efficient generation of high harmonics. Subsequently, the vacuum setup for the generation and characterization of the high harmonics is introduced. The following sections are adapted from the respective ones in [98], a similar description can be found in [87].

5.4.1 High Harmonic Generation

The CEP-stable, high intense, few-fs pulses propagate via a reflecting mirror in a small vacuum cube into the HHG chamber. This mirror and all other alignment optics in the entire vacuum beamline after the HCF are indispensably motorized by piezo actuators and can be remote controlled via a sophisticated LabVIEW^{TM} environment developed by Michael Mittermair and Christian Schröder. The HHG chamber has larger volume and an aluminum cover plate, but apart from that it is very similar to the compression chamber, see figure A.7 in the appendix. During operation with a high neon gas load, the chamber is evacuated down to about 10^{-4} mbar.

Besides the already mentioned detection layout for the second beam stabilization, a motorized iris for beam alignment and intensity control for the HHG focus as well as a reflective filter, which drastically attenuates the beam for alignment purposes, are installed in the chamber. Dependent on the experiment and the photoelectron detection scheme applied, either an s- or a p-polarization of the laser pulses for the HHG process can be justified by the insertion of a small optical setup (two polarization-rotating periscopes) for

changing the p-polarization of the incoming laser pulses to an s-polarization into the HHG chamber [87]. For the beam focusing into the HHG gas target, a curved mirror ($R = 3$ m) is utilized in a standard configuration. To reach extremely high XUV energies, a mirror with a shorter focusing length can be easily implemented by minor changes to the beam path. The HHG target itself is a small ceramic tube (2 mm inner diameter) with an aperture of 250 µm for the focused NIR beam and the generated XUV radiation. The neon gas flow out through the aperture can be accurately adjusted by a high-precision dosing valve. The target is mounted on a 3D translation stage, which facilitates a precise alignment of the target in relation to the beam focus position. Within the target, the NIR focus (100 µm diameter) reaches an intensity of about $I_p = 1.5 \cdot 10^{15}$ W/cm^2, which is considerable higher than the required threshold (10^{13} W/cm^2) for the generation of attosecond XUV bursts via the three-step model (see section 2.2.3) [87], as mentioned before. The HHG chamber with all the relevant components installed inside is depicted in figure A.7 in the appendix.

Despite the maximum operating pressure of $1{\cdot}10^{-3}$ mbar in the HHG chamber, it is essential to prevent neon gas from flooding into the subsequent UHV part of the beamline, otherwise the XUV beam quality would drastically decrease. Thus, a skimmer, a conically shaped tube with an aperture of 1.5 mm, is positioned in front of the vacuum connection to the subsequent beam diagnostics chamber and reduces the pressure by up to four orders of magnitude [87, 232]. The HHG chamber can be hermetically sealed off by two gate valves (with a central window for rough alignment) in the beam path on both sides of the chamber.

5.4.2 XUV Diagnostics Chamber

The generated high harmonic XUV radiation, propagating collinearly with the NIR beam, can be spectrally studied and optimized by using the self-designed, in vacuo XUV spectrometer installed in the XUV diagnostics chamber. The chamber itself is a smaller and adapted version of the HHG chamber design. It is pumped down to a pressure of just below 10^{-7} mbar. The diagnostics chamber with all the relevant components installed inside, which are explained below, and the beam path within the chamber are depicted in figure A.8.

A gold mirror in grazing incidence geometry can be moved into to beam path to deflect the beam with a maximum XUV intensity towards an aberration-corrected, blazed, concave grating. The grating spatially separates the various wavelengths and focuses the light onto a Peltier-cooled, back-illuminated charge-coupled device (CCD) camera (*Princeton Instruments PIXIS-XO:400B*) to detect an XUV spectrum of the HHG radiation [87, 98]. In front of the grating, two remote-controlled filter wheels are positioned, so zirconium high pass filters of different thickness (300 nm and 500 nm) can be moved into the beam to reduce XUV intensity and to block any fundamental NIR intensity for preventing any damage of the sensible CCD. Additionally, a silicon and an aluminum filter are mounted in the filter wheels for an energy calibration of the spectra, since they

provide sharp absorption edges at 72 eV (Al) and 100 eV (Si) [233, 234]. Three exemplary HHG spectra, optimized for three different cutoff photon energies E_c, are presented in figure 5.4.

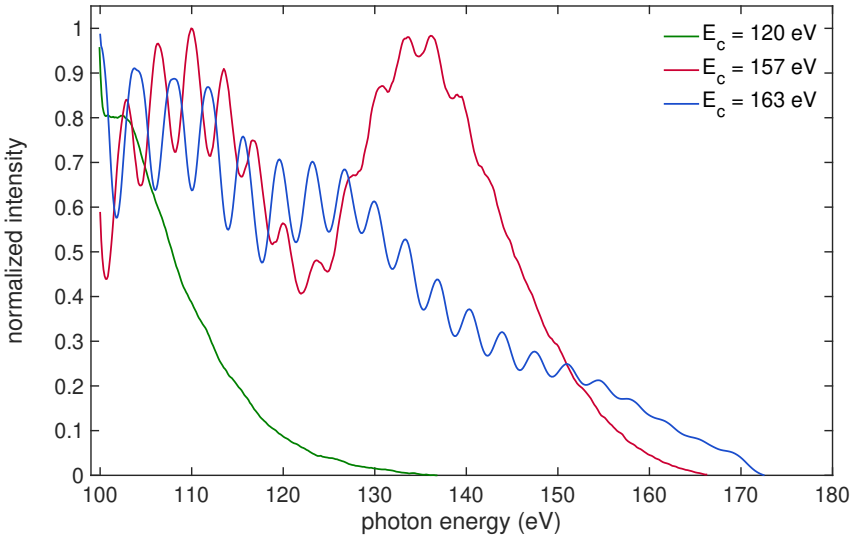

Figure 5.4: Calibrated high harmonic spectra measured with the XUV spectrometer in the diagnostics chamber. Three different, calibrated HHG spectra with three distinct XUV cutoff energies E_c (defined as the 10% threshold) are presented. The high harmonic generation is optimized to receive an XUV spectrum with a moderate XUV cutoff energy of E_c = 120 eV (green) and two spectra with considerable higher cutoff energies of E_c = 157 eV (red) and E_c = 163 eV (blue). Filter transmission and absorption of silicon in the CCD chip must be considered for further analysis of the HHG spectra. The modulated part and the almost flat cutoff region in the spectra are good distinguishable, especially for the spectrum with E_c = 155 eV. Adapted from [87].

Furthermore, a motorized iris, mounted on a 2D translation stage perpendicular to the beam axis, is installed in the diagnostics chamber to adjust the NIR intensity in the experimental end station. Eventually, an XUV filter doublet (ZR and Mo) can be inserted into the beam path to block the NIR beam while guiding the beams onto a multi-channel plate (MCP) mounted at the backside of the experimental chamber (see section 5.5.2). Utilizing the MCP, the XUV beam profile and intensity can be optimized [87].

For attosecond streaking experiments a spatial separation of the XUV and the NIR beams is stringently necessary. For this purpose, a self-designed, home-built wire grid is employed: It comprises a tiny zirconium filter (d = 3 mm) glued in between two extremely thin, hollow copper rings (ring thickness: 1 mm), that is centered in a hollow aluminum ring of d = 30 mm by the help of thin tungsten wires. Thus, the NIR contribution is blocked in the center part of the collinearly propagating beams. The wire grid is mounted in a separate vacuum cube that is installed in between the diagnostics chamber and the experimental chamber, at the end of laser table, so that the distance between the NIR focus at the target and the wire grid is maximized for avoiding filter damage due to high NIR intensities. The vacuum cube can be precisely positioned to the laser beam in the horizontal axis and the wire grid can be aligned to the beam in vertical axis by a linear manipulator.

5.5 Attosecond Metrology End Station

The experimental UHV end station of the AS101 beamline mainly comprises a big vacuum chamber, an electron time-of-flight spectrometer, the central double-mirror assembly and a sample manipulator with a gas lead system. Originally, the end station has been designed for streaking spectroscopy on gaseous iodine compounds [31, 235], but has been successfully employed for various attosecond metrology experiments on amorphous, solid-state samples, too. Furthermore, the end station has been utilized for the recently published time-dependent study on ionization dynamics in krypton via combined, simultaneous ion spectroscopy and transient absorption spectroscopy measurements [236]. The experimental UHV chamber and the double-mirror assembly have been designed and commissioned by Alexander Späh [232], a former master student under my and Martin Wagner's supervision, and are briefly introduced in this section. An overview sketch of the whole vacuum beamline is presented in figure 5.5 and a photography of the entire experimental laboratory is shown in figure A.4 in the appendix.

As an alternative experimental end station, a vacuum setup especially designed for attosecond streaking spectroscopy experiments on liquid targets can be adapted to the AS101 beamline, as presented in chapter 6.

5.5.1 Double Mirror Assembly

A state-of-the-art common-path interferometer embodies the main component in the experimental end station. It is employed for introducing a time delay between the co-propagating but spatially separated NIR and XUV laser pulses, which is required for streaking spectroscopy. Centerpiece of the double-mirror assembly is the double-mirror delay unit. The double-mirror itself comprises an outer, annular silver-coated mirror with an outer diameter of $d = 25.4$ mm, which reflects the NIR light, and an inner, multilayer XUV mirror ($d = 3$ mm) that fits into the circular recess of the outer mirror. Both beams are focused by their respective mirrors with a focal length of $f = 125$ mm onto the same spot on the target. The specially designed bandpass-like reflection properties (Gaussian-like reflection curve) of the XUV mirror define central energy, temporal shape and duration of the reflected, isolated XUV attosecond pulse. Any specific delay between the XUV and the NIR pulses can be precisely set by moving the XUV mirror along the beam path axis via a closed-loop, piezo nano-positioning device, where the inner mirror is mounted on, with a minimum delay step size of converted 2.6 as [87, 232].

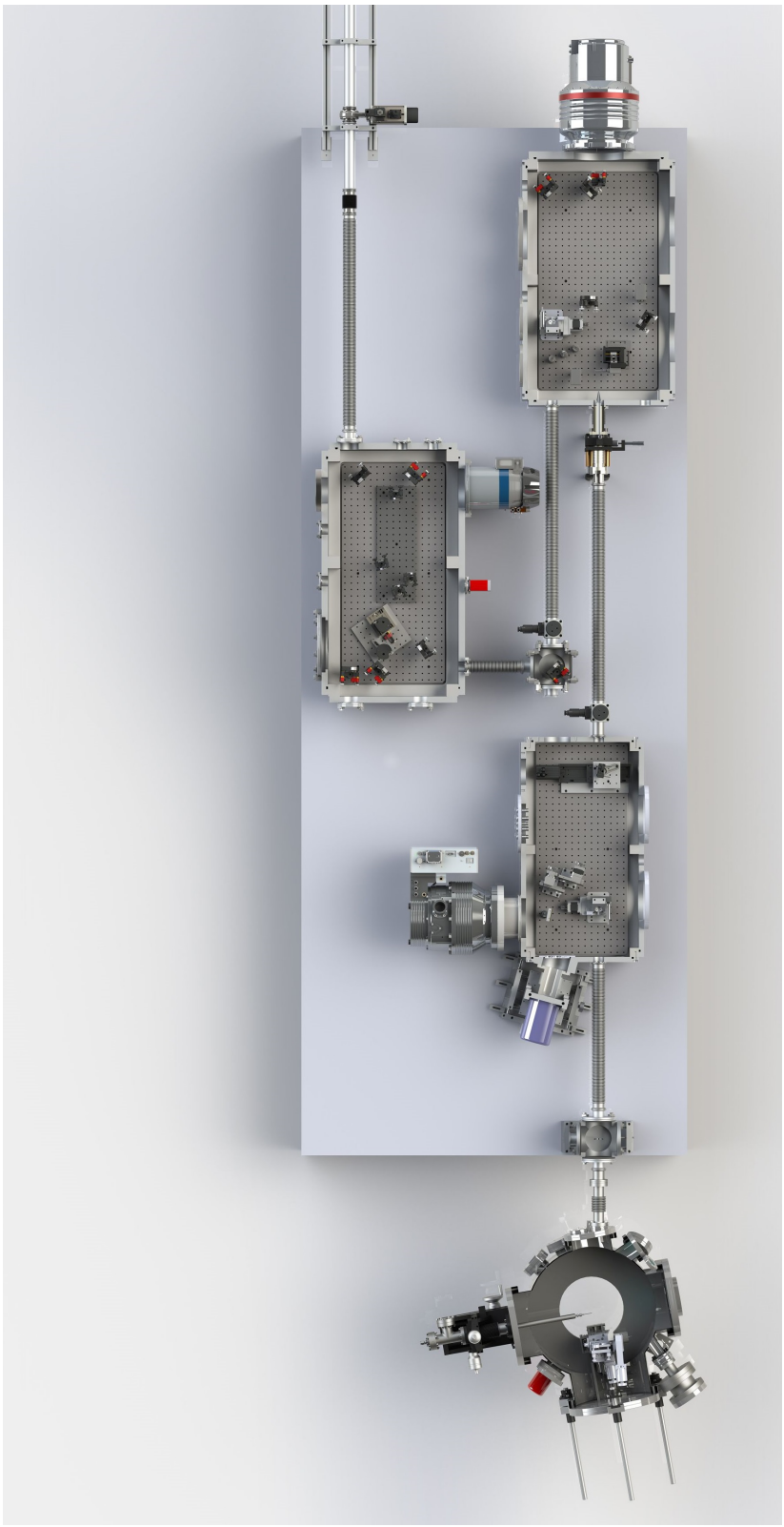

Figure 5.5: Overview of the AS101 beamline. The entire vacuum beamline AS101 in the experimental laboratory is illustrated by a detailed, comprehensive CAD model. In the depiction, the laser beam, coming out of the hollow-core fiber in the laser laboratory, enters the laboratory from the top through a wall breakthrough. Pulse compression chamber, HHG chamber and diagnostics chamber, as well as the experimental end station are clearly visible. Credit: Andreas Duensing, Technical University of Munich, Chair for Laser- and X-ray physics.

The outer mirror is mounted in an especially designed motorized UHV mirror mount. A separate adjustment of the outer mirror (NIR pointing) relative to the pointing of the inner XUV mirror, which is required for a precise spatial overlap of the focused NIR and XUV beams on the target, is enabled through three linear piezo actuators in the mirror mount. The pointing of the two mirrors together can be adjusted by a stack of various motorized rotation and translation stages via remote-control. Two linear translation stages with a total travel range of $\pm$ 25 mm and a precision of 0.2 µm facilitate a two-dimensional positioning of the double mirror-mount, along the beam axis and in the horizontal axis perpendicular to the beam path. Two gimbaled rotation stages enable a tilt of the double-mirror mount along the vertical and the horizontal axis with a total range of $\pm$ 15° and a precision of 0.004°. Due to the gimbal mounting of the two stages, the double mirror is centered to the Pivot point of the construction [232]. The entire double-mirror assembly with a total height of 21 cm is shown in figure 5.6. A vertical alignment of the double-mirror is achieved via the height adjustment of the whole experimental chamber.

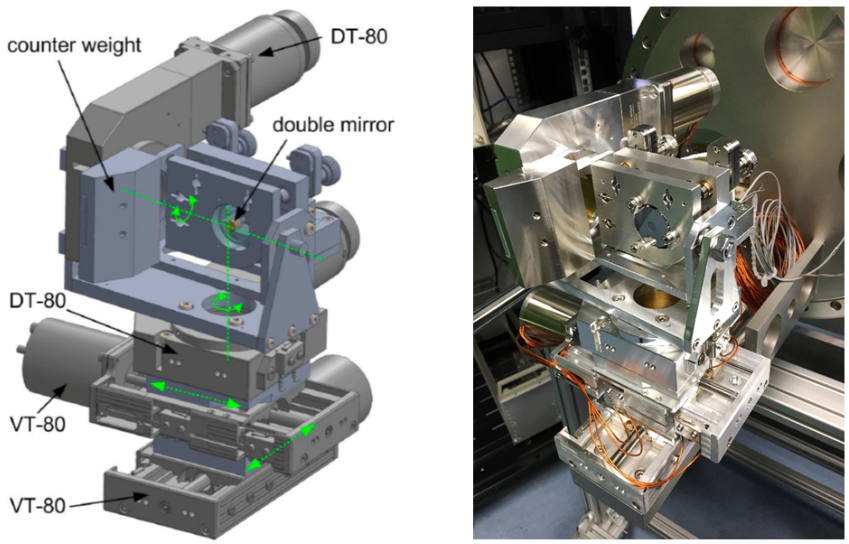

Figure 5.6: XUV/NIR double-mirror assembly. Left: Labeled technical drawing of the double-mirror mount and the stack of motorized translation and rotation stages (two axes each, marked in green) below, taken from [232]. A counter weight is required for minimizing any torque exerted on the upper rotation stage. Right: Photography of the assembly with the double-mirror mount on top, connected to its supporting flange [87].

5.5.2 Experimental Chamber

The experimental UHV vacuum chamber specially designed for attosecond streaking experiments on gas-phase targets is built of a big cylindrical tube from stainless steel with a length of 400 mm and a diameter of 500 mm and reaches UHV conditions up to 10^{-9} mbar. The chamber is equipped with 24 CF flanges of various size hosting various components, such as XUV/NIR double mirror assembly, TOF spectrometer, gas target manipulator, turbo pump, MCP detector, beam diagnostic CCD cameras, deflection mirrors, gate valves, feedthroughs, pressure gauges, view ports and laser beam entrance and exit [232].

An overview of the geometry of the setup inside the experiment chamber is illustrated by a top view in figure 5.7 for a streaking experiment with p-polarized laser beams, with the spectrometer mounted on a CF205 flange in horizontal orientation. The large-angle, anode-segmented electron time-of-flight spectrometer, which is implemented in the experimental chamber, has been designed and built by Andreas Kim and is described in details in his thesis [237]. For streaking measurements using s-polarized beams, the spectrometer can be mounted to the equally-sized flange on the top of the chamber (vertical orientation). Further details on the individual components of the chamber can be found in [232].

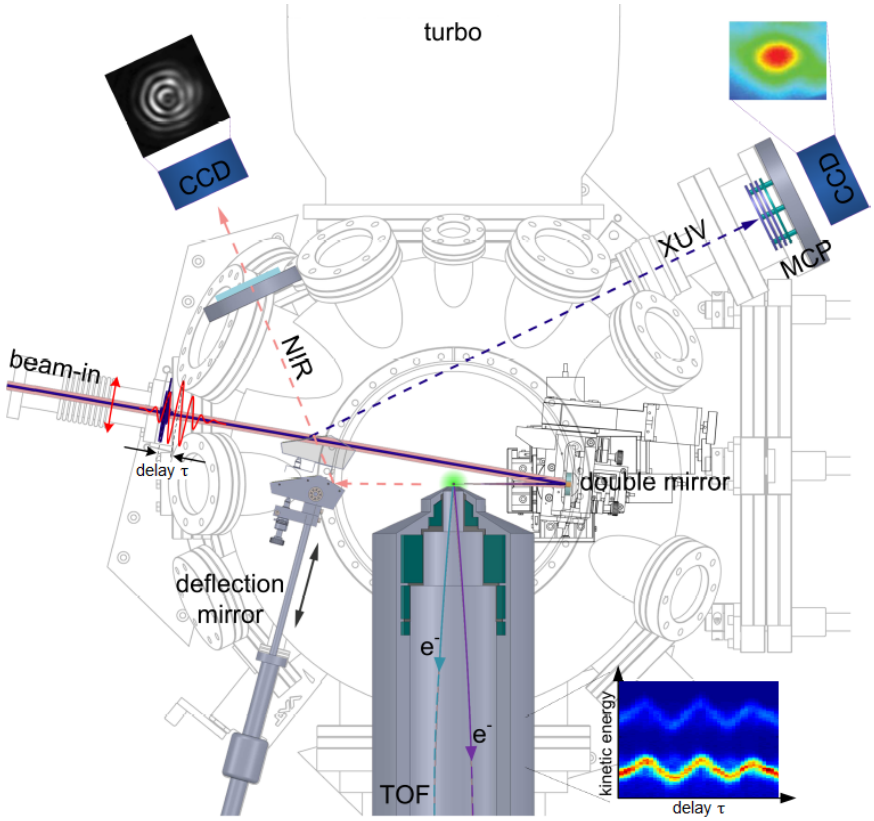

Figure 5.7: Top view sketch of the experimental chamber with its main attached components and a depiction of the beam path within the chamber. The co-propagating XUV (blue) and NIR (red, p-polarized) pulses enter the chamber from the left and impinge the double-mirror under an angle of incidence of 5°. The relative delay between the two spatially separated beams is precisely adjusted by the double-mirror delay unit, that focuses both beams directly into the gas target (green) directly in front of the aperture of the TOF spectrometer. An exemplary streaking trace, recorded with the spectrometer during an XUV/NIR delay scan, is shown in the inset (bottom right corner). Furthermore, a moveable deflection mirror is installed, which guides the XUV beam onto the MCP detector for XUV mode characterization. On the same manipulator, a second mirror is mounted, that sends the NIR beam through a vacuum window out of the chamber and to a CCD beam profiler for an adjustment of spatial and temporal overlap of light reflected from both parts of the double-mirror. Adapted from [232].

5.5.3 Characterization of the Beamline Output Pulses

The novel attosecond metrology beamline shall be conclusively characterized by the provided output laser pulses generated. Its capabilities of generating few-cycle, CE-stable, high-power NIR laser pulses and isolated XUV attosecond pulses can be approved by an exemplary gas phase streaking measurement in neon and a subsequent attosecond pulse reconstruction, see [87]. The excitation of the neon 2p photoline by an XUV photon energy of E_{XUV} = 125 eV (bandwidth ΔE = 5 eV) generates photoelectrons with a kinetic energy of about 103 eV. A common LSPGA pulse retrieval algorithm has been applied and successfully delivers reliable results [87]. The bandwidth limit calculated from the XUV mirror reflection curve provides an XUV pulse duration of 360 as, whereas the retrieval delivers a duration of 230 as. The electric field of the few-cycle NIR pulse is well reconstructed and its duration is determined to 2.9 fs (FWHM), which matches perfectly with the Fourier limit of the HCF output pulses (see section 5.3.1) [87]. Summarized, the capabilities of the novel AS101 beamline are impressively corroborated by these pulse parameters as well as by the first attosecond streaking spectroscopy experiments on liquid water, as shortly presented in the following chapter.

Chapter 6

Attosecond Metrology in Liquid H_2O

The first attosecond metrology experiments at the newly designed and commissioned attosecond beamline have been performed only a few weeks after the first generation and characterization of XUV radiation via HHG, within the frame of a collaboration with the group of Prof. Hans Jakob Wörner from the ETH Zurich. The objective of the collaboration is the first-time application of attosecond streaking spectroscopy on a liquid-phase sample, which has not yet been reported before. Liquid H_2O had been chosen as the first sample, since it is the most prominent and interesting liquid existing at all.
Acting as a solvent in many biological and chemical reactions it plays an essential role for almost all life processes on earth [34]. The origin of many of its extraordinary physical and chemical properties is the famous intermolecular network of hydrogen bonding (H-bonding). Albeit H-bonding is extremely important, as it highly influences chemical processes and governs solvation of ionic and neutral species, it is still insufficiently understood [238] and plenty open questions remain, e.g. how H-bonding influences the electronic structure in H_2O. Thus, the water molecule and H-bonding are subject to intensive and persistent study and a consistent model for the description of the H-bonding network is of great interest. The dynamical and structural characteristics of water have been investigated for over a century [239–249], but up to today the electronic structure and dynamics in liquid water on the molecular level are rudimentary understood [35, 250]. The H-bonding network experiences complex structural changes on ultrashort time periods, hence raising the complexity in structures and properties [251–260].

For the experiments, which have been performed at the presented beamline in Garching, an experimental chamber, specially developed and designed for the handling of liquid samples within a high-vacuum environment [33, 261], has been brought from the ETH Zurich and adapted to the beamline. For achieving time-resolved attosecond spectroscopy in the liquid phase, the exposure of a liquid-phase sample to attosecond XUV pulses in a high-vacuum vicinity is a crucial, experimental premise. This challenge is solved by the liquid-microjet technique introduced by Manfred Faubel in 1997 [262]. It has been successfully applied for static photoelectron spectroscopy [35], X-ray absorption and X-ray emission spectroscopy of liquids and solvated species [263]. Such a liquid microjet constitutes the centerpiece of the experimental setup shipped from Zurich to Garching. The very first exploitable streaking spectrograms acquired have been recorded only a few days after the start-up of the project. These measurements also represented the streaking

premiere of the newly commissioned attosecond beamline AS101 and give proof of its operational readiness and capabilities providing few-cycle NIR laser pulses and isolated attosecond pulses in the XUV-range.

In this chapter, a short introduction on the studied sample, the experimental setup applied for the measurements and the experimental procedure shall be given. Detailed information on the photoemission from liquid water can be found in the thesis of Martin Wagner [87] or in more specific publications [35, 211, 262, 264, 265]. The applied experimental apparatus is comprehensively explained by Inga Jordan [33, 266]. Moreover, the unprecedented results of this beamtime, the retrieved attosecond delays between two specific electron states of the water molecule and a preliminary theoretical interpretation, are shortly presented in the following. A detailed elaboration on the whole topic is presented as the centerpiece in the dissertation of my colleague Martin Wagner [87], whereas here only a concise summary is given.

6.1 Photoemission and Electronic Structure of Liquid Water

The electronic as well as geometric characteristics of the H_2O molecule are highly interesting and important for the scientific understanding of the fundamental structure of its condensed, liquid aggregate state and the interaction with solvated species [35]. The local electronic structure of liquid H_2O has been investigated by emission spectroscopy and X-ray absorption experiments as well as theoretically studied utilizing complex numerical simulations and molecular modelling techniques [35, 263, 267].

Generally, the usage of liquid samples exhibiting high vapor pressures of typically 1 mbar – 30 mbar in a high-vacuum environment, which is indispensable for photoelectron spectroscopy, issues a huge challenge. The application of the liquid-microjet technique [262, 268], in combination with XUV synchrotron radiation used for photoionization, enables photoelectron spectroscopy on liquid targets and hence, investigations on the inner-shell and valence electronic features of liquid H_2O [264]. Prior to time-resolved experiments, the photoemission from liquid water is examined. Photoemission (PE) from a liquid virtually intertwines aspects from gas-phase and solid-state photoemission. Suitable PE spectra have been recorded with an energy resolution of roughly 100 meV at the MBI-BESSY undulator beamline utilizing highly brilliant synchrotron radiation at excitation energies from 60 eV up to 120 eV [264]. Basically, owing to a continuous vaporization from the liquid surface in the high-vacuum vicinity, the recorded spectra of the liquid target throughout comprise contributions from the gaseous phase surrounding the liquid surface in vacuum. Such a combined photoemission spectrum is displayed in figure 6.1 at the top, along with a separately recorded spectrum of purely gaseous water. For obtaining precise values for the binding energies of the respective orbitals in liquid water, contributions from the liquid and the gaseous phase must be distinguishable. Eventually, by a subtraction of the two upper traces from each other, an appropriate difference spectrum, separating the

contribution of gas- and liquid-phase water, is depicted at the bottom in figure 6.1 and reveals solely the contribution of liquid-phase H_2O. The liquid-phase and the gas-phase PE signals originate from the same potentials.

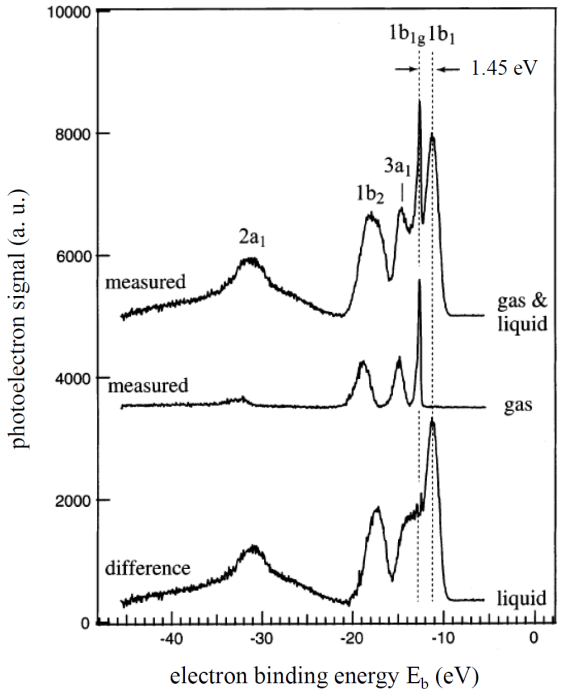

Figure 6.1: Photoemission spectra from water in the liquid and the gaseous phase. Photoemission spectra from measurements with a liquid microjet and an excitation energy of 60 eV are depicted for an H_2O sample, where contributions of both, the liquid and the gaseous phase, are involved (top) as well as for a pure gas-phase water target (middle). Additionally, a calculated difference spectrum displays the mere liquid-phase signal of H_2O (bottom). Photopeaks labeled $1b_1$, $3a_1$, $1b_2$ and $2a_1$ correspond to the photoemission of the four molecular valence orbitals. Spectral peak intensities are normalized to the $1b_1$ peak in the liquid phase, the binding energies are referenced to the prominent $1b_{1g}$ gas-phase peak and given with regard to vacuum. The gas–liquid shift of roughly 1.45 eV in binding energy of the $1b_1$ peak is also marked. Adapted from [264].

The depicted binding energies turned out to be independent from the respective excitation energy and are therefore utilized for the experiment and the analysis presented within this thesis. The accordingly marked photolines in the spectra are assigned to the underlying molecular orbitals where the photoelectrons are emitted from. The molecular orbital (MO) structure of the H_2O molecule is illustrated in figure A.9 in the appendix. The major peaks in the PE spectra in figure 6.1 at the retrieved binding energies of -11.16 eV, -13.50 eV, -17.34 eV and -30.90 eV are assigned to the four valence molecular orbitals $1b_1$, $3a_1$, $1b_2$ and $2a_1$ of H_2O in the liquid phase, respectively. These orbitals can be split into inner valence (iv) and outer valence (ov) bands: The $1b_1$, $3a_1$ and $1b_2$ orbitals build the outer valence band (p-bonding character) and the $2a_1$ orbital the inner band (s-bonding character). The sharpest peak at -12.6 eV in the two upper traces corresponds to the common $1b_{1g}$ valence molecular orbital of water in its gaseous aggregate state [264, 265]. The enormous broadening of the $2a_1$ peak in the spectra is caused by two electron loss features close to the peak due to optical excitations in liquid water [35].

The PE spectrum for the liquid sample is considerably shifted to lower energy and the individual peaks are noticeably broadened compared to the PE spectrum for the gas-phase sample. The distinct energy shift (1.4 eV – 1.7 eV) of the valence peaks originates from a weaker binding of valence electrons in the liquid phase, owing to surface dipoles and an electronic polarization by neighboring H_2O molecules while photoionization [264]. The substantial broadening of the red-shifted PE peaks in the liquid spectrum as compared to the gaseous one results from the statistical distribution of various configurations of the H-bonding system surrounding the individual water molecules [35, 264].

6.2 Setup for Attosecond Streaking Spectroscopy on Liquid Targets

For time-resolved photoelectron spectroscopy of liquid water a special vacuum setup, which provides an in vacuo liquid target, is required. In general, high-vacuum conditions are hereby obligatory for an efficient electron detection and owing to the strong attenuation of XUV radiation in air. However, introducing and preserving a liquid sample in vacuum is rather challenging. A custom-built vacuum setup, which copes with that issues and meets all requirements, had been developed by the group of Prof. Wörner from ETH Zurich and has been used for the attosecond metrology experiments on liquid water in Garching. The setup shall be just briefly described in the following, a detailed description can be found in [33, 266]. The whole experimental end station comprises a small vacuum chamber for XUV pulse filtering, a central interaction chamber containing a liquid-microjet assembly and a small chamber hosting an XUV/NIR double-mirror (see figure 6.2).

The XUV and the NIR laser beams enter the cylindrical filter chamber collinearly and pass a motorized iris, which is required for beam alignment and adjustments of the NIR intensity for the streaking measurements. After the iris, a Zirconium wire grid, provided by our working group (see section 5.4.2), is inserted into the beam path to block the NIR light in the center of the beams for recording streaking spectrograms. Additionally, for recording steady-state XUV-induced photoelectron spectra, a thin (about 250 nm) Zr high pass filter can be inserted into the beam path. After the filter chamber, the laser beams cross the interaction chamber with an offset to the liquid microjet and enter the double-mirror chamber. There, an XUV/NIR double-mirror reflects and focuses ($f = 250$ mm) the two beams back into the interaction chamber and onto the liquid jet, directly in front of the aperture of the TOF spectrometer [87]. The operation principle of the utilized double-mirror assembly is very similar to the one developed for the AS101 beamline (see 5.5.1). In comparison to our costly and sophisticated double-mirror assembly, the double-mirror assembly utilized by the Zurich group has been designed in order to decrease its costs and dimensions (to fit into its small chamber). Indeed, at cost of a less reproducible beam pointing and less versatility.

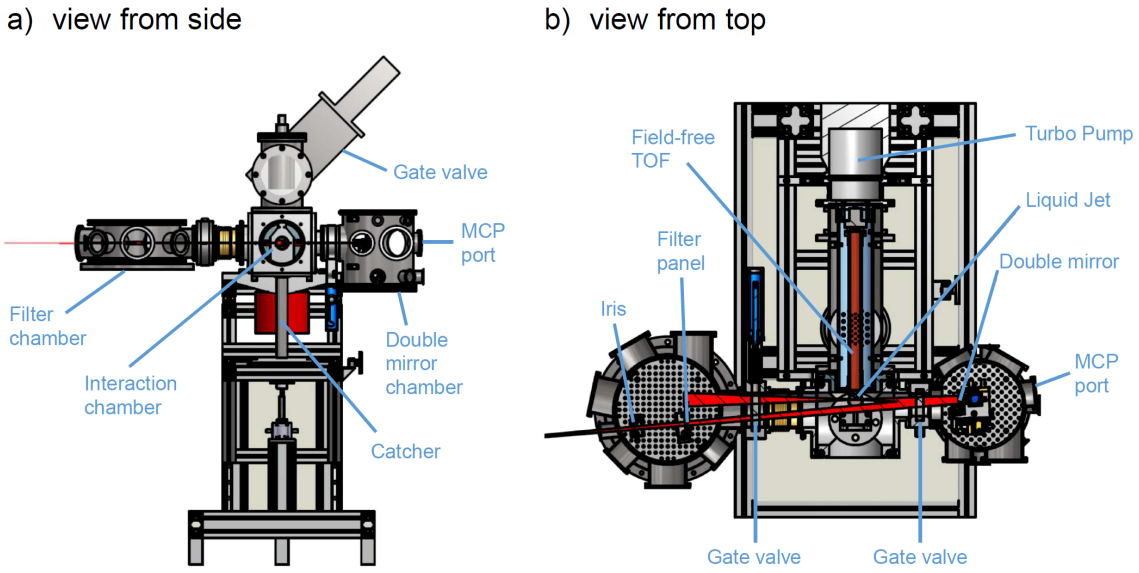

Figure 6.2: Technical drawing of the high-vacuum experimental end station for photoelectron spectroscopy of liquid water. The setup is displayed in a view from the side (a) and from the top (b), the beam enters the construction from the left. The entire setup is mounted on a custom-built aluminum rack (just the filter chamber needs additional support from below) that can be adjusted in height for a rough beam alignment. The setup consists of three main parts: a filter chamber, the central interaction chamber with the liquid-microjet assembly and a double-mirror chamber. Important components of the setup are labeled in the drawing. Taken from [87].

Centerpiece of the end station is the liquid microjet: The basic idea of the liquid-microjet technique is the generation of a thin filament of fast flowing liquid in a high-vacuum vicinity to perceive a stationary, cylindrical, free surface with just a tiny surface area cross section. In this way, liquid water or other liquids and aqueous solutions are delivered as a sample in a high-vacuum environment of down to 10^{-5} mbar. The liquid-microjet assembly basically comprises a thin quartz capillary as an injection nozzle, a high-pressure chromatography (HPLC) pump providing an extremely stable and constant flow, a vacuum feedthrough and a PEEK (polyether ether ketone) piping as well as a sophisticated system of liquid nitrogen (LN_2) cooling traps [87]. A schematic drawing, showing the liquid microjet assembled in a similarly constructed version of the experimental end station applied in the measurements presented here, can be seen in figure 6.3.

The created filament has typically a diameter of about 5 µm – 50 µm, according to the size of the selected injection nozzle. For our measurements, the diameter was set to 15 µm. The nozzle can be adjusted with a precision of 1 µm in each direction by means of piezo-motors. Below the laminar flow region, the liquid jet fragments into water droplets, which then rapidly start to freeze out [211]. Utilizing a fast flowing jet (velocity of up to 140 m/s) allows a constantly and fast exchange of the liquid target, which considerably reduces electrostatic charging of the liquid sample as well as any effects of evaporative cooling [35]. The water droplets from the jet stream into a liquid-nitrogen cooled catcher, which is mounted below the microjet. Additionally, above the microjet a large LN_2 cooling trap collects any water vapor in the chamber released from the water jet.

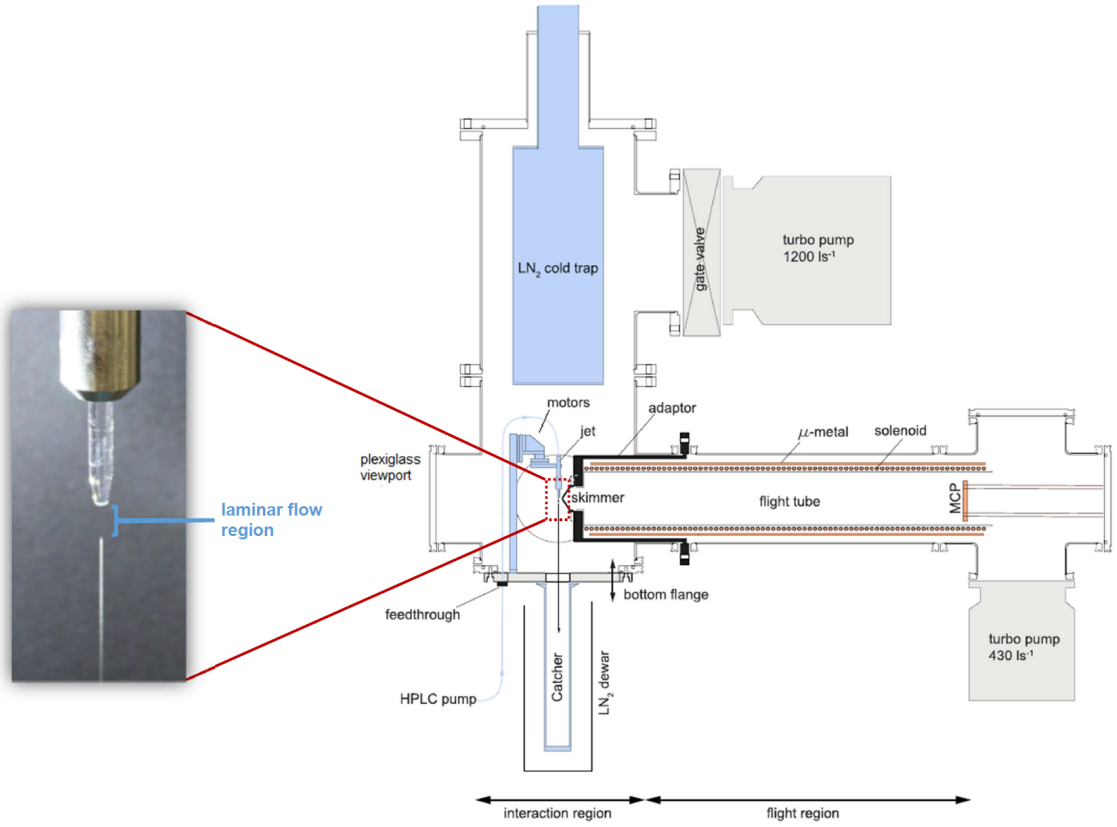

Figure 6.3: Schematic illustration of the interaction chamber hosting the liquid microjet assembly and the electron time-of-flight spectrometer. The liquid microjet in the center of the chamber, a water ice catcher, the liquid nitrogen cooling traps and a spectrometer comparable to the one used for the presented measurements are displayed. Water vapor released in the vacuum chamber gets frozen at the cold traps and the water droplets from the liquid jet are collected within the cooled catcher below the jet. Together with the turbomolecular pumps, these components ensure high-vacuum conditions that are required for photoelectron streaking experiments. In the zoomed inset, a photography of the quartz injection nozzle and the laminar flow region of the liquid jet filament is shown. Adapted from [87].

In combination with the cooling traps, a large turbomolecular pump preserves high vacuum of below 10^{-3} mbar. An ice breaker periodically cuts any growing ice from the bottom and thus hinders a freezing of the liquid jet [33]. Furthermore, a constant potential of -20 V is applied to the liquid-microjet assembly to strongly suppress signal from the gas-phase H_2O around the jet. For more information on this, see [33, 87].

The attosecond photoelectron streaking measurements on liquid water have been performed with three different excitation energies for the ionizing XUV pulses, namely $E_{\mathrm{XUV}} = 80$ eV, $E_{\mathrm{XUV}} = 90$ eV and $E_{\mathrm{XUV}} = 105$ eV, in order to retrieve a potential energy-dependence of the finally determined attosecond delays in photoemission. For this purpose, three multilayer XUV mirrors have been especially designed and produced for the respective XUV energies by Alexander Guggenmoos [145, 146]. Their reflection characteristics are shown in [87]. For the attosecond streaking measurements, a state-of-the-art field-free electron time-of-flight spectrometer has been used.

The liquid H_2O sample has been freshly prepared every day. Hereby, a small quantity of sodium chloride (0.05 mol/l) is added to highly demineralized and purified H_2O to prevent electro-kinetic charging of the water sample [33].

6.3 Experiment and Results

In this section, the experimental outcomes of the first-time attosecond photoelectron streaking measurements in the liquid phase of H_2O are briefly summarized. Moreover, the results of the data analysis, focusing on the disclosure of an intra-species attosecond delay in photoemission between the outer and the inner valence band of water, are presented. Eventually, a preliminary interpretative approach for the determined attosecond delays is introduced. Beyond the presented streaking spectroscopy of liquid-phase water, also measurements in the gaseous phase have been successfully conducted. The experimental results and data analysis thereof are presented in the dissertation of my colleague Martin Wagner [87].

Steady-state Photoelectron Spectra and Time-resolved Streaking Measurements

For the streaking measurements, XUV-multilayer mirrors with a bandwidth of 5 eV are applied in the double-mirror assembly, reflecting isolated attosecond pulses with a duration of roughly 360 as onto the water jet target. This bandwidth limits the energy resolution of our recorded photoelectron spectra, so the individual photolines of the outer valence molecular orbitals (1_b1, $3a_1$ and $1b_2$) cannot be resolved. Instead, photoelectron spectra comparable to a convolution of the reflectivity bandwidth of the mirror with the high-resolution spectrum (depicted in figure 6.1) are recorded, as can be seen in figure 6.4. Here, a measured steady-state photoelectron spectrum of liquid H_2O and the convoluted synchrotron spectrum are comparatively displayed. Obviously, within the scope of our attosecond streaking experiments one can just distinguish between photoelectron from the inner and the outer valence band. One should have in mind that the outer valence photoline is a composition of various electronic states and comprises, as mentioned before, to some extent also a contribution from the gaseous phase. This gas-phase contribution in the liquid-phase measurements can be efficiently suppressed by applying a sufficiently large electric potential to the liquid microjet [269]. Thus, only liquid-phase effects can be retrieved from the measurements with the liquid microjet. A detailed discussion on this can be found in [266]. Nevertheless, within the scope of the data analysis, it has been recognized that the gaseous phase is mostly suppressed within our experiments even without the applied potential, since both types of data sets showed comparable results for the attosecond delay within the actual error margins [87].

As commonly used for measuring time-resolved attosecond streaking spectra, the center parts of the collinearly propagating XUV and NIR beams are guided through a thin Zirconium (or Molybdenum) filter foil to cut out only the desired part of the pulse spectra and are then reflected by the XUV mirror. For the adjustment of the respective time delay

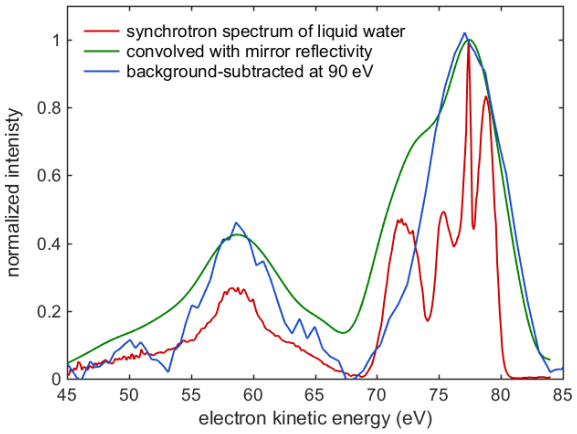

Figure 6.4: Steady-state photoemission of liquid H_2O. A measured photoemission spectrum of liquid water (blue) is compared to a high-resolution synchrotron spectrum (red, data taken from [264]) and its convolution with the energy resolution-limiting reflectivity of the XUV multilayer mirror (green). For the measured PE spectrum, isolated attosecond pulses at an excitation energy of 90 eV have been utilized, the NIR streaking laser had been blocked by a 200-nm thick Zirconium filter. Adapted from [87].

between the XUV pulse (inner mirror) and the NIR streaking pulse (outer mirror), the mirrors can be moved relative to each other along the beam path by a piezo actuator. For the present measurements, a delay step size of 15 nm, being equivalent to 0.1 fs, has been utilized. Following the common sign convention in the attosecond community, the direction of this movement has been chosen in a way that for negative XUV/NIR delay values the ionizing XUV pulse is retarded, whereas for positive delays it is advanced in relation to the co-propagating NIR streaking pulse [87].

Experimental Results and Statistical Analysis

In raw streaking spectrograms, the temporal shift between the streaking traces of the inner and the outer valence band is hardly discernable by eye, which already gives a hint for a quite small relative delay in photoemission $\Delta\tau_{\mathrm{ov-iv}}$ for the two lines. This attosecond delay has been reliably determined by the application of the restricted TDSE retrieval using a differential background subtraction, as mentioned in 2.2.5.
An exemplary raw streaking spectrogram of a randomly selected streaking scan, the appropriate TDSE retrieval result and the residual difference between both are presented in figure 6.5. The latter primarily comprises the remaining background signal, but also a small, insignificant streaking-dependent contribution that results from a non-perfect agreement of the retrieval with the experimental streaking traces. For obtaining a high quality of the retrieval results, certain scans need to be excluded from the further analysis. All raw data spectrograms with insufficient quality (signal-to-noise ratio, sudden signal drops, etc.) and spectrograms where the retrieval did not converge or just with a huge merit have been discarded. Within the frame of the experiment, a satisfying number of suitable streaking scans has been evaluated and employed for the statistically significant analysis of the retrieved attosecond delay in photoemission for the three different XUV excitation energies:

altogether, 55 streaking scans recorded at an XUV excitation energy of E_{XUV} = 80 eV, 76 scans at E_{XUV} = 90 eV and 72 scans at E_{XUV} = 105 eV have been considered for the further analysis, especially for obtaining a reliable value for the retrieved attosecond delay [87]. The results of the statistical analysis, namely the distribution, the mean and the standard

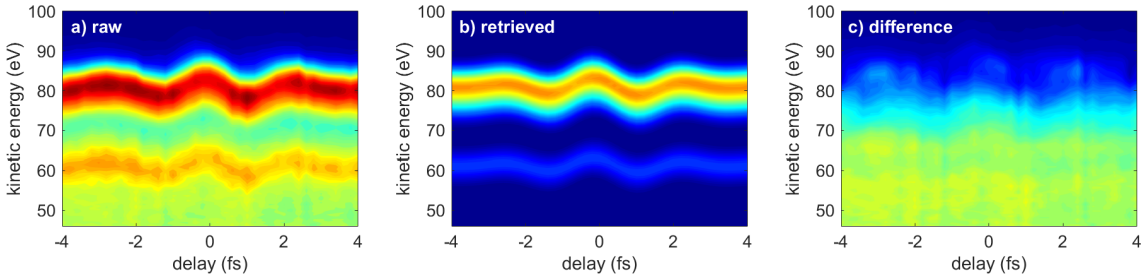

Figure 6.5: Retrieval of a measured streaking spectrogram of liquid H_2O at an XUV excitation energy of 90 eV. In panel (a) a raw, energy-calibrated streaking spectrogram is shown. The appropriate TDSE fit is depicted in panel (b) and the corresponding difference spectrum in panel (c). In the latter, the time-independent background as well as a weak, modulated contribution not retrieved by the TDSE fit are visible.

deviation of the retrieved attosecond delay in photoemission between the outer and the inner valence band photoelectrons $\Delta\tau_{\mathrm{ov-iv}}$ in the liquid phase of H_2O, are presented in figure 6.6 for all three XUV excitation energies. Apart from the considerable standard deviations especially at E_{XUV} = 80 eV, the distributions reveal a positive value of the attosecond delay $\Delta\tau_{\mathrm{ov-iv}}$. This implies a delayed arrival of the photoelectrons from the outer valence with regard to those emitted from the inner valence. Eventually, one obtains the final mean values and the 95% confidence intervals (given in brackets behind the mean value) for liquid H_2O of $\Delta\tau_{\mathrm{ov-iv}}$ = 19 (14 , 24) as for E_{XUV} = 80 eV, $\Delta\tau_{\mathrm{ov-iv}}$ = 14 (11 , 18) as for E_{XUV} = 90 eV and $\Delta\tau_{\mathrm{ov-iv}}$ = 12 (10 , 15) as for E_{XUV} = 105 eV. Scrutinizing these values conclusively, the obtained relative delays in photoemission $\Delta\tau_{\mathrm{ov-iv}}$ in liquid H_2O are basically rather small though certainly positive with the given confidence interval and exhibit a slightly declining tendency with rising XUV excitation energy, starting from 19 as at E_{XUV} = 80 eV to 12 as at E_{XUV} = 105 eV [87].

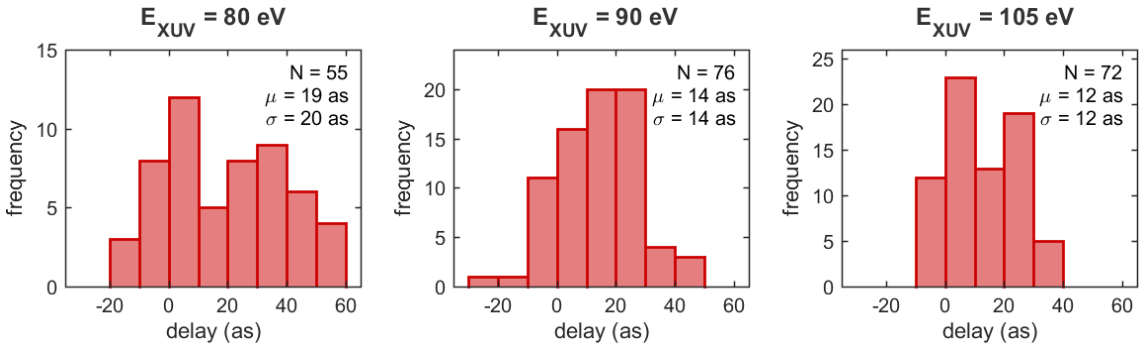

Figure 6.6: Results of the statistical analysis of the retrieved attosecond delay in photoemission $\Delta\tau_{\mathrm{ov-iv}}$ in the liquid phase of H_2O. The statistical distribution of the retrieved relative delay in photoemission $\Delta\tau_{\mathrm{ov-iv}}$ in liquid H_2O is displayed for an XUV excitation energy of 80 eV (left), 90 eV (middle) and 105 eV (right). Additionally, the total number N of the streaking scans being included in the distribution, the mean μ and the standard deviation σ of the distribution are shown.

6.4 Preliminary Theoretical Interpretation

The experimentally determined attosecond delays $\Delta\tau_{\mathrm{ov-iv}}$ in liquid-phase and gaseous H_2O [87] are subject to current theoretical studies by our collaborators at the ETH Zurich, which are unfortunately not finalized yet.
Within the frame of the analysis of photoemission delays in a liquid-phase sample, the local vicinity of a molecule in condensed matter plays an essential role, since the propagation of a released electron is further, strongly affected by elastic and inelastic scattering processes [24, 270]. Any single elastic collision causes a so-called *scattering delay* between electrons with different kinetic energy and contributes to the total delay retrieved from recorded streaking spectrograms [87].

Streaking measurements performed for gas-phase H_2O have revealed a considerable smaller delay of 5 ± 7 as and decline with increasing XUV photon energy [87]. These results match quantitatively with theoretical state-of-the-art calculations of molecular photoionization delays [271]. For the analysis of underlying electron dynamics in liquid H_2O however, not only the bigger effect of scattering events, but also the highly-dynamic hydrogen bonding network, strongly influencing the complex structure of water, come into play [87]. The significantly bigger attosecond delays retrieved for liquid H_2O contain comprehensive information about scattering dynamics of electrons within the liquid-phase medium. A complete 3D Monte-Carlo simulation of electron propagation, comprising photoemission, elastic and inelastic scattering, is currently being performed by our collaborators at the ETH Zurich to accomplish a theoretical interpretation of the attosecond delay results. The theoretical modelling of these structures in water is tedious and still necessitates approximating different sized water clusters [267], since these calculations are based on precise scattering calculations of electrons with water clusters of growing size. It turned out that the differential scattering cross sections converge dependent on the cluster size for typically 6 to 8 water molecules [272]. Starting from these converged differential scattering cross sections, combined with the associated scattering delays, a detailed model of the electron–liquid scattering dynamics can be developed. The Monte-Carlo simulations deliver attosecond delays that are consistent with our experimentally obtained values and reveal that the determined delays are sensitive to the elastic and inelastic mean-free paths (EMFP, IMFP) of electrons in liquid H_2O [273].

Thus, soon a conclusive comparison of theory and experiment will enable us to obtain exact values for EMFP and IMFP over a distinct range of electron kinetic energies. Currently, values for EMFP and IMFP vary by up to an order of magnitude [87, 274, 275], which causes considerably diverse transport models. Consequently, our results will provide the first profound, experimental values on mean-free paths of electrons in liquid H_2O for this kinetic energy range. Consequently, these quantities will be extremely valuable for benchmarking theories and precise, theoretical modeling of radiation chemistry in general.

Chapter 7

Conclusion and Outlook

The main goals of this thesis have been the first direct determination of the temporal substructure and the pulse duration of X-ray FEL pulses through a self-developed algorithm via two-color angular streaking on the one side and the design and commissioning of a novel, state-of-the-art attosecond metrology beamline as well as the first-time application of attosecond streaking spectroscopy on a liquid-phase sample on the other side.
X-ray FELs are primarily based on the self-amplified spontaneous emission process and generate pulses with a stochastic temporal substructure and without any correlation between subsequent pulses. X-ray SASE pulses also exhibit a considerable inherent, single-shot arrival time jitter relative to any externally synchronized laser source, limiting the temporal resolution of X-ray pump/optical probe experiments to the level of that timing jitter. Thus, a direct, single-shot pulse characterization for obtaining the spike structure and the pulse duration of SASE X-ray pulses, as well as an accurate determination of the relative optical/X-ray arrival time are urgently needed. Both issues are fundamental prerequisites for any two-color, intensity-dependent experiments, especially for ultrafast time-resolved pump/probe studies in the few-femtosecond range. Up to today, no such measurement approach is available yet. Applying a two-color angular streaking approach combined with a self-developed analysis algorithm, a direct and accurate, non-invasive single-shot characterization of X-ray FEL pulses at the Linac Coherent Light Source (LCLS) has been successfully demonstrated. Representing the key task of this thesis, this scheme allows the determination of the X-ray pulse duration and its temporal substructure with few-femtosecond resolution as well as a precise measurement of the relative arrival time, and is usable for a wide range of X-ray pulse settings.

In the course of these experiments, single X-ray pulses with three different pulse durations have been employed. Hereby, electrons stemming from two different generation processes have been deployed as measuring probes: neon 1s photoelectrons and neon K-LL Auger electrons. In addition to the investigations with a single ionizing X-ray pulse, also measurements with instead an X-ray double-pulse train for the ionization of the target have been conducted. For a direct X-ray FEL pulse characterization in the time domain from these angular streaking data, a novel algorithm has been developed. This approach is simple, straightforward and intuitive in view of the classical concept of angular streaking, but it provides no spectral information about the X-ray pulse. The idea of the algorithm can be summarized as an angle-dependent, thresholded integration of angularly streaked

photoelectron intensity and a subsequent translation of this integrated signal — a representation of the temporal intensity profile of the X-ray pulse — from an angle axis onto a time axis via the *attoclock principle*. In the reconstruction, the distinctive temporal substructure of single X-ray FEL pulses can be clearly resolved and shows the expected series of random pulse shapes. It is demonstrated that the number of SASE spikes within the pulse changes considerably from shot to shot and the pulse duration is reliably ascertained. Either Auger electrons or photoelectrons, producing remarkably consistent results, can be used to measure the profile of single X-ray SASE FEL pulses with a resolution of about 2.2 fs, without substantial X-ray beam intensity losses and independent from simultaneously ongoing experiments. The Gaussian-like distributions of the retrieved pulse durations match very well with the respective expectations. Furthermore, for all measurements an average arrival time jitter of 56 fs (FWHM) and the single-shot arrival time itself have been determined with the same resolution of about 2.2 fs.

The characterization of X-ray FEL double-pulse trains clearly reveals the substructure of the two individual pulses as well as their separation (delay) on a single-shot basis. However, the analysis does not prove the sequence of the double pulses beyond doubt but it provides at least a tendency or an indication for the chronological order. Especially for the neon 1s data sets, the results are hard to interpret. This is explained by a nascent merging of the two pulses on the *attoclock* time axis, since the awaited delay between both pulses is close to the rotation period of the streaking vector, hence causing ambiguities in the analysis. Nevertheless, the retrieved double-pulse delay fits very well to the estimated average value of 23 fs, as announced by LCLS. The single peak pulse duration statistics yield an average rms duration of 2 fs, which also matches the nominal, predicted duration very well. For studies of correlation dynamics on the femtosecond time scale, these results realize the urgently desired availability of an X-ray pump/probe setup, deploying the unique properties of SASE FEL pulses with adjustable delay and pulse durations, and enough pulse intensity, at current FEL facilities.

An iterative projection algorithm developed within our collaboration retrieves the full attosecond time–energy information of the X-ray pulse and is corroborated by an application to a full quantum-mechanical simulation. For an evaluation of the integration pulse characterization algorithm presented in this thesis, both retrieval approaches are comparatively applied to an identical angular streaking data set for a time-domain pulse characterization. Eventually, the fidelity and the capabilities of the here presented pulse characterization are impressively corroborated. Furthermore, this proves the high reliability, robustness and versatility of the algorithm at orders of magnitude lower computing time, in comparison. These outcomes demonstrate the applicability of this approach (with an actual repetition rate of 2 MHz) as a smart, fast yet reliable, online tool for pulse characterization (pulse vetoing tool), which is urgently required for the implementation of real-time pulse tagging at the next-generation MHz-repetition rate XFEL facilities. In this respect, this technique is the only one currently available.

Regarding the current analysis speed, the angular streaking concept is readily scalable to the higher repetition rates of the future high-repetition rate XFEL facilities. With exact profiling of SASE pulses available during ongoing measurements, the resolution of few-femtosecond X-ray imaging experiments can be substantially improved by incorporating the X-ray substructure intensity distribution into the analysis process. Single-shot knowledge of the separation and the single-peak pulse duration of X-ray double pulses also paves the way for high-repetition rate X-ray pump/ X-ray probe experiments. Demonstrated for soft X-rays, the two-color angular streaking method, combined with the presented pulse characterization algorithm, is also scalable to hard X-rays with their concomitant shorter SASE spike durations. The experimental setup can easily and in a straightforward way be adapted to the specific needs of hard X-ray pulses just by changing the target gas, and thus the absorption edges to the higher X-ray energy range, and by simultaneously decreasing the wavelength of the streaking laser [172]. In the performed experiments, a 10.6 µm streaking laser wavelength has been utilized, corresponding to a 35-fs carrier period. This wavelength has been selected to cover the estimated sub-10 fs duration of the XFEL pulses, as no reliable method for attosecond XFEL pulse generation has existed then. The angular streaking technique can easily be extended to a resolution in the attosecond timescale, just by applying a streaking field with an accordingly shorter wavelength. This directly results in a shorter rotation period of the close-to-circularly polarized streaking field, and thus an enhancement of the angular (and temporal) resolution [172]. An appropriate laser source at a standard wavelength of 1.064 µm and with a convenient repetition rate is planned to be readily available at LCLS-II.

Within our collaboration a proposal for a beamtime at the European XFEL in Hamburg is already planned. Applying a comparable setup and the same *cookiebox* time-of-flight spectrometer assembly, again angular streaking experiments shall be performed. Setting various streaking laser wavelengths or increasing the X-ray photon energy to the hard X-ray regime will further demonstrate the superior, tremendous capabilities of this approach for X-ray FEL pulse characterization. In future beamtimes, especially at LCSL, one should also conduct more double-pulse measurements to further improve the double-pulse characterization method regarding the determination of the sequence of double-pulse trains. This can be done by choosing different settings for the streaking laser wavelength or by varying the pulse separation between the two pulses and the pulse duration of the individual pulses. The presented double-pulse technique is also capable of resolving even smaller double-pulse delays through a variation of the streaking laser rotation period. Furthermore, the construction of a TOF spectrometer array with a smaller angular distance between its single detectors should also be of great interest, as this constitutes an intrinsic increase of the temporal resolution of the measurements, independent of the selected streaking laser wavelength. Eventually, initial plans for the implementation of a *cookiebox* time-of-flight spectrometer assembly at LCLS-II as an online time tool via the angular streaking approach should be intensively pursued.

In a complementary approach in the framework of this thesis, the design and commissioning of a novel and versatile, state-of-the-art attosecond metrology beamline have been achieved. The very first attosecond streaking measurements at the beamline have been successfully performed within less than a year after initial operation of the laser system. The basic conception of the beamline builds on experiences gained from existing high-end attosecond beamlines and incorporates recent experimental developments, resulting in a sophisticated and thoroughly designed beamline for the next-generation experiments in attosecond metrology. The self-designed, custom-built hollow-core fiber pulse compressor with a double-differentially pumped HCF design, utilizing the conjugate-gradient pressure method, provides waveform-controlled, few-cycle high-intensity pulses with pulse durations of below 5 fs and a central wavelength of about 650 nm. The subsequent vacuum setup for the generation and characterization of high harmonics comes up with several special, refined peculiarities at the individual stages of the vacuum beamline. The self-designed, ultra-high vacuum experimental end station including an XUV/NIR double-mirror assembly, especially developed for attosecond streaking experiments in the gaseous phase, has already been used for several attosecond metrology experiments. Conclusively, the capabilities of the novel AS101 beamline are impressively corroborated by a characterization of its output pulses via a retrieval of the pulse parameters from recorded streaking spectrograms as well as by the first-time attosecond streaking spectroscopy experiments on liquid water as premiere experiment only a few weeks after the first generation of high harmonics.

For the upcoming experiments, some further improvements of the beamline are already planned, e.g. regarding the polarization of the laser pulses in the entire beamline, the beam stabilization system in the experimental laboratory and a noble gas mixture as an input gas for the hollow-core fiber. Nevertheless, the beamline is well-prepared and ready for further experiments in the near future: The electron dynamics within various siliceous molecules in the gas phase, triggered by an Auger decay in a localized silicon atom, shall be studied on the attosecond time-scale at an excitation energy of about 160 eV. Furthermore, attosecond streaking measurements on solid-state samples, e.g. H_2O ice (see below) as well as the study of ultrafast electron transfer in light-to-chemical energy conversion on semiconductors suitable for an application in photocatalytic systems, e.g. WO_3 or α-Fe_2O_3, shall be performed within the next months.

Within the scope of this thesis, the first-time attosecond streaking spectroscopy measurements on a liquid-phase sample (H_2O) have been successfully demonstrated at the newly designed and commissioned attosecond beamline. These measurements also represented the streaking premiere of the newly commissioned attosecond beamline AS101 and give proof of its operational readiness and capabilities providing isolated attosecond pulses in the XUV-range and few-cycle NIR laser pulses. The experiments have enabled the measurement of attosecond photoemission delays between valence shells of liquid

H_2O, the outer-valence band (ov) and the inner-valence band (iv), and thus establish the feasibility of attosecond metrology with liquid samples: Attosecond photoelectron streaking has revealed mean delays and 95 % confidence intervals of $\Delta\tau_{\mathrm{ov-iv}}$= 19 (14 , 24) as at a photon energy of 80 eV , $\Delta\tau_{\mathrm{ov-iv}}$= 14 (11 , 18) as at 90 eV and $\Delta\tau_{\mathrm{ov-iv}}$= 12 (10 , 15) as at 105 eV. The attosecond delays are strongly affected by the H-bonding network in water and comprise comprehensive information about scattering dynamics of electrons within the liquid-phase medium.

Theoretical data interpretation, mainly consisting of complete 3D Monte-Carlo simulations of electron propagation involving photoemission, elastic and inelastic scattering will be finalized in the near future by our collaborators at ETH Zurich. This will reveal the first profound, experimental values on mean-free paths of electrons in liquid H_2O for this kinetic energy range. These quantities will be extremely valuable for benchmarking theories of electronic properties of water in the liquid phase and precise, theoretical modeling of radiation chemistry in general, since current values for the EMFP and the IMFP vary by up to an order of magnitude. Conclusively, attosecond streaking spectroscopy on liquid-phase samples opens the door to a huge variety of experimental samples. Therefore, this will open new insights into the effect of a surrounding solvent on the electron dynamics in molecules and into ultrafast processes in chemical and biological systems, such as solvation dynamics, solvent reorganization and electron transfer [33].
As the intra-species delays between the inner and outer valence shells in liquid water have been studied for three different excitation energies, these streaking measurements shall be equally conducted at the same energies with H_2O ice, prepared in at least two of its different crystalline structures. These different environments influence the attosecond delay and should be quantified in the planned experiments by studying non-crystalline, amorphous solid water H_2O (asw) as well as the hexagonal phase of ice H_2O (Ih), showing crystalline structure. These combined investigations allow a systematic analysis of the contribution of electron transport times between scattering sites to the total attosecond delay in photoemission.

Appendix

A.1 Details on the Pacman Reconstruction Algorithm

In the following, a more detailed and mathematical description of the *Pacman* algorithm shall be given. The entire section is a slightly adapted version of the Supplementary information of [172]. We recall equation 2.61 for the recorded streaking trace within the angular streaking experiment, defined as the integrated photoelectron intensity over time

$$I_{\mathrm{total}} = \int dt\, I(E_f, \theta, t)\ , \tag{A.1}$$

with θ being the actual observation angle and E_f the final photoelectron kinetic energy. Now, the Pacman algorithm approximates I_{total} as a sum of several individually streaked electron distributions

$$I_{\mathrm{total}}(E_f, \theta) \approx \sum_{i,j,k} \alpha\,(i,j,k)\ B\,(i,j,k)\ , \tag{A.2}$$

with

$$B\,(i,j,k) = \left[1 - \cos\left(2\,(\theta - \theta_x)\right)\right]\ e^{-\frac{E_f - E_i(t) - \sigma(\theta)\cos(\theta - \omega_L t)^2}{2\beta^2}}\ . \tag{A.3}$$

Here again, θ_x is the orientation of the X-ray polarization in the detector frame, E_i is the initial photoelectron kinetic energy after the ionization, β is the energy resolution and σ is the streaking kick. We evaluate the vectors $B\,(i,j,k)$ on a predefined grid $\tilde{E_f} \times \tilde{P} \times \tilde{S}$ with $E_{f,i} \in \tilde{E_f}$ = 270, 271, …, 320 eV and $\sigma_k \in \tilde{S}$ = 0.0, 0.1, …, 35 eV. The phase grid $\phi_j \in \tilde{P} = \left\{0, \frac{\pi}{40}, \ldots, 2\pi\right\}$ rad is related to a temporal sampling of 0.44 fs at the IR streaking wavelength of 10.6 µm and a polarization period of ≈ 35 fs. The vectors $B\,(i,j,k)$ are linearly dependent and span the relevant vector space, thus do not form a vector basis and the coefficient matrix $\alpha(i,j,k)$ cannot be determined via a simple projection onto every vector B [172].

First, the algorithm searches for the streaking kick $\sigma_{k=k'}$ in each single FEL shot, as we assume $\hat{\sigma}(t)$ to be constant over the entire duration of the X-ray pulse. With this set streaking kick the coefficient matrix is reduced to $\alpha(i,j,k=k')$ and the remaining coefficients are determined by minimization of the difference between experimental measurement and reconstruction

$$\min_{i,j \in \tilde{E_f} \times \tilde{P}} \int\int d\theta\, dE_f \left(I_{\mathrm{total}}(E_f, \theta) - \sum_{i,j} \alpha\left(i,j,k=k'\right) B(i,j,k) \right)^2 \tag{A.4}$$

This results in a reconstruction composed of two optimization problems with roughly two million coefficients per single FEL shot. For an improvement of the speed of the routine a quick, iterative routine is applied to receive a globally optimized streaking kick and hence, to avoid any local minima in the first optimization process. As a starting point, one determines the vector $B\left(i', j', k'\right)$ on the parameter grid that optimizes the overlap integral I_{overlap} with the recorded streaking trace:

$$I_{\mathrm{overlap}}(i,j,k) = \int\int d\theta dE_f \; I_{\mathrm{total}}(E_f,\theta) B(i,j,k) \tag{A.5}$$

For a given streaking kick $\sigma_{k=k'}$, the determined vector b is iteratively subtracted from the recorded streaking trace $I_{\mathrm{total}}(E_f, \theta)$. After each subtraction, one again searches the vector $B\left(i', j', k'\right)$ that maximizes the overlap integral $I_{\mathrm{overlap}}(i, j, k = k')$. After a sequence of 100 iterations, all remaining photoelectron signal is integrated. By doing so, the streaking kick which results in the smallest integral of remaining photoelectron counts and hence in the best overlap between the measurement and the vector set $B(i, j, k)$, is found. This procedure utilizes only fast matrix multiplications, but provides results that are consistent with typical least-squares routines. Thus, it accelerates the first optimization problem by roughly one order of magnitude [172].

The speed of the routine is further improved by a restriction of the parameter space in $\tilde{E}_f$ for every single FEL shot for the subsequent, second optimization step. The first moment of E_f is calculated as a baseline

$$\langle E_f \rangle = \int\int dE_f d\theta E_f I_{\mathrm{total}}(E_f,\theta) \; . \tag{A.6}$$

Utilizing the streaking kick σ_k, determined in the first optimization step one, can limit $\tilde{E}_f$ symmetrically around $\langle E_f \rangle$ to $[\langle E_f \rangle - \sigma_k - \delta, \; \langle E_f \rangle + \sigma_k + \delta]$ with a margin δ. Hence, all maximally and minimally streaked electrons are included. The reduced coefficient matrix is then solved by utilizing a non-negative least squares routine (NNLS) [276] in combination with an L_2-regularization, or else ridge regression, to avoid overfitting. Additionally, as further constraints just partial waves, which hit the entire region of the recorded streaking trace, are used for the reconstruction and low intensity noise is neglected in the optimization [172].

Eventually, the coefficient matrix α is delivered by the two-step optimization algorithm representing the extent of every photoelectron contribution as a function of time (in units of the phase ϕ of the streaking field) and its initial kinetic energy E_i. Here, the X-ray energy is calculated by adding the applied retardation voltage of the TOF detector and the neon 1s binding energy to the photoelectrons' kinetic energy E_i. Consequently, based on the coefficient matrix α one obtains a time–energy retrieval of the X-ray pulse. The intensity profile of the X-ray pulse and its spectrum are yielded by the projections of the coefficient matrix onto the time and the energy axis, respectively [172].

A.2 Further Information on the Angular Streaking Data Analysis

Neon 1s Transmission Correction and Energy Calibration

The integrated scaling factors for the transmission calibration of the Ne1s photoelectron spectra (see section 4.1.1), which is required owing to the dumbbell-shaped angular emission characteristic of the photoelectrons, are presented in table A.1.

Detector	Transmission Coefficient
0°	27.12
22.5°	156.30
45°	449.43
67.5°	702.43
90°	1136.75
112.5°	912.45
135°	612.85
157.5°	248.36
180°	38.89
202.5°	147.11
225°	497.41
247.5°	684.94
270°	792.79
292.5°	766.36
315°	392.14
337.5°	175.28

Table A.1: Transmission calibration factors for the neon 1s data sets.

Detector	A [$1/ns^2$]	t_0 [ns]	E_0 [eV]
0°	29317	1.09	265.63
22.5°	29918	0.82	276.65
45°	30569	0.71	275.84
67.5°	29710	0.97	265.41
90°	29979	1.64	264.44
112.5°	29755	1.04	264.99
135°	30006	1.01	265.64
157.5°	28487	1.17	267.14
180°	29317	1.09	265.63
202.5°	28398	1.25	266.00
225°	29459	0.96	266.21
247.5°	29140	0.96	265.77
270°	29094	0.97	265.49
292.5°	29315	0.97	265.44
315°	29621	1.01	264.82
337.5°	28845	1.14	266.17

Table A.2: Fit coefficients for the Neon 1s energy calibration.

For each individual detector of the TOF spectrometer array, the respective values of the fitting parameters for the neon 1s energy calibration (see section 4.1.2), associated with the calibration function 4.4, are displayed in table A.2.

Energy Calibration of the Auger Data Sets

For the energy calibration of the neon Auger data sets, Auger electron emission energies are extracted from synchrotron measurements and subsequently compared to an averaged signal of 2.000 unstreaked time-of-flight traces out of a calibration run without the IR streaking laser. The synchrotron spectrum is presented in figure A.1.

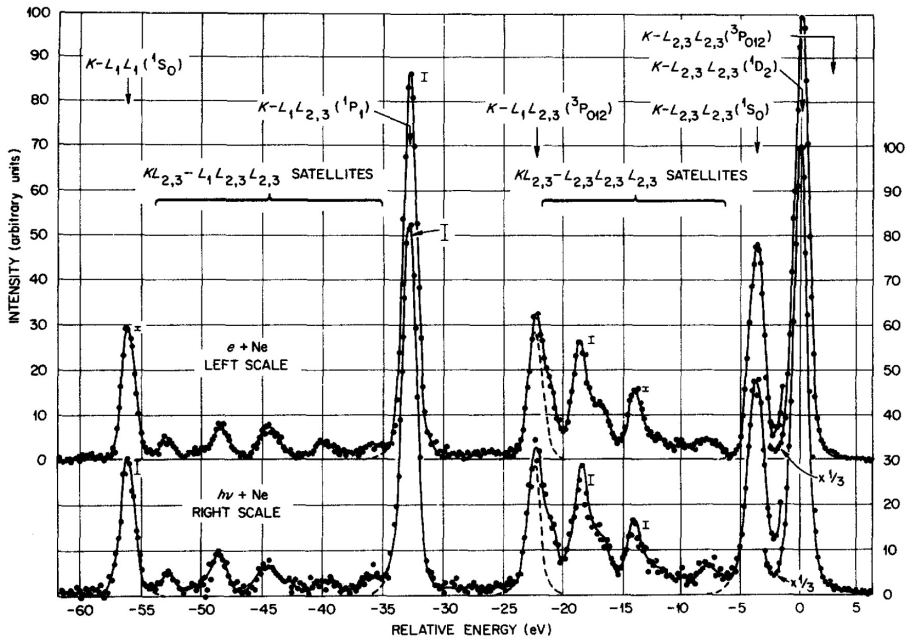

Figure A.1: K-Auger spectrum of neon excited by electrons with a kinetic energy of 3.2 keV (upper spectrum) and by photons with an energy of 1.5 keV (lower spectrum). Only intense lines are denoted. The resolution amounts to 0.17% FWHM. Taken from [206].

Polarization Ellipse for Double Pulse Data Sets

The polarization ellipse illustrated by the angle-dependent overall streaking limit $E_{\mathrm{Ell}}(\varphi)$ is depicted in a polar plot in figure A.2 for a) the two Auger electron and b) the two photoelectron double pulse data sets (see sections 4.1.3 and 4.1.5), respectively.

A.3 Additional Drawings and Photographs of the Attosecond Metrology Beamline

In this section, some further photographs and technical drawings of the individual vacuum chambers, which show all relevant components installed inside and the beam path within the chamber are presented.

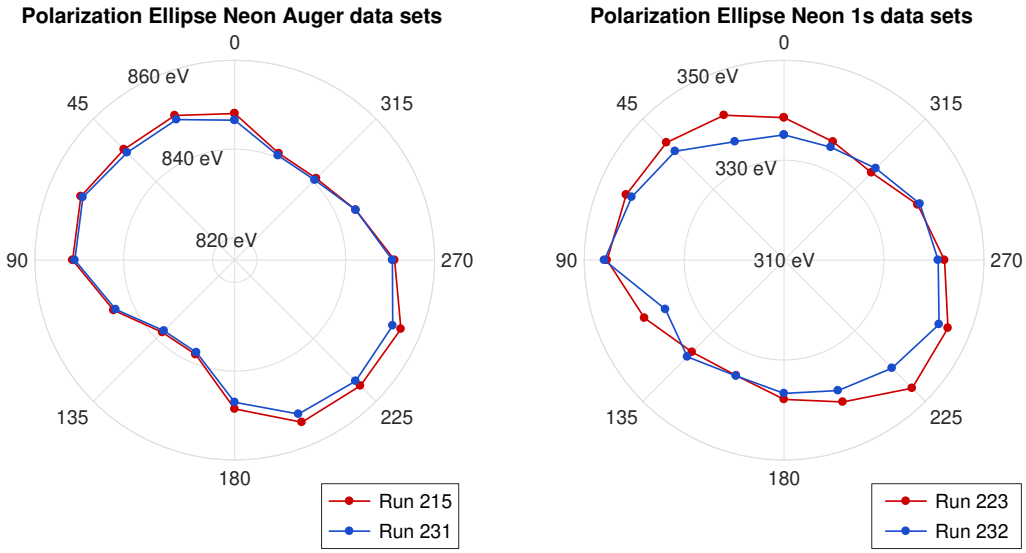

Figure A.2: Illustration of the ascertained polarization ellipse for double-pulse data sets.

The overview photography in figure A.3 shows the central laser laboratory (see chapter 5) hosting the commercial frontend amplifier system, which provides laser pulses for the two experimental laboratories. The housing of the beam path from the laser system until the hollow-core fiber and the HCF vacuum setup itself are displayed in the foreground.

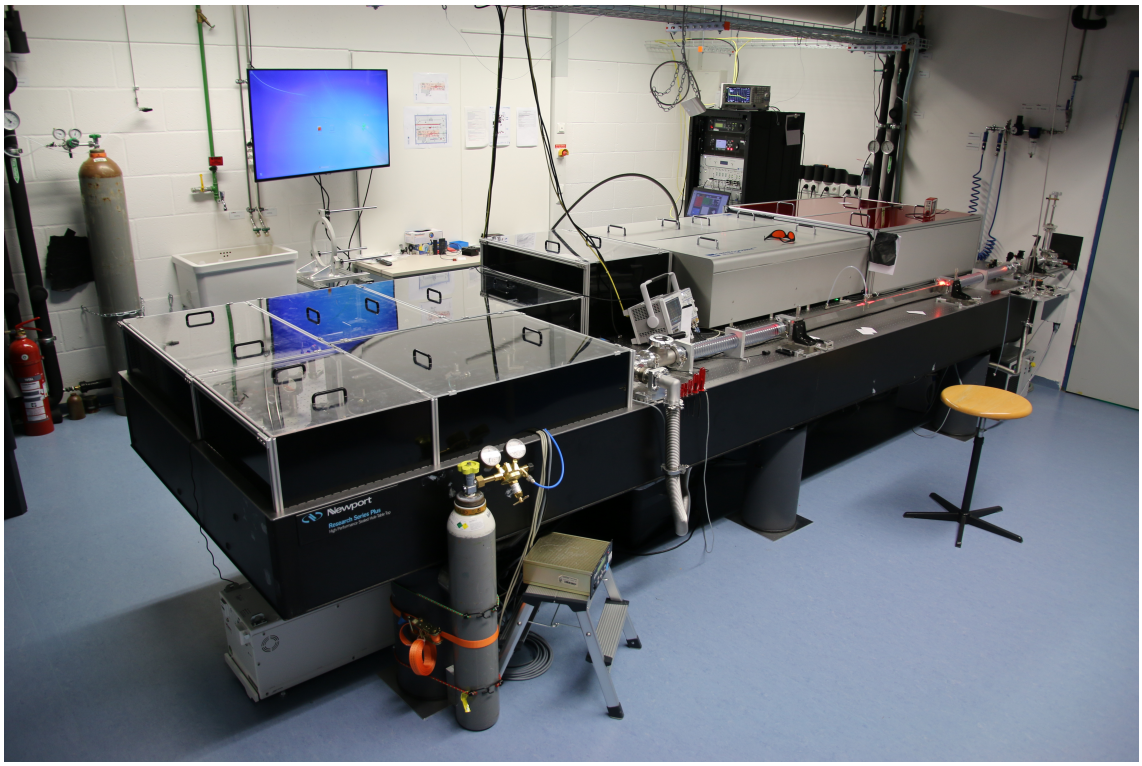

Figure A.3: Overview of the central laser laboratory.

The overview in figure A.4 shows the AS101 beamline in the experimental laboratory (see chapter 5) with the three vacuum chambers for pulse compression, HHG and XUV diagnostics as well as the experimental end station including the double mirror assembly and the large-angle, anode-segmented TOF spectrometer in the foreground.

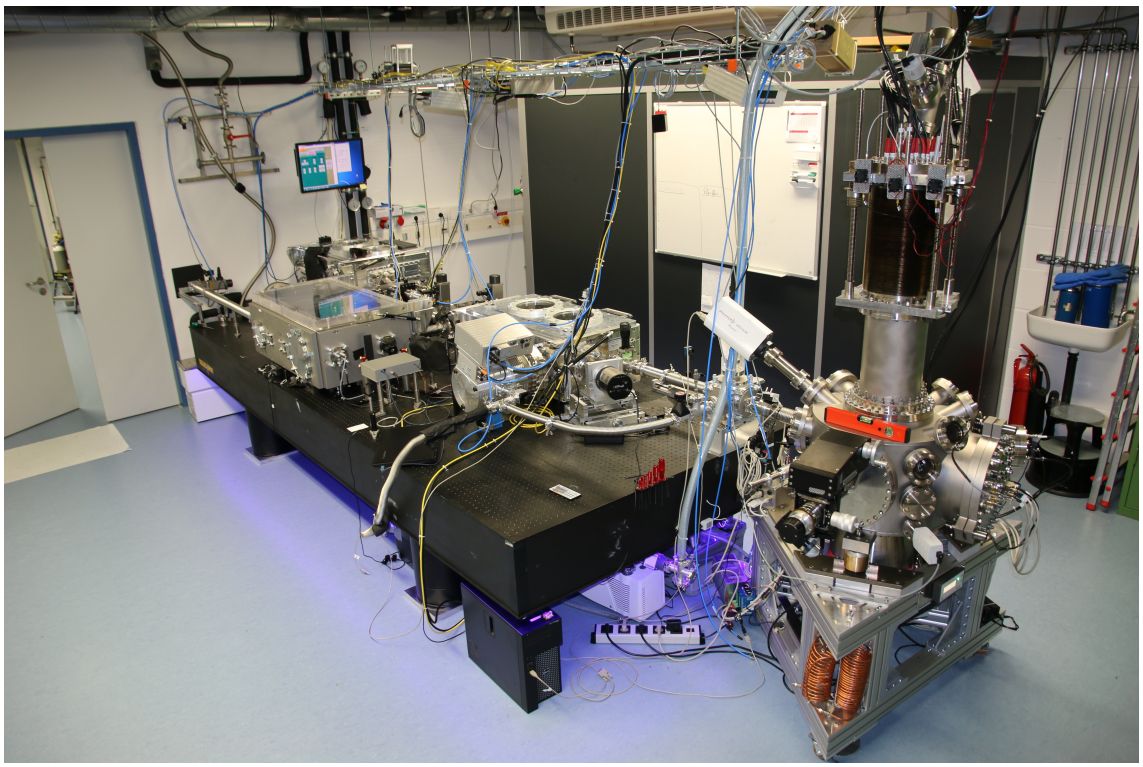

Figure A.4: Overview of the experimental laboratory hosting the AS101 beamline.

A photography of the hollow-core fiber (see section 5.3.1) during operation is shown in figure A.5. The spectral broadening along the differentially pumped HCF is distinctly visible by the color of the strayed light changing from red at the fiber entrance to a bright orange, nearly white at the end of the setup. The two support mounts, the gas inlet and the gas feed line setup can also be seen.

Illustrations of the main vacuum chambers of the AS101 vacuum beamline in the experimental laboratory are presented in the following. The chambers themselves, their interior and the beam path within the respective chamber are clearly depicted. The pulse compression chamber is shown in A.6, the high harmonic generation chamber in A.7 and the HHG diagnostics chamber in A.8.

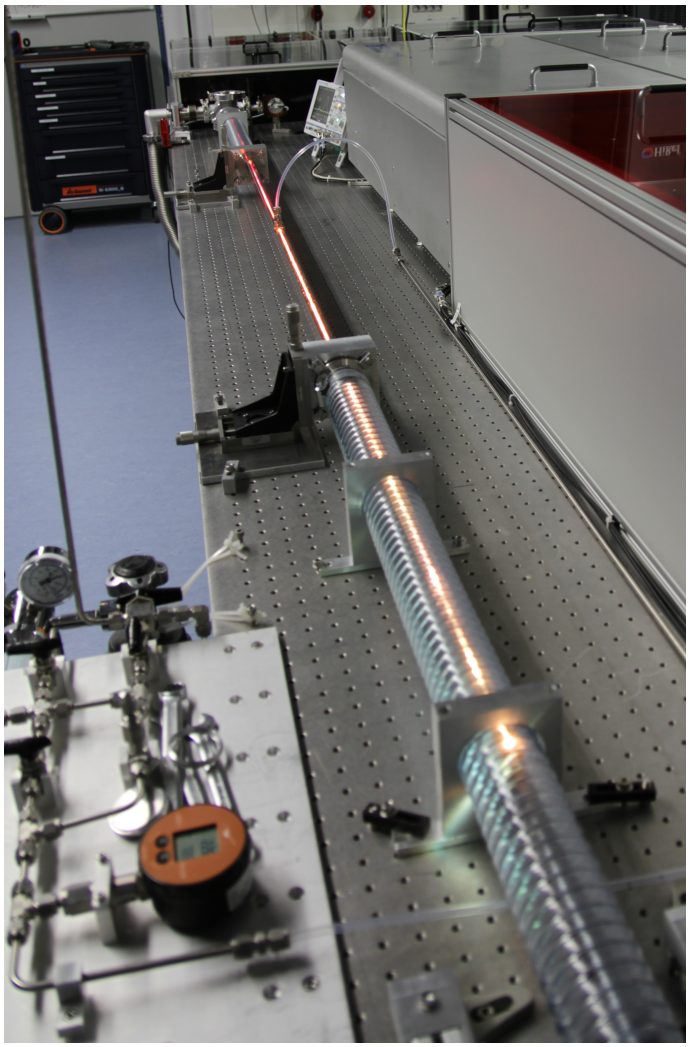

Figure A.5: Photography of the hollow-core fiber in operation.

A.4 The Molecular Orbital Structure of the H_2O Molecule

The energy level diagram of occupied MOs for the H_2O molecule (see section 6.1) is shown on the left in figure A.9. Solid and dashed lines indicate the different signs of the respective wave functions and the contributions of the single hydrogen and oxygen atomic orbitals to the specific water MOs. The latter are split into inner valence (iv) and outer valence (ov) bands. These orbitals are correspondingly illustrated on the right side in figure A.9. Here, blue and red volumes mark again the different sign of the wave functions. The $2a_1$ state is strongly O $2s$ – H $1s$ bonding and of oxygen O $2s$ character in the main. The $1b_2$ and $3a_1$ molecular orbitals are oriented in the molecular plane and largely mixed of O $2p_y$ and $2p_z$ with hydrogen H $1s$ states to build an OH bonding orbital. The $1b_1$ orbital is mainly built by the oxygen lone pair $2p_x$ and is non-bonding.

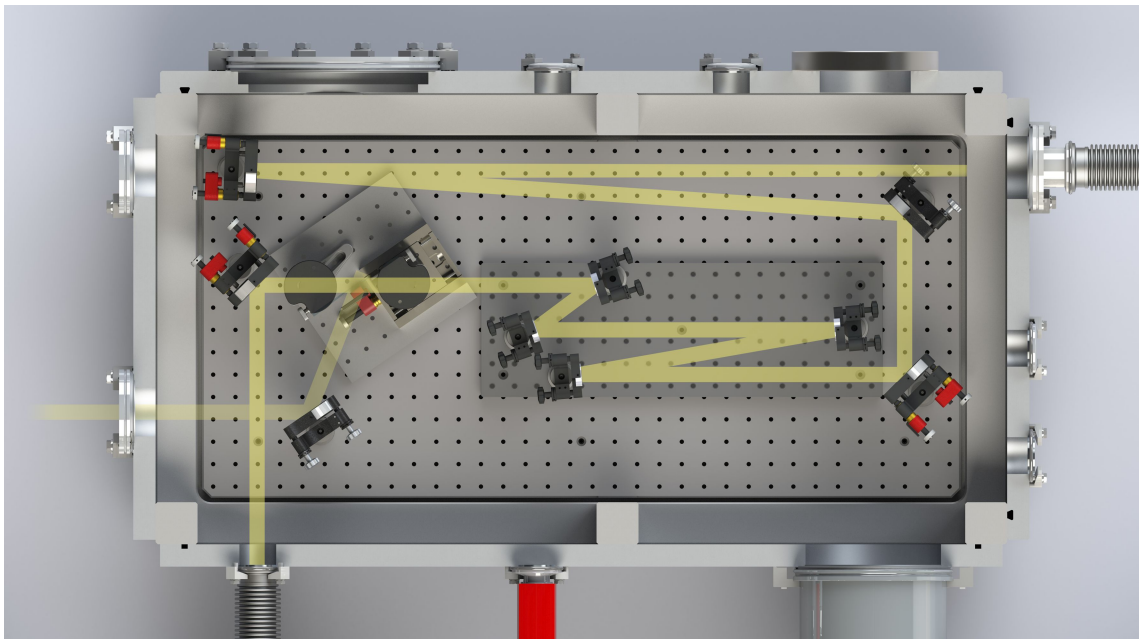

Figure A.6: Schematic CAD model of the pulse compression chamber with the chirped-mirror pulse compressor. The beam path is shown in yellow. Credit: Andreas Duensing, Technical University of Munich, Chair for Laser- and X-ray physics.

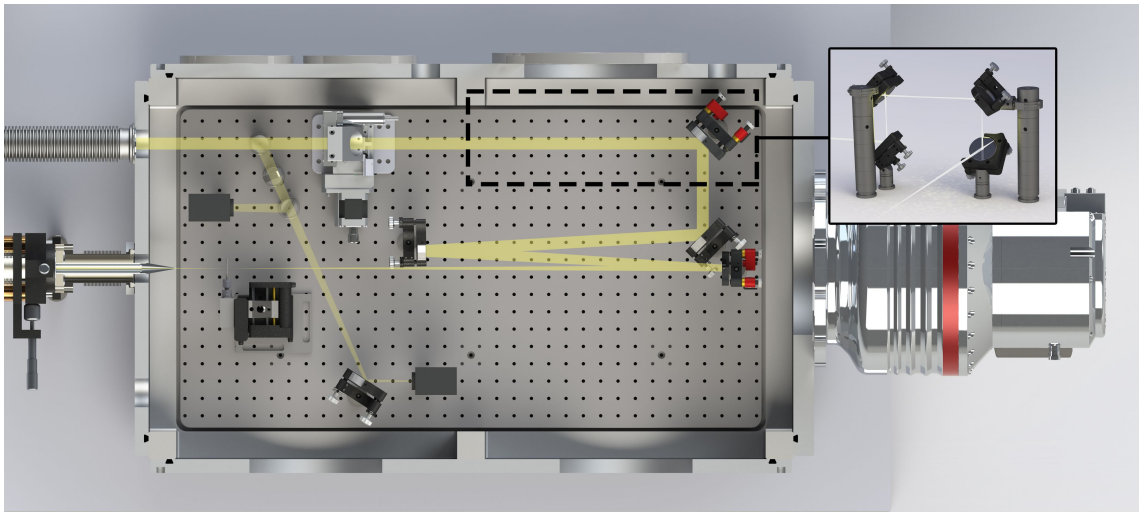

Figure A.7: Schematic depiction of the high harmonic generation chamber with the neon gas target. The beam path is shown in yellow. The periscope setup, that can be inserted for changing the polarization of the incoming laser beam from p-polarization to s-polarization, is shown in the inset. Credit: Andreas Duensing.

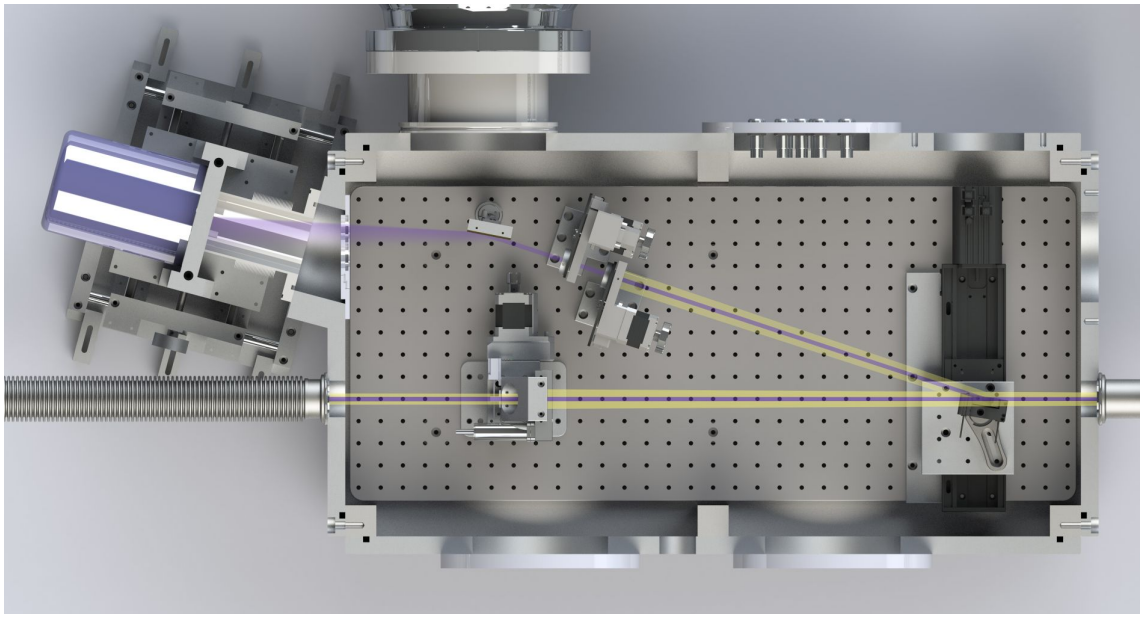

Figure A.8: Illustration of the HHG diagnostics chamber with the XUV spectrometer. The beam can be guided through filtzer wheels and via a blazed grating onto the CCD camera to detect an XUV spectrum. Credit: Andreas Duensing.

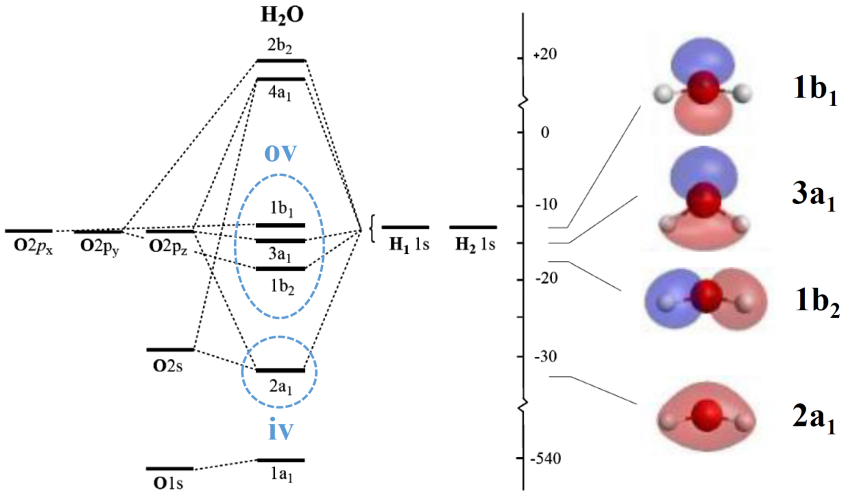

Figure A.9: Valence orbital energy level diagram and a depiction of the molecular orbitals of gas-phase H_2O. Adapted from [87].

Bibliography

1. Bhattacharjee, Y. Measuring the immeasurable. *Nature* **412,** 474–476 (2001).
2. Zewail, A. H. Femtochemistry: Atomic-scale dynamics of the chemical bond using ultrafast lasers (Nobel Lecture). *Angewandte Chemie International Edition* **39,** 2586–2631 (2000).
3. Zewail, A. H. Laser femtochemistry. *Science* **242,** 1645–1653 (1988).
4. Zewail, A. H. Femtochemistry: Atomic-Scale Dynamics of the Chemical Bond †. *The Journal of Physical Chemistry A* **104,** 5660–5694 (2000).
5. Hentschel, M., Kienberger, R., Spielmann, C., Reider, G. A., Milosevic, N., Brabec, T., Corkum, P., Heinzmann, U., Drescher, M. & Krausz, F. Attosecond metrology. *Nature* **414,** 509–513 (2001).
6. Scrinzi, A., Ivanov, M. Y., Kienberger, R. & Villeneuve, D. M. Attosecond physics. *Journal of Physics B: Atomic, Molecular and Optical Physics* **39,** R1 (2005).
7. Bucksbaum, P. H. The future of attosecond spectroscopy. *Science* **317,** 766–769 (2007).
8. Kling, M. F. & Vrakking, M. J. J. Attosecond electron dynamics. *Annual review of physical chemistry* **59,** 463–492 (2008).
9. Gallmann, L., Cirelli, C. & Keller, U. Attosecond science: Recent highlights and future trends. *Annual review of physical chemistry* **63,** 447–469 (2012).
10. Krausz, F. The birth of attosecond physics and its coming of age. *Physica Scripta* **91,** 063011 (2016).
11. Kienberger, R., Goulielmakis, E., Uiberacker, M., Baltuska, A., Yakovlev, V., Bammer, F., Scrinzi, A., Westerwalbesloh, T., Kleineberg, U., Heinzmann, U., *et al.* Atomic transient recorder. *Nature* **427,** 817 (2004).
12. Pazourek, R., Nagele, S. & Burgdörfer, J. Attosecond chronoscopy of photoemission. *Reviews of Modern Physics* **87,** 765–802 (2015).
13. Corkum, P. & Krausz, F. Attosecond science. *Nature physics* **3,** 381 (2007).
14. Krausz, F. & Ivanov, M. Attosecond physics. *Reviews of Modern Physics* **81,** 163–234 (2009).
15. Itatani, J., Quéré, F., Yudin, G. L., Ivanov, M. Y., Krausz, F. & Corkum, P. B. Attosecond streak camera. *Physical review letters* **88,** 173903 (2002).
16. Quéré, F., Mairesse, Y. & Itatani, J. Temporal characterization of attosecond XUV fields. *Journal of Modern Optics* **52,** 339–360 (2005).

17. Cavalieri, A. L., Müller, N., Uphues, T., Yakovlev, V. S., Baltuska, A., Horvath, B., Schmidt, B., Blümel, L., Holzwarth, R., Hendel, S., *et al.* Attosecond spectroscopy in condensed matter. *Nature* **449,** 1029–1032 (2007).

18. Schultze, M., Fiess, M., Karpowicz, N., Gagnon, J., Korbman, M., Hofstetter, M., Neppl, S., Cavalieri, A. L., Komninos, Y., Mercouris, T., *et al.* Delay in photoemission. *Science* **328,** 1658–1662 (2010).

19. Ossiander, M., Siegrist, F., Shirvanyan, V., Pazourek, R., Sommer, A., Latka, T., Guggenmos, A., Nagele, S., Feist, J., Burgdörfer, J., *et al.* Attosecond correlation dynamics. *Nature Physics* **13,** 280–285 (2016).

20. Drescher, M., Hentschel, M., Kienberger, R., Uiberacker, M., Yakovlev, V., Scrinzi, A., Westerwalbesloh, T., Kleineberg, U., Heinzmann, U. & Krausz, F. Time-resolved atomic inner-shell spectroscopy. *Nature* **419,** 803–807 (2002).

21. Uiberacker, M., Uphues, T., Schultze, M., Verhoef, A. J., Yakovlev, V., Kling, M. F., Rauschenberger, J., Kabachnik, N. M., Schröder, H., Lezius, M., *et al.* Attosecond real-time observation of electron tunnelling in atoms. *Nature* **446,** 627–632 (2007).

22. Klünder, K., Dahlström, J. M., Gisselbrecht, M., Fordell, T., Swoboda, M., Guénot, D., Johnsson, P., Caillat, J., Mauritsson, J., Maquet, A., *et al.* Probing single-photon ionization on the attosecond time scale. *Physical review letters* **106,** 143002 (2011).

23. Neppl, S., Ernstorfer, R., Bothschafter, E. M., Cavalieri, A. L., Menzel, D., Barth, J. V., Krausz, F., Kienberger, R. & Feulner, P. Attosecond time-resolved photoemission from core and valence states of magnesium. *Physical review letters* **109,** 087401 (2012).

24. Neppl, S., Ernstorfer, R., Cavalieri, A. L., Lemell, C., Wachter, G., Magerl, E., Bothschafter, E. M., Jobst, M., Hofstetter, M., Kleineberg, U., *et al.* Direct observation of electron propagation and dielectric screening on the atomic length scale. *Nature* **517,** 342–346 (2015).

25. Sansone, G., Kelkensberg, F., Pérez-Torres, J. F., Morales, F., Kling, M. F., Siu, W., Ghafur, O., Johnsson, P., Swoboda, M., Benedetti, E., *et al.* Electron localization following attosecond molecular photoionization. *Nature* **465,** 763–766 (2010).

26. Schultze, M., Ramasesha, K., Pemmaraju, C. D., Sato, S. A., Whitmore, D., Gandman, A., Prell, J. S., Borja, L. J., Prendergast, D., Yabana, K., *et al.* Ultrafast dynamics. Attosecond band-gap dynamics in silicon. *Science* **346,** 1348–1352 (2014).

27. Mauritsson, J., Johnsson, P., Mansten, E., Swoboda, M., Ruchon, T., L'Huillier, A. & Schafer, K. J. Coherent electron scattering captured by an attosecond quantum stroboscope. *Physical review letters* **100,** 073003 (2008).

28. Goulielmakis, E., Loh, Z.-H., Wirth, A., Santra, R., Rohringer, N., Yakovlev, V. S., Zherebtsov, S., Pfeifer, T., Azzeer, A. M., Kling, M. F., *et al.* Real-time observation of valence electron motion. *Nature* **466,** 739–743 (2010).

29. Calegari, F., Ayuso, D., Trabattoni, A., Belshaw, L., de Camillis, S., Anumula, S., Frassetto, F., Poletto, L., Palacios, A., Decleva, P., *et al.* Ultrafast electron dynamics in phenylalanine initiated by attosecond pulses. *Science* **346,** 336–339 (2014).

30. Schultze, M., Bothschafter, E. M., Sommer, A., Holzner, S., Schweinberger, W., Fiess, M., Hofstetter, M., Kienberger, R., Apalkov, V., Yakovlev, V. S., *et al.* Controlling dielectrics with the electric field of light. *Nature* **493,** 75–78 (2013).

31. Ossiander, M., Riemensberger, J., Neppl, S., Mittermair, M., Schäffer, M., Duensing, A., Wagner, M. S., Heider, R., M.Wurzer, Gerl, M., *et al.* Absolute Timing of the Photoelectric Effect. *Nature* **561,** 374–377 (2018).

32. Schultze, M., Wirth, A., Grguras, I., Uiberacker, M., Uphues, T., Verhoef, A. J., Gagnon, J., Hofstetter, M., Kleineberg, U., Goulielmakis, E., *et al.* State-of-the-art attosecond metrology. *Journal of Electron Spectroscopy and Related Phenomena* **184,** 68–77 (2011).

33. Jordan, I., Huppert, M., Brown, M. A., van Bokhoven, J. A. & Wörner, H. J. Photoelectron spectrometer for attosecond spectroscopy of liquids and gases. *The Review of scientific instruments* **86,** 123905 (2015).

34. Werhahn, J. C. *Theoretical & Experimental Investigations of Hydrogen Bonded Systems from Cluster to Bulk* (Verlag Dr. Hut, 2012).

35. Winter, B. & Faubel, M. Photoemission from liquid aqueous solutions. *Chemical reviews* **106,** 1176–1211 (2006).

36. Madey, J. M. J. Stimulated Emission of Bremsstrahlung in a Periodic Magnetic Field. *Journal of Applied Physics* **42,** 1906–1913 (1971).

37. Deacon, D. A., Elias, L., Madey, J. M., Ramian, G., Schwettman, H. & Smith, T. I. First operation of a free-electron laser. *Physical Review Letters* **38,** 892 (1977).

38. Ding, Y., Brachmann, A., Decker, F.-J., Dowell, D., Emma, P., Frisch, J., Gilevich, S., Hays, G., Hering, P., Huang, Z., *et al.* Measurements and simulations of ultralow emittance and ultrashort electron beams in the linac coherent light source. *Physical review letters* **102,** 254801 (2009).

39. Emma, P., Bane, K., Cornacchia, M., Huang, Z., Schlarb, H., Stupakov, G. & Walz, D. Femtosecond and subfemtosecond x-ray pulses from a self-amplified spontaneous-emission-based free-electron laser. *Physical review letters* **92,** 074801 (2004).

40. Huang, Z. & Kim, K.-J. Review of x-ray free-electron laser theory. *Physical Review Special Topics - Accelerators and Beams* **10,** 207 (2007).

41. Emma, P., Akre, R., Arthur, J., Bionta, R., Bostedt, C., Bozek, J., Brachmann, A., Bucksbaum, P., Coffee, R., Decker, F.-J., *et al.* First lasing and operation of an ångstrom-wavelength free-electron laser. *Nature Photonics* **4,** 641–647 (2010).

42. Pile, D. First light from SACLA. *Nature Photonics* **5,** 456–457 (2011).

43. Ackermann, W., Asova, G., Ayvazyan, V., Azima, A., Baboi, N., Bähr, J., Balandin, V., Beutner, B., Brandt, A., Bolzmann, A., *et al.* Operation of a free-electron laser from the extreme ultraviolet to the water window. *Nature Photonics* **1,** 336–342 (2007).

44. Ishikawa, T., Aoyagi, H., Asaka, T., Asano, Y., Azumi, N., Bizen, T., Ego, H., Fukami, K., Fukui, T., Furukawa, Y., *et al.* A compact X-ray free-electron laser emitting in the sub-ångström region. *Nature Photonics* **6,** 540–544 (2012).

45. Allaria, E., Appio, R., Badano, L., Barletta, W. A., Bassanese, S., Biedron, S. G., Borga, A., Busetto, E., Castronovo, D., Cinquegrana, P., *et al.* Highly coherent and stable pulses from the FERMI seeded free-electron laser in the extreme ultraviolet. *Nature Photonics* **6,** 699–704 (2012).

46. Bostedt, C., Boutet, S., Fritz, D. M., Huang, Z., Lee, H. J., Lemke, H. T., Robert, A., Schlotter, W. F., Turner, J. J. & Williams, G. J. Linac Coherent Light Source: The first five years. *Reviews of Modern Physics* **88,** 207 (2016).

47. Helml, W., Grguraš, I., Juranić, P., Düsterer, S., Mazza, T., Maier, A., Hartmann, N., Ilchen, M., Hartmann, G., Patthey, L., *et al.* Ultrashort Free-Electron Laser X-ray Pulses. *Applied Sciences* **7,** 915 (2017).

48. Young, L., Kanter, E. P., Krässig, B., Li, Y., March, A. M., Pratt, S. T., Santra, R., Southworth, S. H., Rohringer, N., DiMauro, L. F., *et al.* Femtosecond electronic response of atoms to ultra-intense X-rays. *Nature* **466,** 56–61 (2010).

49. Rudenko, A., Inhester, L., Hanasaki, K., Li, X., Robatjazi, S. J., Erk, B., Boll, R., Toyota, K., Hao, Y., Vendrell, O., *et al.* Femtosecond response of polyatomic molecules to ultra-intense hard X-rays. *Nature* **546,** 129–132 (2017).

50. Boll, R., Anielski, D., Bostedt, C., Bozek, J. D., Christensen, L., Coffee, R., De, S., Decleva, P., Epp, S. W., Erk, B., *et al.* Femtosecond photoelectron diffraction on laser-aligned molecules: Towards time-resolved imaging of molecular structure. *Physical Review A* **88,** 061402 (2013).

51. Rohringer, N., Ryan, D., London, R. A., Purvis, M., Albert, F., Dunn, J., Bozek, J. D., Bostedt, C., Graf, A., Hill, R., *et al.* Atomic inner-shell X-ray laser at 1.46 nanometres pumped by an X-ray free-electron laser. *Nature* **481,** 488–491 (2012).

52. Vinko, S. M., Ciricosta, O., Cho, B. I., Engelhorn, K., Chung, H.-K., Brown, C. R. D., Burian, T., Chalupský, J., Falcone, R. W., Graves, C., *et al.* Creation and diagnosis of a solid-density plasma with an X-ray free-electron laser. *Nature* **482,** 59–62 (2012).

53. Mara, M. W., Hadt, R. G., Reinhard, M. E., Kroll, T., Lim, H., Hartsock, R. W., Alonso-Mori, R., Chollet, M., Glownia, J. M., Nelson, S., *et al.* Metalloprotein entatic control of ligand-metal bonds quantified by ultrafast x-ray spectroscopy. *Science* **356,** 1276–1280 (2017).

54. Neutze, R., Wouts, R., van der Spoel, D., Weckert, E. & Hajdu, J. Potential for biomolecular imaging with femtosecond X-ray pulses. *Nature* **406,** 752–757 (2000).

55. Chapman, H. N., Fromme, P., Barty, A., White, T. A., Kirian, R. A., Aquila, A., Hunter, M. S., Schulz, J., DePonte, D. P., Weierstall, U., *et al.* Femtosecond X-ray protein nanocrystallography. *Nature* **470,** 73–77 (2011).

56. Seibert, M. M., Ekeberg, T., Maia, F. R. N. C., Svenda, M., Andreasson, J., Jönsson, O., Odić, D., Iwan, B., Rocker, A., Westphal, D., *et al.* Single mimivirus particles intercepted and imaged with an X-ray laser. *Nature* **470,** 78–81 (2011).

57. Barty, A., Caleman, C., Aquila, A., Timneanu, N., Lomb, L., White, T. A., Andreasson, J., Arnlund, D., Bajt, S., Barends, T. R. M., *et al.* Self-terminating diffraction gates femtosecond X-ray nanocrystallography measurements. *Nature photonics* **6,** 35–40 (2012).

58. Wernet, P., Kunnus, K., Josefsson, I., Rajkovic, I., Quevedo, W., Beye, M., Schreck, S., Grübel, S., Scholz, M., Nordlund, D., *et al.* Orbital-specific mapping of the ligand exchange dynamics of Fe(CO)5 in solution. *Nature* **520,** 78–81 (2015).

59. Minitti, M. P., Budarz, J. M., Kirrander, A., Robinson, J. S., Ratner, D., Lane, T. J., Zhu, D., Glownia, J. M., Kozina, M., Lemke, H. T., *et al.* Imaging Molecular Motion: Femtosecond X-Ray Scattering of an Electrocyclic Chemical Reaction. *Physical review letters* **114,** 255501 (2015).

60. Coquelle, N., Sliwa, M., Woodhouse, J., Schirò, G., Adam, V., Aquila, A., Barends, T. R. M., Boutet, S., Byrdin, M., Carbajo, S., *et al.* Chromophore twisting in the excited state of a photoswitchable fluorescent protein captured by time-resolved serial femtosecond crystallography. *Nature chemistry* **10,** 31–37 (2018).

61. Pande, K., Hutchison, C. D. M., Groenhof, G., Aquila, A., Robinson, J. S., Tenboer, J., Basu, S., Boutet, S., DePonte, D. P., Liang, M., *et al.* Femtosecond structural dynamics drives the trans/cis isomerization in photoactive yellow protein. *Science* **352,** 725–729 (2016).

62. Zhang, W., Alonso-Mori, R., Bergmann, U., Bressler, C., Chollet, M., Galler, A., Gawelda, W., Hadt, R. G., Hartsock, R. W., Kroll, T., *et al.* Tracking excited-state charge and spin dynamics in iron coordination complexes. *Nature* **509,** 345–348 (2014).

63. Mankowsky, R., Subedi, A., Först, M., Mariager, S. O., Chollet, M., Lemke, H. T., Robinson, J. S., Glownia, J. M., Minitti, M. P., Frano, A., *et al.* Nonlinear lattice dynamics as a basis for enhanced superconductivity in $YBa_2Cu_3O_{6.5}$. *Nature* **516,** 71–73 (2014).

64. Gorkhover, T., Adolph, M., Rupp, D., Schorb, S., Epp, S. W., Erk, B., Foucar, L., Hartmann, R., Kimmel, N., Kühnel, K.-U., *et al.* Nanoplasma dynamics of single large xenon clusters irradiated with superintense x-ray pulses from the linac coherent light source free-electron laser. *Physical review letters* **108,** 245005 (2012).

65. Milathianaki, D., Boutet, S., Williams, G., Higginbotham, A., Ratner, D., Gleason, A., Messerschmidt, M., Seibert, M. M., Swift, D., Hering, P., *et al.* Femtosecond visualization of lattice dynamics in shock-compressed matter. *Science* **342,** 220–223 (2013).

66. Fletcher, L. B., Lee, H. J., Döppner, T., Galtier, E., Nagler, B., Heimann, P., Fortmann, C., LePape, S., Ma, T., Millot, M., *et al.* Ultrabright X-ray laser scattering for dynamic warm dense matter physics. *Nature Photonics* **9,** 274–279 (2015).

67. Gauthier, M., Fletcher, L. B., Ravasio, A., Galtier, E., Gamboa, E. J., Granados, E., Hastings, J. B., Heimann, P., Lee, H. J., Nagler, B., *et al.* New experimental platform to study high density laser-compressed matter. *The Review of scientific instruments* **85,** 11E616 (2014).

68. Bonifacio, R., Pellegrini, C. & Narducci, L. M. Collective instabilities and high-gain regime free electron laser. *Optics Communications* **50,** 373 –378 (1984).

69. Krinsky, S. & Gluckstern, R. L. Analysis of statistical correlations and intensity spiking in the self-amplified spontaneous-emission free-electron laser. *Physical Review Special Topics - Accelerators and Beams* **6,** 415 (2003).

70. Helml, W., Maier, A. R., Schweinberger, W., Grguraš, I., Radcliffe, P., Doumy, G., Roedig, C., Gagnon, J., Messerschmidt, M., Schorb, S., *et al.* Measuring the temporal structure of few-femtosecond free-electron laser X-ray pulses directly in the time domain. *Nature Photonics* **8,** 950–957 (2014).

71. Grguraš, I., Maier, A. R., Behrens, C., Mazza, T., Kelly, T. J., Radcliffe, P., Düsterer, S., Kazansky, A. K., Kabachnik, N. M., Tschentscher, T., *et al.* Ultrafast X-ray pulse characterization at free-electron lasers. *Nature Photonics* **6,** 852–857 (2012).

72. Lehmann, C. S., Picón, A., Bostedt, C., Rudenko, A., Marinelli, A., Moonshiram, D., Osipov, T., Rolles, D., Berrah, N., Bomme, C., *et al.* Ultrafast x-ray-induced nuclear dynamics in diatomic molecules using femtosecond x-ray-pump–x-ray-probe spectroscopy. *Physical Review A* **94,** 013426 (2016).

73. Erk, B., Rolles, D., Foucar, L., Rudek, B., Epp, S. W., Cryle, M., Bostedt, C., Schorb, S., Bozek, J., Rouzee, A., *et al.* Ultrafast charge rearrangement and nuclear dynamics upon inner-shell multiple ionization of small polyatomic molecules. *Physical review letters* **110,** 053003 (2013).

74. Tschentscher, T. Investigation of ultrafast processes using X-ray free-electron laser radiation. *Chemical Physics* **299,** 271–276 (2004).

75. Bonifacio, R, De Salvo, L, Pierini, P, Piovella, N & Pellegrini, C. Spectrum, temporal structure, and fluctuations in a high-gain free-electron laser starting from noise. *Physical review letters* **73,** 70 (1994).

76. Saldin, E. L., Schneidmiller, E. A. & Yurkov, M. V. Statistical properties of radiation from VUV and X-ray free electron laser. *Optics Communications* **148,** 383–403 (1998).

77. Picón, A., Lehmann, C. S., Bostedt, C., Rudenko, A., Marinelli, A., Osipov, T., Rolles, D., Berrah, N., Bomme, C., Bucher, M., *et al.* Hetero-site-specific X-ray pump-probe spectroscopy for femtosecond intramolecular dynamics. *Nature communications* **7,** 11652 (2016).

78. Cavalieri, A. L., Fritz, D. M., Lee, S. H., Bucksbaum, P. H., Reis, D. A., Rudati, J., Mills, D. M., Fuoss, P. H., Stephenson, G. B., Kao, C. C., *et al.* Clocking femtosecond X rays. *Physical review letters* **94,** 114801 (2005).

79. Maltezopoulos, T., Cunovic, S., Wieland, M., Beye, M., Azima, A., Redlin, H., Krikunova, M., Kalms, R., Frühling, U., Budzyn, F., *et al.* Single-shot timing measurement of extreme-ultraviolet free-electron laser pulses. *New Journal of Physics* **10,** 033026 (2008).

80. Frühling, U., Wieland, M., Gensch, M., Gebert, T., Schütte, B., Krikunova, M., Kalms, R., Budzyn, F., Grimm, O., Rossbach, J., *et al.* Single-shot terahertz-field-driven X-ray streak camera. *Nature Photonics* **3,** 523–528 (2009).

81. Düsterer, S., Radcliffe, P., Bostedt, C., Bozek, J., Cavalieri, A. L., Coffee, R., Costello, J. T., Cubaynes, D., DiMauro, L. F., Ding, Y., *et al.* Femtosecond x-ray pulse length characterization at the Linac Coherent Light Source free-electron laser. *New Journal of Physics* **13,** 093024 (2011).

82. Riedel, R., Al-Shemmary, A., Gensch, M., Golz, T., Harmand, M., Medvedev, N., Prandolini, M. J., Sokolowski-Tinten, K., Toleikis, S., Wegner, U., *et al.* Single-shot pulse duration monitor for extreme ultraviolet and X-ray free-electron lasers. *Nature communications* **4,** 1731 (2013).

83. Maxwell, T. J., Behrens, C., Ding, Y., Fisher, A. S., Frisch, J., Huang, Z. & Loos, H. Coherent-radiation spectroscopy of few-femtosecond electron bunches using a middle-infrared prism spectrometer. *Physical review letters* **111,** 184801 (2013).

84. Behrens, C., Decker, F.-J., Ding, Y., Dolgashev, V. A., Frisch, J., Huang, Z., Krejcik, P., Loos, H., Lutman, A., Maxwell, T. J., *et al.* Few-femtosecond time-resolved measurements of X-ray free-electron lasers. *Nature communications* **5,** 3762 (2014).

85. Harmand, M., Coffee, R., Bionta, M. R., Chollet, M., French, D., Zhu, D., Fritz, D. M., Lemke, H. T., Medvedev, N., Ziaja, B., *et al.* Achieving few-femtosecond time-sorting at hard X-ray free-electron lasers. *Nature Photonics* **7,** 215–218 (2013).

86. Hartmann, N., Helml, W., Galler, A., Bionta, M. R., Grünert, J., L. Molodtsov, S., Ferguson, K. R., Schorb, S., Swiggers, M. L., Carron, S., *et al.* Sub-femtosecond precision measurement of relative X-ray arrival time for free-electron lasers. *Nature Photonics* **8,** 706–709 (2014).

87. Wagner, M. *Advancements of Attosecond Photoelectron Spectroscopy – Streaking Spectroscopy in the Liquid Phase and X-ray Pulse Characterization* PhD thesis (Technische Universität München, 2018).

88. Pellegrini, C., Marinelli, A. & Reiche, S. The physics of x-ray free-electron lasers. *Reviews of Modern Physics* **88,** 1337 (2016).

89. Schmüser, P., Dohlus, M., Rossbach, J. & Behrens, C. *Free-Electron Lasers in the Ultraviolet and X-Ray Regime* (Springer, 2014).

90. Galayda, J. N., Arthur, J., Ratner, D. F. & White, W. E. X-ray free-electron lasers—present and future capabilities [Invited]. *Journal of the Optical Society of America B* **27,** B106 (2010).

91. Murphy, J. & Pellegrini, C. Generation of high-intensity coherent radiation in the soft-x-ray and vacuum-ultraviolet region. *Journal of the Optical Society of America B* **2,** 259–264 (1985).

92. Kondratenko, A. & Saldin, E. Generating of coherent radiation by a relativistic electron beam in an ondulator. *Particle Accelerators* **10,** 207–216 (1980).

93. Kim, K.-J. Three-dimensional analysis of coherent amplification and self-amplified spontaneous emission in free-electron lasers. *Physical review letters* **57,** 1871 (1986).

94. Milton, S. V., Gluskin, E., Arnold, N. D., Benson, C., Berg, W., Biedron, S. G., Borland, M., Chae, Y. C., Dejus, R. J., Den Hartog, P. K., *et al.* Exponential gain and saturation of a self-amplified spontaneous emission free-electron laser. *Science* **292,** 2037–2041 (2001).

95. Saldin, E. L., Schneidmiller, E. A. & Yurkov, M. V. Statistical and coherence properties of radiation from x-ray free-electron lasers. *New Journal of Physics* **12,** 035010 (2010).

96. Yu, L. H. & Krinsky, S. in *Free Electron Lasers 1997* 261–266 (Elsevier, 1998).

97. Wang, J.-M. & Yu, L.-H. A transient analysis of a bunched beam free electron laser. *Nuclear Instruments and Methods in Physics Research Section A: Accelerators, Spectrometers, Detectors and Associated Equipment* **250,** 484–489 (1986).

98. Wurzer, M. *Implementation and Characterization of an Attosecond Beamline* (Technische Universität München, 2016).

99. Saleh, B. E. A. & Teich, M. C. *Fundamentals of Photonics* (John Wiley & Sons, Inc., 2007).

100. Boyd, R. W. *Nonlinear optics* (Academic press, 2008).

101. Reider, G. A. *Photonik* (Springer, 2012).

102. Diels, J.-C. & Rudolph, W. *Ultrashot Laser Pulse Phenomena: Fundamentals, Techniques, and Applications on a Femtosecond Time Scale* 2006.

103. Brabec, T. & Krausz, F. Intense few-cycle laser fields: Frontiers of nonlinear optics. *Reviews of Modern Physics* **72,** 545–591 (2000).

104. Treacy, E. Optical pulse compression with diffraction gratings. *IEEE Journal of Quantum Electronics* **5,** 454–458 (1969).

105. Szipöcs, R., Ferencz, K., Spielmann, C. & Krausz, F. Chirped multilayer coatings for broadband dispersion control in femtosecond lasers. *Optics letters* **19,** 201–203 (1994).

106. Pervak, V., Tikhonravov, A. V., Trubetskov, M. K., Naumov, S., Krausz, F. & Apolonski, A. 1.5-octave chirped mirror for pulse compression down to sub-3 fs. *Applied Physics B* **87,** 5–12 (2007).

107. Verluise, F., Laude, V., Cheng, Z., Spielmann, C. & Tournois, P. Amplitude and phase control of ultrashort pulses by use of an acousto-optic programmable dispersive filter: Pulse compression and shaping. *Optics Letters* **25,** 575 (2000).

108. Tournois, P. Acousto-optic programmable dispersive filter for adaptive compensation of group delay time dispersion in laser systems. *Optics Communications* **140,** 245–249 (1997).

109. Duensing, A. M. *Generation of High-Power, Few-Cycle Laser Pulses by Spectral Broadening in a Dfferentially Pumped Hollow-Core Fiber Setup* (Technische Universität München, 2016).

110. Zinth, W. & Körner, H.-J. *Optik, Quantenphänomene und Aufbau der Atome* 3., überarb. Aufl. (Oldenbourg, München and Wien, 1998).

111. DeMartini, F., Townes, C., Gustafson, T. & Kelley, P. Self-steepening of light pulses. *Physical Review* **164,** 312 (1967).

112. Le Blanc, C., Curley, P. & Salin, F. Gain-narrowing and gain-shifting of ultra-short pulses in Ti: Sapphire amplifiers. *Optics Communications* **131,** 391–398 (1996).

113. Nisoli, M., de Silvestri, S., Svelto, O., Szipöcs, R., Ferencz, K., Spielmann, C., Sartania, S. & Krausz, F. Compression of high-energy laser pulses below 5 fs. *Optics Letters* **22,** 522 (1997).

114. Stolen, R. & Lin, C. Self-phase-modulation in silica optical fibers. *Physical Review A* **17,** 1448 (1978).

115. Shank, C. V., Fork, R. L., Yen, R., Stolen, R. H. & Tomlinson, W. J. Compression of femtosecond optical pulses. *Applied Physics Letters* **40,** 761–763 (1982).

116. Fujimoto, J. G., Weiner, A. M. & Ippen, E. P. Generation and measurement of optical pulses as short as 16 fs. *Applied Physics Letters* **44,** 832–834 (1984).

117. Nisoli, M., de Silvestri, S. & Svelto, O. Generation of high energy 10 fs pulses by a new pulse compression technique. *Applied Physics Letters* **68,** 2793–2795 (1996).

118. Walker, B., Sheehy, B., DiMauro, L. F., Agostini, P., Schafer, K. J. & Kulander, K. C. Precision measurement of strong field double ionization of helium. *Physical review letters* **73,** 1227 (1994).

119. Bishop, D. M. & Lam, B. Ab initio study of third-order nonlinear optical properties of helium. *Physical Review A* **37,** 464 (1988).

120. Vozzi, C., Nisoli, M., Sansone, G., Stagira, S. & De Silvestri, S. Optimal spectral broadening in hollow-fiber compressor systems. *Applied Physics B* **80,** 285–289 (2005).

121. Marcatili, E. A. & Schmeltzer, R. Hollow metallic and dielectric waveguides for long distance optical transmission and lasers. *Bell Labs Technical Journal* **43,** 1783–1809 (1964).

122. Abrams, R. Coupling losses in hollow waveguide laser resonators. *IEEE Journal of Quantum Electronics* **8,** 838–843 (1972).

123. Nisoli, M., Stagira, S., de Silvestri, S., Svelto, O., Sartania, S., Cheng, Z., Lenzner, M., Spielmann, C. & Krausz, F. A novel-high energy pulse compression system: Generation of multigigawatt sub-5-fs pulses. *Applied Physics B* **65,** 189–196 (1997).

124. Robinson, J. S., Haworth, C. A., Teng, H., Smith, R. A., Marangos, J. P. & Tisch, J. The generation of intense, transform-limited laser pulses with tunable duration from 6 to 30 fs in a differentially pumped hollow fibre. *Applied Physics B* **85,** 525–529 (2006).

125. Cavalieri, A. L., Goulielmakis, E., Horvath, B., Helml, W., Schultze, M., Fieß, M., Pervak, V., Veisz, L., Yakovlev, V., Uiberacker, M., *et al.* Intense 1.5-cycle near infrared laser waveforms and their use for the generation of ultra-broadband soft-x-ray harmonic continua. *New Journal of Physics* **9,** 242 (2007).

126. McPherson, A., Gibson, G., Jara, H., Johann, U., Luk, T. S., McIntyre, I., Boyer, K. & Rhodes, C. K. Studies of multiphoton production of vacuum-ultraviolet radiation in the rare gases. *Journal of the Optical Society of America B* **4,** 595–601 (1987).

127. L'Huillier & Balcou. High-order harmonic generation in rare gases with a 1-ps 1053-nm laser. *Physical review letters* **70,** 774–777 (1993).

128. Neppl, S. *Attosecond Time-Resolved Photoemission from Surfaces and Interfaces* PhD thesis (Technische Universität München, 2012).

129. Corkum, P. B. Plasma perspective on strong field multiphoton ionization. *Physical Review Letters* **71,** 1994 (1993).

130. Lewenstein, M., Balcou, P., Ivanov, M. Y., L'Huillier, A. & Corkum, P. B. Theory of high-harmonic generation by low-frequency laser fields. *Physical Review A* **49,** 2117 (1994).

131. Constant, E., Taranukhin, V. D., Stolow, A. & Corkum, P. B. Methods for the measurement of the duration of high-harmonic pulses. *Physical Review A* **56,** 3870–3878 (1997).

132. Bucksbaum, P. H., Freeman, R. R., Bashkansky, M. & McIlrath, T. J. Role of the ponderomotive potential in above-threshold ionization. *Journal of the Optical Society of America B* **4,** 760–764 (1987).

133. Goulielmakis, E., Schultze, M., Hofstetter, M., Yakovlev, V. S., Gagnon, J., Uiberacker, M., Aquila, A. L., Gullikson, E. M., Attwood, D. T., Kienberger, R., *et al.* Single-cycle nonlinear optics. *Science* **320,** 1614–1617 (2008).

134. Antoine, L'Huillier & Lewenstein. Attosecond Pulse Trains Using High-Order Harmonics. *Physical review letters* **77,** 1234–1237 (1996).

135. Paul, P., Toma, E., Breger, P, Mullot, G., Augé, F, Balcou, P., Muller, H. & Agostini, P. Observation of a train of attosecond pulses from high harmonic generation. *Science* **292,** 1689–1692 (2001).

136. Varjú, K., Johnsson, P., Mauritsson, J., L'Huillier, A. & López-Martens, R. Physics of attosecond pulses produced via high harmonic generation. *American Journal of Physics* **77,** 389–395 (2009).

137. Baltuška, A., Udem, T., Uiberacker, M., Hentschel, M., Goulielmakis, E., Gohle, C., Holzwarth, R., Yakovlev, V., Scrinzi, A., Hänsch, T. W., *et al.* Attosecond control of electronic processes by intense light fields. *Nature* **421,** 611 (2003).

138. Chipperfield, L., Gaier, L., Knight, P., Marangos, J. & Tisch, J. Conditions for the reliable production of attosecond pulses using ultra-short laser-generated high harmonics. *Journal of Modern Optics* **52,** 243–260 (2005).

139. Christov, I. P., Murnane, M. M. & Kapteyn, H. C. High-Harmonic Generation of Attosecond Pulses in the "Single-Cycle" Regime. *Physical Review Letters* **78,** 1251–1254 (1997).

140. Drescher, M., Hentschel, M., Kienberger, R., Tempea, G., Spielmann, C., Reider, G. A., Corkum, P. B. & Krausz, F. X-ray pulses approaching the attosecond frontier. *Science* **291,** 1923–1927 (2001).

141. Kienberger, R., Hentschel, M., Uiberacker, M., Spielmann, C., Kitzler, M., Scrinzi, A., Wieland, M., Westerwalbesloh, T., Kleineberg, U., Heinzmann, U., *et al.* Steering attosecond electron wave packets with light. *Science* **297,** 1144–1148 (2002).

142. Sansone, G., Benedetti, E., Calegari, F., Vozzi, C., Avaldi, L., Flammini, R., Poletto, L., Villoresi, P., Altucci, C., Velotta, R., *et al.* Isolated single-cycle attosecond pulses. *Science* **314,** 443–446 (2006).

143. Vinogradov, A. V. Multilayer X-ray optics. *Quantum Electronics* **32,** 1113–1121 (2002).

144. Wonisch, A., Neuhäusler, U., Kabachnik, N. M., Uphues, T., Uiberacker, M., Yakovlev, V., Krausz, F., Drescher, M., Kleineberg, U. & Heinzmann, U. Design, fabrication, and analysis of chirped multilayer mirrors for reflection of extreme-ultraviolet attosecond pulses. *Applied Optics* **45,** 4147 (2006).

145. Hofstetter, M., Schultze, M., Fiess, M., Dennhardt, B., Guggenmos, A., Gagnon, J., Yakovlev, V. S., Goulielmakis, E., Kienberger, R., Gullikson, E. M., *et al.* Attosecond dispersion control by extreme ultraviolet multilayer mirrors. *Optics Express* **19,** 1767–1776 (2011).

146. Hofstetter, M., Aquila, A., Schultze, M., Guggenmos, A., Yang, S., Gullikson, E., Huth, M., Nickel, B., Gagnon, J., Yakovlev, V. S., *et al.* Lanthanum–molybdenum multilayer mirrors for attosecond pulses between 80 and 130 eV. *New Journal of Physics* **13,** 063038 (2011).

147. Salieres, P., Ditmire, T., Budil, K. S., Perry, M. D. & L'Huillier, A. Spatial profiles of high-order harmonics generated by a femtosecond Cr: LiSAF laser. *Journal of Physics B: Atomic, Molecular and Optical Physics* **27,** L217–L222 (1994).

148. Salières, P., Ditmire, T., Perry, M. D., L'Huillier, A. & Lewenstein, M. Angular distributions of high-order harmonics generated by a femtosecond laser. *Journal of Physics B: Atomic, Molecular and Optical Physics* **29,** 4771–4786 (1996).

149. Macklin, J., Kmetec, J. & Gordon III, C. High-order harmonic generation using intense femtosecond pulses. *Physical Review Letters* **70,** 766 (1993).

150. Schnürer, M., Cheng, Z., Hentschel, M., Krausz, F., Wilhein, T., Hambach, D., Schmahl, G., Drescher, M., Lim, Y. & Heinzmann, U. Few-cycle-driven XUV laser harmonics: Generation and focusing. *Applied Physics B* **70,** S227–S232 (2000).

151. Trebino, R., DeLong, K. W., Fittinghoff, D. N., Sweetser, J. N., Krumbügel, M. A., Richman, B. A. & Kane, D. J. Measuring ultrashort laser pulses in the time-frequency domain using frequency-resolved optical gating. *Review of Scientific Instruments* **68,** 3277–3295 (1997).

152. Yakovlev, V. S., Bammer, F. & Scrinzi, A. Attosecond streaking measurements. *Journal of modern optics* **52,** 395–410 (2005).

153. Goulielmakis, E., Uiberacker, M., Kienberger, R., Baltuska, A., Yakovlev, V., Scrinzi, A., Westerwalbesloh, T., Kleineberg, U., Heinzmann, U., Drescher, M., *et al.* Direct measurement of light waves. *Science* **305,** 1267–1269 (2004).

154. Nagele, S., Pazourek, R., Feist, J., Doblhoff-Dier, K., Lemell, C., Tökési, K. & Burgdörfer, J. Time-resolved photoemission by attosecond streaking: Extraction of time information. *Journal of Physics B: Atomic, Molecular and Optical Physics* **44,** 081001 (2011).

155. Bradley, D. J., Liddy, B. & Sleat, W. E. Direct linear measurement of ultrashort light pulses with a picosecond streak camera. *Optics Communications* **2,** 391–395 (1971).

156. Kinoshita, K., Ito, M. & Suzuki, Y. Femtosecond streak tube. *Review of Scientific Instruments* **58,** 932–938 (1987).

157. Siegrist, F. *Attosecond Dynamics Based on Electron Correlation and Excitation* (Technische Universität München, 2016).

158. Gallagher, T. Above-threshold ionization in low-frequency limit. *Physical review letters* **61,** 2304 (1988).

159. Corkum, P., Burnett, N. & Brunel, F. Above-threshold ionization in the long-wavelength limit. *Physical review letters* **62,** 1259 (1989).

160. Ossiander, M. T. *On the Expansion of Attosecond Streaking Spectroscopy towards Ultrafast Surface Dynamics* (Technische Universität München, 2014).

161. Mairesse, Y. & Quéré, F. Frequency-resolved optical gating for complete reconstruction of attosecond bursts. *Physical Review A* **71,** 803 (2005).

162. Gagnon, J. *Attosecond Electron Spectroscopy Theory and its Applications* PhD thesis (Ludwig-Maximilians-Universität München, 2010).

163. Kitzler, M., Milosevic, N., Scrinzi, A., Krausz, F. & Brabec, T. Quantum theory of attosecond XUV pulse measurement by laser dressed photoionization. *Physical review letters* **88,** 173904 (2002).

164. Wolkow, D. über eine klasse von lösungen der diracschen gleichung. *Zeitschrift für Physik* **94,** 250–260 (1935).

165. Wigner, E. P. Lower limit for the energy derivative of the scattering phase shift. *Physical Review* **98,** 145 (1955).

166. Shirley, D. A. High-resolution X-ray photoemission spectrum of the valence bands of gold. *Physical Review B* **5,** 4709 (1972).

167. Eckle, P., Smolarski, M., Schlup, P., Biegert, J., Staudte, A., Schöffler, M., Muller, H. G., Dörner, R. & Keller, U. Attosecond angular streaking. *Nature Physics* **4,** 565–570 (2008).

168. Eckle, P., Pfeiffer, A., Cirelli, C., Staudte, A., Dörner, R., Muller, H., Büttiker, M. & Keller, U. Attosecond ionization and tunneling delay time measurements in helium. *Science* **322,** 1525–1529 (2008).

169. Pfeiffer, A. N., Cirelli, C., Smolarski, M., Dörner, R. & Keller, U. Timing the release in sequential double ionization. *Nature Physics* **7,** 428–433 (2011).

170. Pfeiffer, A. N., Cirelli, C., Smolarski, M. & Keller, U. Recent attoclock measurements of strong field ionization. *Chemical Physics* **414,** 84–91 (2013).

171. Dietrich, P., Krausz, F. & Corkum, P. B. Determining the absolute carrier phase of a few-cycle laser pulse. *Optics Letters* **25,** 16 (2000).

172. Hartmann, N., Hartmann, G., Heider, R., Wagner, M. S., Ilchen, M., Buck, J., Lindahl, A. O., Benko, C., Grünert, J., Krzywinski, J., *et al.* Attosecond time–energy structure of X-ray free-electron laser pulses. *Nature Photonics* **12,** 215–220 (2018).

173. Kazansky, A. K., Sazhina, I. P., Nosik, V. L. & Kabachnik, N. M. Angular streaking and sideband formation in rotating terahertz and far-infrared fields. *Journal of Physics B: Atomic, Molecular and Optical Physics* **50,** 105601 (2017).

174. Kazansky, A. K., Bozhevolnov, A. V., Sazhina, I. P. & Kabachnik, N. M. Interference effects in angular streaking with a rotating terahertz field. *Physical Review A* **93,** 1307 (2016).

175. Lutman, A. A., Ding, Y., Feng, Y., Huang, Z., Messerschmidt, M., Wu, J. & Krzywinski, J. Femtosecond x-ray free electron laser pulse duration measurement from spectral correlation function. *Physical Review Special Topics - Accelerators and Beams* **15,** 030705 (2012).

176. Finetti, P., Höppner, H., Allaria, E., Callegari, C., Capotondi, F., Cinquegrana, P., Coreno, M., Cucini, R., Danailov, M. B., Demidovich, A., *et al.* Pulse Duration of Seeded Free-Electron Lasers. *Physical Review X* **7,** 021043 (2017).

177. Bionta, M. R., Hartmann, N., Weaver, M., French, D., Nicholson, D. J., Cryan, J. P., Glownia, J. M., Baker, K., Bostedt, C., Chollet, M., *et al.* Spectral encoding method for measuring the relative arrival time between x-ray/optical pulses. *The Review of scientific instruments* **85,** 083116 (2014).

178. Gahl, C., Azima, A., Beye, M., Deppe, M., Döbrich, K., Hasslinger, U., Hennies, F., Melnikov, A., Nagasono, M., Pietzsch, A., *et al.* A femtosecond X-ray/optical cross-correlator. *Nature Photonics* **2,** 165–169 (2008).

179. Ganter, R. *SwissFEL-Conceptual design report* tech. rep. (Paul Scherrer Institute (PSI), 2010).

180. Altarelli, M., Brinkmann, R, Chergui, M, Decking, W, Dobson, B, Düsterer, S, Grübel, G, Graeff, W, Graafsma, H, Hajdu, J, *et al.* The European x-ray free-electron laser. *Technical design report, DESY* **97,** 1–26 (2006).

181. Kang, H.-S., Han, J. H., Kang, T.-H., Kim, C., Kim, D. E., Kim, S. H., Ko, I. S., Lee, H.-S., Park, K.-H. & Park, S.-J. *Current Status of PAL-XFEL Project* in (2013).

182. *LCLS Overview* <https://lcls.slac.stanford.edu/overview> (2018).

183. *LCLS Parameters* <https://lcls.slac.stanford.edu/parameters> (2018).

184. Brachmann, A. LCLS-parameters-3-22-17 (2017).

185. Neal, R. B. & Blewett, J. P. The Stanford two-mile accelerator. *Physics Today* **23,** 76 (1970).

186. Akre, R., Dowell, D., Emma, P., Frisch, J., Gilevich, S., Hays, G., Hering, P., Iverson, R., Limborg-Deprey, C., Loos, H., *et al.* Commissioning the Linac Coherent Light Source injector. *Physical Review Special Topics - Accelerators and Beams* **11,** 158 (2008).

187. Fraser, J. S., Sheffield, R. L. & Gray, E. R. A new high-brightness electron injector for free electron lasers driven by RF linacs. *Nuclear Instruments and Methods in Physics Research Section A: Accelerators, Spectrometers, Detectors and Associated Equipment* **250,** 71–76 (1986).

188. Saldin, E. L., Schneidmiller, E. A. & Yurkov, M. in *Free Electron Lasers 2003* 355–359 (Elsevier, 2004).

189. Huang, Z., Borland, M., Emma, P., Wu, J., Limborg, C., Stupakov, G. & Welch, J. Suppression of microbunching instability in the linac coherent light source. *Physical Review Special Topics - Accelerators and Beams* **7** (2004).

190. Nuhn, H.-D. *LCLS undulator commissioning, alignment, and performance* tech. rep. (2009).

191. Ding, Y., Behrens, C., Coffee, R., Decker, F.-J., Emma, P., Field, C., Helml, W., Huang, Z., Krejcik, P., Krzywinski, J., *et al.* Generating femtosecond X-ray pulses using an emittance-spoiling foil in free-electron lasers. *Applied Physics Letters* **107,** 191104 (2015).

192. Ding, Y., Decker, F.-J., Emma, P., Feng, C., Field, C., Frisch, J., Huang, Z., Krzywinski, J., Loos, H., Welch, J., *et al.* Femtosecond x-ray pulse characterization in free-electron lasers using a cross-correlation technique. *Physical review letters* **109,** 254802 (2012).

193. *SLAC Today* <http://today.slac.stanford.edu/feature/2010/lcls-slotted-foil.asp> (2018).

194. Schorb, S., Rupp, D., Swiggers, M. L., Coffee, R. N., Messerschmidt, M., Williams, G., Bozek, J. D., Wada, S.-I., Kornilov, O., Möller, T., *et al.* Size-dependent ultrafast ionization dynamics of nanoscale samples in intense femtosecond x-ray free-electron-laser pulses. *Physical review letters* **108,** 233401 (2012).

195. Bozek, J. D. AMO instrumentation for the LCLS X-ray FEL. *The European Physical Journal Special Topics* **169,** 129–132 (2009).

196. Ferguson, K. R., Bucher, M., Bozek, J. D., Carron, S., Castagna, J.-C., Coffee, R., Curiel, G. I., Holmes, M., Krzywinski, J., Messerschmidt, M., *et al.* The Atomic, Molecular and Optical Science instrument at the Linac Coherent Light Source. *Journal of synchrotron radiation* **22,** 492–497 (2015).

197. *AMO Overview* <https://lcls.slac.stanford.edu/instruments/amo/overview> (2018).

198. Bostedt, C., Bozek, J. D., Bucksbaum, P. H., Coffee, R. N., Hastings, J. B., Huang, Z., Lee, R. W., Schorb, S., Corlett, J. N., Denes, P., *et al.* Ultra-fast and ultra-intense x-ray sciences: First results from the Linac Coherent Light Source free-electron laser. *Journal of Physics B: Atomic, Molecular and Optical Physics* **46,** 164003 (2013).

199. Minitti, M. P., Robinson, J. S., Coffee, R. N., Edstrom, S., Gilevich, S., Glownia, J. M., Granados, E., Hering, P., Hoffmann, M. C., Miahnahri, A., *et al.* Optical laser systems at the Linac Coherent Light Source. *Journal of synchrotron radiation* **22,** 526–531 (2015).

200. Meitner, L. Über die β-Strahl-Spektra und ihren Zusammenhang mit der γ-Strahlung. *Zeitschrift für Physik* **11,** 35–54 (1922).

201. Auger, P. Sur l'effet photoélectrique composé. *Journal de Physique et le Radium* **6,** 205–208 (1925).

202. Burhop, E. H. S. *The Auger effect and other radiationless transitions* (Cambridge University Press, 2014).

203. Chattarji, D. *The theory of Auger transitions* (Elsevier, 2012).

204. Allaria, E., Diviacco, B., Callegari, C., Finetti, P., Mahieu, B., Viefhaus, J., Zangrando, M., de Ninno, G., Lambert, G., Ferrari, E., *et al.* Control of the Polarization of a Vacuum-Ultraviolet, High-Gain, Free-Electron Laser. *Physical Review X* **4,** 1 (2014).

205. Gagnon, J. & Yakovlev, V. S. The direct evaluation of attosecond chirp from a streaking measurement. *Applied Physics B* **103,** 303–309 (2011).

206. Krause, M. O., Stevie, F. A., Lewis, L. J., Carlson, T. A. & Moddeman, W. E. Multiple excitation of neon by photon and electron impact. *Physics Letters A* **31,** 81–82 (1970).

207. Schmidt, V. Photoionization of atoms using synchrotron radiation. *Reports on Progress in Physics* **55,** 1483–1659 (1992).

208. Schmidt, V. *Electron Spectrometry of Atoms using Synchrotron Radiation* (Cambridge University Press, 1997).

209. Cooper, J. & Zare, R. N. Angular Distribution of Photoelectrons. *The Journal of chemical physics* **48,** 942–943 (1968).

210. Becker, U. & Shirley, D. A. *VUV and Soft X-ray Photoionization* (Springer Science & Business Media, 2012).

211. Ottosson, N., Faubel, M., Bradforth, S. E., Jungwirth, P. & Winter, B. Photoelectron spectroscopy of liquid water and aqueous solution: Electron effective attenuation lengths and emission-angle anisotropy. *Journal of Electron Spectroscopy and Related Phenomena* **177,** 60–70 (2010).

212. Hoffmann, M. C., Grguraš, I., Behrens, C., Bostedt, C., Bozek, J., Bromberger, H., Coffee, R., Costello, J. T., DiMauro, L. F., Ding, Y., *et al.* Femtosecond profiling of shaped x-ray pulses. *New Journal of Physics* **20,** 033008 (2018).

213. Kazansky, A. K., Sazhina, I. P. & Kabachnik, N. M. Angle-resolved electron spectra in short-pulse two-color XUV + IR photoionization of atoms. *Physical Review A* **82,** 1847 (2010).

214. Ding, Y., Behrens, C., Emma, P., Frisch, J., Huang, Z., Loos, H., Krejcik, P. & Wang, M.-H. Femtosecond x-ray pulse temporal characterization in free-electron lasers using a transverse deflector. *Physical Review Special Topics - Accelerators and Beams* **14,** 120701 (2011).

215. Schneidmiller, E. & Yurkov, M. *Photon beam properties at the European XFEL* (DESY, 2011).

216. Raubenheimer, T. *et al. The LCLS-II, a new FEL facility at SLAC* in *These Proceedings: Proc. 36th Int. Free-Electron Laser Conf., Basel* (2014).

217. Raubenheimer, T. *et al.* LCLS-II: status of the CW X-ray FEL upgrade to the SLAC LCLS facility. *Proceedings of FEL 2015* (2015).

218. *FEMTOSOURCE rainbow - OPERATORS MANUAL* V1.2. Femtolasers Produktions GmbH (Fernkorngasse 10, 1100 Vienna, Austria, 2014).

219. Stingl, A., Lenzner, M., Spielmann, C., Krausz, F. & Szipöcs, R. Sub-10-fs mirror-dispersion-controlled Ti: sapphire laser. *Optics letters* **20,** 602–604 (1995).

220. *Femtopower HEHR CEP4 - User manual* V1.00. Femtolasers Produktions GmbH (Fernkorngasse 10, 1100 Vienna, Austria, 2015).

221. Strickland, D. & Mourou, G. Compression of amplified chirped optical pulses. *Optics Communications* **55,** 447–449 (1985).

222. Sartania, S., Cheng, Z., Lenzner, M., Tempea, G., Spielmann, C., Krausz, F. & Ferencz, K. Generation of 01-TW 5-fs optical pulses at a 1-kHz repetition rate. *Optics Letters* **22,** 1562 (1997).

223. *CEP4 SEED Module for FEMTOSOURCE rainbow - OPERATORS MANUAL* V1.3. Femtolasers Produktions GmbH (Fernkorngasse 10, 1100 Vienna, Austria, 2013).

224. Koke, S., Grebing, C., Frei, H., Anderson, A., Assion, A. & Steinmeyer, G. Direct frequency comb synthesis with arbitrary offset and shot-noise-limited phase noise. *Nature Photonics* **4,** 462–465 (2010).

225. Lücking, F., Assion, A., Apolonski, A., Krausz, F. & Steinmeyer, G. Long-term carrier-envelope-phase-stable few-cycle pulses by use of the feed-forward method. *Optics letters* **37,** 2076–2078 (2012).

226. Nurhuda, M., Suda, A., Midorikawa, K., Hatayama, M. & Nagasaka, K. Propagation dynamics of femtosecond laser pulses in a hollow fiber filled with argon: Constant gas pressure versus differential gas pressure. *Journal of the Optical Society of America B* **20,** 2002 (2003).

227. Nurhuda, M., Suda, A., Midorikawa, K. & Budiono, H. Control of self-phase modulation and plasma-induced blueshifting of high-energy, ultrashort laser pulses in an argon-filled hollow fiber using conjugate pressure-gradient method. *Journal of the Optical Society of America B* **22,** 1757 (2005).

228. Nurhuda, M., Suda, A., Kaku, M. & Midorikawa, K. Optimization of hollow fiber pulse compression using pressure gradients. *Applied Physics B* **89,** 209–215 (2007).

229. Shirvanyan, V. *Generation of sub-4-fs, mJ pulses via hollow-core fiber nonlinear pulse compression by the conjugate pressure-gradient method* (Technische Universität München, 2015).

230. Pollanka, M. *Characterization and Optimization of a Hollow-Core Fiber Compressor for Attosecond Experiments* (Technische Universität München, 2017).

231. Telle, H. R., Steinmeyer, G., Dunlop, A. E., Stenger, J., Sutter, D. H. & Keller, U. Carrier-envelope offset phase control: A novel concept for absolute optical frequency measurement and ultrashort pulse generation. *Applied Physics B* **69,** 327–332 (1999).

232. Späh, A. J. *Development, Design and Implementation of an Ultra-High Vacuum Chamber for Gas-Phase Attosecond Streaking Spectroscopy* (Technische Universität München, 2015).

233. Waki, I. & Hirai, Y. The silicon L-edge photoabsorption spectrum of silicon carbide. *Journal of Physics: Condensed Matter* **1,** 6755–6762 (1989).

234. Neddermeyer, H. X-ray emission and absorption edges of magnesium and aluminum. *Physical Review B* **13,** 2411 (1976).

235. Ossiander, M. *Attosecond Photoemission Timing* PhD thesis (Technische Universität München, 2018).

236. Hütten, K., Mittermair, M., Stock, S. O., Beerwerth, R., Shirvanyan, V., Riemensberger, J., Duensing, A., Heider, R., Wagner, M. S., Guggenmos, A., *et al.* Ultrafast quantum control of ionization dynamics in krypton. *Nature communications* **9,** 719 (2018).

237. Kim, A. *Attosecond time-resolved photoemission from solid samples* PhD thesis (Technische Universität München, 2015).

238. Maréchal, Y. The hydrogen bond and the water molecule (2007).

239. Onsager, L. & Samaras, N. N. T. The Surface Tension of Debye–Hückel Electrolytes. *The Journal of chemical physics* **2,** 528–536 (1934).

240. Hertz, H. & Franks, F. Water: A comprehensive treatise. *by F. Franks, Plenum Press, New York* **3** (1973).

241. Stillinger, F. H. Water revisited. *Science* **209,** 451–457 (1980).

242. Wilse, R. G., Surjit, S., *et al. Water in biology, chemistry and physics: experimental overviews and computational methodologies* (World Scientific, 1996).

243. Barthel, J. M., Krienke, H. & Kunz, W. *Physical chemistry of electrolyte solutions: modern aspects* (Springer Science & Business Media, 1998).

244. Bockris, J. O. & Reddy, A. K. Ion-ion interactions. *Modern Electrochemistry 1: Ionics,* 225–359 (1998).

245. Adamson, A. Physical Chemistry of Surfaces,(5th ed.) *Wiley: New York* (1990).

246. Gouy, G. Sur la constitution de la charge électrique à la surface d'un électrolyte. *Journal de Physique Théorique et Appliquée* **9,** 457–468 (1910).

247. Gouy, G. Sur la fonction électrocapillaire. **9,** 129–184 (1917).

248. Chapman, D. L. LI. A contribution to the theory of electrocapillarity. *The London, Edinburgh, and Dublin Philosophical Magazine and Journal of Science* **25,** 475–481 (1913).

249. Debye, P & Hückel, E. De la theorie des electrolytes. I. abaissement du point de congelation et phenomenes associes. *Physikalische Zeitschrift* **24,** 185–206 (1923).

250. Ball, P. Water: Water – an enduring mystery. *Nature* **452,** 291 (2008).

251. Fecko, C., Eaves, J., Loparo, J., Tokmakoff, A. & Geissler, P. Ultrafast hydrogen-bond dynamics in the infrared spectroscopy of water. *Science* **301,** 1698–1702 (2003).

252. Asbury, J. B., Steinel, T., Stromberg, C., Corcelli, S. A., Lawrence, C. P., Skinner, J. L. & Fayer, M. D. Water Dynamics: Vibrational Echo Correlation Spectroscopy and Comparison to Molecular Dynamics Simulations. *The Journal of Physical Chemistry A* **108,** 1107–1119 (2004).

253. Bakker, H. J., Kropman, M. F., Omta, A. W. & Woutersen, S. Hydrogen-Bond Dynamics of Water in Ionic Solutions. *Physica Scripta* **69,** C14–C24 (2004).

254. Hutzler, D., Werhahn, J. C., Heider, R., Bradler, M., Kienberger, R., Riedle, E. & Iglev, H. Highly Selective Relaxation of the OH Stretching Overtones in Isolated HDO Molecules Observed by Infrared Pump–Repump–Probe Spectroscopy. *J. Phys. Chem. A* **119,** 6831–6836 (2015).

255. Hutzler, D. *Time-Resolved Infrared Spectroscopy on Hydrogen Bonded Systems* PhD thesis (Technische Universität München, 2017).

256. Huse, N., Ashihara, S., Nibbering, E. T. & Elsaesser, T. Ultrafast vibrational relaxation of O–H bending and librational excitations in liquid H2O. *Chemical Physics Letters* **404,** 389–393 (2005).

257. Cowan, M. L., Bruner, B. D., Huse, N., Dwyer, J. R., Chugh, B., Nibbering, E. T. J., Elsaesser, T. & Miller, R. J. D. Ultrafast memory loss and energy redistribution in the hydrogen bond network of liquid H2O. *Nature* **434,** 199 (2005).

258. Woutersen, S. & Bakker, H. J. Resonant intermolecular transfer of vibrational energy in liquid water. *Nature* **402,** 507–509 (1999).

259. Xenides, D., Randolf, B. R. & Rode, B. M. Structure and ultrafast dynamics of liquid water: A quantum mechanics/molecular mechanics molecular dynamics simulations study. *The Journal of chemical physics* **122,** 174506 (2005).

260. Jimenez, R., Fleming, G. R., Kumar, P. V. & Maroncelli, M. Femtosecond solvation dynamics of water. *Nature* **369,** 471 (1994).

261. Brown, M. A., Redondo, A. B., Jordan, I., Duyckaerts, N., Lee, M.-T., Ammann, M., Nolting, F., Kleibert, A., Huthwelker, T., Mächler, J.-P., *et al.* A new endstation at the Swiss Light Source for ultraviolet photoelectron spectroscopy, X-ray photoelectron spectroscopy, and X-ray absorption spectroscopy measurements of liquid solutions. *Review of Scientific Instruments* **84,** 073904 (2013).

262. Faubel, M., Steiner, B. & Toennies, J. P. Photoelectron spectroscopy of liquid water, some alcohols, and pure nonane in free micro jets. *The Journal of chemical physics* **106,** 9013–9031 (1997).

263. Wilson, K. R., Rude, B. S., Catalano, T., Schaller, R. D., Tobin, J. G., Co, D. T. & Saykally, R. J. X-ray Spectroscopy of Liquid Water Microjets. *The Journal of Physical Chemistry B* **105,** 3346–3349 (2001).

264. Winter, B., Weber, R., Widdra, W., Dittmar, M., Faubel, M. & Hertel, I. V. Full Valence Band Photoemission from Liquid Water Using EUV Synchrotron Radiation. *The Journal of Physical Chemistry A* **108,** 2625–2632 (2004).

265. Banna, M. S., McQuaide, B. H., Malutzki, R. & Schmidt, V. The photoelectron spectrum of water in the 30 to 140 eV photon energy range. *The Journal of chemical physics* **84,** 4739–4744 (1986).

266. Jordan, I. *Attosecond time-resolved photoelectron spectroscopy of liquid systems* PhD thesis (ETH Zurich, 2017).

267. Temelso, B., Archer, K. A. & Shields, G. C. Benchmark structures and binding energies of small water clusters with anharmonicity corrections. *The journal of physical chemistry. A* **115,** 12034–12046 (2011).

268. Faubel, M., Schlemmer, S. & Toennies, J. P. A molecular beam study of the evaporation of water from a liquid jet. *Zeitschrift für Physik D Atoms, Molecules and Clusters* **10,** 269–277 (1988).

269. Lundholm, M., Siegbahn, H., Holmberg, S. & Arbman, M. Core electron spectroscopy of water solutions. *Journal of Electron Spectroscopy and Related Phenomena* **40,** 163–180 (1986).

270. Seiffert, L., Liu, Q., Zherebtsov, S., Trabattoni, A., Rupp, P., Castrovilli, M. C., Galli, M., Süßmann, F., Wintersperger, K., Stierle, J., *et al.* Attosecond chronoscopy of electron scattering in dielectric nanoparticles. *Nature Physics* **13,** 766–770 (2017).

271. Baykusheva, D. & Wörner, H. J. Theory of attosecond delays in molecular photoionization. *The Journal of chemical physics* **146,** 124306 (2017).

272. Peper, M. *Electron Scattering Effects on the Attosecond Photoelectron Spectroscopy of Liquid Water* (ETH Zurich, 2016).

273. Wörner, H. J. private communication.

274. Thürmer, S., Seidel, R., Faubel, M., Eberhardt, W., Hemminger, J. C., Bradforth, S. E. & Winter, B. Photoelectron angular distributions from liquid water: Effects of electron scattering. *Physical review letters* **111,** 173005 (2013).

275. Suzuki, Y.-I., Nishizawa, K., Kurahashi, N. & Suzuki, T. Effective attenuation length of an electron in liquid water between 10 and 600 eV. *Physical review. E* **90,** 010302 (2014).

276. Lawson, C. L. & Hanson, R. J. *Solving least squares problems* (Society for Industrial and Applied Mathematics, 1995).

Acknowledgements

At this point, I want to thank all those who have supported me and have contributed to the success of this thesis during the last years. Without these people, this thesis would not have been possible.

First of all, my sincere thank you goes to my doctorate supervisor, **Prof. Dr. Reinhard Kienberger**, for providing me the opportunity to perform my doctoral thesis at the *Chair for Laser and X-ray Physics E11* at the *Technische Universität München*. I want to thank him for all his support, trust and advice. I really appreciate that he has given me plenty of rope in all respects of my work. Thanks for providing me access to an exciting and expensive, state-of-the-art setup and for affording for me the various business trips abroad for fascinating beamtimes and interesting conferences. He supported me in all aspects, comprising scientific discussions, but also organizational and bureaucratic issues. His personal handling and his commitment as well as the various community events, celebrations and traditional chair trips are not self-evident but something special.

A warm thank you to my direct supervisor, colleague and friend, **Dr. Wolfram Helml**, for the great mentoring and guidance. Thank you for the opportunity to actively participate in the FEL beamtimes at LCLS and for entrusting me with the data analysis of this important project. Our collaboration in this project extraordinary. He also supported me in all aspects concerning the commissioning of the beamline and the streaking experiments here at the chair. I am very grateful for long and fruitful discussions, for his advice and for sharing his expertise and experience with me.

Special thanks goes to my direct colleague and fantastic friend, **Martin Wagner**, for the excellent atmosphere and the great collaboration during our projects. Such a close teamwork over such a long period of time is really remarkable and I highly appreciate it. It doesn't need any more words to express that my thesis would not have been possible without him and our team. Thank you for the incredible time within the last years, old friend!

Martin and I had the honor and pleasure of being part of an extraordinary team in our laboratories 101/107 and our office 102/104. A big thank you goes to my teammates and bureau roommates **Andreas Duensing**, **Markus Wurzer**, **Michael Mittermair** and **Alexander Späh,** who, during their master theses and most of them later as PhD students, have substantially contributed to the achievements and successes realized. All this would have never been achievable without these fantastic guys. Thank you so much for all those milestones!

Special thanks goes to **Andreas Duensing** for the CAD models of our AS101 vacuum beamline.

My thanks also goes to California, to **Dr. Ryan Coffee** and **Dr. Nick Hartmann** for an amazing time together and the great collaboration during our FEL beamtimes at LCLS and the subsequent discussions concerning the data analysis. Thank you to all members of our international FEL science collaboration, it was an experience to remember.
I also want to thank our partners from ETH Zurich, **Prof. Dr. Hans-Jakob Wörner**, **Arohi Jain** and **Dr. Thomas Gaumnitz** for the good collaboration during our QUTIF project.

Thanks to all the members of the E11 chair not mentioned before, especially to **Martin Wörle**, for a great time, fruitful cooperation and a fantastic working environment. Thanks to **Marcus Ossiander**, **Johann Riemensberger**, **Vahe Shirvanyan** and **Tobias Latka**, for their help and advice.

A big *Dankeschön* to our workshop team, **Wolfgang Dürichen** and **Lukas Loidl**, who always supported and sometimes rescued us with their work, spontaneity and ideas. They were available for any mechanical issues and requirements that occurred during the experiments and made almost everything realizable. Thank you to our secretaries **Susi Würzinger** and **Stefanie Völkl**, who always helped me with any bureaucratic issues to be dealt with.

I want to thank all my friends, for the quality time together and all the very welcome distractions, for nice conversations about everything except off physical topics and finally, for just being friends. I am glad to have you, guys.

Last but not least, all this could not have come true without the love and support of my family. I want to thank my parents, **Astrid** and **Rupert**, my sisters **Julia** and **Alexandra** and my uncle **Michael** for always being there for me. I am blessed that I can always count on you, no matter what I need. Thank you!

At the very end, I want to express special thanks to my wonderful girlfriend **Pia**. Thank you for your support, your patience and your love.